BIO-INSPIRED ANTENNAL TACTILE SENSING

by

Alican Demir

A dissertation submitted to The Johns Hopkins University in conformity with the requirements for the degree of Doctor of Philosophy.

Baltimore, Maryland

December, 2014

Abstract

Vision dominates perception research in robotics and biology, but for many animals, it is not the dominant sensory system. Indeed, arthropods often rely on sensory cues sampled via a pair of passive head-mounted antennae to achieve navigation and control. These mechanosensory structures support multimodal receptors—tactile, hygrometric, thermal, olfactory—enabling a wide range of sensorimotor behaviors.

One model biological system, *Periplaneta americana* cockroach, performs a remarkably robust escape behavior by using its long, slender, flexible antennae to facilitate rapid closed-loop course control. The antenna is a passive, hyper-redundant kinematic linkage that acts as a distributed tactile sensory structure to mediate mechanical interactions with the environment at very high rates. This thesis demonstrates that the antennal mechanics are tuned to enable high-speed, high-bandwidth locomotor control even in total darkness.

Despite the extraordinary success of antennal sensing in nature, there are few effec-

ABSTRACT

tive bio-inspired antennae. To incorporate similar antennal sensing capability in agile mobile robots, I developed a tunable bio-inspired modular robotic research antenna and experimentation platform. I also synthesized numerical models to approximate antenna mechanics under relevant boundary conditions, which I verified against my physical model. Both numerical simulations and physical experiments were conducted to isolate fundamental parameters that underly the stability and performance I observed in the biological model.

Using a combination of numerical and robotic experiments, in concert with biological experiments conducted by my collaborators, I discovered that several behaviorally relevant characteristics of an antennae are predominantly governed by a combination of (1) the stiffness profile of the antenna and (2) the interaction of hairlike mechano-structures along the length of the antenna. I found that the "right" combination of these features improves the postural stability and the steady state spatial acuity of tactile interaction with the environment. Specifically, antennae with an exponentially decreasing stiffness profile accompanied by distally pointing anisotropic mechano-hairs are ideal for navigation tasks, and greatly facilitate stable high-speed wall following.

Primary Reader: Noah J. Cowan

Secondary Readers: Robert J. Full, Louis Whitcomb, Marin Kobilarov

Acknowledgments

I would like to mention some of those, who accompanied me in this journey and committed time and resources when I needed.

First and foremost I would like to thank my mentor and advisor Prof. Noah Cowan, for giving me the opportunity to follow my dreams in this wonderful institution and seeing me through more than half of my academic life. I would like to thank Jean Michel Mongeau and his advisor Prof. Bob Full for their vital collaboration which provided all that amazing biological context to my research. I also would like to thank my committee members Prof. Louis Whitcomb and Prof. Marin Kobilarov, not only for their valuable comments on this thesis but also for the wonderful courses that I had the privilege to take. I consider myself very fortunate to be tutored by the great and esteemed teachers of the Department of Mechanical Engineering and the Whiting School from Prof. Bill Sharpe to Prof. K.T. Ramesh; from Prof. Carey Priebe to Prof. Danielle Tarraf and from Prof. Russ Taylor to Prof. Allison Okamura. I would

like to thank them for their invaluable mentorship. Throughout eleven years, I got the chance to meet many LIMBS and LCSR members, who became family: Jusuk, Vinutha, John, Terrence, Eatai, Shahin, Sarah, Ali, Mert, Berk, Robert, Ravi and many others. Their friendship as colleagues and workmanship as top class researchers had a true impact on me as an engineer and coworker. I would like to acknowledge Ned and Caitlin, who worked hard in the laboratory, conducted experiments and collected data. I would like to extend a special thanks to Mike Bernard for being the best administrator I have ever known and for just being a wonderful person. I would also like to acknowledge Jamie Meehan, Alison Morrow, Rich Middlestadt, Bob Blakely, Niel Leon and for facilitating my research and National Science Foundation for their generous funding. Last but not least, I would like to thank my love Erin, who had to suffer through the construction of the thesis. Finally, I would like to thank my parents and brother, who have supported me in every way with their unending love and care.

Dedication

To my loving parents and dear brother...

Contents

List of Tables

List of Figures

Chapter 1

Introduction

LT. CMDR. DATA:

Sir, does tactile contact alter your perception of the Phoenix?

CAPT. JEAN-LUC PICARD:

Oh, yes! For humans, touch can connect you to an object in a very personal way, make it seem more real.

LT. CMDR. DATA: [*Puts his hand also on the Phoenix.*]

I am detecting imperfections in the titanium casing... temperature variations in the fuel manifold... it is no more "real" to me now than it was a moment ago.

(Star Trek, The First Contact —1996)

CHAPTER 1. INTRODUCTION

Animals—we humans included—interact with their environment through self movement (or locomotion) and perception. Locomotion is a process of expending energy to move in space, whereas perception is the interpretation of mechanical, electromagnetic and (or) chemical energy transduced by the sensory system. The combination of these two abilities at any degree enables *interaction*, which I simply term *behavior*.

In the field of robotic research, engineers and scientists constantly strive to develop better mechanisms for both perception and locomotion in order to enable complex behaviors, and thus naturally look to the animal kingdom for inspiration.

The analysis and synthesis of animal *behavior* and the underlying mechanisms of both locomotion and perception constitutes the essence of all research at our laboratory: Locomotion in Mechanical and Biological Systems. As a *bio-inspired robotics* laboratory, we use engineering tools from control theory and robotic experiments to come up with useful models to elicit the fundamental mechanics behind the observed behavior of animals.

My research focuses on the mechanics of passive distributed tactile sensing inspired by the American cockroach, a model system and high-performance tactile navigator. It's primary sensing organs, a pair of long slender antennae protruding from its head, are a remarkable example of passive appendages specialized for sensing without discernibly manipulating the environment. In other words, the antennae's configuration cannot be set by the animal without the presence of the environment. On the other

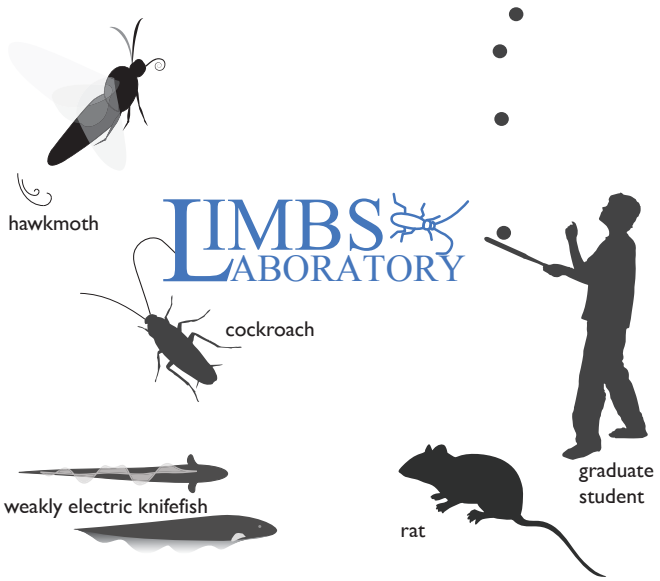

Figure 1.1: In LIMBS, we study multiple behaviors in cockroaches, electric fish, moths, rats, monkeys and last but not least, humans.

hand, when the environment is present, it is a tactile sensing organ whose configuration provides information about the ambient surface properties such as texture, temperature, hardness etc.

Sections 1.1, 1.2 and 1.3 are reproduced from my Master's Essay [1] with updates.

1.1 Tactile Sensing

Tactile sensing is the transduction and measurement of ambient energy through physical contact between the sensor and the object [2, 3]. Mechanical, thermal, chemical, and other physical attributes of objects can be sensed by various tactile receptors [3]

via a general event called *touch*. In animals, the corresponding induced feedback or the "sense of touch", which can occur from multiple points in different forms simultaneously, is then interpreted so that properties such as surface roughness, shape, hardness, viscoelasticity, texture, force distribution, inertia and temperature [3–5] can be perceived. Tactile sensing can be realized by tactile perception organs like the skin in humans [3, 6], antennae in many arthropods [7–12], or whiskers in some mammals [13]. The definition of tactile sensing does not change from biology to technology, so tactile sensing should be considered a blanket term that has as many categories as the different properties that can be measured via physical contact. This includes all the different modes of touch, like single-continuous contacts to measure temperatures or point forces, single-repeated impacts to measure impulses, double contacts to measure point-to-point distances, or 2D array-like contacts to measure heat transfer rate, pressure, etc. The instrument of the sensor that achieves this mechanical to electrical translation are called tactile sensory transducers.

There are many transducer technologies currently available for various tactile applications. Common tactile transducers exploit the changes in electrical properties like resistance, conductance, capacitance and inductance using piezoelectric, pyroelectric, magnetoelectric, mechanical, optical, or ultrasonic methods. Nicholls et al. [4] presents a comprehensive survey of the underlying methods of different transducer technologies. Most of these devices focus on characterizing the direction and magnitude of forces that act on the sensitive surface. A typical device consists of a surface

pad with a linear or rectangular array of scalar valued sensing points [14].

Artificial tactile sensing and active touch in general were slow to develop and sometimes regarded as neglected fields compared to optical sensing and computer vision, which have reached a level of maturity whereby commercial hardware and software packages are now widely available [2,14]. This delay may be caused by the distributed nature of tactile sensing, since it does not have localized sensory organ like the eye or ear that is solely dedicated to a single sensing modality. Indeed, tactile organs like *the skin* or *the antenna*, are in essence substrates or platforms for various distributed single-modal receptors that are all triggered by touch but measure different object properties. Still, despite the extensive utilization of antennae in nature, development and implementation of their mechatronic counterparts – although inspirational and encouraging – has only recently started to gain momentum with the emergence of haptics research. The technology to enable antennal artificial tactile sensing for a large scale of applications already exists, but the supporting research on how to design and tune such sensors for specific tasks is extremely limited.

1.2 Why Insects and Antennae?

Insects are one of the most successful species, if not the most successful. Some of the earliest insect species are still alive; the total insect biomass outweighs all other

animals [15], and their sheer variety dominates all other life forms. In fact, the upper limit for the Earth's entire biological species diversity is estimated from 3 million to 30 million or 50 million with more than 70 % belonging to the animal kingdom [16]. Of all the animal species, more than 95 % are invertebrates with vast majority being taken up by arthropods[1] ranging from an estimated 2.5 million up to 5 million [17] to 30 million [18] species out of which practically all are insects. Also constituting about three quarter million of the actually catalogued 1.5 million life forms [19], terrestrial insects are thus by far the most numerously classified living organisms yet. Indeed from a justifiable perspective (alien point of view) and with quite insignificant error margin, "all species are insects" [16].

Consequently it follows that with a very crude approximation that almost all species on the planet Earth have antennae. So, antennae are arguably nature's multi-sensorial packaging form-factor of choice. With an evolution history over 400 million years [20] and capacity to encompass a very large number (on the order of tens to hundreds of thousands) of diverse sensilla[2] categorized as mechanoreceptors, chemoreceptors, thermoreceptors and hygroreceptors[3] [21], the antennae are indispensable superstructures to all insects and other hexapods—Collembola and Diplura—. In fact, with the exception of members of the subclass, Protura[4], which have neither antennae nor

[1] Arthropods are invertebrate having jointed limbs and a segmented body with an exoskeleton made of chitin

[2] A sensillum is a simple sensory receptor consisting of one cell or a few cells, especially a hair-like epithelial cell projecting through the cuticle of arthropods.

[3] A hygroreceptor is a sensor that discriminates moisture levels

[4] Protura are sometimes classified as a class on its own under the phylum of hexapods.

eyes, all insects (or hexapods) possess a pair of antennae [22].

The ubiquity of this primarily sensory organ [21]—antenna—is not without reason. My model system, the American cockroach (*Periplaneta americana*), for instance, makes use of its antenna as tactile feelers [23] to sense surrounding objects such as walls for navigational guidance. Even if blinded, they execute this task so well that they can reach to speeds up to $80^{cm}/_{s}$ (or about 25 body lengths/s) [24, 25], which would be analogous to a human running in a maze at around 100 mph blindfolded using his arms to feel the walls [12, 25].

1.3 Earlier Related Work

Despite the extensive utilization of antennae in nature, development and implementation of their mechatronic counterparts—although inspirational and encouraging—remains a slowly progressing endeavor. In 2001, Barnes et al. [26] described a bio-inspired lobster robot antenna with three bending sensors embedded in a tapered structure (Figure 1.2). Each bending sensor activated when a set threshold curvature was passed, so the deflections caused by fluid flow and object contact at the tip of the antenna could be distinguished from each other by the robot. The tapered structure considerably enhanced the curvature distribution difference between the two cases which greatly increased performance of the discrimination task [26]. Soon after, in

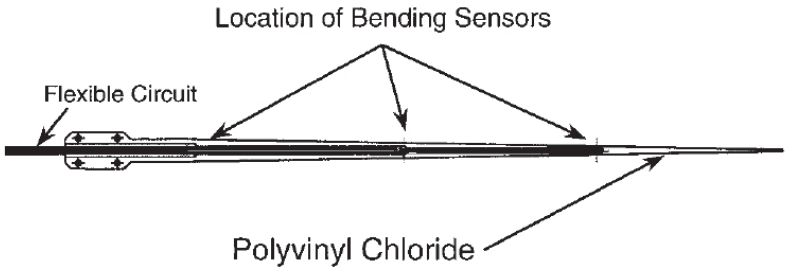

Figure 1.2: The artificial antenna of Barnes, et al. The tapered structure decreases stiffness towards the tip and each of the three bending sensors act as a switch depending upon whether or not a local curvature threshold is passed (Image credit: [26]).

2003, Cowan et al. [27] presented an artificial antenna for facilitating the task of cockroach-like wall following for Sprawlette, a hexapedal running robot (Figure 1.3).

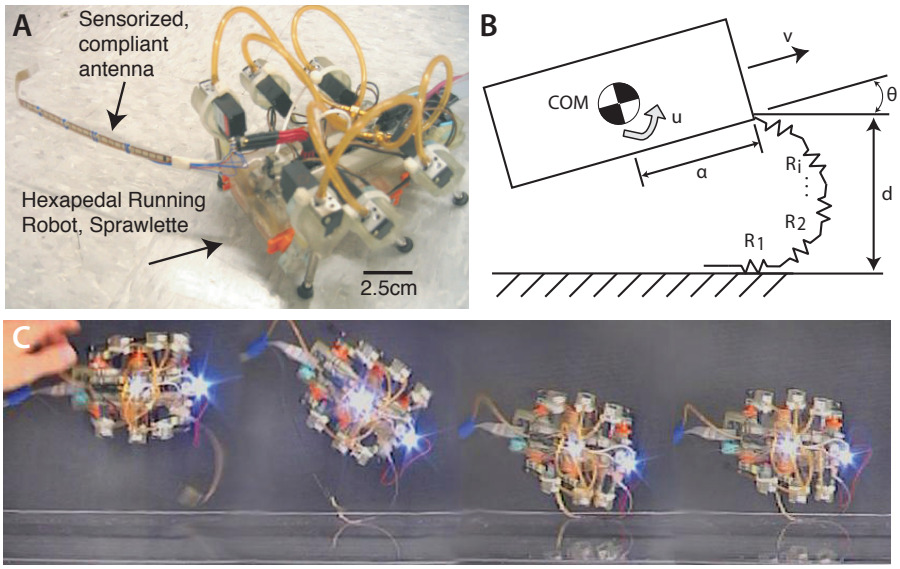

Figure 1.3: **A** Artificial antenna of Cowan, et al. attached to Sprawlette. **B** The varying resistances of the flex sensors allow the distance d and angle θ to be estimated. **C** Multiple exposures of the wall following Sprawlette on a treadmill (Image credit: [27]).

The antenna used five slightly modified compliant flex sensors (Spectra Symbol, Salt Lake City, UT) that changed electrical resistance in proportion to strain for the very large deflections that occur when the antenna touches the wall. Then, based on the resistance changes of the individual sensors, the distance and angular orientation with respect to the wall were inferred, albeit with a fairly large error margin, assuming the global concavity of the antenna was preserved during operation [27]. This assumption was important since the flex sensor resistance would increase in both concave and convex curvatures, suggesting multiple antenna configurations for a given sensor reading.

Beginning in 2004, further antenna prototypes were built, tested and employed in the "Locomotion In Mechanical and Biological Systems Laboratory" (LIMBS Lab) at Johns Hopkins University for some cockroach-based wall following experiments [24, 28–30] which are worth mentioning as part of my motivation.

Kutcher in 2004 as part of his MSE thesis described a single rigid link antenna with five contact sensors located along the outside edge to implement a tactile mapping algorithm via a wall following mobile robot [28]. The antenna was attached to the robot's chassis through a secondary fixed rigid link, which enabled the antenna to detect the wall within an interval defined at some distance in front of the robot (Figure 1.4). This so-called "preview" or "look-ahead" distance is analogous to the "visual range" in sighted systems and in principle allowed the robot to know about

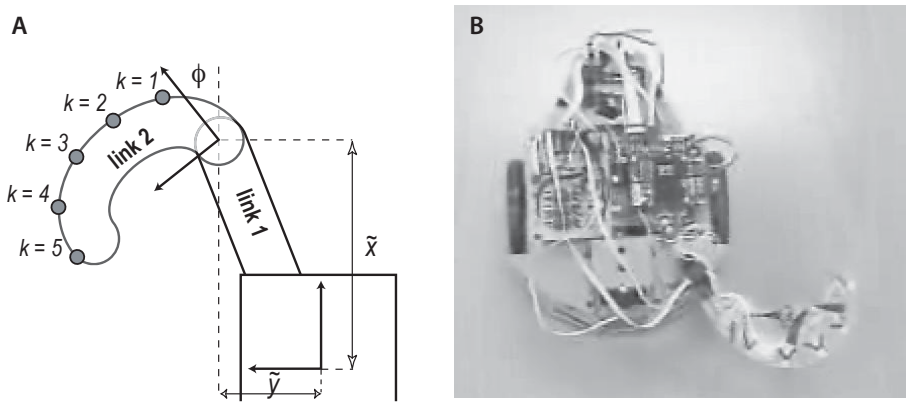

Figure 1.4: **A**. Antenna configuration designed and implemented by Brett Kutcher and Owen Loh: $\tilde{x}$, $\tilde{y}$, describe the position and orientation of the antenna coordinate system with respect to the robot coordinate system. Link 1 and link 2 are connected by a rotational joint located at the origin of the antenna coordinate system. This joint also contains a potentiometer and a torsional spring damper. $k = 1 \ldots 5$ represent the five touch sensors. **B** Single link artificial antenna used for tactile mapping mounted on Garcia robot. (Image credit: [28]).

the impending obstacle beforehand and steer away. In this particular design, the free joint was coupled with a potentiometer, which permitted the determination of the angle ϕ as a linear function of its measured resistance. In the case of multiple contacts, the one with the lowest enumeration k was fed into the controller [28].

In 2005, Lamperski et al. [29] introduced an improvement to the design of the antenna with the purpose of implementing a new dynamic wall following controller to Garcia (Acroname Inc., Boulder, Colorado), a differential drive wheeled robot. The fabricated tactile antenna was a two rigid link, three segment polycarbonate chain hinged on commercial potentiometers with a spring powered cam mechanism providing stiffness to each joint [29]. The device relied on one wide capacitive touch sensor per linkage such that any contact along a given segment registered a touch [29]. Thus,

the contact location was inferred within one segment length. Unlike the antenna used by Kutcher, this design enabled other segments to be added to the chain, which made it the first modular bio-inspired tactile antenna (Image credit: [29]). During testing,

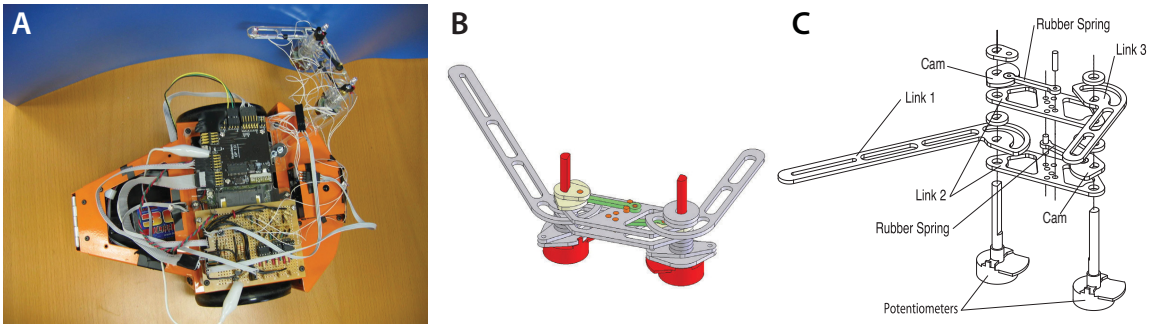

Figure 1.5: **A** Two linked sensorized antenna mounted on Garcia. **B** Assembled model. **C** The antenna is assembled by sliding the links onto the potentiometer shafts (some spacers and other minor parts are omitted from this figure for simplicity). The base of each potentiometer is fixed to the center link [29] (Image credit: [29]).

the rigidity of the antenna caused several problems so a more flexible solution was suggested [29]. On the other hand, Lamperski et al. also ran numerical simulations of a planar n-link kinematic chain structure representing the antenna coupled with the robot. In the simulation parameters such as the number of links, spring and damping constants, link masses and equilibrium configuration were kept user settable for the purpose of forming hypotheses about properties, that might be important in the design of a real antenna.

The work of Lamperski et al. greatly influenced my research. As the prospect of rapid hypothesis verification on the robotic antenna is one of our main goals, the adjustable parameters mentioned in the simulations actually formed the main design criteria of

the robotic antenna.

Two years later Lee et al. [30] published a successful implementation of a simple PD-control, a hypothesis partially shown to be the underlying control law for cockroach wall following behavior, on the Garcia robot. Lee et al. used a continuously flexible antenna designed and built by Owen Loh in 2005, similar in principle but more involved in the mechanical design aspect to the antenna presented by Barnes et al. in 2001 and Cowan et al. in 2003. Namely, the antenna was comprised of an array of shortened flex sensors (Abrams Gentile Entertainment, NYC, New York), which provided local curvature information based on the resistance variations due to deflection (Figure 1.6).

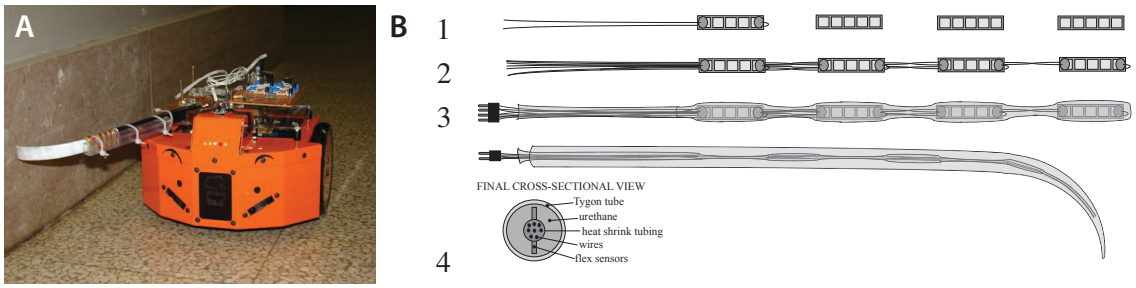

Figure 1.6: **A** The pre-bent, continuously flexible Antenna designed by Loh and utilized by Lee et al. **B** The summary of the antenna's assembly stages (Image credit: [30]).

Bio-inspired by the arthropod antenna physiology, this core disposition is embedded in a tapered, flexible superstructure composed of a Tygon rubber tube shell (Saint-Gobain Corporation, Courbevoie, France), and a cast urethane mantle to accommodate decreasing stiffness [30], a property also highlighted by Barnes et al..

This antenna was the first time a permanent pre-bent tip section was employed. This pre-curvature guaranteed the preservation of the global concavity of the antenna during wall following and thus was one solution to the issue caused by the unidirectional nature of the flex sensors [27]. A large section of the flagellum toward the base is stiffened by an external support structure and clamped at a fixed angle to the robot to facilitate a more consistent preview distance, also demonstrated by Kutcher [28].

Although research on arthropod inspired artificial antennae is limited, the morphologically similar mammal-inspired artificial whiskers have been long incorporated for tactile sensing [31–37]. Certainly, vertebrate-inspired systems such as skin covered fingers and whisker arrays promise to provide nearly instantaneous $2^1/_2$D information about a surface under investigation—a feat not possible with a 1D tactile sensor such as an arthropod antenna. Despite this limitation of an individual tactile antenna, arthropods readily navigate in their local environments using feedback from these 1D probes. Furthermore, advantages of parallel spatial integration notwithstanding, individual whiskers are simply dead hairs – long slender cantilever probes from which environmental tactile properties must be estimated solely based on measurements at the base using subcutaneous receptors. Thus, an individual whisker likely transduces a tiny fraction of the tactile information encoded by a living arthropod antenna which boasts literally thousands of sensory structures distributed along its length. In fact, the cockroaches, rely almost exclusively on flagellar information for high-speed wall following [12]. Thus, I believe the future of fast and robust tactile sensing lies in

densely sensorized flexible structures resembling arthropod antennae.

1.4 Thesis Organization

This thesis is organized in three main chapters. Chapter 2, "Model, Model, Model" describes the biological model system, the antenna of the *Periplaneta americana*, the kinematic model of the antenna, and the physical robotic model of the antenna. Chapter 3 "Making & Maintaining Contact" describes the fundamental mechanics of the antenna in regards to its stiffness profile and also investigates the cutaneous level interactions with environment based on the surface roughness. Chapter 4 "Perceiving & Following the Environment" describes how control based on antennal feedback can be simplified and how the fidelity of the sensing information is affected by the antenna mechanics.

Chapter 2

Model, Model, Model

2.1 The Model System: The American Cockroach

The overall structure and the growth characteristics of the *Periplaneta* antenna are similar to those of other cockroach species [38], so the antennal attributes of the *American cockroach* make it a representative biological model for my goals of understanding antenna-based tactile sensing in cockroaches. Part of this section also appears on my master's thesis [1].

Behavioral studies with unrestrained blinded cockroaches suggest that cockroaches

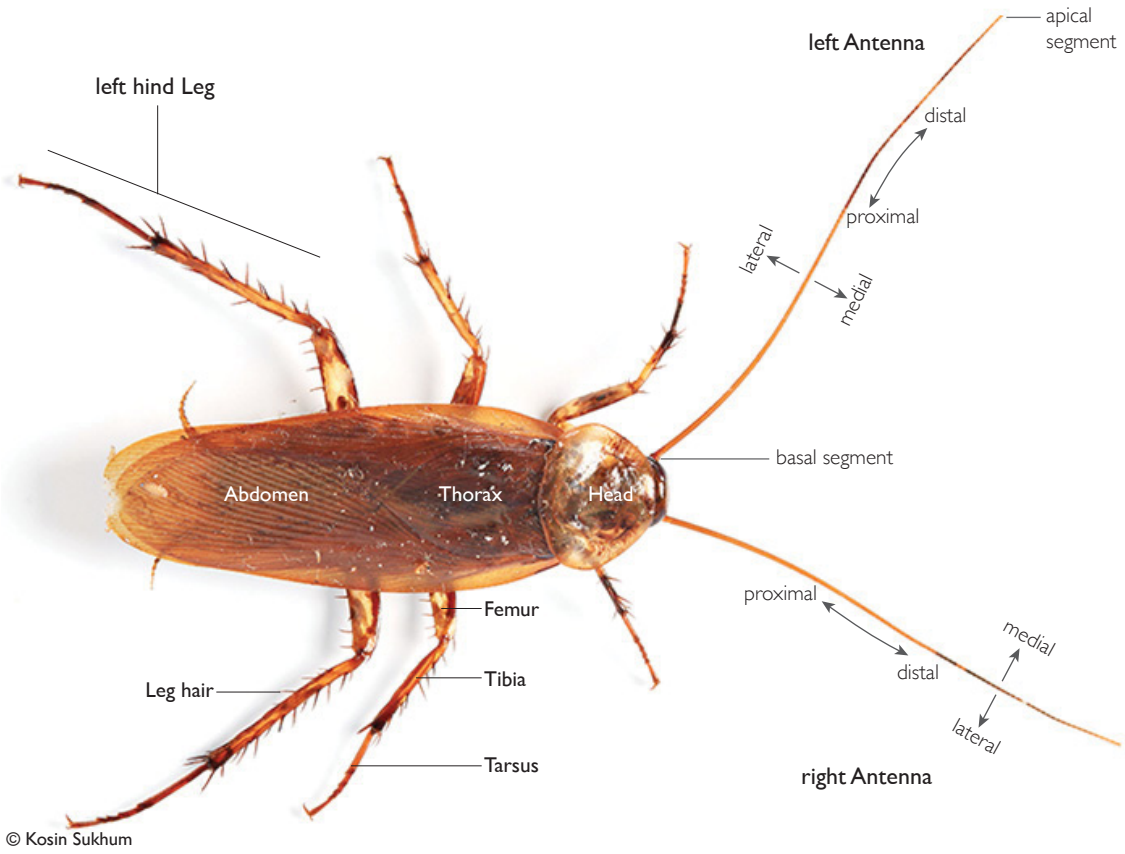

Figure 2.1: The American cockroach *Periplaneta americana*.

can sense both the configuration of their antenna and the position of a contact along their flagellum [11, 39]. The antennal configuration is sensed by sensors between the individual segments, and the contact position is sensed by hair-like distally pointed contact receptors [11, 39]. There are other mechanical and neural features [8, 40] of the antenna which contribute to tactile sensing, but I can only employ a fraction of the intricate biological design concepts towards the development of artificial tactile antenna. The goal of this thesis is to identify and model features of the antenna that make it effective, analyze and understand those features from a synthesis point of view, and translate the design to a useful engineered system.

2.1.1 At A Glance

The evolutionary origins of insect antennae are unclear and are interpreted either as modified appendages homologous with mouth parts and thoracic legs or as sensory structures associated with the presegmental part of the body, analogous to tentacles on the heads of certain worms [20]. Antennae occur in many forms but are always composed of three principal units from base to apex: scape, pedicel, and flagellum (Figure 2.4), which are dotted with diverse mechanosensors called sensilla.

The insect antenna serves many purposes, but one role that favors a long tapered antenna is that of tactile feeler, as in the American cockroach [25]. The extended

length of the antenna not only allows a large number of mechanosensors [21] to be packed along the structure but also provides extreme compliance to the flagellum. Tactile sensing also constitutes the most interesting antenna function from a robotics and mechanical engineering point of view, because the complex mechanics of the flagellum directly affect the sensorimotor control of locomotion of the cockroach and thus will be further investigated in Section 4.

2.1.2 The Base

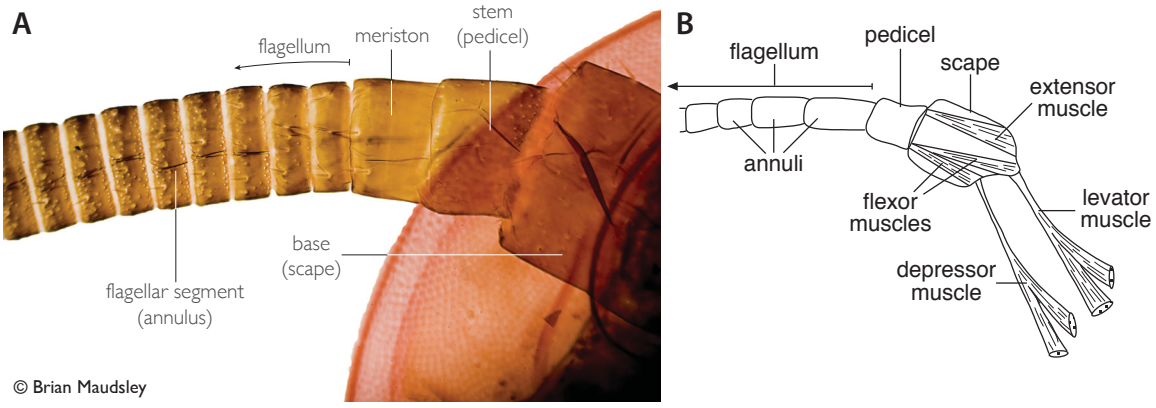

Figure 2.2: **A**: Microscope image (×40) of the antenna base of *Periplaneta americana* The basal segments, pedicel and scape provide actuation for the flagellum. The scape can move both horizontally (medial-lateral) and vertically (dorsal-ventral), while the pedicel moves only vertically. **B**: Basal musculature of a filiform insect antenna (Image credit: [21]).

The base of the antenna consists of two parts: the scape and the pedicel. The scape is inserted into a membranous socket (joint membrane) of the head wall and pivoted on a single marginal point called the antennifier [21], which acts like a ball

joint and facilitates basal antenna rotations in the dorsal-ventral and lateral-medial directions. The scape-pedicel joint is actuated by a flexor-extensor muscle pair only in the dorsal-ventral direction [21,22](Figure 2.4). Both joints contain a specialized cell group called the Johnston's organ, a mechanosensor that encodes deformations [20], mechanical oscillations, and stresses [22] in the cuticle. Since the scape has two rotational degrees of freedom, it enables the flagellum to be swept over both vertical and horizontal [23] planes. In contrast, the pedicel has just one rotational degree of freedom, so it provides extra flagellum flexibility only in the vertical [23] direction.

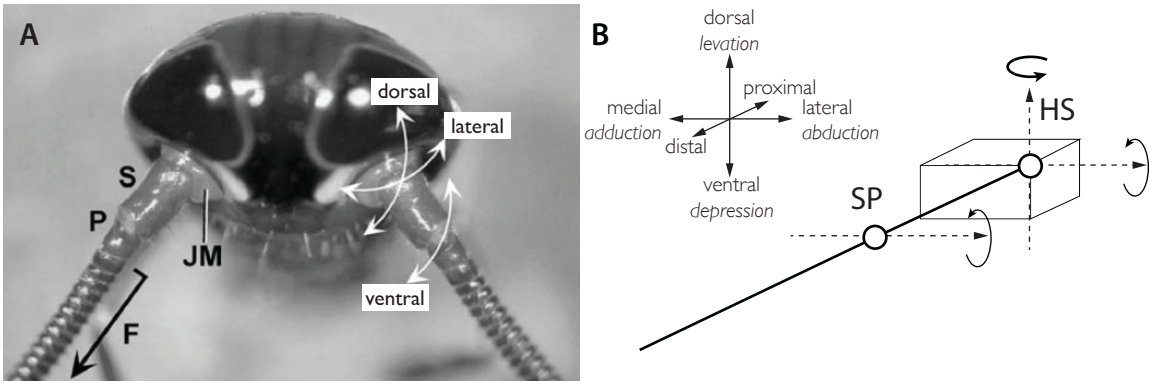

Figure 2.3: **A**: Surface view of antennae of *P. americana*. The scape-head joint facilitates medial-lateral and dorsal-ventral movements, while the scape-pedicel joint can only move in the dorsal-ventral directions [23]. **B**: In the simplest case, an insect antenna can be modeled as a kinematic chain consisting of the head (box), two segments (heavy black lines) and two hinge joints (open circles) [11]. Image is reproduced from: [11].

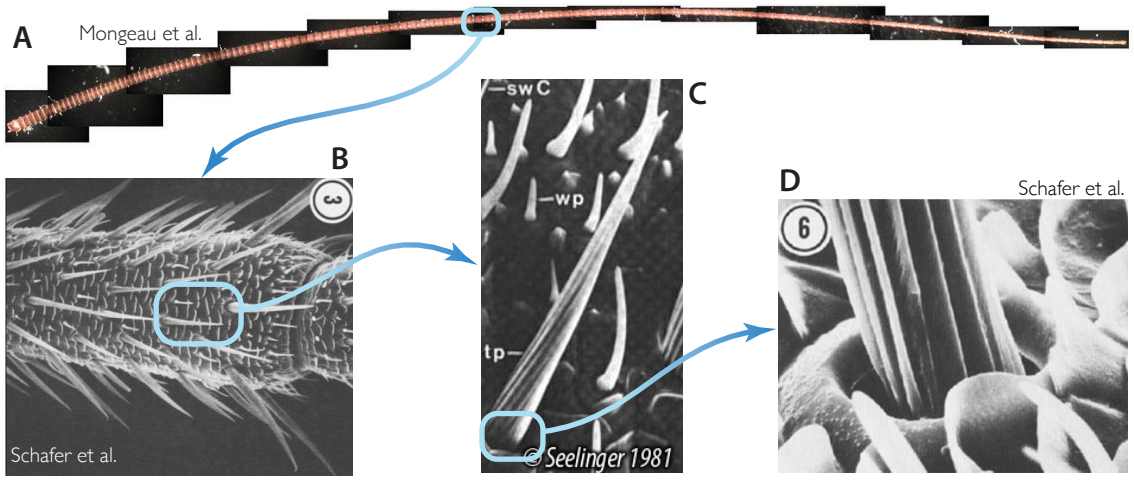

Figure 2.4: **A**: The flexible part of the cockroach antenna (also known as the flagellum) consists of about 150 segments geometrically tapering from the head to the tip [41]. **B**: Every segment is covered with cutaneous sensory mechano-structures called sensilla (Image credit: [38]).**C**: The *sensilla Chaetica B* are large, stiff thick walled contact chemoreceptors pointing towards the distal end (Image credit: [42]).**D**: The insertion cavity of the base of the sensillum is wide, allowing basal shaft movements over a range of 35° to 250° (Image credit: [38]).

2.1.3 The Flagellum & Sensilla

The flagellum is further divided into many similar subsegments called annulus or flagellomere [20]. These annuli forming the flagellum are connected to each other by soft membranes such that the entire superstructure is flexible [21]. The approximately 50 mm long flagellum of an adult *P. americana* consist of 150-170 segments (Figure 2.4), innervated by various chemo-, hygro-, thermo-, and mechanoreceptors [42] (Table 2.1). In some hexapods[1], there are additional intrinsic musculature between each unit of flagellum providing actuation and are therefore regarded as segments, not annuli [21, 22]. Still, throughout this dissertation *segment* nomenclature is used to refer to individual flagellum units instead of *annulus*.

All the nerves traversing the flagellum are entirely sensory, not motor [20]. These nerves are connected to minute sensory structures (sensilla), which, depending on their number, diversity and density dictate the overall shape and function of the antenna itself [21, 22]. Correspondingly, the mechanical properties of the flagellum in the global sense tends to favor the function, especially the mass and stiffness profiles. For instance, applying a preset force to a locust flagellum will cause different amounts of bending for different directions [11]. This directionality is set in such a way that air drag cannot bend the flagellum easily backwards during flight. Non-uniform stiffness profiles are also utilized by the crayfish [26], *Cherax destructor* whose

[1] Collembola (springtails) and Diplura (two-pronged bristletails)

Type of sense organ	*Probable modality*	*Total no. units in adult antenna*	*Location and distribution on flagellum*
S. Chaetica B (Thick-walled chemoreceptors)	(a) Contact chemoreception (b) Tactile sense	(a) 2×10^4 (b) 6.5×10^3	Occur on all segments as orderly peripheral rings. Especially dense on flagellum.
S. Trichodea (Thin-walled chemoreceptors)	Olfaction	Male: 8.6×10^4 Female: 4.8×10^4	Occur primarily on antennal flagellum distal to meristal segments.
S. Basiconica (Thin-walled chemoreceptors)	Olfaction	1×10^2	Occur distal to first ring of S. Chaetica B on flagellar segments
Cold Receptor Sensillum	Thermoreception	1×10^2	Occur on ventral side of distal alternating segments in one-third of antenna, distal to first ring of S. Chaetica B
S. Campaniformia (Sensory domes)	Detection of stress in cuticle	2×10^2	Occur dorsally in flagellum with one sensillum/segment.
Marginal sensilla	Joint proprioception	2×10^2	Occur in threes on alternating segments of flagellum

Table 2.1: Sense organs of *Periplaneta* antenna flagellum. *Reproduced based on the table from Schafer et al. 1973*

flagellum consist of 220-250 tapered segments [10]. This tapering differs among species to allow the distal tip of the antenna to deflect more easily than the proximal end. The cross-sectional shape of the flagellum is a natural parameter that can introduce directionality to the stiffness of the antenna. If the cross-section area is an ellipse, like that of the crayfish, then the deflections with the least mechanical resistance will occur around an axis that is parallel to the major semi-axis.

Of the diverse sensors given in Table 2.1, the thick-walled mechanosensory hairs (S. Chaetica B) triggered by external contacts are of interest, not only due to their obvious contribution to the tactile perception but also to their potential affect on the overall mechanical behavior of the flagellum during sensing. This particular type of hair-like contact sensor occurs on all segments (concentrated in the middle third of the flagellum [38]) and arranged around the entire circumference of the *Periplaneta* antenna (about 6500 per flagellum) [38] (Figure 2.4).

2.2 The Numerical Model

Figure 2.5 illustrates the kinematic model of the antenna. I model the flexible part of the antenna (i.e. *flagellum*) as a planar serial chain of n links, each with length l and connected by n revolute (pivot) joints each having a finite rotational stiffness $\kappa_j > 0$. I assume the links to have a uniform mass m and that the joints are frictionless. Every

flagellar joint angle θ_j $j \in \{1, 2, \ldots, n\}$ has an angular limit $\gamma_j = (\gamma_{\text{ccw,j}}, \gamma_{\text{cw,j}})$, which is an ordered pair of two angles with respect to the previous link's Cartesian coordinate frame $\mathcal{C}_{j-1}$, specifying counterclockwise and clockwise limits respectively. The first joint couples the flagellum at an angle θ_1 to the base, which is a link with length $l_0 = l$ attached to the ground frame $\mathcal{C}_G$ with a fixed angle θ_0 (a.k.a *base angle*). The ground frame x-axis is always aligned with the direction of base motion so that θ_0 can always be thought as the angle with respect to the base velocity vector. In my convention, positive angular velocities are counterclockwise, all link coordinate frames $\mathcal{C}_j$ are located at the distal end, and their x axes are aligned with their respective linkage bodies (see corner panel in Figure 2.5).

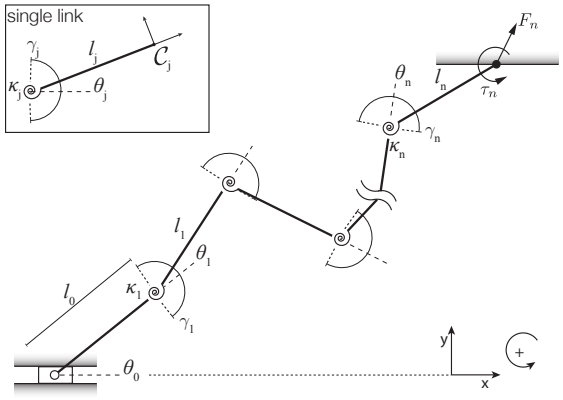

Figure 2.5: Kinematic model of the antenna with base angle θ_0, flagellum joint angles θ_j, joint limits γ_j, joint stiffnesses κ_j, tip forces F_n and tip torque τ_n.

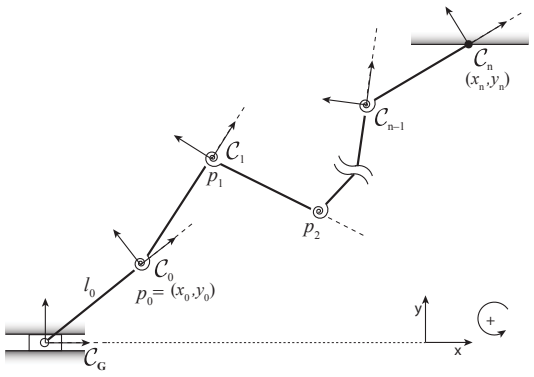

Figure 2.6: Coordinate frames $\mathcal{C}_i$ of the antenna model. $\mathcal{C}_G$ is the ground frame and corresponds to $i = -1$ (i.e. $\mathcal{C}_G = \mathcal{C}_{-1}$)

2.2.1 Active Frames α,$\mathcal{A}$

While forward and differential kinematics for serial kinematic chains are well understood, here I formulate a particularly convenient expression for calculating the positions and velocities of all links. This approach enables the simultaneous computation of the positions and velocities of all the links with arbitrary spatial (inertial) coordinate frames; see Sections 2.2.3.1 and 2.2.3.2. A full derivation is provided in Appendix 6.

The serial kinematic chain model for the antenna has a total of $n + 2$ coordinate frames $\mathcal{C}_i$ as illustrated in Figure 2.6. Of those $n + 2$ frames, one is the ground frame $\mathcal{C}_G$ (also denoted as $\mathcal{C}_{-1}$) located at the most proximal extreme of the antenna, and the other is the tip frame $\mathcal{C}_n$ located at the most distal extreme point of the antenna. The remaining frames ($\mathcal{C}_0$ to $\mathcal{C}_{n-1}$) are located at the joints. Let any of the $n+2$ frame indices ($\{-1, \ldots, n\}$) be designated as the spatial frame $\mathcal{C}_s$, and all the remaining $n+1$ frame indices are automatically designated as body frames $\mathcal{C}_b$. The spatial frame is the frame of reference for all other frames. That is, all body frame positions and all body velocities are measured relative to $\mathcal{C}_s$. The forward and differential kinematic mappings between the body frame positions and velocities in the distal and proximal directions are given in appendix 6, equations 6.1.1.3, 6.1.2.8. Close inspection on these explicit expressions reveals a relationship between the kinematic pattern and both frame indices s and b.

Definition 2.2.1. Consider an open planar serial chain with $n+1$ uniform links, where the body coordinate frame of each link is located at their distal end as illustrated in 2.6. Starting from the ground frame C_{-1}, let each body frame C_i be enumerated consecutively from 0 to n from proximal to the distal frame. Let s be the spatial frame index and b be the target body frame index such that $s, b \in \{-1, 0, \ldots, n\}$. For any given frame pair indices s and b, the *active frames* vector $\alpha_{sb} \in \{-1, 0, 1\}^{n+1}$ is defined as:

$$\alpha_{sb} = \begin{pmatrix} a_0 \\ a_1 \\ \vdots \\ a_n \end{pmatrix}$$

$$\text{where} \quad a_i = \begin{cases} -1 & \text{if } -1 \leq b < i \leq s \leq n \\ 0 & \text{else} \\ 1 & \text{if } n \geq b \geq i > s \geq -1 \end{cases} \tag{2.2.1.1}$$

Example:

Consider a planar serial open kinematic chain with $n = 8$ segments. Let the spatial frame index s be 5 and the target body frame index b be 1. Then using Definition 2.2.1, the the active frames vector $\alpha_{sb} = \alpha_{5,1}$ with size 9×1 is constructed as:

$$\alpha_{sb} = \alpha_{s,b} = \alpha_{5,1} = \begin{pmatrix} 0 & 0 & -1 & -1 & -1 & -1 & 0 & 0 & 0 \end{pmatrix}^{\top}_{9\times 1}$$

where $^\top$ denotes the transpose operator.

Example:

Consider the opposite case with same $n = 8$ segments, where the spatial frame index s is 1 and body frame b is 5. Then the active frames vector $\alpha_{sb} = \alpha_{1,5}$ would be:

$$\alpha_{sb} = \alpha_{s,b} = \alpha_{1,5} = \begin{pmatrix} 0 \\ 0 \\ 1 \\ 1 \\ 1 \\ 1 \\ 0 \\ 0 \\ 0 \end{pmatrix}$$

Definition 2.2.2. Consider an open planar serial chain with $n + 1$ uniform links, where the body coordinate frame of each link is located at their distal end as illustrated in 2.6. Starting from the ground frame C_{-1}, let each body frame C_i be enumerated consecutively from 0 to n from proximal to the distal frame. Let s be the spatial frame index and b be the target body frame index such that $s, b \in \{-1, 0, \ldots, n\}$. For any given frame pair indices s and b and its associated active frames vector α_{sb} (2.2.1), the square *active frames* matrix $\mathcal{A}_{sb} \in \{-1, 0, 1\}^{n+1 \times n+1}$ is defined as:

$$\mathcal{A} = \underbrace{(\alpha\alpha^\top)^{\triangle} + \frac{1}{2}\left(\alpha\,|\alpha|^\top - \alpha\alpha^\top\right)}_{n+1 \times n+1} \tag{2.2.1.2}$$

where the $\triangle$ operator yields the *lower triangular* part of the matrix including the main diagonal.

Example:

Consider a planar serial open kinematic chain with $n = 8$ segments. Let the spatial frame index s be 5 and the target body frame index b be 1. Then using Definition 2.2.2, the the active frames matrix $\mathcal{A}_{sb} = \alpha_{5,1}$ with size 9×9 is constructed as:

$$\mathcal{A}_{s,b} = \mathcal{A}_{5,1} \begin{pmatrix} 0 & 0 & 0 & 0 & 0 & 0 & 0 & 0 & 0 \\ 0 & 0 & 0 & 0 & 0 & 0 & 0 & 0 & 0 \\ 0 & 0 & 0 & -1 & -1 & -1 & 0 & 0 & 0 \\ 0 & 0 & 0 & 0 & -1 & -1 & 0 & 0 & 0 \\ 0 & 0 & 0 & 0 & 0 & -1 & 0 & 0 & 0 \\ 0 & 0 & 0 & 0 & 0 & 0 & 0 & 0 & 0 \\ 0 & 0 & 0 & 0 & 0 & 0 & 0 & 0 & 0 \\ 0 & 0 & 0 & 0 & 0 & 0 & 0 & 0 & 0 \\ 0 & 0 & 0 & 0 & 0 & 0 & 0 & 0 & 0 \end{pmatrix}_{9\times 9}$$

Example:

Consider the opposite case with same $n = 8$ segments, where the spatial frame index

s is 1 and body frame b is 5. Then the active frames matrix $\mathcal{A}_{sb} = \mathcal{A}_{1,5}$ would be:

$$\mathcal{A}_{s,b} = \mathcal{A}_{1,5} \begin{pmatrix} 0 & 0 & 0 & 0 & 0 & 0 & 0 & 0 & 0 \\ 0 & 0 & 0 & 0 & 0 & 0 & 0 & 0 & 0 \\ 0 & 0 & 1 & 0 & 0 & 0 & 0 & 0 & 0 \\ 0 & 0 & 1 & 1 & 0 & 0 & 0 & 0 & 0 \\ 0 & 0 & 1 & 1 & 1 & 0 & 0 & 0 & 0 \\ 0 & 0 & 1 & 1 & 1 & 1 & 0 & 0 & 0 \\ 0 & 0 & 0 & 0 & 0 & 0 & 0 & 0 & 0 \\ 0 & 0 & 0 & 0 & 0 & 0 & 0 & 0 & 0 \\ 0 & 0 & 0 & 0 & 0 & 0 & 0 & 0 & 0 \end{pmatrix}$$

Inherent to their construction, reverse frame relationships α_{sb} to α_{bs} (both $n+1 \times 1$ column vectors) and $\mathcal{A}_{sb}$ to $\mathcal{A}_{sb}$ (both $n+1 \times n+1$ square matrices) for any spatial and body indices b, s are very easy to compute. These relationships are:

$$\alpha_{sb} = -\alpha_{bs} \tag{2.2.1.3}$$

$$\underbrace{\mathcal{A}_{sb}}_{n+1 \times n+1} = \mathcal{A}_{bs} - \underbrace{|\alpha_{bs}| \, \alpha_{bs}^{\top}}_{n+1 \times n+1} \tag{2.2.1.4}$$

where $|\cdot|$ operator is the element-wise absolute value. The absolute value of the *active frames* matrix also satisfies the following relationship:

$$\begin{aligned} |\mathcal{A}_{sb}| &= \alpha_{bs}\alpha_{bs}^{\top} - |\mathcal{A}_{bs}| \\ |\mathcal{A}_{sb}| - \alpha_{sb}\alpha_{sb}^{\top} &= -|\mathcal{A}_{bs}| \end{aligned} \tag{2.2.1.5}$$

2.2.1.1 Positions

I use the active frames vector α_{sb} and matrix $\mathcal{A}_{sb}$ to simplify the forward mapping equation 6.1.1.6 such that:

$$H_{sb} = \left[\begin{array}{cc|c} \overbrace{\cos(\alpha_{sb}^{\top}\theta) & -\sin(\alpha_{sb}^{\top}\theta)}^{R_{sb}} & \overbrace{\begin{pmatrix}\alpha_{sb}^{\top}\cos\left(\mathcal{A}_{sb}\theta\right)\\ \alpha_{sb}^{\top}\sin\left(\mathcal{A}_{sb}\theta\right)\end{pmatrix} l}^{p_{sb}} \\ \sin(\alpha_{sb}^{\top}\theta) & \cos(\alpha_{sb}^{\top}\theta) & \\ \hline 0 & & \alpha_{sb}^{\top}\theta \end{array}\right]_{3\times 3}$$

where $\theta \in \mathbb{R}^{n+1}$ is the joint angle vector; $\alpha_{sb}^{\top}\theta$ is a scalar; $R_{sb} \in SO2$ is the rotation matrix; and finally $\cos\left(\mathcal{A}_{sb}\theta\right) \in \mathbb{R}^{n+1}$ and $p_{sb} \in \mathbb{R}^2$ are column vectors.

$$H_{sb} = \left[\begin{array}{cc|c} \cos(\alpha_{sb}^{\top}\theta) & -\sin(\alpha_{sb}^{\top}\theta) & \begin{bmatrix}\cos\left(\mathcal{A}_{sb}\theta\right)^{\top}\\ \sin\left(\mathcal{A}_{sb}\theta\right)^{\top}\end{bmatrix} l\alpha_{sb} \\ \sin(\alpha_{sb}^{\top}\theta) & \cos(\alpha_{sb}^{\top}\theta) & \\ \hline 0 & & \alpha_{sb}^{\top}\theta \end{array}\right] \tag{2.2.1.6}$$

I wrap equation 2.2.1.6 in the following lemma:

Lemma 2.2.1. *For an open serial kinematic chain with uniform link length l, the transformation H_{sb} as a mapping from the relative coordinates p_b^a of a point "a" on the body "b" with respect to the body frame $\mathcal{C}_b$ to the spatial position and orientation $\begin{pmatrix} p_{sb}^a & \theta_{sb}\end{pmatrix}^{\top}$ of the same point with respect to the spatial frame $\mathcal{C}_s$ can be constructed*

as:

$$H_{sb} = \left[\begin{array}{cc:c} \cos(\alpha_{sb}^{\top}\theta) & -\sin(\alpha_{sb}^{\top}\theta) & \left[\begin{array}{c} \cos\left(\mathcal{A}_{sb}\theta\right)^{\top} \\ \hdashline \sin\left(\mathcal{A}_{sb}\theta\right)^{\top} \end{array}\right] l\alpha_{sb} \\ \sin(\alpha_{sb}^{\top}\theta) & \cos(\alpha_{sb}^{\top}\theta) & \\ \hdashline \multicolumn{2}{c:}{0} & \alpha_{sb}^{\top}\theta \end{array}\right]$$

such that:

$$\begin{pmatrix} p_{sb}^{a} \\ \theta_{sb} \end{pmatrix}_{3\times 1} = H_{sb} \begin{pmatrix} p_{b}^{a} \\ 1 \end{pmatrix}_{3\times 1}$$

where α and $\mathcal{A}$ are the active frames vector and the active frames matrix as defined in equations 2.2.1.1 and 2.2.1.2 respectively.

Recall $R_{sb}^{-1} = R_{sb}^{\top} = R_{bs}$ and $\mathcal{C}_{sb}^{-1} = \mathcal{C}_{bs} = \left[\begin{array}{c:c} {R_{sb}}^{\top} & -{R_{sb}}^{\top} p_{sb} \\ \hdashline 0 & 1 \end{array}\right]$, then I can prove the following relationships:

Proof.

$$\begin{aligned} R_{bs} = \begin{pmatrix} \cos\alpha_{bs}^{\top}\theta & -\sin\alpha_{bs}^{\top}\theta \\ \sin\alpha_{bs}^{\top}\theta & \cos\alpha_{bs}^{\top}\theta \end{pmatrix} &= \begin{pmatrix} \cos -\alpha_{sb}^{\top}\theta & -\sin -\alpha_{sb}^{\top}\theta \\ \sin -\alpha_{sb}^{\top}\theta & \cos -\alpha_{sb}^{\top}\theta \end{pmatrix} \\ &= \begin{pmatrix} \cos\alpha_{sb}^{\top}\theta & \sin\alpha_{sb}^{\top}\theta \\ -\sin\alpha_{sb}^{\top}\theta & \cos\alpha_{sb}^{\top}\theta \end{pmatrix} = R_{sb}^{\top} \end{aligned}$$

$$\begin{aligned} p_{bs} &= -R_{sb}^{\top} \left[\begin{array}{c} \cos\left(\mathcal{A}_{sb}\theta\right)^{\top} \\ \hdashline \sin\left(\mathcal{A}_{sb}\theta\right)^{\top} \end{array}\right] l\alpha_{sb} \\ &= \begin{pmatrix} \cos\alpha_{sb}^{\top}\theta & \sin\alpha_{sb}^{\top}\theta \\ -\sin\alpha_{sb}^{\top}\theta & \cos\alpha_{sb}^{\top}\theta \end{pmatrix} \left[\begin{array}{c} \cos\left(\mathcal{A}_{sb}\theta\right)^{\top} \\ \hdashline \sin\left(\mathcal{A}_{sb}\theta\right)^{\top} \end{array}\right] l\alpha_{bs} \end{aligned}$$

$$
\begin{aligned}
&= \begin{bmatrix} \cos\left(\alpha_{sb}^{\top}\theta\right)\cos\left(\mathcal{A}_{sb}\theta\right)^{\top} + \sin\left(\alpha_{sb}^{\top}\theta\right)\sin\left(\mathcal{A}_{sb}\theta\right)^{\top} \\ \hdashline -\sin\left(\alpha_{sb}^{\top}\theta\right)\cos\left(\mathcal{A}_{sb}\theta\right)^{\top} + \cos\left(\alpha_{sb}^{\top}\theta\right)\sin\left(\mathcal{A}_{sb}\theta\right)^{\top} \end{bmatrix}^{\top} l\alpha_{bs} \\
&= \begin{bmatrix} \cos\left(\begin{pmatrix} \alpha_{sb}^{\top}\theta & \cdots & \alpha_{sb}^{\top}\theta \end{pmatrix}^{\top} - A_{sb}\theta\right) \\ \hdashline -\sin\left(\begin{pmatrix} \alpha_{sb}^{\top}\theta & \cdots & \alpha_{sb}^{\top}\theta \end{pmatrix}^{\top} - A_{sb}\theta\right) \end{bmatrix}^{\top} l\alpha_{bs} \\
&= \begin{bmatrix} \cos\left(\left[A_{sb} - \begin{pmatrix} \alpha_{sb} & \cdots & \alpha_{sb} \end{pmatrix}^{\top}\right]\theta\right) \\ \hdashline \sin\left(\left[A_{sb} - \begin{pmatrix} \alpha_{sb} & \cdots & \alpha_{sb} \end{pmatrix}^{\top}\right]\theta\right) \end{bmatrix}^{\top} l\alpha_{bs} \\
&= \begin{bmatrix} \cos\left(\left[A_{sb} - |\alpha_{sb}|\,\alpha_{sb}^{\top}\right]\theta\right) \\ \hdashline \sin\left(\left[A_{sb} - |\alpha_{sb}|\,\alpha_{sb}^{\top}\right]\theta\right) \end{bmatrix}^{\top} l\alpha_{bs} \\
&= \begin{bmatrix} \cos\left(\mathcal{A}_{bs}\theta\right)^{\top} \\ \hdashline \sin\left(\mathcal{A}_{bs}\theta\right)^{\top} \end{bmatrix} l\alpha_{bs}
\end{aligned}
$$

$$
\implies R_{sb}^{\top}\begin{bmatrix} \cos\left(\mathcal{A}_{sb}\theta\right)^{\top} \\ \hdashline \sin\left(\mathcal{A}_{sb}\theta\right)^{\top} \end{bmatrix}\alpha_{sb} = \begin{bmatrix} \cos\left(\mathcal{A}_{bs}\theta\right)^{\top} \\ \hdashline \sin\left(\mathcal{A}_{bs}\theta\right)^{\top} \end{bmatrix}\alpha_{sb} \tag{2.2.1.7}
$$

$$
\implies R_{sb}^{\top}\begin{bmatrix} \cos\left(\mathcal{A}_{sb}\theta\right)^{\top} \\ \hdashline \sin\left(\mathcal{A}_{sb}\theta\right)^{\top} \end{bmatrix}\mathcal{A}_{sb} = \begin{bmatrix} \cos\left(\mathcal{A}_{bs}\theta\right)^{\top} \\ \hdashline \sin\left(\mathcal{A}_{bs}\theta\right)^{\top} \end{bmatrix}\mathcal{A}_{sb} \tag{2.2.1.8}
$$

□

Standard trigonometric identities were used in the above simplifications.

2.2.1.2 Velocities

The active frames expressions can now be used to simplify the differential kinematics 6.1.2.11 mapping. Description and dimensions of the symbolic quantities are given in appendix 6.1.2:

$$\dot{H}_{sb} = \left[\begin{array}{c:c} \overbrace{\underbrace{\alpha_{sb}^{\top}\dot{\theta}\begin{pmatrix}0 & -1\\ 1 & 0\end{pmatrix}}_{\widehat{\omega}_{sb}} R_{sb}}^{\dot{R}_{sb}} & \overbrace{\begin{bmatrix}\frac{\partial p_{sb}}{\partial \theta_0} & \frac{\partial p_{sb}}{\partial \theta_1} & \dots & \frac{\partial p_{sb}}{\partial \theta_n}\end{bmatrix}\dot{\theta}}^{\dot{p}_{sb}} \\ \hdashline 0 & \underbrace{\alpha_{sb}^{\top}\dot{\theta}}_{\omega_{sb}} \end{array}\right]_{3\times 3}$$

Thus, using the active frames vector, the angular velocity of any point on the desired body "b" with respect to the spatial frame $\mathcal{C}_s$ written in any body frame coordinate can be written as:

$$\boxed{\omega_{sb}^{a} = \omega_{sb} = \omega_b = \alpha_{sb}^{\top}\dot{\theta}} \tag{2.2.1.9}$$

The translational velocity of the desired frame origin $\dot{p}_{sb}$ can be more explicitly expressed using the active frames:

$$p_{sb} = \begin{bmatrix} \cos\left(\mathcal{A}_{sb}\theta\right)^\top \\ \hdashline \sin\left(\mathcal{A}_{sb}\theta\right)^\top \end{bmatrix} l\alpha_{sb}$$
$$= \begin{bmatrix} \alpha_{sb}^\top \cos\left(\mathcal{A}_{sb}\theta\right) \\ \hdashline \alpha_{sb}^\top \sin\left(\mathcal{A}_{sb}\theta\right) \end{bmatrix} l$$

Using chain rule, I get:

$$\dot{p}_{sb} = \frac{\mathrm{d}}{\mathrm{d}t} p_{sb} = \begin{pmatrix} \frac{\partial \alpha_{sb}^\top \cos\left(\mathcal{A}_{sb}\theta\right)}{\partial \cos\left(\mathcal{A}_{sb}\theta\right)} \frac{\partial \cos\left(\mathcal{A}_{sb}\theta\right)}{\partial \mathcal{A}_{sb}\theta} \frac{\partial \mathcal{A}_{sb}\theta}{\partial \theta} \\ \frac{\partial \alpha_{sb}^\top \sin\left(\mathcal{A}_{sb}\theta\right)}{\partial \sin\left(\mathcal{A}_{sb}\theta\right)} \frac{\partial \sin\left(\mathcal{A}_{sb}\theta\right)}{\partial \mathcal{A}_{sb}\theta} \frac{\partial \mathcal{A}_{sb}\theta}{\partial \theta} \end{pmatrix} l\dot{\theta} \tag{2.2.1.10}$$

$$\text{Recall identities:} \quad \frac{\partial \alpha_{sb}^\top x}{\partial x} = \alpha_{sb}^\top \quad \frac{\partial \mathcal{A}_{sb} x}{\partial x} = \mathcal{A}_{sb}$$

Substituting into 2.2.1.10 yields:

$$\dot{p}_{sb} = \begin{bmatrix} \alpha_{sb}^\top \dfrac{\partial \cos\left(\mathcal{A}_{sb}\theta\right)}{\partial \mathcal{A}_{sb}\theta} \mathcal{A}_{sb} \\ \hdashline \alpha_{sb}^\top \dfrac{\partial \sin\left(\mathcal{A}_{sb}\theta\right)}{\partial \mathcal{A}_{sb}\theta} \mathcal{A}_{sb} \end{bmatrix} l\dot{\theta} \tag{2.2.1.11}$$

The cos and sin operators act on matrices and vectors on an element-by-element basis.

$$\cos \begin{pmatrix} x_1 \\ \vdots \\ x_n \end{pmatrix} = \begin{pmatrix} \cos x_1 \\ \vdots \\ \cos x_n \end{pmatrix}$$

Thus the following identities hold:

$$\frac{\partial \sin(Ax)}{\partial x} = \text{diag}(\cos(Ax))A$$
$$\frac{\partial \cos(Ax)}{\partial x} = \text{diag}(-\sin(Ax))A \tag{2.2.1.12}$$

where "diag(.)" is the diagonal matrix constructed from a given vector. Now, substituting these identities (2.2.1.12) into equation 2.2.1.11 yields the explicit expression for $\dot{p}_{sb}$:

$$\dot{p}_{sb} = \begin{bmatrix} -\alpha_{sb}^{\top}\text{diag}(\sin(\mathcal{A}_{sb}\theta))\mathcal{A}_{sb} \\ \hdashline \alpha_{sb}^{\top}\text{diag}(\cos(\mathcal{A}_{sb}\theta))\mathcal{A}_{sb} \end{bmatrix} l\dot{\theta} \tag{2.2.1.13}$$

The active frames vector α and matrix $\mathcal{A}$ also satisfy the following relationships:

$$\text{diag}(\mathcal{A}x)\alpha = |\mathcal{A}|\, x$$
$$\mathcal{A}^{\top}\text{diag}(\sin(\mathcal{A}x))\alpha = |\mathcal{A}|^{\top}\sin(\mathcal{A}x)$$
$$\mathcal{A}^{\top}\text{diag}(\cos(\mathcal{A}x))\alpha = |\mathcal{A}|^{\top}\cos(\mathcal{A}x)$$

Substituting into 2.2.1.13 yields:

$$\dot{p}_{sb} = \begin{bmatrix} -\sin(\mathcal{A}_{sb}\theta)^{\top}|\mathcal{A}_{sb}| \\ \hdashline \cos(\mathcal{A}_{sb}\theta)^{\top}|\mathcal{A}_{sb}| \end{bmatrix} l\dot{\theta} \tag{2.2.1.14}$$

Thus, the simplified expression for the differential kinematics mapping becomes:

$$\dot{H}_{sb} = \left[\begin{array}{c:c} \widehat{\alpha_{sb}^{\top}\dot{\theta}} R_{sb} & \begin{bmatrix} -\sin(\mathcal{A}_{sb}\theta)^{\top} \\ \hdashline \cos(\mathcal{A}_{sb}\theta)^{\top} \end{bmatrix} l\,|\mathcal{A}_{sb}|\,\dot{\theta} \\ \hdashline 0 & \alpha_{sb}^{\top}\dot{\theta} \end{array}\right] \tag{2.2.1.15}$$

I wrap this result in the following lemma as:

Lemma 2.2.2. *For an open serial kinematic chain with uniform link length l, the mapping $\dot{H}_{sb}$ from the relative coordinates p_b^a of a point "a" on the body "b" with respect to the body frame $\mathcal{C}_b$ to the total velocity $\dot{p}_{sb}^a$ and angular velocity ω_{sb}^a of the same point with respect to the spatial frame $\mathcal{C}_s$ can be constructed as:*

$$\dot{H}_{sb} = \left[\begin{array}{c:c} \widehat{\alpha_{sb}^{\top}\dot{\theta}} R_{sb} & \begin{bmatrix} -\sin(\mathcal{A}_{sb}\theta)^{\top} \\ \hdashline \cos(\mathcal{A}_{sb}\theta)^{\top} \end{bmatrix} l\,|\mathcal{A}_{sb}|\,\dot{\theta} \\ \hdashline 0 & \alpha_{sb}^{\top}\dot{\theta} \end{array}\right]$$

such that:

$$\begin{pmatrix} \dot{p}_{sb}^a \\ \omega_{sb}^a \end{pmatrix} = \dot{H}_{sb} \begin{pmatrix} p_b^a \\ 1 \end{pmatrix}$$

where α and $\mathcal{A}$ are the active frames vector and the active frames matrix as defined in equations 2.2.1.1 and 2.2.1.2 respectively.

2.2.2 Segment Jacobians

The last (third) column of $\dot{H}_{sb}$ in equations 6.1.2.11 or 2.2.1.15 is referred as the *hybrid velocity* [43] $V_h = \begin{pmatrix} \dot{p}_{sb} & \omega_{sb} \end{pmatrix}^\top$, which is simply the translational and angular velocity of the body frame $\mathcal{C}_b$ relative to the spatial frame $\mathcal{C}_s$ and written in the spatial frame $\mathcal{C}_s$. It is desirable to have an explicit mapping $J_{sb} : \mathbb{R}^{n+1} \mapsto \mathbb{R}^3$ from the joint angular velocities vector $\dot{\theta} \in \mathbb{R}^{n+1}$ to the *hybrid velocity* V_h. I will refer to this particular mapping J_{sb} as the *hybrid* Jacobian matrix.

In this section, I will state two other planar case Jacobians in terms of the active frames I defined in section 2.2.1: the body manipulator Jacobian and the spatial manipulator Jacobian matrices as defined in [43].

2.2.2.1 Hybrid Jacobian J_{sb}

Fortunately, the previously introduced *active frames* expression for the differential kinematics 2.2.1.15 provides J_{sb} immediately.

$$J_{sb} = \begin{bmatrix} \begin{bmatrix} -\sin(\mathcal{A}_{sb}\theta)^\top \\ \cos(\mathcal{A}_{sb}\theta)^\top \end{bmatrix} l\,|\mathcal{A}_{sb}| \\ \alpha_{sb}^\top \end{bmatrix} \tag{2.2.2.1}$$

where the first two rows are equivalent to $\left[\begin{array}{c:c:c:c} \frac{\partial p_{sb}}{\partial \theta_0} & \frac{\partial p_{sb}}{\partial \theta_1} & \cdots & \frac{\partial p_{sb}}{\partial \theta_n} \end{array}\right]$.

2.2.2.2 Body Jacobian J_b

The body Jacobian matrix $J_b : \mathbb{R}^{n+1} \mapsto \mathbb{R}^3$ is a mapping from the joint angular velocities vector $\dot{\theta} \in \mathbb{R}^{n+1}$ to the *body velocity* V_b, which is the translational and angular velocity of the body frame $\mathcal{C}_b$ relative to the spatial frame $\mathcal{C}_s$ but written in the body frame $\mathcal{C}_b$. The relationship between *body velocity* V_b and the *hybrid velocity* V_h is explained in Appendix 6.1.3. Here I present the explicit expression for the planar body Jacobian J_b, which is referred as the *body manipulator Jacobian* in [43]. Starting from equation 6.1.3.4 I have:

$$V_h = \left[\begin{array}{c:c} R_{sb} & 0 \\ \hdashline 0 & 1 \end{array}\right] V_b$$

$$\left[\begin{array}{c:c} R_{sb}^\top & 0 \\ \hdashline 0 & 1 \end{array}\right] J_{sb}\dot{\theta} = J_b\dot{\theta}$$

$$\left[\begin{array}{c} R_{sb}^\top \left[\begin{array}{c} -\sin(\mathcal{A}_{sb}\theta)^\top \\ \hdashline \cos(\mathcal{A}_{sb}\theta)^\top \end{array}\right] l\,|\mathcal{A}_{sb}| \\ \hdashline \alpha_{sb}^\top \end{array}\right] = J_b$$

Recall equation 2.2.1.8

$$J_b = \left[\begin{array}{c} \left[\begin{array}{c} -\sin(\mathcal{A}_{bs}\theta)^\top \\ \hdashline \cos(\mathcal{A}_{bs}\theta)^\top \end{array}\right] l\,|\mathcal{A}_{sb}| \\ \hdashline \alpha_{sb}^\top \end{array}\right] \qquad (2.2.2.2)$$

2.2.2.3 Spatial Jacobian J_σ

Another useful Jacobian matrix arises when mapping absolute coordinates of point p^a_{sb} to its translational and angular velocities with respect to the spatial frame $\begin{pmatrix} \dot{p}^a_{sb} & \omega^a_{sb} \end{pmatrix}^\top$ such that:

$$\begin{aligned} \begin{pmatrix} \dot{p}^a_{sb} \\ \omega^a_{sb} \end{pmatrix} &= V_s^\wedge \begin{pmatrix} p^a_{sb} \\ 1 \end{pmatrix} \\ &= \left[\begin{array}{c:c} \widehat{\omega}_{sb} & -\widehat{\omega}_{sb} p_{sb} + \dot{p}_{sb} \\ \hdashline 0 & \omega_{sb} \end{array}\right] \begin{pmatrix} p^a_{sb} \\ 1 \end{pmatrix} \end{aligned}$$

The transformation $V_s^\wedge$ is called the *spatial velocity* matrix and its relation with the hybrid velocity matrix $\dot{H}_{sb}$ is shown in 6.1.4. Similar to the case with $V_b^\wedge$, the last (third) column of $V_s^\wedge$ in equation 6.1.4.2 is referred as the *spatial velocity* V_s, whose direct geometrical interpretation is somewhat unintuitive [43]. Starting from equation 6.1.4.5:

$$V_h = \left[\begin{array}{c:c} I & \begin{pmatrix} 0 & -1 \\ 1 & 0 \end{pmatrix} p_{sb} \\ \hdashline 0 & 1 \end{array}\right] V_s$$

$$\left[\begin{array}{c:c} I & -\begin{pmatrix} 0 & -1 \\ 1 & 0 \end{pmatrix} p_{sb} \\ \hdashline 0 & 1 \end{array}\right] J_{sb}\dot{\theta} = J_\sigma \dot{\theta}$$

$$J_\sigma = \left[\begin{array}{c:c} I & -\begin{pmatrix} 0 & -1 \\ 1 & 0 \end{pmatrix} \left[\begin{array}{c} \cos\left(\mathcal{A}_{sb}\theta\right)^\top \\ \hdashline \sin\left(\mathcal{A}_{sb}\theta\right)^\top \end{array}\right] l\alpha_{sb} \\ \hdashline 0 & 1 \end{array}\right] \left[\begin{array}{c} \left[\begin{array}{c} -\sin(\mathcal{A}_{sb}\theta)^\top \\ \hdashline \cos(\mathcal{A}_{sb}\theta)^\top \end{array}\right] l\,|\mathcal{A}_{sb}| \\ \hdashline \alpha_{sb}^\top \end{array}\right]$$

$$= \begin{bmatrix} \left[\begin{array}{c} -\sin(\mathcal{A}_{sb}\theta)^\top \\ \hdashline \cos(\mathcal{A}_{sb}\theta)^\top \end{array}\right] l\,|\mathcal{A}_{sb}| - \left[\begin{array}{c} -\sin(\mathcal{A}_{sb}\theta)^\top \\ \hdashline \cos(\mathcal{A}_{sb}\theta)^\top \end{array}\right] l\alpha_{sb}\alpha_{sb}^\top \\ \hdashline \alpha_{sb}^\top \end{bmatrix}$$

$$= \begin{bmatrix} \left[\begin{array}{c} -\sin(\mathcal{A}_{sb}\theta)^\top \\ \hdashline \cos(\mathcal{A}_{sb}\theta)^\top \end{array}\right] \left[|\mathcal{A}_{sb}| - \alpha_{sb}\alpha_{sb}^\top\right] l \\ \hdashline \alpha_{sb}^\top \end{bmatrix}$$

Recall identity 2.2.1.5

$$J_\sigma = \begin{bmatrix} -\left[\begin{array}{c} -\sin(\mathcal{A}_{sb}\theta)^\top \\ \hdashline \cos(\mathcal{A}_{sb}\theta)^\top \end{array}\right] l\,|\mathcal{A}_{bs}| \\ \hdashline \alpha_{sb}^\top \end{bmatrix}$$

2.2.3 All Frames, A

I had defined *active frames vector* "α" and *active frames matrix* "$\mathcal{A}$" formulation in section 2.2.1 to construct explicit expressions for positions and velocities of any particular point p^a on a desired segment body "b" with respect to any desired spatial coordinate frame on the antenna "$\mathcal{C}_s$". Often, having the positions and velocities of all joints is necessary, e.g for the computation of total kinetic energy or when evaluating environmental constraints.

The value of the previous few sections—which really amounts to a way of managing a tedious bookkeeping problem—finally becomes clear in this section, where I will take advantage the active frames formulations in lemmas 2.2.1 and 2.2.2 and present expressions which would provide all frame α positions $P_{s\alpha} \in \mathbb{R}^{2\times n}$ and velocities

$V_{s\alpha} \in \mathbb{R}^{2\times n}$ with respect to the spatial frame $\mathcal{C}_s$.

- Let $P_s \in \mathbb{R}^{2(n+2)}$ be the vector of all coordinate frame positions with respect to the spatial frame $\mathcal{C}_s$ such that:

$$P_s = \text{vec}\left(\begin{bmatrix} p_{sG} & \dots & p_{sn} \end{bmatrix}\right) = \begin{bmatrix} p_{sG} \\ \vdots \\ p_{sn} \end{bmatrix}$$

  where vec$(\cdot)$ is the vectorization or *stack* operation.

- Let $\Theta_s \in \mathbb{T}^{n+2}$ be the vector of all coordinate frame (absolute) orientations with respect to the spatial frame $\mathcal{C}_s$ such that:

$$\Theta_s = \begin{pmatrix} \theta_{sG} & \theta_{s0} & \dots & \theta_{sn} \end{pmatrix}^\top$$

- Let $\dot{P}_s \in \mathbb{R}^{2(n+2)}$ be the vector of all coordinate frame translational velocities with respect to the spatial frame $\mathcal{C}_s$ such that:

$$\dot{P}_s = \text{vec}\left(\begin{bmatrix} \dot{p}_{sG} & \dots & \dot{p}_{sn} \end{bmatrix}\right) = \begin{bmatrix} \dot{p}_{sG} \\ \vdots \\ \dot{p}_{sn} \end{bmatrix}$$

- Let $\dot{\Theta}_s \in \mathbb{R}^{n+2}$ be the vector of all coordinate frame angular velocities with respect to the spatial frame $\mathcal{C}_s$ such that:

$$\dot{\Theta}_s = \begin{pmatrix} \dot{\theta}_{sG} & \dot{\theta}_{s0} & \dots & \dot{\theta}_{sn} \end{pmatrix}^\top$$

For any desired spatial frame $\mathcal{C}_s$, up to n+2 active frame vectors α_{sb} $b \in \{-1, 0, 1, \ldots, n\}$ can be constructed, one of which is the zero vector i.e $\alpha_{ss} = 0$.

Example:

Consider a planar serial open kinematic chain with $n = 8$ segments. Say the spatial frame index s is 5 and the target body frame index b is 1. Then, all active frame vectors α_{sb} would be:

$$\alpha_{5,G} = \begin{pmatrix} -1 & -1 & -1 & -1 & -1 & -1 & 0 & 0 & 0 \end{pmatrix}^\top$$
$$\alpha_{5,0} = \begin{pmatrix} 0 & -1 & -1 & -1 & -1 & -1 & 0 & 0 & 0 \end{pmatrix}^\top$$
$$\alpha_{5,1} = \begin{pmatrix} 0 & 0 & -1 & -1 & -1 & -1 & 0 & 0 & 0 \end{pmatrix}^\top$$
$$\alpha_{5,2} = \begin{pmatrix} 0 & 0 & 0 & -1 & -1 & -1 & 0 & 0 & 0 \end{pmatrix}^\top$$
$$\alpha_{5,3} = \begin{pmatrix} 0 & 0 & 0 & 0 & -1 & -1 & 0 & 0 & 0 \end{pmatrix}^\top$$
$$\alpha_{5,4} = \begin{pmatrix} 0 & 0 & 0 & 0 & 0 & -1 & 0 & 0 & 0 \end{pmatrix}^\top$$
$$\alpha_{5,5} = \begin{pmatrix} 0 & 0 & 0 & 0 & 0 & 0 & 0 & 0 & 0 \end{pmatrix}^\top$$
$$\alpha_{5,6} = \begin{pmatrix} 0 & 0 & 0 & 0 & 0 & 0 & 1 & 0 & 0 \end{pmatrix}^\top$$
$$\alpha_{5,7} = \begin{pmatrix} 0 & 0 & 0 & 0 & 0 & 0 & 1 & 1 & 0 \end{pmatrix}^\top$$
$$\alpha_{5,8} = \begin{pmatrix} 0 & 0 & 0 & 0 & 0 & 0 & 1 & 1 & 1 \end{pmatrix}^\top$$

I combine all possible active frame vectors to create the matrix $\mathbf{A} \in \{-1, 0, 1\}^{n+1 \times n+2}$ such that:

$$\mathbf{A} = \left[\alpha_{sG} \vdots \alpha_{s0} \vdots \dots \vdots \alpha_{sn} \right] \quad \forall b \in \{G, 0, \dots, n\} \tag{2.2.3.1}$$

The matrix $\mathbf{A}$ can also be directly synthesized by using two extreme active frame vectors α_{sG} and α_{sn} such that:

$$\begin{aligned} \mathbf{A} &= \left[\alpha_{sG} \vdots \mathcal{A}_{sG}^{\top} + \mathcal{A}_{sn}^{\top} \right] \\ &\text{or} \\ \mathbf{A} &= \left[\alpha_{sG} \vdots \mathcal{A}_{(sG+sn)}^{\top} \right] \end{aligned} \tag{2.2.3.2}$$

where $\mathcal{A}_{sG}$, $\mathcal{A}_{sn}$ and $\mathcal{A}_{(sG+sN)}$ are the *active frames matrices* computed from α_{sG}, α_{sn} and $\alpha_{sG} + \alpha_{sn}$ respectively as defined in section 2.2.1.

Example: Consider a planar serial open kinematic chain with $n = 8$ segments. Say the spatial frame index s is 5 and the target body frame index b is 1. Then the matrix

$\mathbf{A} \in \{-1, 0, 1\}^{9\times 10}$ would be:

$$\begin{pmatrix} -1 & 0 & 0 & 0 & 0 & 0 & 0 & 0 & 0 \\ -1 & -1 & 0 & 0 & 0 & 0 & 0 & 0 & 0 \\ -1 & -1 & -1 & 0 & 0 & 0 & 0 & 0 & 0 \\ -1 & -1 & -1 & -1 & 0 & 0 & 0 & 0 & 0 \\ -1 & -1 & -1 & -1 & -1 & 0 & 0 & 0 & 0 \\ -1 & -1 & -1 & -1 & -1 & -1 & 0 & 0 & 0 \\ 0 & 0 & 0 & 0 & 0 & 0 & 1 & 1 & 1 \\ 0 & 0 & 0 & 0 & 0 & 0 & 0 & 1 & 1 \\ 0 & 0 & 0 & 0 & 0 & 0 & 0 & 0 & 1 \end{pmatrix}$$

2.2.3.1 All frame positions and orientations

The third column of the hybrid transformation H_{sb} contains frame positions and orientations $\begin{pmatrix} p_{sb} & \theta_{sb} \end{pmatrix}^\top \in \mathbb{R}^3$ of the desired frame $\mathcal{C}_b$, with respect to the spatial frame $\mathcal{C}_s$. The coordinates of all frames with respect to the desired spatial frame $\mathcal{C}_s$ can be computed via lemma 2.2.1 as:

$$\begin{aligned} p_{sG2\times 1} &= \left[\begin{array}{c} \cos\left(\mathcal{A}_{sG}\theta\right)^\top \\ \hdashline \sin\left(\mathcal{A}_{sG}\theta\right)^\top \end{array}\right]_{2\times n+1} l\alpha_{sG} \\ p_{s0} &= \left[\begin{array}{c} \cos\left(\mathcal{A}_{s0}\theta\right)^\top \\ \hdashline \sin\left(\mathcal{A}_{s0}\theta\right)^\top \end{array}\right] l\alpha_{s0} \\ &\vdots \end{aligned}$$

$$p_{sn} = \begin{bmatrix} \cos\left(\mathcal{A}_{sn}\theta\right)^{\top} \\ \hdashline \sin\left(\mathcal{A}_{sn}\theta\right)^{\top} \end{bmatrix} l\alpha_{sn}$$

where

With the introduction of the matrix $\mathbf{A}$, all frame positions P_s can be computed as:

$$\begin{bmatrix} p_{sG} \vdots \cdots \vdots p_{sn} \end{bmatrix} = \begin{bmatrix} \cos\left(\mathcal{A}_{(sG+sn)}\theta\right)^{\top} \\ \hdashline \sin\left(\mathcal{A}_{(sG+sn)}\theta\right)^{\top} \end{bmatrix} l\mathbf{A}$$

$$P_s = \text{vec}\left(\begin{bmatrix} p_{sG} \vdots \cdots \vdots p_{sn} \end{bmatrix}\right) \tag{2.2.3.3}$$

Similarly, all body frame orientations Θ_s with respect to $\mathcal{C}_s$ can be simply computed as:

$$\Theta_s = \mathbf{A}^{\top}\theta \tag{2.2.3.4}$$

2.2.3.2 All frame velocities and Jacobians

The hybrid velocity vector V_h—the third column of $\dot{H}_{sb}$—contains coordinate frame translational and angular velocities such that $V_h = \begin{pmatrix} \dot{p}_{sb} & \omega_{sb} \end{pmatrix}^{\top}$. The translational hybrid velocities of all frames with respect to the desired spatial frame $\mathcal{C}_s$ can be

computed via lemma 2.2.2 as:

$$\begin{aligned}
\dot{p}_{sG} &= \begin{bmatrix} -\sin(\mathcal{A}_{sG}\theta)^\top \\ \hdashline \cos(\mathcal{A}_{sG}\theta)^\top \end{bmatrix} l\,|\mathcal{A}_{sG}|\,\dot{\theta} \\
\dot{p}_{s0} &= \begin{bmatrix} -\sin(\mathcal{A}_{s0}\theta)^\top \\ \hdashline \cos(\mathcal{A}_{s0}\theta)^\top \end{bmatrix} l\,|\mathcal{A}_{s0}|\,\dot{\theta} \\
&\vdots \\
\dot{p}_{sn} &= \begin{bmatrix} -\sin(\mathcal{A}_{sn}\theta)^\top \\ \hdashline \cos(\mathcal{A}_{sn}\theta)^\top \end{bmatrix} l\,|\mathcal{A}_{sn}|\,\dot{\theta}
\end{aligned} \tag{2.2.3.5}$$

With the introduction of the matrix $\mathbf{A}$, all frame translational velocities ($\dot{p}_{sb}\ \forall b \in \{G, 0, \ldots, n\}$) can be computed as:

$$\dot{P}_s = \operatorname{vec}\left(\begin{bmatrix} \dot{p}_{sG} \vdots \ldots \vdots \dot{p}_{sn} \end{bmatrix}\right) = \left[\mathbf{A}^\top \odot \begin{bmatrix} -\sin(\mathcal{A}_{(sG+sn)}\theta)^\top \\ \hdashline \cos(\mathcal{A}_{(sG+sn)}\theta)^\top \end{bmatrix} l\right] \mathcal{A}_{(sG+sn)}\dot{\theta} \tag{2.2.3.6}$$

where $\odot$ is the "columnwise" Kronecker product ($\otimes$) called as the *Khatri-Rao product*. Given matrices $A \in \mathbb{R}^{n\times p}$ and $B \in \mathbb{R}^{m\times p}$, their Khatri-Rao product is a matrix of size $nm \times p$ defined by:

$$A \odot B = \begin{bmatrix} a_1 \otimes b_1 & a_2 \otimes b_2 & \cdots & a_p \otimes b_p \end{bmatrix}$$

Similarly, all frame angular velocities ($\dot{\theta}_{sb}\ \forall b \in \{G, 0, \ldots, n\}$) can be computed as:

$$\dot{\Theta}_s = \begin{pmatrix} \dot{\theta}_{sG} & \ldots & \dot{\theta}_{sn} \end{pmatrix}^\top = \mathbf{A}^\top \dot{\theta} \tag{2.2.3.7}$$

2.2.4 Joint Limits

Both the biological and my robotic implementation of the antenna have angular limits at every joint. Introducing joint limits prevent any arbitrary point p^a on a segment to revolve about its joint axis more than once and thus bounds the maximum torque due to the stiffness element at that joint. I also employ joint limits to preload the stiffness elements so that they cannot assume their neutral (zero energy) state.

As I will show in Chapter 3, the antenna is assumed to have the minimum energy configuration during the "quasi-static" flipping event, and unconstrained convex optimization methods are very fast at minimizing quadratic (energy) functions. However, if there are boundaries (joint limits) on the forward kinematics, the problem becomes a *box* or *bound* constrained minimization [44] i.e:

$$\min_{\theta} \mathbf{U}(\theta) = \frac{1}{2}\theta^\top \mathcal{K} \theta$$

$$\text{subject to} \quad \gamma_{\text{cw}} \leq \theta \leq \gamma_{\text{ccw}}$$

where $\mathcal{K}$ is symmetric and γ_{CW} and γ_{CCW} are vectors of lower (clockwise) and upper (counter-clockwise) bounds of the components of joint angles θ. In this case, the energy cost function would not be strictly convex in the neighborhood of those boundaries (see Figure 2.7) where gradient descent based methods encounter a discontinuity for the first derivative. Even though there are various algorithms such as Matlab's *fminbnd* that can circumvent this condition, they may suffer from slow convergence rates around the boundaries.

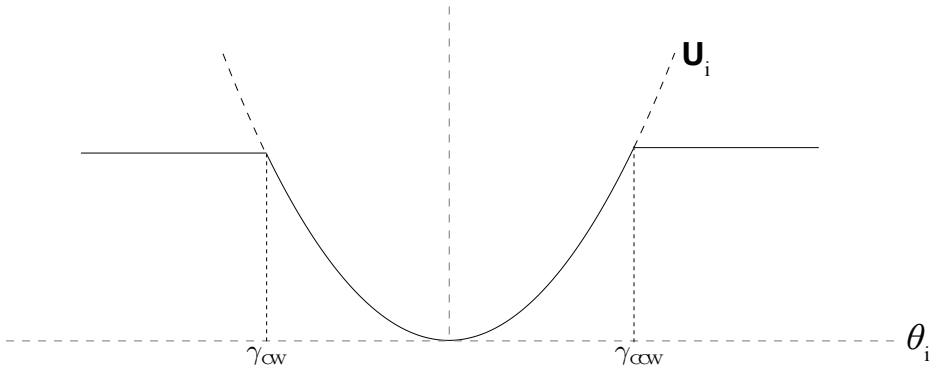

Figure 2.7: The potential energy of a single segment $\mathbf{U}_i$ under the influence of joint limits. Note that the first derivative of the energy function has discontinuities at the boundaries $(\gamma_{\text{CCW}}, \gamma_{\text{CW}})$.

In this section, I introduce a new set of generalized coordinates $\{q, \dot{\theta}\}$ (instead of $\{\theta, \dot{\theta}\}$) and a joint limit mapping g between q and θ, so that the cost function $\mathbf{U}(\theta)$ has a continuous first derivative (C^1) for all values of $q \in \mathbb{R}^{n+1}$ through the mapping $g : q \mapsto \theta$.

- Let $\gamma_{\text{CW,i}}, \gamma_{\text{CCW,i}} \in \mathbb{S}^1$ be the clockwise and counterclockwise angular limits for

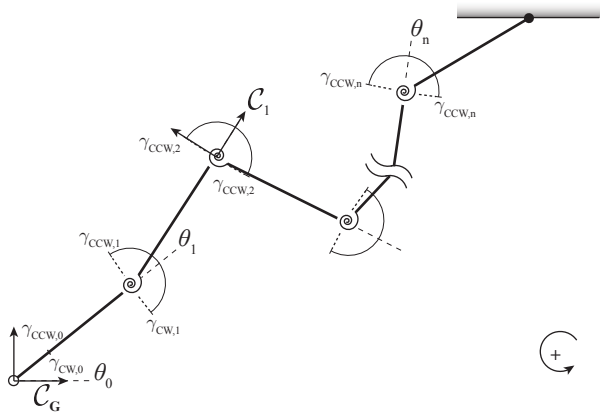

Figure 2.8: Uniform joint limits throughout the flagellum. Note that the base joint limits $\gamma_{\text{CCW},0}$ and $\gamma_{\text{CCW},0}$ are identical, which facilitates a rigid link.

any joint $i \in \{0, 1, 2, ..., n\}$ in radians respectively. Note that each joint limit $\gamma_{\text{CW,i}}$ and $\gamma_{\text{CCW,i}}$ is measured with respect to the proximally neighboring body frame $\mathcal{C}_{i-1}$ (see Figure 2.8).

- Let $\gamma_i = \{\gamma_{\text{CCW,i}}, \gamma_{\text{CW,i}}\}$ be an ordered pair of counterclockwise and clockwise joint angular limits in radians for any given joint $i \in \{0, 1, 2, ..., n\}$ respectively.

- Let $\gamma_{\text{CW}}, \gamma_{\text{CCW}} \in \mathbb{T}^{n+1}$ be the vectors of clockwise and counter-clockwise joint angular limits in radians respectively such that:

$$\gamma_{\text{CW}} = \begin{pmatrix} \gamma_{\text{CW,0}} & \gamma_{\text{CW,1}} & \cdots & \gamma_{\text{CW,n}} \end{pmatrix}^\top$$
$$\gamma_{\text{CCW}} = \begin{pmatrix} \gamma_{\text{CCW,0}} & \gamma_{\text{CCW,1}} & \cdots & \gamma_{\text{CCW,n}} \end{pmatrix}^\top$$

- Let $q \in \mathbb{R}^{n+1}$ be the new joint space coordinate vector for the antenna such

that $q = \begin{pmatrix} q_0 & q_1 & \dots & q_n \end{pmatrix}^\top$ and $\theta = g(q, \gamma_{\text{ccw}}, \gamma_{\text{cw}})$.

- Let $g : q \mapsto \theta$ be the *joint-limit* mapping from q to the joint angles.

I will use the output of the *joint-limit* mapping g as the input for both the forward and differential kinematics in sections 6.1.1 and 6.1.2. The resulting composite functions $(f \circ g) : q \mapsto p^a_{sb}$ and $(df \circ g) : q \mapsto v^a_{sb}$ honor the imposed joint limits for θ without having bounds on their domain (i.e q is unconstrained).

I define the joint limit mapping function g for a single joint angle i as:

$$\theta_i = \frac{1}{2}\left(\gamma_{\text{ccw,i}} + \gamma_{\text{cw,i}}\right) + \frac{1}{2}\left(\gamma_{\text{ccw,i}} - \gamma_{\text{cw,i}}\right)\sin q_i \tag{2.2.4.1}$$

Then, the mapping function g for the joint angle vector θ given the joint limit vectors γ_{ccw} and γ_{cw} can be written as:

$$\theta = g(q, \gamma_{\text{ccw}}, \gamma_{\text{cw}})$$

$$\theta = \frac{1}{2}\left(\gamma_{\text{ccw}} + \gamma_{\text{cw}}\right) + \frac{1}{2}\begin{pmatrix} \sin q_0 & & & \\ & \sin q_1 & & \\ & & \ddots & \\ & & & \sin q_n \end{pmatrix}\left(\gamma_{\text{ccw}} - \gamma_{\text{cw}}\right) \tag{2.2.4.2}$$

$$= \frac{1}{2}\left[\,\text{diag}\left(\gamma_{\text{ccw}} - \gamma_{\text{cw}}\right) \vdots \gamma_{\text{ccw}} + \gamma_{\text{cw}}\,\right]\begin{pmatrix} \sin(q) \\ 1 \end{pmatrix} \tag{2.2.4.3}$$

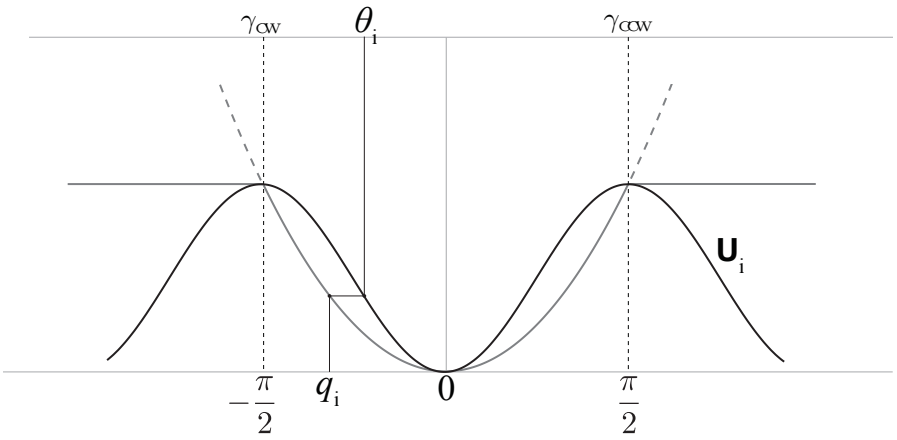

Figure 2.9: The potential energy of a single segment $\mathbf{U}_i$ with joint limits relative to the new joint space coordinates q (superimposed on the case in Figure 2.7). Note that the energy function is now smooth irrespective of joint limits.

The joint-limit mapping g in equation 2.2.4.2 is a sinusoidal function with the following properties:

- The domain of g is the entire real line, i.e $q \in (-\infty, \infty)$ (see Figure 2.10).
- The range of g is between the joint limits, i.e $g(q) \in (\gamma_{\text{CW}}, \gamma_{\text{CCW}}) \subset \mathbb{S}^1$ (see Figure 2.10).
- $q = 0$ corresponds to the half angle between the joint limits, i.e $g(0) = \frac{\gamma_{\text{CW}}+\gamma_{\text{CCW}}}{2}$ (see Figure 2.9).
- $q = (\frac{1}{2} + 2k)\pi \,|\, k \in \mathbb{Z}^{n+1}$ corresponds to the counterclockwise joint limits γ_{CCW}, i.e $g(\frac{\pi}{2} + 2k\pi) = \gamma_{\text{CCW}}$ (see Figure 2.9).
- $q = (-\frac{1}{2} - 2k)\pi \,|\, k \in \mathbb{Z}^{n+1}$ corresponds to the clockwise joint limit vector γ_{CW},

i.e $g(-\frac{\pi}{2} - 2k\pi) = \gamma_{\text{cw}}$ (see Figure 2.9).

- If $\gamma_{\text{cw,i}} = \gamma_{\text{ccw,i}}$ for any i, then $g(q_i) = \gamma_{\text{ccw,i}} = \gamma_{\text{cw,i}}$ for all $q_i \in \mathbb{R}$.

- The total angular range of the joint i is given as $|\gamma_{\text{ccw,i}} - \gamma_{\text{cw,i}}|$.

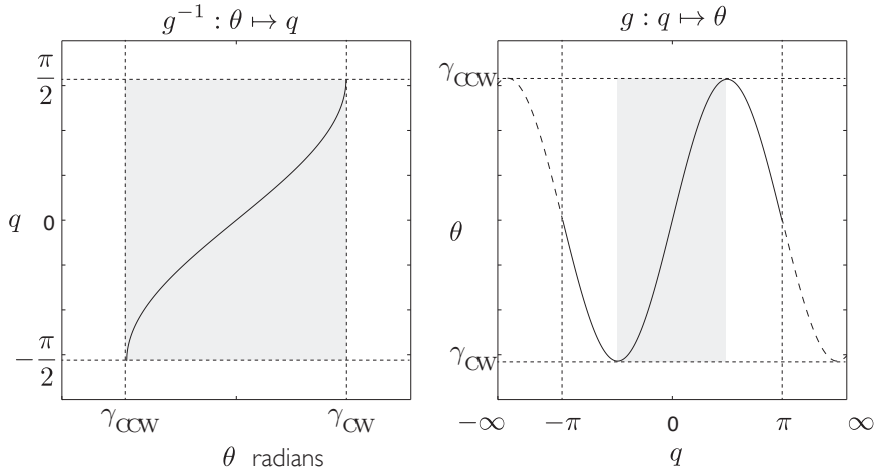

Figure 2.10: g and it's inverse g^{-1} mapping functions

My physical implementations of the antenna have uniform joint limits (see 2.11) except the base such that:

$$\begin{aligned} \gamma_{\text{ccw,j}} &= \frac{\pi}{2} \\ \gamma_{\text{cw,j}} &= -\frac{\pi}{2} \\ \implies \quad \gamma_j &= \{\frac{\pi}{2}, -\frac{\pi}{2}\} \quad \forall\, j \in \{1, 2, \ldots, n\} \end{aligned}$$

On the other hand, the base angular limits $\gamma_{\text{cw,0}}$ and $\gamma_{\text{ccw,0}}$ are both set to the base

angle θ_0 so that it's constant for all values of q_0:

$$\gamma_{\text{CCW},0} = \theta_0$$

$$\gamma_{\text{CW},0} = \theta_0$$

$$\implies \gamma_0 = \{\theta_0, \theta_0\}$$

It's important to note a joint limit is *counterclockwise* (i.e γ_{CCW}) if it can be encountered after an allowed counterclockwise rotation starting from the neutral state (i.e at $g(0)$), and visa versa for the clockwise case. Figure 2.12 illustrates how q values between $-\pi$ and π gets remapped between the joint limits $\{\frac{\pi}{2}, -\frac{\pi}{2}\}$ through g. As a result, any segment i, rotating about the body frame $\mathcal{C}_{i-1}$ of the neighboring proximal segment, can do so until it reaches either the clockwise or counterclockwise limits as shown in Figure 2.11.

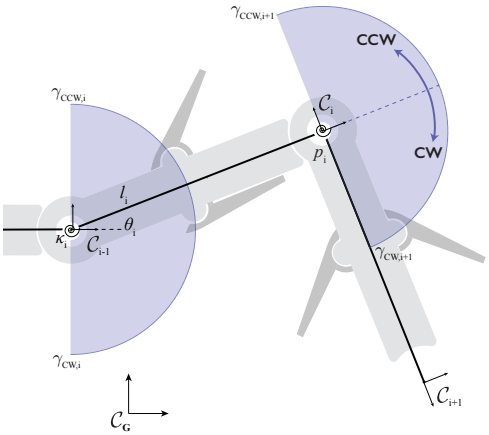

Figure 2.11: Illustration of the antenna as a rigid body hitting clockwise angular limit.

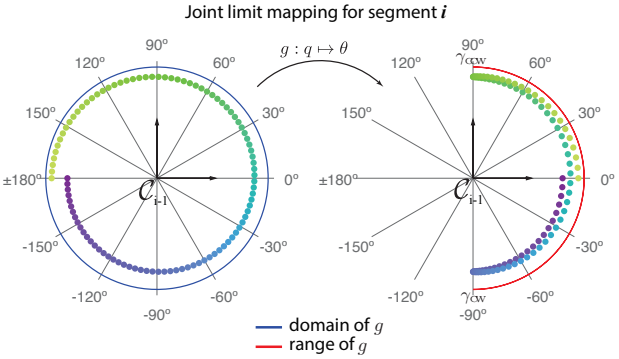

Figure 2.12: The mapping from q_i to θ_i for an individual segment with joint limits about the neighboring proximal segment body frame $\mathcal{C}_{i-1}$.

2.2.4.1 Inverse mapping

Since I changed the joint space coordinates from θ to q, the initial conditions of the simulation experiment have to be provided in the domain of q. Thus the inverse mapping g^{-1} from θ to q is required.

The inverse joint limit mapping $g^{-1} : \theta \mapsto q$ can be derived directly from equation 2.2.4.3 as:

$$
\begin{aligned}
\theta &= \frac{1}{2}\mathrm{diag}(\gamma_{\mathrm{CCW}} - \gamma_{\mathrm{CW}})\sin(q) + \frac{1}{2}(\gamma_{\mathrm{CCW}} + \gamma_{\mathrm{CW}}) \\
2\theta - (\gamma_{\mathrm{CCW}} + \gamma_{\mathrm{CW}}) &= \mathrm{diag}(\gamma_{\mathrm{CCW}} - \gamma_{\mathrm{CW}})\sin(q) \\
\sin(q) &= \mathrm{diag}\left(\gamma_{\mathrm{CCW}} - \gamma_{\mathrm{CW}}\right)^{-1}\left(2\theta - \gamma_{\mathrm{CCW}} - \gamma_{\mathrm{CW}}\right) \qquad \forall \gamma_{\mathrm{CW,i}} \neq \gamma_{\mathrm{CCW,i}} \\
q &= \sin^{-1}\underbrace{\left[\mathrm{diag}\left(\begin{pmatrix} \frac{1}{\gamma_{\mathrm{CCW},0} - \gamma_{\mathrm{CW},0}} & \cdots & \frac{1}{\gamma_{\mathrm{CCW,n}} - \gamma_{\mathrm{CW,n}}} \end{pmatrix}^{\top}\right)\left(2\theta - \gamma_{\mathrm{CCW}} - \gamma_{\mathrm{CW}}\right)\right]}_{\in(-1,1)} \\
q &= \sin^{-1}\left[\mathrm{diag}\left(\gamma_{\mathrm{CCW}} - \gamma_{\mathrm{CW}}\right)^{\dagger}\left(2\theta - \gamma_{\mathrm{CCW}} - \gamma_{\mathrm{CW}}\right)\right] \qquad (2.2.4.4)
\end{aligned}
$$

where † is the Moore–Penrose pseudo-inverse operator.

Note that θ is assumed to be between the realizable joint limits i.e $\gamma_{\mathrm{CW}} \leq \theta \leq \gamma_{\mathrm{CCW}}$. Similarly, q is given between $-\frac{\pi}{2}$ and $\frac{\pi}{2}$ (see Figure 2.10). In the case that $\gamma_{\mathrm{CW,i}} \simeq \gamma_{\mathrm{CCW,i}}$, the inverse function g^{-1} is ill-conditioned because the $\frac{1}{\gamma_{\mathrm{CCW,i}} - \gamma_{\mathrm{CW,i}}}$ terms become arbitrarily large. However since the bounds on the output would also get tighter, the resulting mapping is robust. On the other hand when $\gamma_{\mathrm{CW,i}}$ is equal to $\gamma_{\mathrm{CCW,i}}$, any

value of q would map exactly to the joint limit, which makes the inverse problem ill-posed. To remedy this problem, I set $\frac{1}{\gamma_{\text{CCW,i}} - \gamma_{\text{CW,i}}}$ to zero for all $\gamma_{\text{CW,i}} = \gamma_{\text{CCW,i}}$, which is equivalent of taking the pseudo-inverse of the matrix "diag $(\gamma_{\text{CCW}} - \gamma_{\text{CW}})$".

Notice that due to the sinusoidal nature of g any angular value for θ can be realized by two values of q per period, which are 2π apart (see Figure 2.12). Thus even though the function g has a 2π period, the inverse mapping g^{-1} is not periodic and it's range $(g^{-1}(\theta))$ is always between $-\frac{\pi}{2}$ and $\frac{\pi}{2}$, which is illustrated in Figure 2.13.

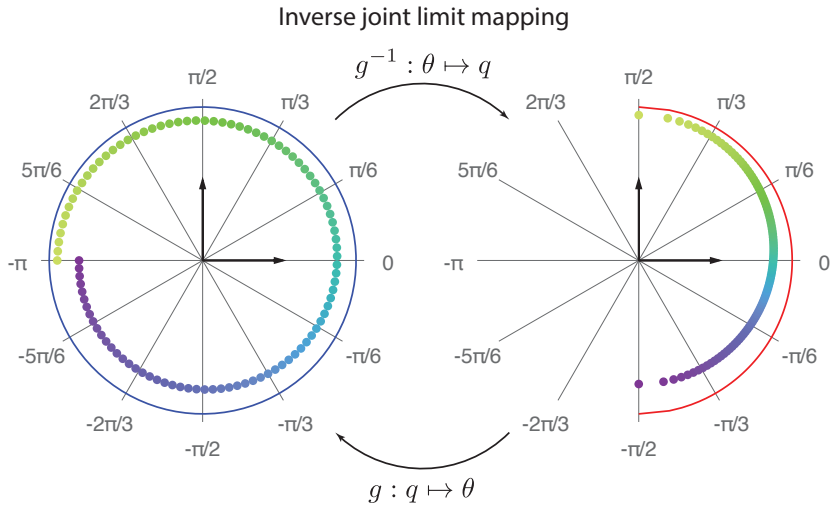

Figure 2.13: Inverse mapping (g^{-1}) example for joint limits $\gamma = \{\pi, -\pi\}$. The range of g^{-1} is always $-\frac{\pi}{2}$ and $\frac{\pi}{2}$.

2.2.4.2 Mapping Jacobian, J_g

The Jacobian of the mapping g $(J_g = \frac{\partial g(q)}{\partial q})$ appears on the differential kinematics when q is the generalized coordinates instead of θ. It's computed directly as:

$$
\begin{aligned}
J_g &= -\frac{1}{2}\mathrm{diag}\left(\cos q\right)\mathrm{diag}\left(\gamma_{\mathrm{CCW}} - \gamma_{\mathrm{CW}}\right) \\
&= -\frac{1}{2}\begin{pmatrix} \cos\left(q_0\right)\left(\gamma_{\mathrm{CCW},0} - \gamma_{\mathrm{CW},0}\right) & & & \\ & \cos\left(q_1\right)\left(\gamma_{\mathrm{CCW},1} - \gamma_{\mathrm{CW},1}\right) & & \\ & & \ddots & \\ & & & \cos\left(q_n\right)\left(\gamma_{\mathrm{CCW,n}} - \gamma_{\mathrm{CW,n}}\right) \end{pmatrix}
\end{aligned} \tag{2.2.4.5}
$$

2.2.4.3 Mapping Hessian, ∇_g^2

The Hessian matrix of the mapping g is the gradient of the mapping Jacobian (i.e $\nabla_g^2 = \nabla J_g$). This Hessian matrix appears in the potential energy minimization problem via quadratic programming. Notice that ∇J_g is a matrix valued function and thus it's Jacobian $\frac{\partial J_g}{\partial q} = \nabla_g^{2\top}$ is not conventional.

$$
\begin{aligned}
\frac{\partial J_g}{\partial q} &= \begin{bmatrix} \frac{\partial J_g}{\partial q_1} \\ \vdots \\ \frac{\partial J_g}{\partial q_n} \end{bmatrix} = -\frac{1}{2}\begin{bmatrix} \begin{pmatrix} -\sin q_0 & & & \\ & 0 & & \\ & & \ddots & \\ & & & 0 \end{pmatrix}\mathrm{diag}\left(\gamma_{\mathrm{CCW}} - \gamma_{\mathrm{CW}}\right) \\ \vdots \\ \begin{pmatrix} 0 & & & \\ & \ddots & & \\ & & 0 & \\ & & & -\sin q_n \end{pmatrix}\mathrm{diag}\left(\gamma_{\mathrm{CCW}} - \gamma_{\mathrm{CW}}\right) \end{bmatrix} \\
\frac{\partial J_g}{\partial q} &= \frac{1}{2}\left[\mathrm{diag}\left(\gamma_{\mathrm{CCW}} - \gamma_{\mathrm{CW}}\right) \odot \mathrm{diag}\left(\cos q\right)\right]
\end{aligned} \tag{2.2.4.6}
$$

Potential Energy

- Let $\kappa \in \mathbb{R}^{n+1}$ be the vector of joint rotational stiffnesses and base rotational (bending) stiffness in Newton-meter per radians ($\frac{Nm}{rad}$) s.t: $\kappa = \begin{pmatrix} \kappa_0 & \kappa_1 & \dots & \kappa_n \end{pmatrix}^\top$

- Let $\kappa_0 \in \mathbb{R} = 0$ be the base rotational stiffness for the base angle, which is modeled as a pin-joint affixed by a joint constraint rather than an infinite stiffness.

- Let $\mathbf{U}_{sb}$ be the potential energy of the desired body b with respect to the inertial frame $\mathcal{C}_s$ in *Joules* (J). Note that the potential energy is measured zero ($\mathbf{U}_{sb} = 0$) if the inertial frame and the body frame are identical ($b = s$).

- Let $\mathbf{U}^a_{sb} \in \mathbb{R}$ be the potential energy of the differential point mass "a" on the body "b" in *Joules* relative to the inertial frame $\mathcal{C}_s$.

- Let $\mathbf{U}$ be the total strain (potential) energy of the antenna in *Joules* (J). Note that the total energy is independent of the choice of inertial frame $\mathcal{C}_s$ such that $\mathbf{U} = \mathbf{U}_s$ for all s.

The total strain (potential) energy of the flagellum is entirely stored in the springs at the joints. For n joint, the total energy $\mathbf{U}$ is given as:

$$\begin{aligned}\mathbf{U} &= \frac{1}{2}\kappa_1\theta_1^2 + \frac{1}{2}\kappa_2\theta_2^2 + \cdots + \frac{1}{2}\kappa_n\theta_n^2 \\ &= \frac{1}{2}\sum_{i=1}^{n}\kappa_i\theta_i^2 \end{aligned} \tag{2.2.4.7}$$

The base joint is a pin-joint and thus has zero bending stiffness. The total strain energy of the antenna then can be written in matrix as:

$$\mathbf{U} = \frac{1}{2}\theta^\top \underbrace{\begin{pmatrix}\kappa_0 & & & \\ & \kappa_1 & & \\ & & \ddots & \\ & & & \kappa_n\end{pmatrix}}_{\mathcal{K}}\theta \tag{2.2.4.8}$$

where $\mathcal{K}$ is the diagonal *joint stiffness matrix*.

2.3 The Robotic Model

Here I present my highly tunable, biologically inspired artificial antenna *template* [45] (Figure 2.14) that I developed in 2009. Most of the engineering details with drawings can be found in [1], so in this section I will only provide a general design overview. Throughout this dissertation, this *physical* model of antenna-based tactile sensing—that is, an embodied mechanical system and environmental testbed—provided an essential experimental component to understand and evaluate performance given the

complex interactions that occur between an antenna and its environment. I conducted various experiments to guide the development of kinematic models as well as complementary but more narrowly focused experiments on the biological antennae. I also addressed synergistic questions regarding the necessary mechanical properties for developing task-specific high performance antennae for robotic applications.

2.3.1 Design

As depicted in Figure 2.14, the antenna is a serially connected planar rigid body chain where the 40 mm long, modular, identical, stand-alone segments can be oriented from 90° to 270° relative to the adjacent segments. Each segment (Figure 2.14) is interconnected through a short diametrically magnetized cylinder acting as the hinge shaft. The top half of the cylindrical magnet is press-fit into a stainless steel ball-bearing on the proximal segment, and the bottom half is slid into the joint hole of the distal segment chassis. A set-screw is tightened to pinch the hinge shaft so that the magnet always turns with the distal segment. The ball-bearing enables the shaft to rotate freely with respect to the proximal segment. A Hall-effect rotary position sensor chip is positioned underneath the cylindrical magnet on the distal segment (Melexis NV, Ieper, Belgium). It facilitates contactless absolute angular orientation measurement of the shaft's magnetic poles in 0.09° resolution and outputs it as an analog voltage.

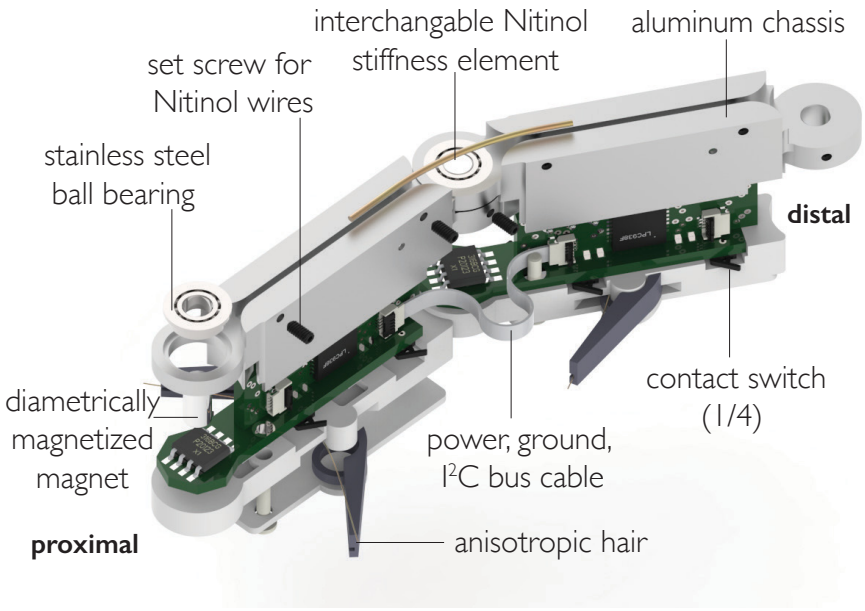

Figure 2.14: Exploded CAD rendering of two interlocking antenna segments.

I incorporated four directional detector switches as binary touch sensors on the segment, uniformly distributed along its length. These detector switches are actuated by the distally pointing anisotropic hairs under external contact, so contact forces larger than the maximum operating force of 0.3 N are absorbed by the chassis (Figure 2.16).

The chassis for each segment is a sagittally symmetric, two piece, thin-walled, precision-machined aluminum shell structure that encapsulates the segment circuitry. For most of the experiments presented in this dissertation, I have replaced the bottom aluminum shell with a rapid prototyped counterpart which enabled me to change the orientation of the hairs. When a hair is bent towards the distal (or proximal) end of the antenna, then the lever arm of the associated contact sensor is engaged.

The segment electronics subassembly is built upon two orthogonally joined PCB

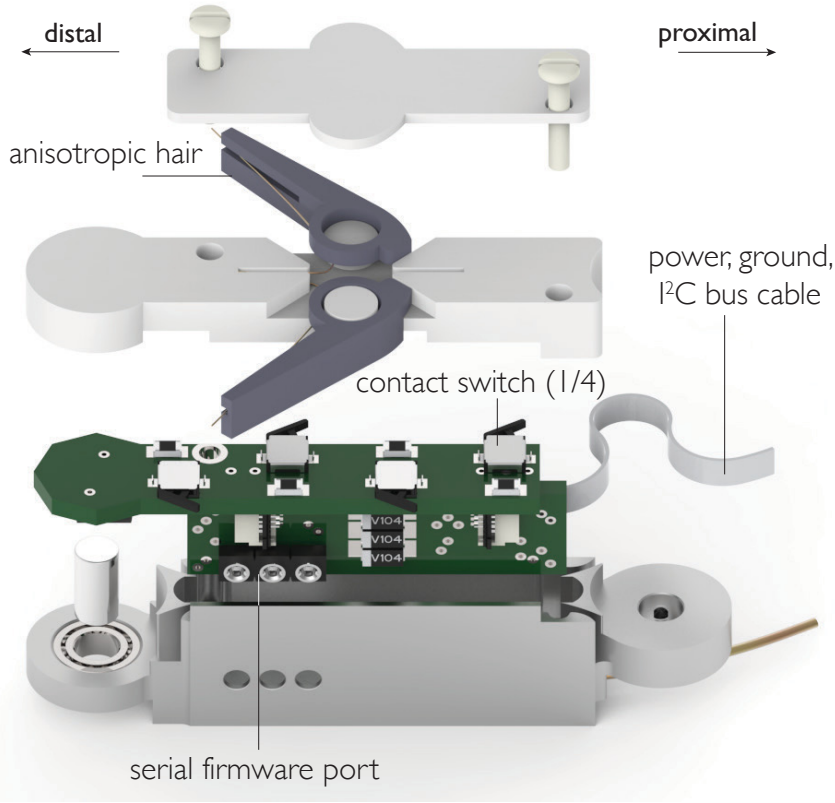

Figure 2.15: Exploded CAD rendering of a single segment (side view).

boards. There is a single I^{2}C bus along with the power and ground lines that connects all segments and the host robot computer, for which 0.5 mm Flat Flex ribbon cable (FFC) is used between each segment. As shown on Figure 2.14, this coupling cable enters and leaves a segment from a side of the user's choice through special slits designed to prevent force propagation towards the connectors on the PCB during large antennal deflections.

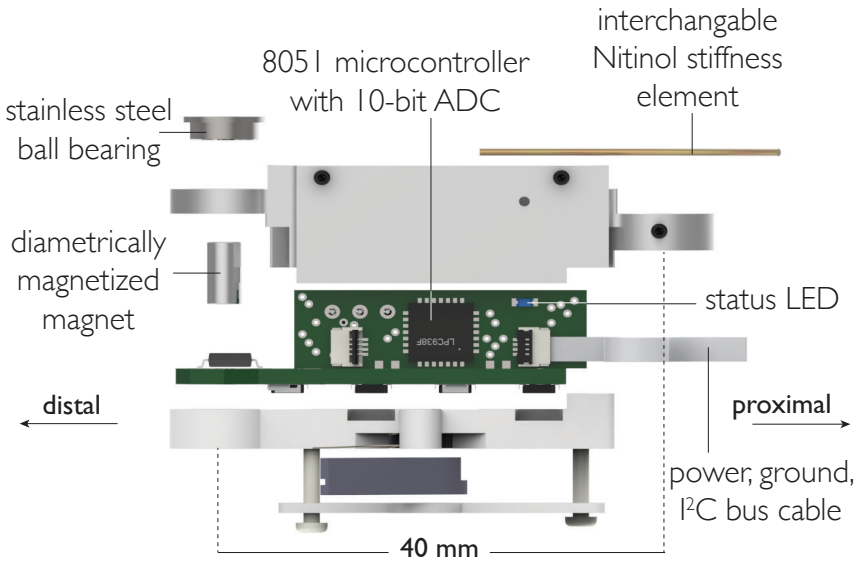

Figure 2.16: Exploded CAD rendering of a single segment (bottom view).

The contact detection switches are routed to four separate I/O pins and the Hall-effect sensor output is fed into the 10-bit analog to digital converter (ADC) on the segment's 8051 microcontroller (NXP Semiconductors N.V., Eindhoven, Netherlands). Each segment is equipped with a custom RS-232 serial port, which allows the firmware to be updated.

All relevant I/O pins are read at the same time using a keyboard interrupt routine defined for the microcontroller. No-contact and contact correspond to binary 0 and 1 respectively, which are then concatenated together to form a 4-bit value. This 4-bit constitutes the least 4 significant bits of the 2 byte package sent to the host microcontroller. The Hall-effect sensor output signal is processed and then appended in front of the touch data to fill the remaining 12-bits.

2.3.2 Static Configurations

I verified the accuracy of the imposed stiffness profile from the shape of several static equilibrium configurations of the antenna spanning between the body and the environment.

My multi-segmented antenna can be fitted with elastic wires up to 0.033 inch diameter in order to impose a specific inter-segmental stiffness profile. Even though there is no material constraint for this wire-form stiffness element, I have decided to limit my scope to Nitinol for its good elasticity and shape-memory characteristics. Throughout this study, the tunability of antennal stiffness profile is facilitated by Nitinol wires (56% Nickel vs 44% Titanium) at the segments, which I ordered from a single manufacturer to avoid material composition differences. Note that the inter-segmental stiffness is also affected by the 4-Channel *Flat Flex Cable* (FFC) 2.14

coupling element which adds a parallel stiffness.

2.3.2.1 Methods

I performed natural frequency experiments with my robotic antenna and empirically determined the diameter to antenna joint stiffness ratio. See Appendix 6.1.4 for the methods, data, and result.

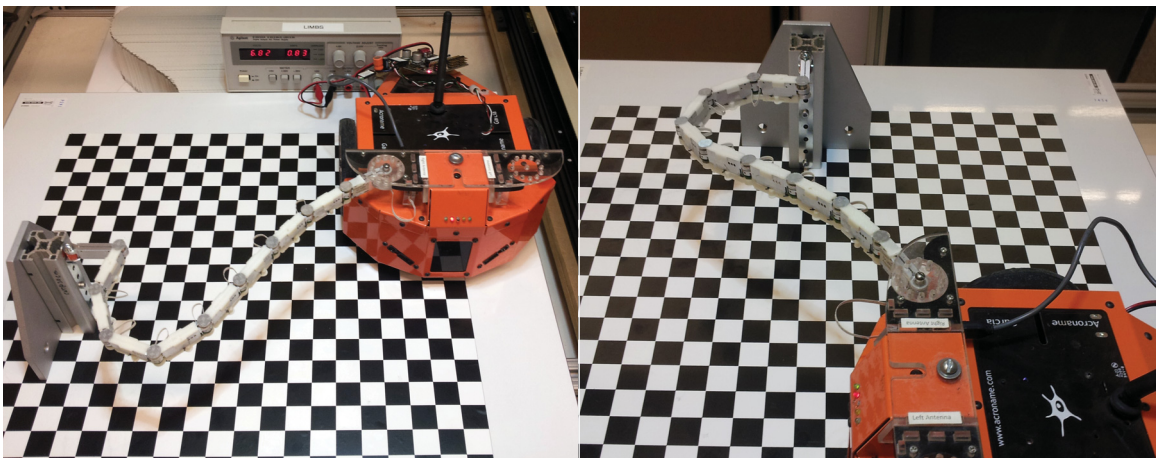

Figure 2.17: Static antenna configuration test setup. The robotic antenna configuration feedback is tested against optical tracking and simulation results.

For the stiffness profile verification experiments, I constrained the antenna between a pin joint and the robot body at a known base angle. For any given trial, I placed the pin joint at the tip of the antenna at a different position relative to the base and let the antenna assume its natural shape (Figure 2.17). I conducted a total of 15 trials, for each the antenna joint positions were sampled both by my custom optical tracking rig (see Appendix 6.3) and the antenna's onboard angle sensors. The 1200×720 at

$30fps$ optical tracking system captured the retroreflective marker positions at the joints for ten seconds using an template matching algorithm (see Figure 2.19). The pixel positions were then back projected to the pre-calibrated 3D plane of the antenna (see Figures 2.18,2.20,2.21). I used the average position values over the duration of the camera recording as the ground truth for the antenna configuration in that trial. I compared the ground truth configuration to the joint angle data sampled by the robotic antenna to characterize the error of the antenna at different configurations. Simultaneously, I numerically fitted an antenna with the same number of joints and the prescribed stiffness profile between the two extreme points given by the optical tracking. I measured the stiffness profile deviation between this simulated antenna and my robotic antenna.

The numerical fitting of the antenna between two points is nontrivial due to the existence of multiple solutions. Specifically, by the *principle of minimum potential energy*, there are as many stable equilibrium configurations as the number of local minima of the system's potential energy landscape. In the case of the antenna, the aforementioned base-tip constraints enable the antenna to assume two distinct equilibrium mode shapes and their symmetries, which correspond to the local potential energy minima. The first mode shape is the general "C" shape which corresponds to the lowest energy state (global minimum) of the antenna given the constraints. The second achievable mode shape is the "S" shape which corresponds to the next local energy minimum. Figure 2.22 shows the two symmetric statically stable equilibria

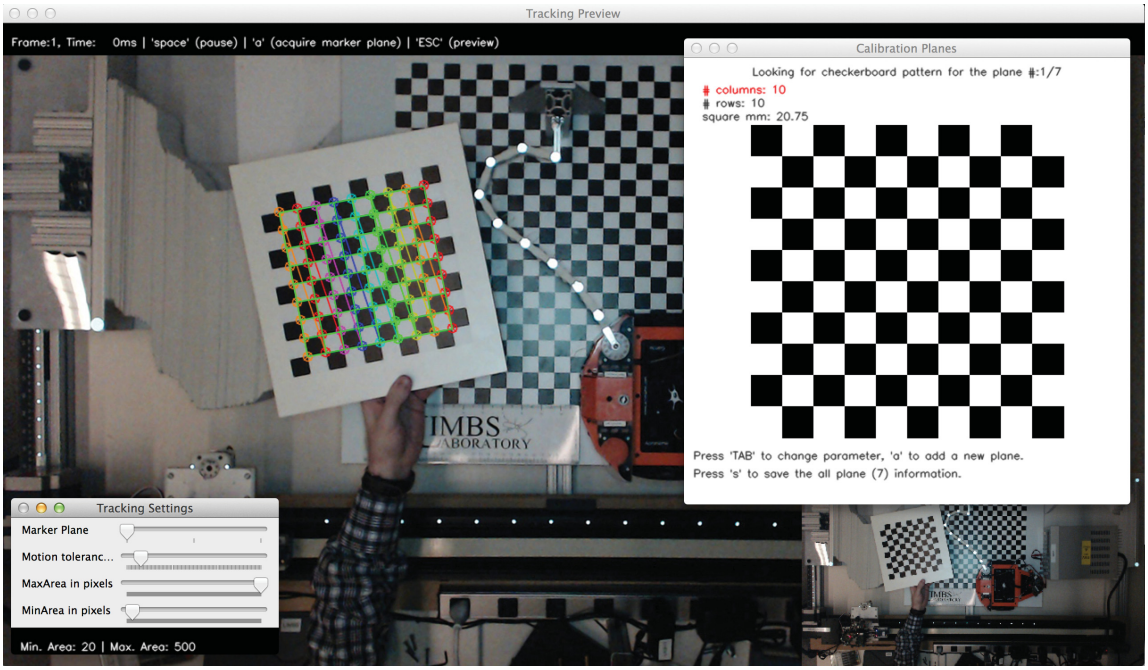

Figure 2.18: Plane orientations are captured using a checkerboard pattern. Since the antenna is not perfectly straight, my program enables me to choose an approximate oblique plane for the antenna markers to be projected onto.

with the same and different mode shapes respectively.

In order to achieve the correct configuration, I fed the optically captured joint angles to my antenna simulation in MATLAB. Then I applied a force on the tip and "pull" on the antenna towards the desired tip position according to equation 3.2.2.15. After the antenna tip reached the desired position, I minimized the antenna potential energy by projecting the joint vector that follows the negative gradient of the potential energy to the null space of the antenna Jacobian. Since initial configuration—recorded from the optical tracking—was already close to the solution, the simulation converged to the correct stable equilibrium configuration. Figure 2.23 shows an example of the two

stable equilibrium configurations for the same antenna and same boundary constraints from my MATLAB simulation.

2.3.2.2 Results

As explained in Appendix 6.1.4, I computed the relationship between the radius of the Nitinol stiffness element to the bending stiffness as:

$$\kappa = 2.06 \cdot 10^{12} r^4 + 1.56 \cdot 10^{-3} \tag{2.3.2.1}$$

My setup is intended to verify the fourth degree power trend equation I found empirically in equation 2.3.2.1. If the empirical formulation is correct, then I expect both mode shapes that can be achieved on the tuned physical antenna to be predicted by my simulation. Indeed both the optical and direct antenna data in all of my 15 trials are in remarkable agreement with the simulated static antennae. Figure 2.24 presents the results from each trial individually with overlaid configurations acquired from the simulation, optical tracking and the robotic antenna. Small deviations are expected due to Coulomb friction at the joints, which I assumed to be zero in my simulations.

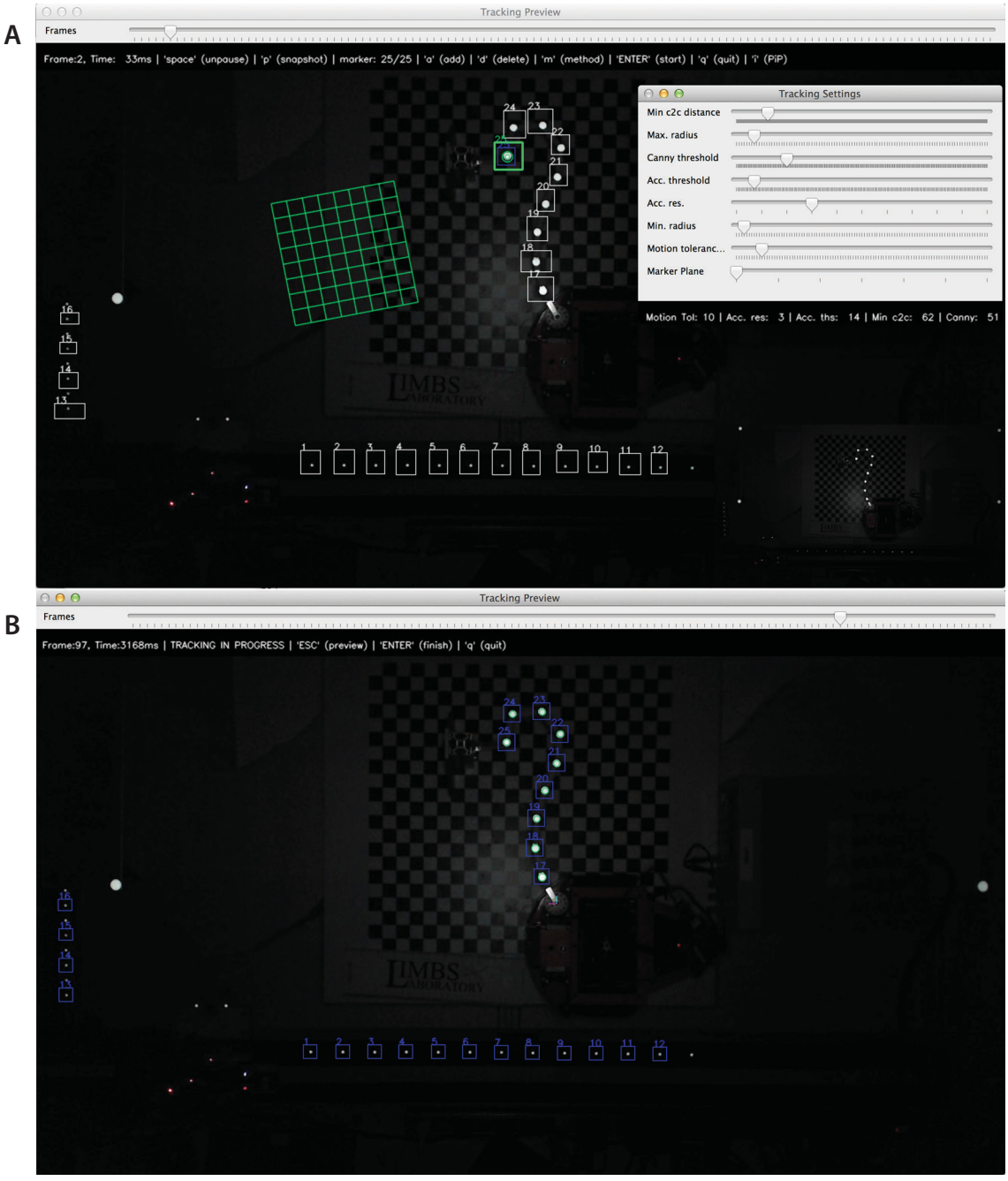

Figure 2.19: **A** My software enables users to choose the markers of interest on the videography and define the tracking preferences. The green grid specifies the plane to which the selected marker belongs.**B** The program can track multiple different markers with different methods. The blue rectangles around each marker indicates the local region of interest for the corresponding marker in the next video frame.

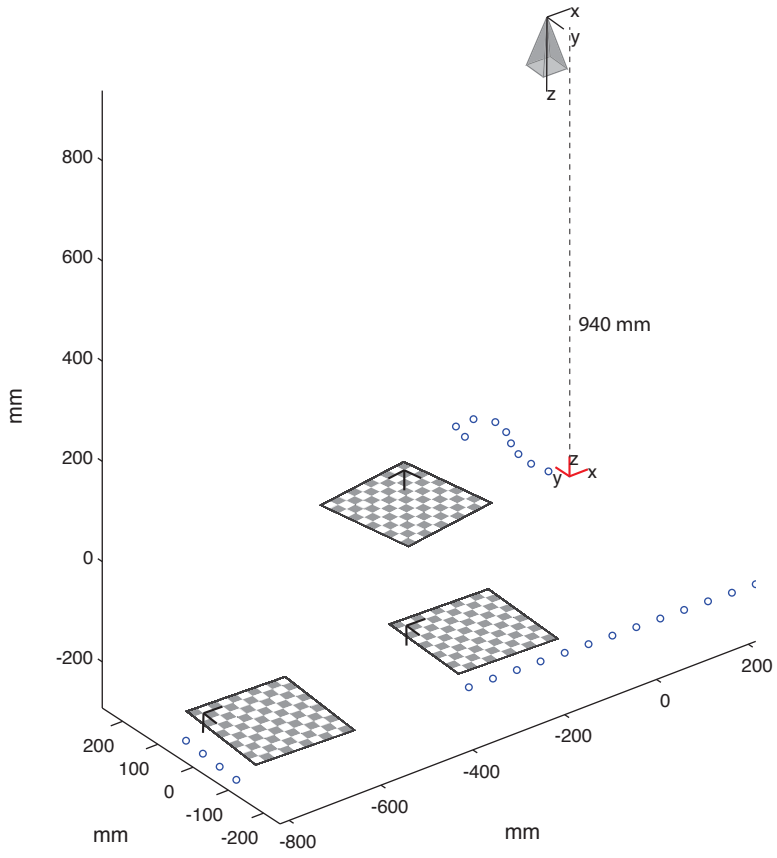

Figure 2.20: 3D reconstruction of the markers on the videography after the data is exported into matlab. The coordinate system location is also determined by the user during the marker definition.

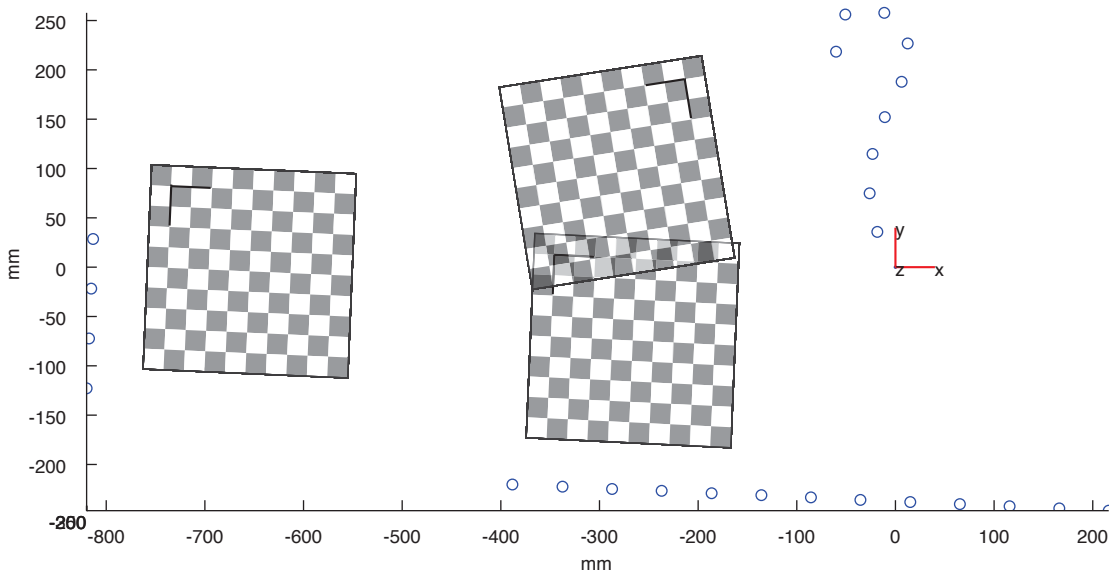

Figure 2.21: Planar view of the antenna markers

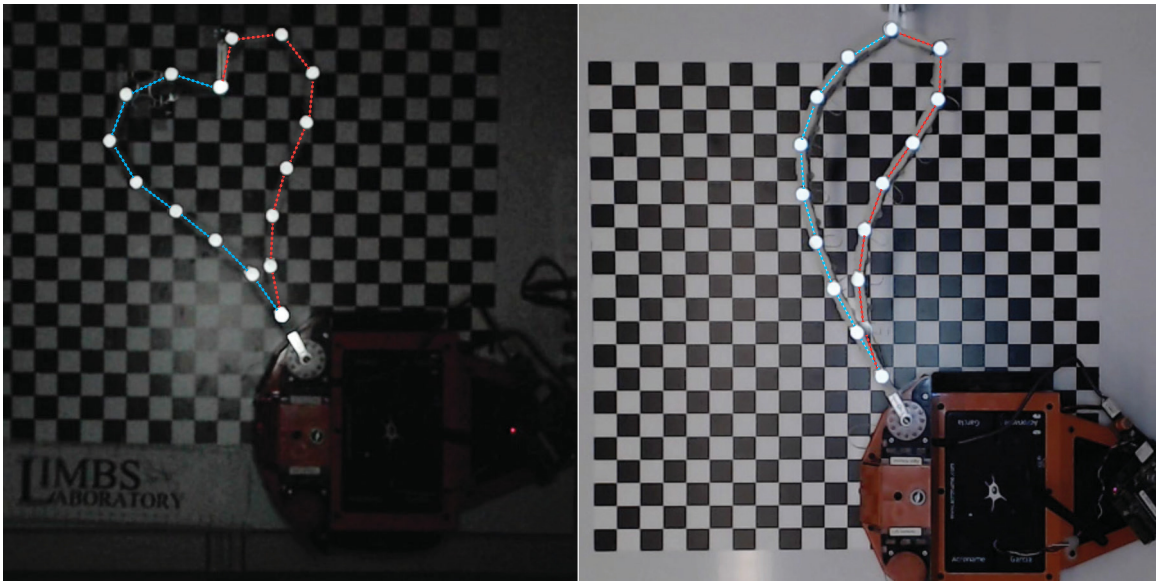

Figure 2.22: **A** Overlaid images from two experiments showing two symmetric static equilibriums with the same mode shapes. **B** Overlaid images from two experiments showing two symmetric static equilibria with different mode shapes.

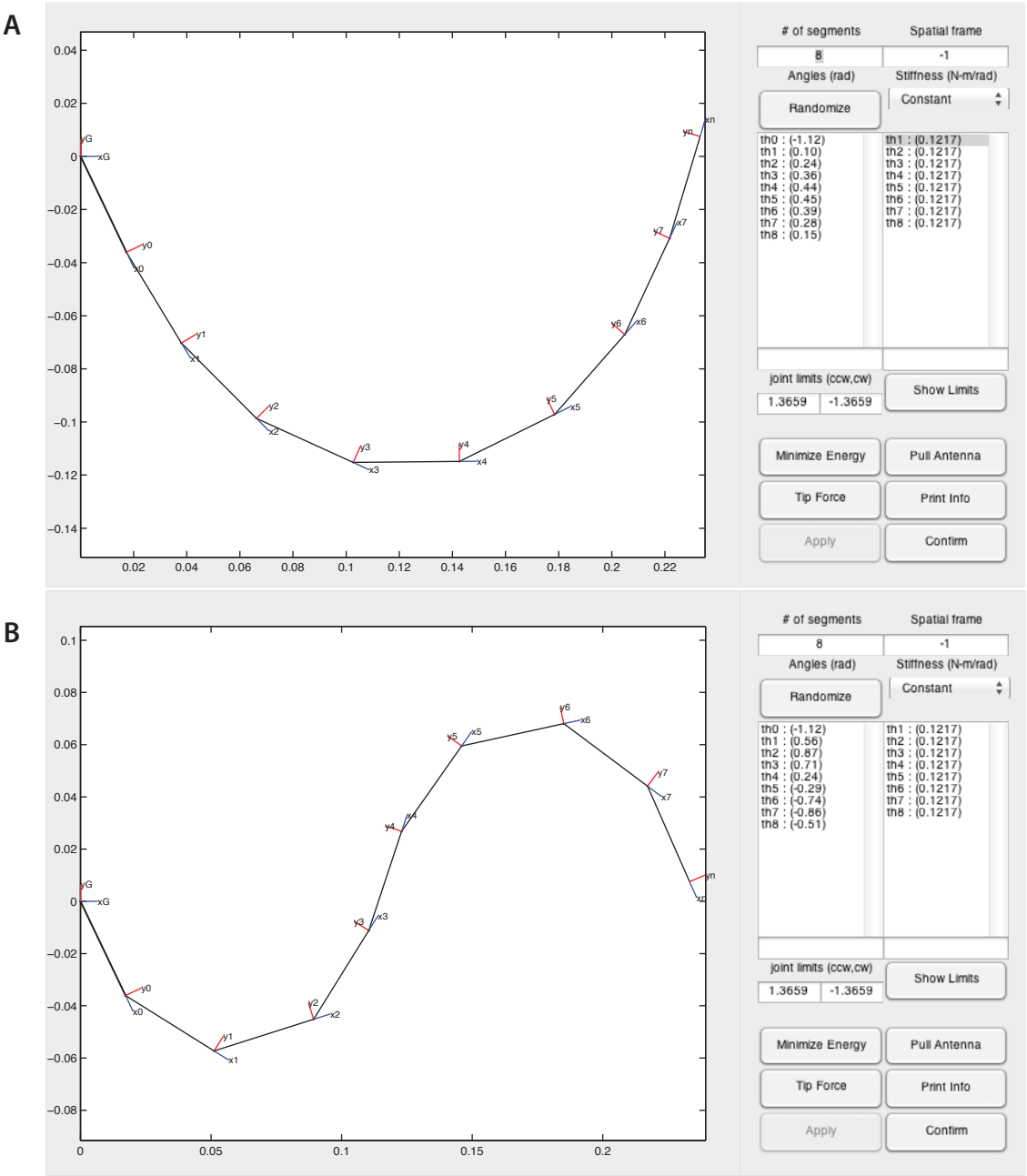

Figure 2.23: Simulation showing two static equilibria with two different mode shapes. In both cases, the base and tip positions are identical and the antenna potential energy is at a local minimum.

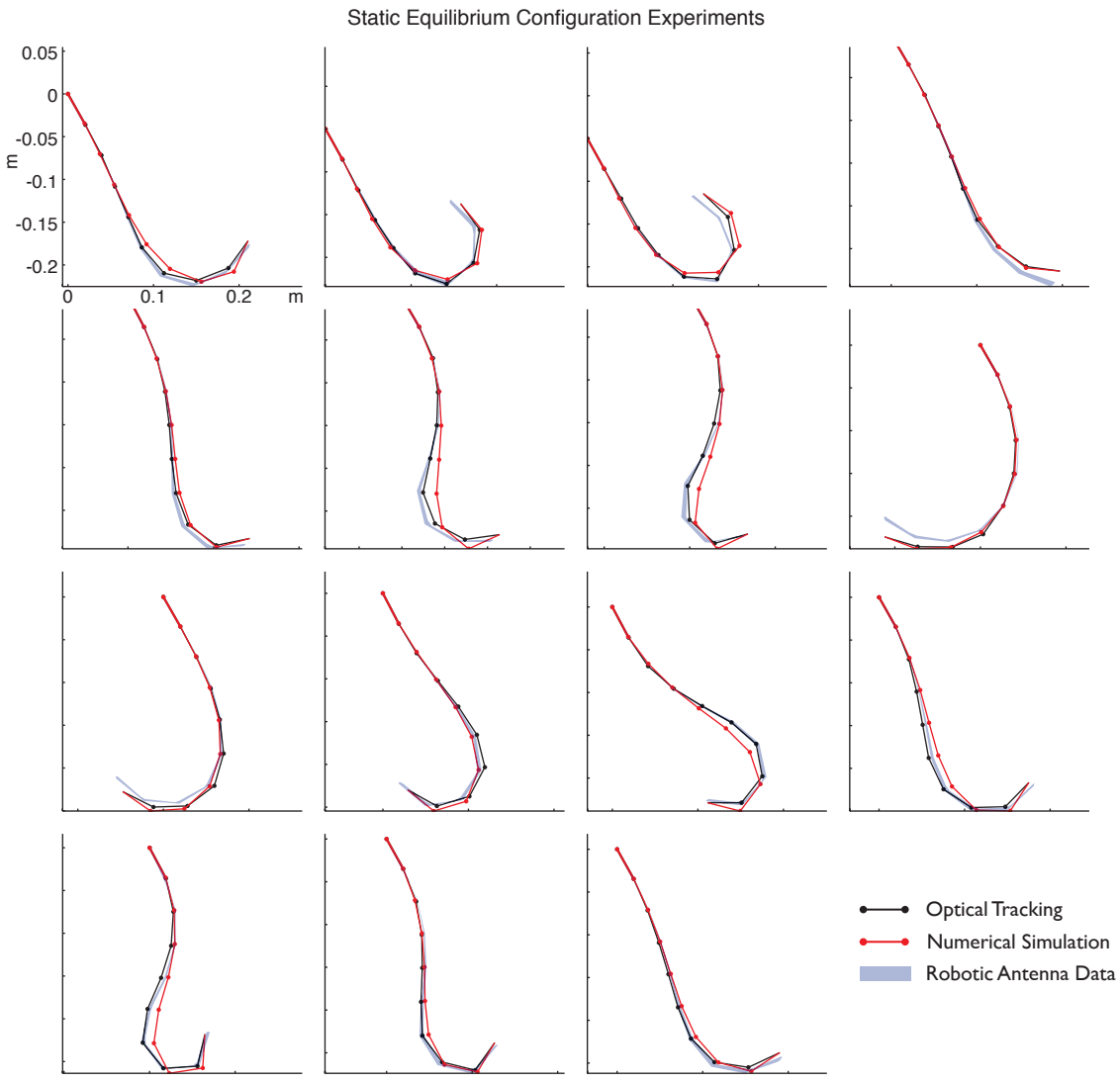

Figure 2.24: Experimental results comparing static equilibrium configurations of an exponentially decreasing stiffness profile antenna with their numerical predictions.

Chapter 3

Making & Maintaining Contact

In this chapter, I investigate how the antenna stiffness profile and wall properties play a role in robust maintenance of wall contact. In particular, I studied the mechanics of postural transitions of the antenna that can occur during high speed wall following. Sections 3.1 and 3.3.1 of this chapter are published in [46][1] and are reproduced with minimal paraphrasing. All biological experiments involving the cockroach were performed by my collaborators at the University of California at Berkeley and are included here to provide context for my robotic experiments.

[1] J Exp Biol thesis policy:http://jeb.biologists.org/site/journal/rights_permissions.xhtml

3.1 The Biological Antenna

3.1.1 Antenna Configuration vs Environment

The configuration of the antenna at the moment it contacts the wall can be expressed as two states: *looking forward* and *looking backward* (Fig. 3.1). In this section, I show that during wall-following in cockroaches, an antenna's mechanical state can be switched between the two states regardless of the initial state. Furthermore, I show evidence that this switch in postural state is only dependent on the wall roughness and is mediated passively by interactions between the antenna and the environment.

I compare the frequency of states for smooth walls versus rough walls, effectively pushing the mechanical performance of the antenna. We determined the relationship between wall surface roughness and ipsilateral antenna configuration during high-speed wall-following by tracking cockroaches as they encountered a turn perturbation with smooth acrylic walls and rough wood walls. We recorded the initiation of a stride by manually determining the onset of stance initiation of the hindleg contralateral to the wall perturbation. We rejected strides in which the antenna position could not be clearly determined to be either projecting forward or backward for the entire stride (4% of strides). To ensure sufficient interaction between the antenna and the wall, we rejected strides in which the antenna was not in contact with the wall for

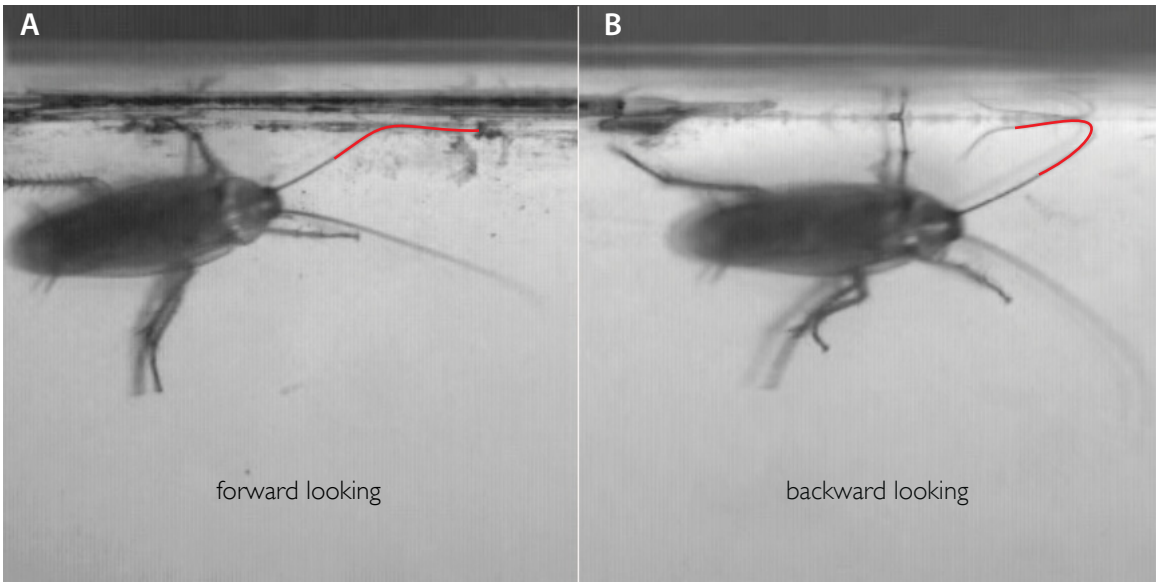

Figure 3.1: **A**: Forward-looking antenna state. **B**: Backward-looking antenna state.

at least 80% of the stride (35% of strides). In these rejected strides, the animals would often steer away from the wall, which would cause the ipsilateral antenna to momentarily lose contact with the wall. We defined an antenna "flip" as when an antenna moved from a forward-projecting to a backward-projecting position and vice versa. Only animals with at least 15 accepted strides ($N = 8$ animals total) were included in the final analysis. In addition to wall roughness, antennal joint angles possibly affected the distribution of antenna states. While previous studies suggested little variation in antenna angles and almost no contribution from basal segments during wall-following [12], we measured whether animals actively modulate antennal joint angles as a control. We randomly sampled trials from smooth and rough walls.

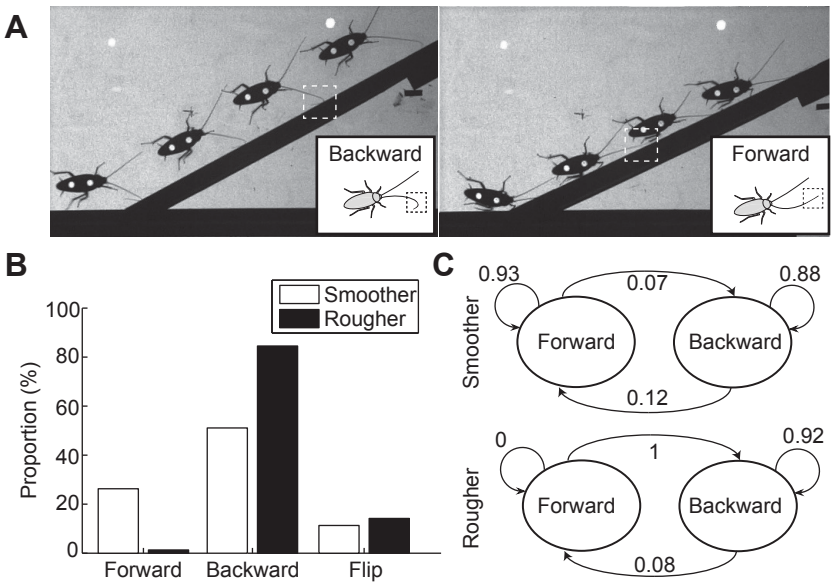

Figure 3.2: Effect of wall properties on antenna mechanical state. **A**: Two wall-following sequences during a turn perturbation recorded from high-speed video. The left panel shows a cockroach running with its antenna bent, projecting backward, and the right panel shows the same animal in a different trial running with the antenna straight, projecting forward. Wall properties are the same for the two trials. Boxes with dashed lines highlight the shape of the antenna as it interacts with the wall. **B**: Proportion of antennae pointing forward, backward, or flipping for smooth and rough wall surfaces. Wall surfaces categorically affected the antenna state ($P < 0.001$). **C**: By modeling antenna reconfiguration as a two-state discrete Markov chain, I found the transition probabilities within and between states. Transition probabilities calculated from the transition matrices for both smooth and rough walls are shown by arrows. Image credit [46]

3.1.1.1 Result: Postural Convergence

We accepted a total of 259 strides from 39 trials with $N = 3$ animals (body length $3.57 \pm 0.2cm$, ipsilateral antenna length $4.10 \pm 0.4cm$, mean $\pm$ standard deviation, unless otherwise noted) running along smooth walls. We accepted a total of 354 strides from 40 trials with $N = 5$ animals (body length $3.60 \pm 0.2cm$, ipsilateral antenna length $4.420.4cm$) running along rough walls. The animals ran with a mean

speed of $37.8^{cm}/_{s}$, ranging from 34.8 to $41.1^{cm}/_{s}$. Speed was not significantly different between the two groups (t-test, $p = 0.15$). With a 2D dorsal projection, we observed antennae to determine the antenna tip's flipped state (between forward- and backward-projecting) as the antenna interacted with the wall (Fig. 3.2A). We found these backward and forward states to be the dominant antenna configurations, persisting for many strides. In the backward-projecting configuration, most of the flagellum was typically in front of the animal, but the tip was projecting rearward, so the flagellum assumed an inverted-J shape. When comparing wall-following performance for the two groups, we found that animals encountering rough walls had their antennae projecting backward more often than animals running along smooth acrylic walls (smooth 51%, rough 85%; Fig. 3.2B). Similarly, for animals following smooth walls, the ipsilateral antennae assumed a forward position more often than animals running along rough walls (smooth 26%, rough 1%). Antennae "flipped" (either forward-to-backward or backward-to-forward) at similar frequencies for the two wall surfaces (smooth 11%, rough 14%). When comparing the proportion of forward versus backward antennal positions during a stride (excluding strides when the antenna flipped), we found that four out of five individuals never had a forward-projecting antenna on the rough surface ($^{0}/_{34}, {}^{0}/_{48}, {}^{0}/_{17}, {}^{0}/_{102}$), and only one individual showed five instances in 102 strides. By contrast, all individuals following smooth walls showed a large proportion of strides with forward-projecting antennae ($^{16}/_{83}, {}^{40}/_{95}, {}^{15}/_{23}$). We found a significant association between wall properties and the state of the antenna

(Pearson χ^2-test, $p < 0.001$). To investigate antenna flips further, we calculated transition probabilities within and between states by treating antenna positions as a two-state discrete Markov chain (Fig. 3.2C). We found that if the antenna was in a forward state on smooth walls, the probability that it remained in that state in the next stride was 93%, whereas if it was forward on rough walls, it never remained in the forward state in the next stride.

3.1.1.2 Discussion

We found that when cockroaches were presented with smooth and rough walls, the antenna could assume two states: projecting backward and forward (Fig. 3.2A). This result suggested that the transition between the observed antennal mechanical states was mediated by the mechanical properties of the environment coupled with locomotion. To understand how the environment affects antennal state, we compared the antennal posture of wall-following cockroaches running along smooth and rough surfaces, and found significant differences in the proportions of forward- and backward-projecting antennae (Fig. 3.2B). Furthermore, by comparing transition probabilities for a simple two-state Markov chain, we found that transition probabilities were significantly different when the antenna occupied a forward state when comparing smooth and rough walls (Fig. 3.2C).

3.1.2 Necessity of Anisotropic Hairs

In this section, we show that passive mechanical hair sensillae on the antenna are *necessary* for mediating a change in the overall mechanical state of the antenna from its resting position to projecting *backward*. We reached to this conclusion by simply ablating the sensillae with a high-precision laser system and observing the change in flipping frequency.

3.1.2.1 Methods

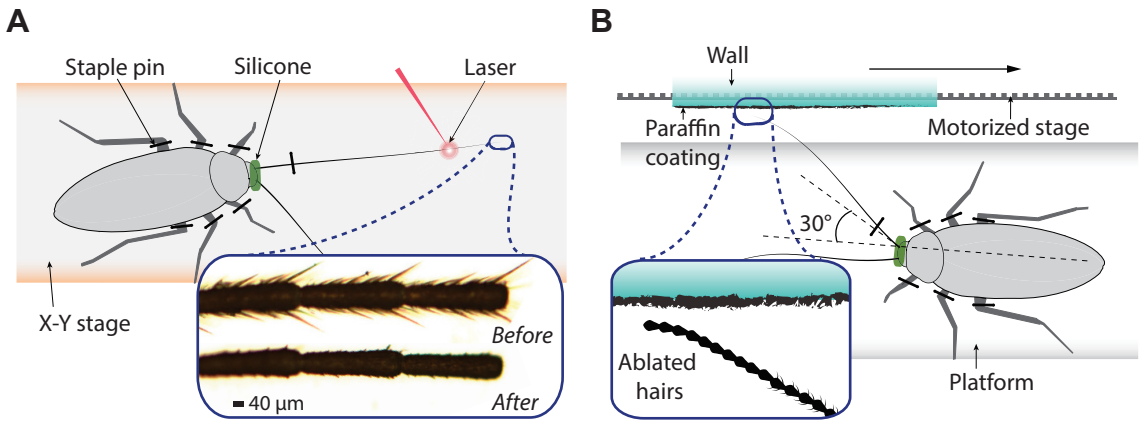

Figure 3.3: Methods for determining the mechanical role of hairs. (**A**) Procedure for laser hair ablation. The body and antennae of cockroaches were restrained on an x-y stage while we applied laser pulses at the tip of the antenna on both the ventral and dorsal sides. The inset shows high-resolution images of the three distal-most annuli of a cockroach antenna viewed from the ventral position. The top image shows the antenna before hair ablation and the bottom image shows the same antenna annuli after laser hair ablation. (**B**) Experimental procedure for determining the role of hairs in reconfiguring the antenna. We mounted body- and antenna-fixed animals on a platform and allowed the tip of the antenna to slide along a rough (paraffin) wall mounted on a motorized stage. The inset shows a representation of a treated antenna prior to interacting with the wall. Image credit [46]

We measured the effect of passive hairs on the antenna state by using a diode-pumped Q-switched micromachining laser (Matrix 355, Coherent, Santa Clara, CA, USA) to ablate hair arrays on each antennal segments. High-precision laser ablation has been successfully used on arthropods in the past for procedures such as ablation of genital hairs in Drosophila bipectinata [47]. Hairs on individual annuli were ablated by pulsing the laser at $20kHz$ while drawing a rectangle the size of each annulus at $10\mu m$ spacing at a speed of $250^{mm}/_{s}$. For each annulus, we manually defined coordinates at $1\mu m$ resolution to avoid hitting the intersegmental membranes. We ablated hairs of the first 10 distal annuli in head- and antenna-fixed animals in the dorsal and ventral directions. We found that orienting the antenna with dorsal and ventral side up was sufficient to ablate hairs circumferentially. We acquired high-magnification ($25-50\times$) images of individual annuli in both the dorsal and ventral direction to determine the quality of the ablation process. After ablation, under a high-magnification microscope, we observed that the treated portion of the antenna retained hemolymph flow and that the cockroach responded to touch on the treated antenna. To demonstrate the effect of antenna hairs, we compared the performance of ablated and non-ablated antenna when sliding along a surface (Fig. 3.3A). After cold-anesthetizing the animals by placing them in glass beakers on ice for $30min$ (thus avoiding direct contact with the ice), we used staple pins to mount the animal on a gel plate and fixed the head and base of the antenna with dental silicone (President light body, Coltène, Altstätten, Switzerland). We fixed the base of the antenna at an angle

of 30deg relative to the body long axis, which is similar to the angle observed in wall-following [12]. The candidate antenna was allowed to rest freely against a paraffin plate. The paraffin plate was made by melting paraffin on a glass plate placed on a hot plate. Because of surface tension, the paraffin melted to a thin coat. The plate was attached to a linear micro- translation stage (M112.1DG, Physik Instrumente, Palmbach, Germany). After carefully allowing the antenna to come into contact with the wall under a microscope with the antenna in a forward-projecting position, we drove the wall towards, but parallel to, the cockroach at a speed of $2^{mm}/_{s}$ over a distance of 2.5cm (Fig. 3.3B). To control for the possible effect of antenna contact area biasing our results, we varied the initial conditions such that the antenna was initially mounted with one to ten annuli in contact with the wall. To control for surface irregularities on the wall, we randomized the initial position of the antenna against the wall for all annulus numbers. We noted whether or not the antenna flipped and measured the frequency for each condition from high-resolution video recordings of each trial. After a trial, we measured the antenna length from the scape to the last annulus of the flagellum. To test whether the angle of attack of the flagellum could affect the likelihood of reconfiguration or flipping, we repeated this experiment with abduction angles of 15, 50 and 70deg with non-treated, control antennae.

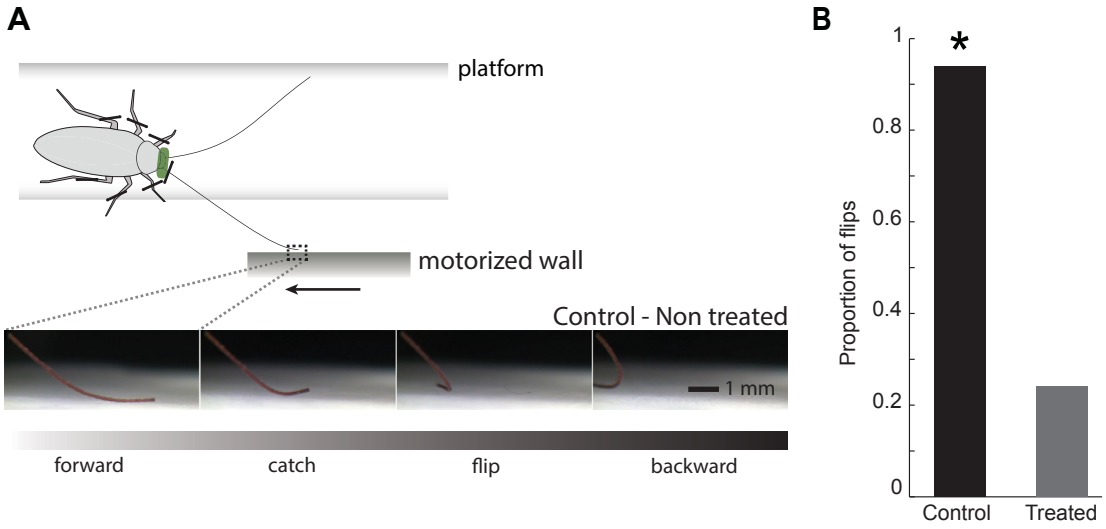

Figure 3.4: **A** Sequence of a flip from a non-treated, intact (control) cockroach antenna. The antenna is initially in a forward- projecting state. As the wall moves, the antenna catches and flips to a backward-projecting state. **B** Proportion of flips between non-treated and treated cockroach antennae. The proportion of non-laser-treated (intact) antennae that flipped was statistically higher than for treated antennae ($^*p < 0.001$). Image credit [46]

3.1.2.2 Results

Our hypothesis was that large chemo-mechanosensory hairs enable the antenna to effectively stick to walls and mediate the transition from forward- to backward-bending. We performed annulus-by-annulus hair ablation treatment on the first ten annuli from the tip using the high-resolution micromachining laser. The results from one treatment are shown in (Fig. 3.3A). We compared the performance of control ($N = 5$, 50 trials; mass $0.81 \pm 0.09g$, antenna length $4.24 \pm 0.43cm$) and experimental antennae ($N = 5$ animals, 50 trials; mass $0.91 \pm 0.06g$, antenna length $4.35 \pm 0.33cm$) while sliding along a paraffin surface for head-fixed animals (Fig. 3.3B, Fig. 3.4A). During

a flip, the hairs at the tip first engaged with the wall, causing the tip to stick. As the wall progressed, the tip began to twist backward (Fig. 3.4A). With ablated hairs, the flagellum would catch, fail to engage, and slip back into a forward-projecting state. We found a significant difference in flipping frequency between control and treated antennae (Pearson χ^2-test, $p < 0.001$) (Fig. 3.4B). We found no effect of the number of segments in contact with the wall on flipping frequency (Cochran-Mantel-Haenszel test, $p < 0.001$). Interestingly, contact of a single annulus with the wall often was sufficient for interlocking and subsequent flipping. For non-treated, control antennae ($N = 3$ with eight trials per angle; mass $0.74 \pm 0.04g$, antennal length $4.8 \pm 0.2cm$), we found no significant effect of antennal abduction angle on the likelihood of flipping (Pearson χ^2-test, $P = 0.36$) even after considering the possible effect of individuals (Cochran-Mantel-Haenszel test, $p = 0.37$).

3.1.2.3 Discussion

The role of directionally tuned hair arrays has previously been studied during high-speed terrestrial locomotion in cockroaches, spiders, and crabs [48]. Leg hairs or spines were shown to function as distributed contact points by increasing the probability of foot engagement when animals ran over terrain with sparse contacts. Cockroaches, spiders, and crabs running at high speed attained increased mobility with collapsible spines without any detectable changes in neural feedback. Spagna and colleagues pro-

vided evidence for a novel mechanical function for these spines, which were previously thought to only play a role in sensing [48].

We discovered that hairs on antennae, also once thought to only play a role in sensing, have mechanical function. Specifically, the hairs mechanically interlock with surfaces and enable the antenna to adopt a different configuration when coupled with locomotion. The study on leg spines reinforced the importance of integrating passive mechanics to understand the principles of stability and maneuverability in high- speed terrestrial locomotion when the neuromechanical system is pushed near its limits [45]. Analogously, we provide support that understanding the biomechanical processing of sensory appendages prior to neural transduction is crucial to understanding sensorimotor integration during rapid behaviors [49]. While we found that the properties of the wall surface can influence the mechanical state of the antenna, it is also affected by the angle of the antenna flagellum with respect to the wall. [12]. However, we found that the angle of attack of the flagellum did not affect the likelihood of antenna flipping in intact antennae, thus supporting the hypothesis that antennal biomechanics are the predominant factor influencing antennal configuration. While antennal reconfiguration at the tip is robust to changes in base angle, it remains an open question to what extent cockroaches precisely control antennal muscles during the task of high-speed wall-following. In future studies it will be important to carefully examine the effect of antennal abduction angle on turning, as studies during slow, exploratory behavior have shown that proprioceptors at the base affect tactile orientation [39].

3.2 Numerical Model

We hypothesized that the contact and postural transition mechanics of the antenna were significantly influenced by the presence of the distally oriented hairs, so I integrated them into my simulation framework.

3.2.1 Anisotropic Hairs

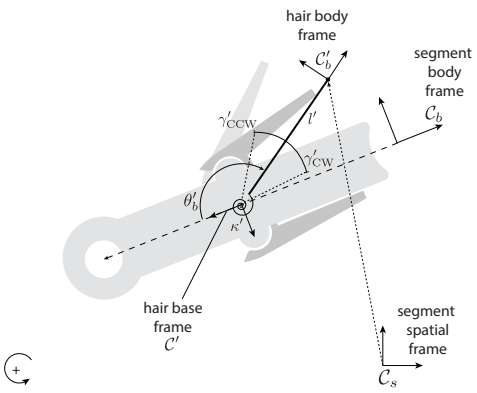

Figure 3.5: Collapsible distally oriented hair with base bending stiffness of κ'. The angular limits push the hair against the counterclockwise limit γ'_{CCW} in absence of external forces.

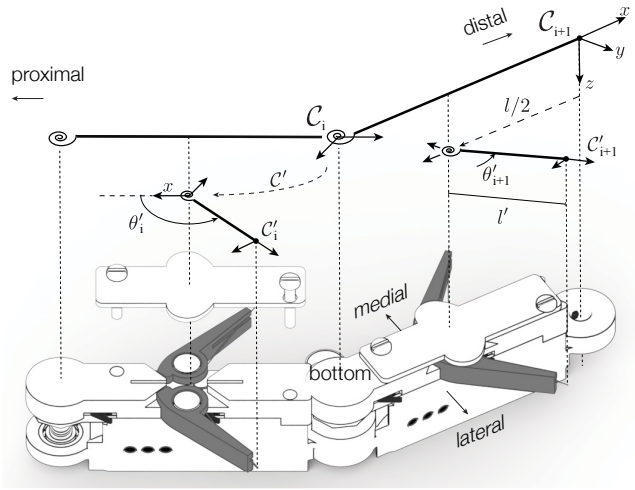

Figure 3.6: 3D orthographic illustration of two antenna segments from the bottom showing the mechanism and the coordinate frames of the distally pointing hairs.

My physical implementation enables both medial and lateral hairs (Fig. 3.6), but for simplicity, I am only considering the left antenna with anisotropic distally oriented hairs on the lateral side in this simulation. Furthermore, the base link $\mathcal{C}_G$ does not

have a hair associated with it. Thus for an n segment antenna (not including the base), there are at most $n+1$ lateral anisotropic hairs.

I model each hair as single massless rigid thin rod pinned to the segment link via a torsion spring. The hair link has an angular range of $\approx 45^\circ$ constrained by limits γ'_{ccw} and γ'_{cw}. Within these limits, the torsion spring is always in tension and thus pushes the hair against the counterclockwise limit γ'_{ccw} in the absence of external forces. In the presence of a clockwise net moment, the hair is allowed to "collapse" against the clockwise angular limit γ'_{cw}.

In this section, my goal is to give expressions for the positions and velocities of every collapsible hair on the antenna. Specifically, I want to develop a composite forward kinematics function, $\mathbf{f}(\theta, \theta', \dot{\theta}, \dot{\theta}', \Pi) \mid \Pi = \{l, s\}$, that would provide the antenna base, antenna tip, antenna joint and all lateral hair tip position coordinates. Similarly, I want to come up with a composite differential kinematics function $\mathbf{df}(\theta, \theta', \dot{\theta}, \dot{\theta}', \Pi)$ $\mid \Pi = \{l, s\}$ that would provide the angular and translational velocities of the aforementioned coordinate frames as well as their Jacobian's.

- Let the notation *prime* "$\prime$" be the identifier for quantities pertinent to the distally oriented anisotropic collapsible hairs.
- Let $p' = \begin{pmatrix} -\frac{l}{2} & 0 \end{pmatrix}^\top$ be the location of the anisotropic hair base origin with respect to the segment body frame $\mathcal{C}_b$.

- Let $R' \in SO(2)$ be the *distally oriented* anisotropic hair base orientation with respect to the segment body frame $\mathcal{C}_b$. The hair base frame is oriented at an angle of π due to the hair stiffness element.

$$R' = \begin{pmatrix} -1 & 0 \\ 0 & -1 \end{pmatrix}$$

- Let $\mathcal{C}' \in SE(2)$ be the base coordinate frame for all *distally oriented* hairs with respect to the segment body frame $\mathcal{C}_b$, and note that $\mathcal{C}'$ is constant and is uniform for all segments (i.e the hair bases have in the same location for every antenna segment).

$$\mathcal{C}' = \left[\begin{array}{c:c} R' & p' \\ \hdashline 0 & 1 \end{array}\right]$$

- Let $\mathcal{C}'_{sb} \in SE(2)$ be the hair body coordinate frame of the desired segment "b" relative to spatial frame $\mathcal{C}_s$.

- Let $\mathcal{C}'_b \in SE(2)$ be the hair body coordinate frame of the desired segment "b" relative to the associated segment frame $\mathcal{C}_b$.

- Let l' be the constant, uniform hair length for all hairs in meters.

- Let $\theta'_b \in \mathbb{S}^1$ $b \in \{0, \ldots, n\}$ be the hair angle on the segment "b" measured with respect to the associated hair base frame in radians.

- Let $\theta' \in \underbrace{\mathbb{S}^1 \times \ldots \times \mathbb{S}^1}_{n+1} = \mathbb{T}^{n+1}$ be the vector of hair angles in radians s.t: $\theta' = \begin{pmatrix} \theta'_0 & \ldots & \theta'_n \end{pmatrix}^\top$

- Let $\theta'_{sb} \in \mathbb{S}^1$ $s, b \in \{0, \ldots, n\}$ be the angular orientation of the desired hair body frame $\mathcal{C}'_b$ measured with respect to spatial frame $\mathcal{C}_s$ in radians.

- Let $\Theta'_s \in \mathbb{T}^{n+1}$ $s \in \{-1, \ldots, n\}, b \in \{0, \ldots, n\}$ be all the hair body frame $\mathcal{C}'_b$ orientations measured with respect to spatial frame $\mathcal{C}_s$ in radians.

- Let $p'_b \in \mathbb{R}^2$ be the hair tip (body frame) position of the segment "b" in meters with respect to the associated segment frame $\mathcal{C}_b$.

- Let $p'_{sb} \in \mathbb{R}^2$ be the hair tip (body frame) position of the segment "b" in meters with respect to the spatial frame $\mathcal{C}_s$.

- Let $\dot{p}'_b$ be the translational velocity of the hair body frame $\mathcal{C}'_b$ measured with respect to the spatial frame $\mathcal{C}_s$ in m/s and written in the associated segment frame $\mathcal{C}_b$.

- Let $\dot{p}'_{sb} \in \mathbb{R}^2$ be the total translational velocity of the hair body frame $\mathcal{C}'_b$ measured with respect to a spatial coordinate frame $\mathcal{C}_s$ and written in spatial coordinate frame $\mathcal{C}_s$ in meters per second (m/s).

- Let $\omega'_b \equiv \omega'_{sb} = \dot{\theta}'_{sb} \in \mathbb{R}$ be the angular velocity of the hair body frame $\mathcal{C}'_b$ of the

segment "*b*".

- Let $v'_{sb} = \begin{pmatrix} \dot{p}'_{sb} & \omega'_{sb} \end{pmatrix}^\top \in \mathbb{R}^3$ describe the hair body frame translational velocity with respect to the spatial frame $\mathcal{C}_s$ in *m/sec* and the angular velocity in *rad/sec*, respectively. This vector is also called the hybrid velocity of the hair body frame of segment "*b*".

- Let $\kappa'_b \in \mathbb{R}$ be the hair bending stiffness in *N-m/rad* on the segment "*b*".

- Let $\kappa' \in \mathbb{R}^n$ be the vector of hair angles in radians s.t:
  $\kappa' = \begin{pmatrix} \kappa'_0 & \dots & \kappa'_n \end{pmatrix}^\top$

- Let $\gamma'_{\mathrm{CW,b}}, \gamma'_{\mathrm{CCW,b}} \in \mathbb{S}^1$ be the clockwise and counterclockwise angular limits for any segment hair $b \in \{0, 1, ..., n\}$ in radians respectively. Each hair limit $\gamma'_{\mathrm{CW,b}}$ and $\gamma'_{\mathrm{CCW,b}}$ is measured with respect to the hair base frame (Fig. 3.5).

- Let $\gamma'_b = \{\gamma_{\mathrm{CCW,b}}, \gamma_{\mathrm{CW,b}}\}$ be an ordered pair of counterclockwise and clockwise hair angular limits in radians for the hair on the given segment $b \in \{0, 1, ..., n\}$ respectively.

- Let $\gamma'_{\mathrm{CW}}, \gamma'_{\mathrm{CCW}} \in \mathbb{T}^{n+1}$ be the vectors of clockwise and counter-clockwise hair angular limits in radians respectively such that:

$$\gamma'_{\mathrm{CW}} = \begin{pmatrix} \gamma'_{\mathrm{CW},0} & \dots & \gamma'_{\mathrm{CW,n}} \end{pmatrix}^\top$$

$$\gamma'_{\mathrm{ccw}} = \begin{pmatrix} \gamma'_{\mathrm{ccw,0}} & \dots & \gamma'_{\mathrm{ccw,n}} \end{pmatrix}^{\top}$$

- Let $q' \in \mathbb{R}^{n+1}$ be the new generalized coordinate vector for all the hairs such that $q = \begin{pmatrix} q_0 & \dots & q_n \end{pmatrix}^{\top}$ and $\theta' = g'(q', \gamma'_{\mathrm{ccw}}, \gamma'_{\mathrm{cw}})$.

- Let $g' : q' \mapsto \theta'$ be the *hair-limit* mapping from q' to the hair angles.

- Let $\mathbf{g} : \begin{bmatrix} q \\ \cdots \\ q' \end{bmatrix} \mapsto \begin{bmatrix} \theta \\ \cdots \\ \theta' \end{bmatrix}$ be the composite angular limit mapping for all the segment joints and hairs.

- Let $P'_s \in \mathbb{R}^{2(n+1)}$ be the vector of all hair coordinate frame positions with respect to the spatial frame $\mathcal{C}_s$ such that:

$$P'_s = \mathrm{vec}\left(\begin{bmatrix} {p'}_{s0} \vdots \dots \vdots {p'}_{sn} \end{bmatrix} \right) = \begin{bmatrix} {p'}_{s0} \\ \vdots \\ {p'}_{sn} \end{bmatrix}$$

- Let $\mathbf{P}_s \in \mathbb{R}^{4n+6}$ be the vector of combined segment and hair coordinate frame positions with respect to the spatial frame $\mathcal{C}_s$ such that:

$$\mathbf{P}_s = \mathrm{vec}\left(\begin{bmatrix} P_s \vdots P'_s \end{bmatrix} \right) = \begin{bmatrix} p_{sG} \\ \vdots \\ p_{sn} \\ p'_{s0} \\ \vdots \\ p'_{sn} \end{bmatrix}$$

Every individual hair behaves like a single segment flagellum, so all of the expressions

I provided for segment positions, velocities, and joint limits are also applicable to the hairs.

3.2.1.1 Hair positions and orientations

The tip position of desired distally pointing hair p'_b with respect to the corresponding segment frame $\mathcal{C}_b$ is simply:

$$\begin{aligned}\begin{pmatrix} p'_b \\ 1 \end{pmatrix} &= \mathcal{C}' \begin{pmatrix} \cos\theta'_b \\ \sin\theta'_b \\ 1 \end{pmatrix} l' \\ p'_b &= R' \begin{pmatrix} \cos\theta'_b \\ \sin\theta'_b \end{pmatrix} l' + p' \\ &= -\begin{pmatrix} \frac{l}{2} + \cos\theta'_b l' \\ \sin\theta'_b l' \end{pmatrix} \end{aligned} \tag{3.2.1.1}$$

The hair body frame $\mathcal{C}'_b \in SE(2)$ with respect to the associated segment frame can be constructed as:

$$\begin{aligned}\mathcal{C}'_b &= \mathcal{C}' \left[\begin{array}{c:c} \begin{pmatrix} \cos\theta'_b & -\sin\theta'_b \\ \sin\theta'_b & \cos\theta'_b \end{pmatrix} & \begin{pmatrix} \cos\theta'_b \\ \sin\theta'_b \end{pmatrix} l' \\ \hdashline 0 & 1 \end{array}\right] \\ &= \left[\begin{array}{c:c} -\begin{pmatrix} \cos\theta'_b & -\sin\theta'_b \\ \sin\theta'_b & \cos\theta'_b \end{pmatrix} & -\begin{pmatrix} \frac{l}{2} + \cos\theta'_b l' \\ \sin\theta'_b l' \end{pmatrix} \\ \hdashline 0 & 1 \end{array}\right]\end{aligned}$$

Then, the tip position of desired distally pointing hair p'_{sb} with respect to the spatial frame $\mathcal{C}_s$ is given by:

$$\begin{pmatrix} p'_{sb} \\ 1 \end{pmatrix} = \mathcal{C}_{sb} \begin{pmatrix} p'_b \\ 1 \end{pmatrix}$$

$$\begin{aligned} p'_{sb} &= R_{sb} p'_b + p_{sb} \\ &= R_{sb} \left(R' \begin{pmatrix} \cos\theta'_b \\ \sin\theta'_b \end{pmatrix} l' + p' \right) + p_{sb} \\ &= R_{sb} R' \begin{pmatrix} \cos\theta'_b \\ \sin\theta'_b \end{pmatrix} l' + R_{sb} p' + p_{sb} \\ &= p_{sb} - \begin{pmatrix} \cos(\alpha_{sb}^\top \theta) \\ \sin(\alpha_{sb}^\top \theta) \end{pmatrix} \frac{l}{2} - \begin{pmatrix} \cos(\alpha_{sb}^\top \theta + \theta'_b) \\ \sin(\alpha_{sb}^\top \theta + \theta'_b) \end{pmatrix} l' \end{aligned}$$

The desired hair body frame $\mathcal{C}'_{sb} \in SE(2)$ (and simultaneously the rigid body transformation from the spatial frame) can be then constructed as:

$$\begin{aligned} \mathcal{C}'_{sb} &= \mathcal{C}_{sb} \cdot \mathcal{C}'_b \\ &= \left[\begin{array}{cc:c} \underbrace{\begin{matrix} \cos(\alpha_{sb}^\top \theta) & -\sin(\alpha_{sb}^\top \theta) \\ \sin(\alpha_{sb}^\top \theta) & \cos(\alpha_{sb}^\top \theta) \end{matrix}}_{R_{sb}} & \underbrace{\begin{bmatrix} \cos\left(\mathcal{A}_{sb}\theta\right)^\top \\ \sin\left(\mathcal{A}_{sb}\theta\right)^\top \end{bmatrix} l\alpha_{sb}}_{p_{sb}} \\ \hdashline 0 & 1 \end{array} \right] \mathcal{C}'_b \\ &= \left[\begin{array}{cc:c} \underbrace{-\begin{pmatrix} \cos(\alpha_{sb}^\top \theta + \theta'_b) & -\sin(\alpha_{sb}^\top \theta + \theta'_b) \\ \sin(\alpha_{sb}^\top \theta + \theta'_b) & \cos(\alpha_{sb}^\top \theta + \theta'_b) \end{pmatrix}}_{R'_{sb}} & \multicolumn{2}{c}{\underbrace{p_{sb} - \begin{pmatrix} \cos(\alpha_{sb}^\top \theta) \\ \sin(\alpha_{sb}^\top \theta) \end{pmatrix} \frac{l}{2} - \begin{pmatrix} \cos(\alpha_{sb}^\top \theta + \theta'_b) \\ \sin(\alpha_{sb}^\top \theta + \theta'_b) \end{pmatrix} l'}_{p'_{sb}}} \\ \hdashline 0 & \multicolumn{2}{c}{1} \end{array} \right] \end{aligned}$$

3.2.1.2 All hair and segment frame positions and orientations

The array of all the hair tip positions with respect to their respective segment body frames can be computed as:

$$\begin{bmatrix} {p'}_0 & \cdots & {p'}_n \\ \hline 1 & & \end{bmatrix} = \mathcal{C}' \begin{pmatrix} \cos(\theta')^\top \\ \sin(\theta')^\top \\ 1 \end{pmatrix} l'$$

$$\begin{bmatrix} {p'}_0 & \cdots & {p'}_n \end{bmatrix} = R' \begin{bmatrix} \cos(\theta')^\top \\ \hline \sin(\theta')^\top \end{bmatrix} l' + p' {\alpha'_s}^\top \tag{3.2.1.2}$$

Finally, I would like to have an expression for all the hair tip positions with respect to the spatial frame $\mathcal{C}_s$. Combining the above equation with 2.2.3.3 I obtain:

$$P'_s = \begin{bmatrix} {p'}_{s0} \\ \hline \vdots \\ \hline {p'}_{sn} \end{bmatrix} = \underbrace{\begin{bmatrix} p_{s0} \\ \hline \vdots \\ \hline p_{sn} \end{bmatrix}}_{P_s} + \begin{bmatrix} R_{s0} & & \\ \hline & \ddots & \\ \hline & & R_{sn} \end{bmatrix} \begin{bmatrix} {p'}_0 \\ \hline \vdots \\ \hline {p'}_n \end{bmatrix} \tag{3.2.1.3}$$

Since the antenna is a highly structured system, the array of all tip positions P'_s and all segment frame positions P_s can be constructed simply through the *active frames*

matrices I used in section 2.2.3.1.

$$\mathbf{P}_s = \begin{bmatrix} P_s \\ \hdashline P'_s \end{bmatrix} = \begin{bmatrix} \cos\left(\begin{bmatrix} \mathcal{A}_{(sG+sn)} & 0 \\ \hdashline \mathcal{A}_{(sG+sn)} & I \end{bmatrix}\begin{bmatrix} \theta \\ \hdashline \theta' \end{bmatrix}\right)^{\top} \\ \hdashline \sin\left(\begin{bmatrix} \mathcal{A}_{(sG+sn)} & 0 \\ \hdashline \mathcal{A}_{(sG+sn)} & I \end{bmatrix}\begin{bmatrix} \theta \\ \hdashline \theta' \end{bmatrix}\right)^{\top} \end{bmatrix} \begin{bmatrix} \mathbf{A}\cdot l & \mathcal{A}^{\top}_{(sG+sn)}l + \operatorname{diag}\left(-\frac{l}{2}\right) \\ \hdashline 0 & -I\cdot l' \end{bmatrix}$$

(3.2.1.4)

where I is the appropriately sized i.e $(n+1)\times(n+1)$ identity matrix, $-\frac{l}{2}$ is the x coordinate of p' and $\mathbf{A} = \begin{bmatrix} \alpha_{sG} & \mathcal{A}^{\top}_{(sG+sn)} \end{bmatrix}$ is the matrix defined in equation 2.2.3.2.

3.2.1.3 Hair translational and angular velocities

The translational and angular velocities $\{\dot{p}'_{sb}, \omega'_{sb}\}$ of the desired hair body frame $\mathcal{C}'_{sb} \in SE(2)$ with respect to the desired spatial frame $\mathcal{C}_s$ can be computed using the lemma 2.2.2 and equation 3.2.1.1:

$$\begin{pmatrix} \dot{p}'_{sb} \\ \omega'_{sb} \end{pmatrix} = \dot{H}_{sb}\begin{pmatrix} p'_b \\ 1 \end{pmatrix}$$

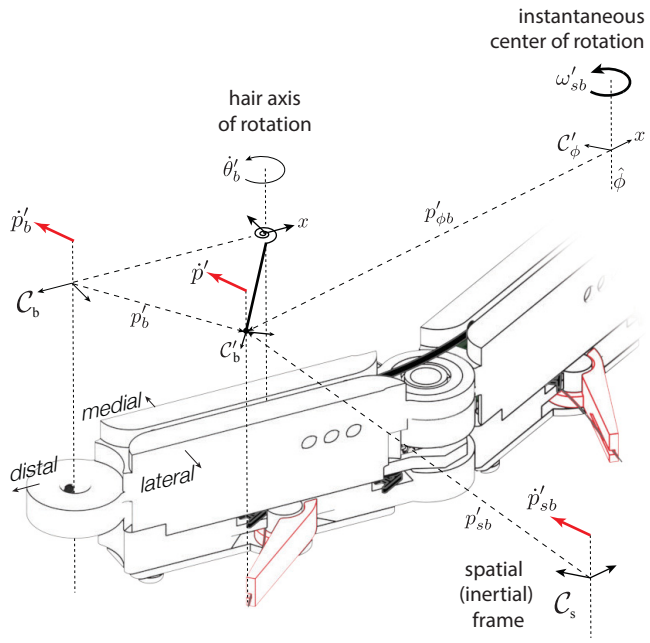

Figure 3.7: Anisotropic hair velocities.

$$= \left[\begin{array}{c|c} \widehat{\alpha_{sb}^{\top}\dot{\theta}} R_{sb} & \begin{bmatrix} -\sin(\mathcal{A}_{sb}\theta)^{\top} \\ \hdashline \cos(\mathcal{A}_{sb}\theta)^{\top} \end{bmatrix} l\,|\mathcal{A}_{sb}|\,\dot{\theta} \\ \hdashline 0 & \alpha_{sb}^{\top}\dot{\theta} \end{array}\right] \begin{pmatrix} -\frac{l}{2} - \cos\theta_b' l' \\ -\sin\theta_b' l' \end{pmatrix}$$

3.2.1.4 Hair angular limits

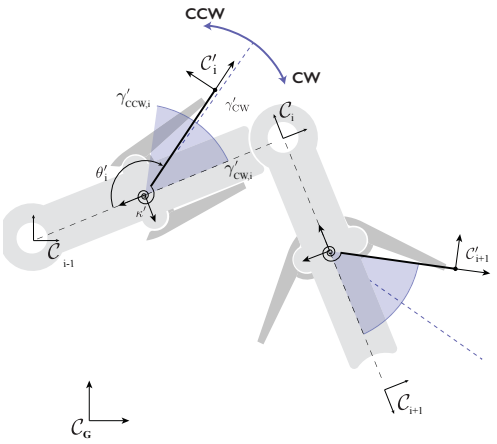

Figure 3.8: Illustration of the anisotropic hairs as a rigid body. Within the angular limits, the hairs have the minimum strain energy at the counterclockwise angular limit.

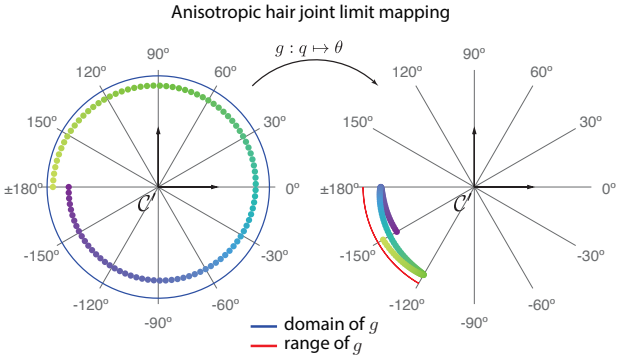

Figure 3.9: The mapping from q_i' to θ_i' for an individual hair with joint limits about its base frame $\mathcal{C}'$.

3.2.2 Contact Forces on the Antenna

In this section, I compute the forces acting on the antenna to find a function that generates the net tip force acting on the environment by the antenna $F_{n,E}$ at equilibrium, balanced by the forces acting on the antenna at both ands F_E and F_G, with respect to any desired coordinate frame $\mathcal{C}_s$ given the joint angles θ, joint stiffnesses κ, joint velocities $\dot{\theta}$.

I am considering the equilibrium condition where no coordinate frame is moving with respect to each other. I model the base as an actuated joint by a servo motor and the tip as a free pin-joint (Fig. 3.10). The applied torque by the base servo motor is

such that the base angle θ_0 is kept constant. The torque τ_E applied to the antenna tip $\mathcal{C}_n$ by the environment is always zero because of the pin-joint assumption.

- Let $\mathcal{C}_E$ be the environment coordinate frame, which share the same orientation as the spatial frame and located at the point of contact with the antenna and the wall (Fig. 3.10).

- Let the notation $F_G \in \mathbb{R}^2$ be the Cartesian force vector acting on the base frame $\mathcal{C}_G$ origin with respect to a spatial coordinate frame (also $\mathcal{C}_G$) in Newtons. In the quasi-static case (no acceleration), this is the ground reaction force due to the flexural stiffness of the antenna.

- Let the notation $F_E \in \mathbb{R}^2$ be the Cartesian force vector acting on the tip frame $\mathcal{C}_n$ origin with respect to a spatial coordinate frame $\mathcal{C}_G$ in Newtons. This is the wall (environment) reaction force due to the flexural stiffness of the antenna.

- Let $\tau_E \in \mathbb{R} = 0$ be the torque applied to the antenna tip frame $\mathcal{C}_n$ by the environment. Since the tip is free to rotate, this quantity is always zero.

- Let τ_{servo} be the base motor torque applied to the antenna base coordinate $\mathcal{C}_G$ origin in Newton-meter.

- Let $\tau \in \mathbb{R}^{n+1}$ be the vector of joint torques due to joint stiffnesses in Newton-meters s.t: $\tau = \Big(\tau_0, \tau_1, \ldots, \tau_n\Big)^\top$

- Let $F_{n,E} = -F_E$ be the Cartesian force vector acting on the environment from the antenna.

- Let $F_{i-1,i} \in \mathbb{R}^2$ be the intersegmental force vector representing the linear force acting from segment $i-1$ to segment i.

- Let $M_{i-1,i} \in \mathbb{R}$ be the intersegmental net moment applied to segment i by the segment $i-1$.

- Observe that $-F_{i,i+1} \in \mathbb{R}^2$ is the intersegmental force vector representing the linear force acting from segment $i+1$ to segment i due to the joint connection between consecutive segments.

- Observe that $-M_{i,i+1} \in \mathbb{R}$ is the intersegmental net moment applied to segment i by the segment $i+1$ due to the joint connection between consecutive segments.

Figure 3.10 depicts the internal joint torques and the tip force F_n acting on the antenna model.

The main assumption of the model is that all rotational springs of the antenna are linear and governed by *Hooke's Law*. Then, for any joint θ_j, the relationship between torque angular angular displacement is given by:

$$\tau_j = -\kappa_j \theta_j \tag{3.2.2.1}$$

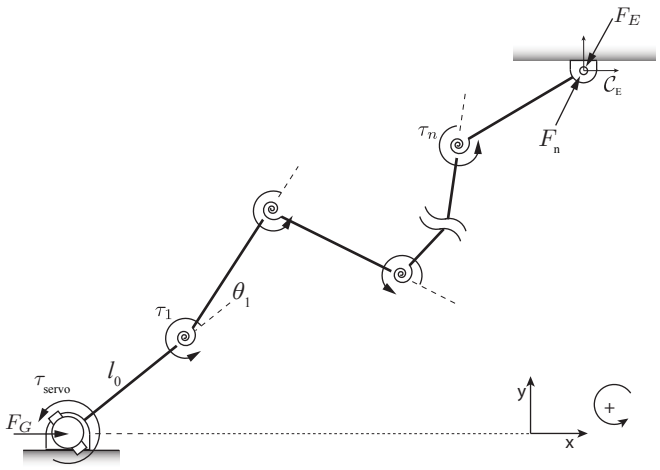

Figure 3.10: Forces F_i and torques τ_i acting on the antenna coordinate frames. The wall reaction force F_W counteracts the antenna tip force F_n.

where θ_j is the relative joint angle in *rad* and κ is the joint rotational stiffness in *[N-m/rad]*.

Consider an isolated individual segment in an equilibrium (Fig. 3.11A). The segment is affixed to the base $\mathcal{C}_G$ through a torsion spring with stiffness κ_n at an angle θ_n, and thus applys torque about $\mathcal{C}_G$. To facilitate equilibrium, to keep θ_n at the same angle without allowing both extreme frames $\mathcal{C}_G$ and $\mathcal{C}_n$ to move, there are reaction forces at those frame origins $\mathcal{C}_G$ and $\mathcal{C}_n$ due to joint constraints. The distal end is a pin joint, so there is no torque about $\mathcal{C}_n$. There are no external forces applied to neither end, so the only linear forces present are the reaction forces due to the single torsional spring at the base. This physical fact provides the final piece of information, which is that there is no net tension or compression on the segment. Thus, the resultant force component along the segment length must be zero (i.e the resultant force $F_{n,E}$ has to

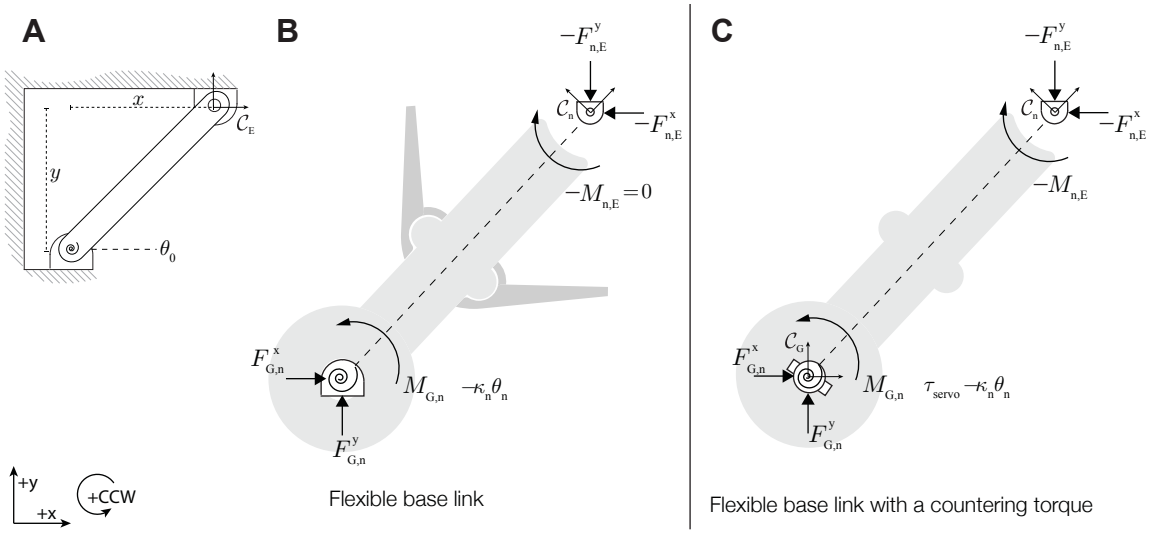

Figure 3.11: **A**: Toy problem setup with a single segment **B**: Free body diagram of a single segment in equilibrium. The proximal end is affixed to the base frame $\mathcal{C}_G$ through a loaded torsion spring with stiffness κ_0 at an angle θ_0. The distal end $\mathcal{C}_n$ affixed through a pin joint.**C**: Free body diagram of a single segment in equilibrium. The proximal end is affixed to the base frame $\mathcal{C}_G$ through a loaded torsion spring with stiffness κ_0 at an angle θ_0, whose torque is countered by a servo motor.

be perpendicular to the segment). From the free body diagram for this special toy case (Fig. 3.11B), I want to compute the four unknown reaction force components, $F^x_{G,n}, F^y_{G,n}, F^x_{n,E}, F^y_{n,E}$, based on the joint constraints and the known spring torque (driven by base angle θ_n). The location of the end joints and the base angle cannot be independently specified since there is only one segment. In the planar case, from the free body diagram of a single segment in equilibrium, I find three equations, two relating to sum of linear forces and one for the sum of torques. The definition of torque $\tau = r \times F$ where $r \in \mathbb{R}^3$ is the point of load $F \in \mathbb{R}^3$ is the force vector can be equivalently written $\tau = (\widehat{1}r)^\top F$ for the planar case. The three equilibrium equations are:

$$\begin{aligned}
\sum F^x &= F^x_{G,n} - F^x_{n,E} = 0 \\
\sum F^y &= F^y_{G,n} - F^y_{n,E} = 0 \\
\sum M &= -\kappa_n \theta_n + \left(\widehat{1}\begin{pmatrix} x \\ y \end{pmatrix}\right)^\top \begin{pmatrix} -F^x_{n,E} \\ -F^y_{n,E} \end{pmatrix} \\
&= -\kappa_n \theta_n + y F^x_{n,E} - x F^y_{n,E}
\end{aligned}$$

The fourth equation for this toy case comes from $F_{n,E} \perp \begin{pmatrix} x & y \end{pmatrix}^\top$:

$$\begin{aligned}
\begin{pmatrix} F^x_{n,E} \\ F^y_{n,E} \end{pmatrix}^\top \begin{pmatrix} x \\ y \end{pmatrix} &= 0 \\
F^x_{n,E} x + F^y_{n,E} y &= 0
\end{aligned} \tag{3.2.2.2}$$

Putting the information in the $Ax + b = 0$ format yields:

$$\begin{pmatrix} 1 & 0 & -1 & 0 \\ 0 & 1 & 0 & -1 \\ 0 & 0 & y & -x \\ 0 & 0 & x & -y \end{pmatrix} \begin{pmatrix} F^x_{G,n} \\ F^y_{G,n} \\ F^x_{n,E} \\ F^y_{n,E} \end{pmatrix} = \begin{pmatrix} 0 \\ 0 \\ \kappa_n \theta_n \\ 0 \end{pmatrix} \tag{3.2.2.3}$$

Equation 3.2.2.3 is in general nonsingular and yields a unique solution for the ground reaction force $F_{G,n}$ and the applied force $F_{n,E}$.

Now I consider the same single segment system, but with a servo motor parallel to the torsion spring with a known stiffness κ_n (Fig. 3.2.2.3C). The servo motor receives a position command θ_n and applies an unknown torque $\tau_{\text{servo}} = \kappa_n \theta_n$ to achieve this angle. Now, even though this system is rather silly —the tip force and ground reaction forces are by zero by inspection—, it helps to get an insight on how the system generalizes for the n-link case. So in this modified system I get another unknown τ_{servo}, but also get another equation. Again, from the free body diagram I get three equations:

$$\begin{aligned} \sum F^x &= F^x_{G,n} - F^x_{n,E} = 0 \\ \sum F^y &= F^y_{G,n} - F^y_{n,E} = 0 \\ \sum M &= \tau_{\text{servo}} - \kappa_n \theta_n + \begin{pmatrix} x \\ y \\ 0 \end{pmatrix} \times \begin{pmatrix} -F^x_{n,E} \\ -F^y_{n,E} \\ 0 \end{pmatrix} \end{aligned}$$

$$= -\kappa_n\theta_n + \left(\widehat{1}\begin{pmatrix}x\\y\end{pmatrix}\right)^\top \begin{pmatrix}-F^x_{n,E}\\-F^y_{n,E}\end{pmatrix}$$
$$\sum M = \tau_{\text{servo}} - \kappa_n\theta_n + yF^x_{n,E} - xF^y_{n,E}$$

Combining it with equation 3.2.2.2 and $\tau_{\text{servo}} = \kappa_n\theta_n$ yields the modified system of equations:

$$\begin{pmatrix}1 & 0 & -1 & 0 & 0\\ 0 & 1 & 0 & -1 & 0\\ 0 & 0 & y & -x & 1\\ 0 & 0 & x & y & 0\\ 0 & 0 & 0 & 0 & 1\end{pmatrix}\begin{pmatrix}F^x_{G,n}\\F^y_{G,n}\\F^x_{n,E}\\F^y_{n,E}\\\tau_{\text{servo}}\end{pmatrix} = \begin{pmatrix}0\\0\\\kappa_n\theta_n\\0\\\kappa_n\theta_n\end{pmatrix} \tag{3.2.2.4}$$

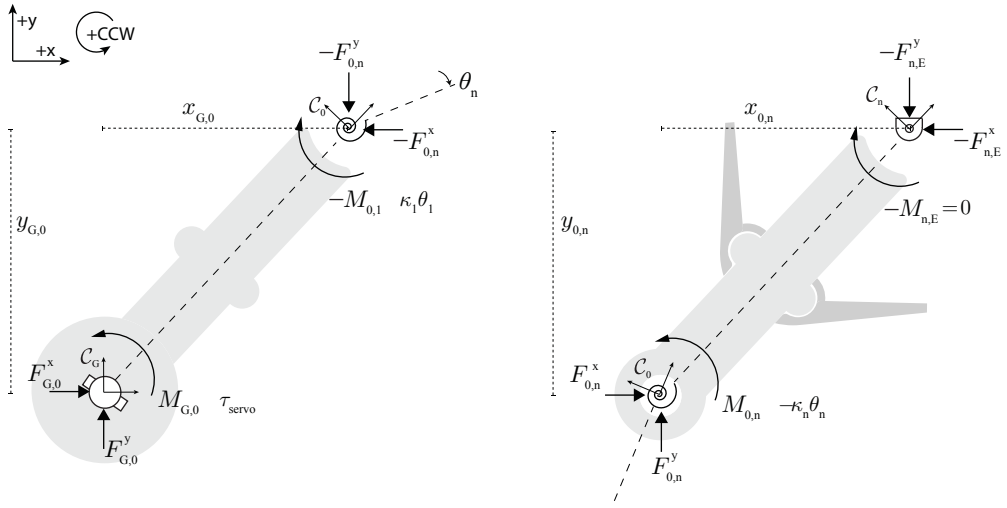

Figure 3.12: Toy problem setup with two segments. The proximal end is affixed to the base frame $\mathcal{C}_G$ through a servo motor at an angle θ_0. The distal end $\mathcal{C}_n$ affixed through a pin joint.

Now I consider a two segment system in equilibrium (Fig. 3.12). The base segment is affixed to the base frame $\mathcal{C}_G$ through a servo motor at an angle θ_0. The distal segment is a pin joint again, so there is no torque about $\mathcal{C}_n$. From the free body diagram (Fig. 3.12), I have six unknown force components $F^x_{G,0}, F^y_{G,0}, F^x_{0,n}, F^y_{0,n}, F^x_{n,E}, F^y_{n,E}$ and the unknown servo motor torque τ_{servo}. Each free body diagram provides three equations:

$$\begin{aligned}
\sum F^x_0 &= F^x_{G,0} - F^x_{0,n} = 0 \\
\sum F^y_0 &= F^y_{G,0} - F^y_{0,n} = 0 \\
\sum M_0 &= \tau_{\text{servo}} + \kappa_n \theta_n + \left(\widehat{1}\begin{pmatrix} x_{G,0} \\ y_{G,0} \end{pmatrix}\right)^\top \begin{pmatrix} -F^x_{0,n} \\ -F^y_{0,n} \end{pmatrix} \\
&= \tau_{\text{servo}} + \kappa_n \theta_n + y_{G,0} F^x_{n,E} - x_{G,0} F^y_{n,E} \\
\sum F^x_n &= F^x_{0,n} - F^x_{n,E} = 0 \\
\sum F^y_n &= F^y_{0,n} - F^y_{n,E} = 0 \\
\sum M_n &= -\kappa_n \theta_n + y_{0,n} F^x_{n,E} - x_{0,n} F^y_{n,E}
\end{aligned}$$

The two segment system with the base servo is also trivial. This is because for any two link planar RR-arm in equilibrium, there are at most two configurations (elbow-up and elbow-down) and thus neither the base angle nor the joint angle can be independently specified. Similar to the previous case, if the servo motor is already at one of the feasible angles and because there is only one spring, the distal segment cannot be in net tension or compression. So again, I have the final constraint: $F_{n,E} \perp \begin{pmatrix} x_{0,n} & y_{0,n} \end{pmatrix}^\top$. Grouping the linear force and torque equations yields the following

system of equations for Figure 3.12:

$$\begin{pmatrix} 1 & 0 & -1 & 0 & 0 & 0 & 0 \\ 0 & 1 & 0 & -1 & 0 & 0 & 0 \\ 0 & 0 & 1 & 0 & -1 & 0 & 0 \\ 0 & 0 & 0 & 1 & 0 & -1 & 0 \\ 0 & 0 & y_{G,0} & -x_{G,0} & 0 & 0 & 1 \\ 0 & 0 & 0 & 0 & y_{0,n} & -x_{0,n} & 0 \\ 0 & 0 & 0 & 0 & x_{0,n} & y_{0,n} & 0 \end{pmatrix} \begin{pmatrix} F^x_{G,0} \\ F^y_{G,0} \\ F^x_{0,n} \\ F^y_{0,n} \\ F^x_{n,E} \\ F^y_{n,E} \\ \tau_{\text{servo}} \end{pmatrix} = \begin{pmatrix} 0 \\ 0 \\ 0 \\ 0 \\ -\kappa_n \theta_n \\ \kappa_n \theta_n \\ 0 \end{pmatrix} \tag{3.2.2.5}$$

Equation 3.2.2.5 is also nonsingular in general and provides a unique solution for all intersegmental forces. A pattern in the expression emerges as well.

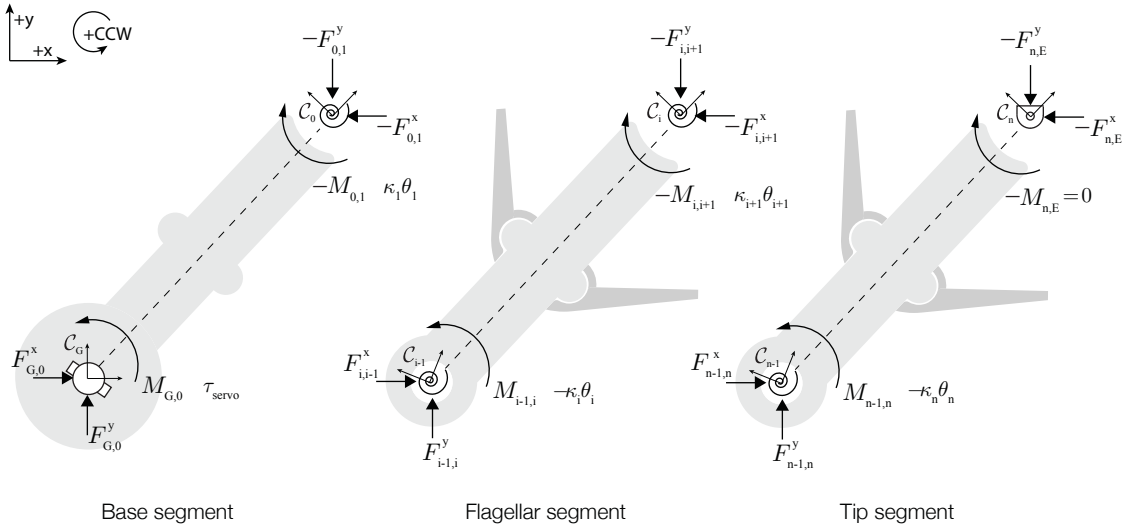

Figure 3.13: Free body diagram for the antenna segments. The base segment is affixed to the base frame $\mathcal{C}_G$ through a servo motor at an angle θ_0. The distal end $\mathcal{C}_n$ affixed through a pin joint.

Now I move to the non-trivial cases with at least three segments: the base, flagellar, and end segements (Fig. 3.13). For a three segment antenna, there are nine unknown

quantities (eight force components, one base torque) and nine equations directly from the free body diagrams, so an additional constraint to solve for the forces is not necessary. Furthermore, every additional segment brings two unknown internal reaction forces but three independent equations. For the three segment case, the equations are:

$$\begin{aligned}
\sum F_0^x &= F_{G,0}^x - F_{0,1}^x = 0 \\
\sum F_0^y &= F_{G,0}^y - F_{0,1}^y = 0 \\
\sum F_1^x &= F_{0,1}^x - F_{1,n}^x = 0 \\
\sum F_1^y &= F_{0,1}^y - F_{1,n}^y = 0 \\
\sum F_n^x &= F_{1,n}^x - F_{n,E}^x = 0 \\
\sum F_n^y &= F_{1,n}^y - F_{n,E}^y = 0 \\
\sum M_0 &= \tau_{\text{servo}} + \kappa_1\theta_1 + y_{G,0}F_{0,1}^x - x_{G,0}F_{0,1}^y \\
\sum M_1 &= -\kappa_1\theta_1 + \kappa_n\theta_n + y_{0,1}F_{1,n}^x - x_{0,1}F_{1,n}^y \\
\sum M_n &= -\kappa_n\theta_n + y_{1,n}F_{n,E}^x - x_{1,n}F_{n,E}^y
\end{aligned}$$

In matrix form:

$$\begin{bmatrix} 1 & & -1 & & & & & & & \\ & 1 & & -1 & & & & & & \\ & & 1 & & -1 & & & & & \\ & & & 1 & & -1 & & & & \\ & & & & 1 & & -1 & & & \\ & & & & & 1 & & -1 & & \\ & & y_{G,0} & -x_{G,0} & & & & & 1 & \\ & & & & y_{0,1} & -x_{0,1} & & & & \\ & & & & & & y_{1,n} & x_{1,n} & & \end{bmatrix} \begin{bmatrix} F^x_{G,0} \\ F^y_{G,0} \\ F^x_{0,1} \\ F^y_{0,1} \\ F^x_{1,n} \\ F^y_{1,n} \\ F^x_{n,E} \\ F^y_{n,E} \\ \tau_{\text{servo}} \end{bmatrix} = \begin{bmatrix} 0 \\ 0 \\ 0 \\ 0 \\ 0 \\ 0 \\ -\kappa_1\theta_1 \\ -\kappa_n\theta_n + \kappa_1\theta_1 \\ \kappa_n\theta_n \end{bmatrix} \tag{3.2.2.6}$$

For an n-segment antenna, the system of equations are over-constrained. The number of unknowns and free body diagram equations are:

$$2(n+2)+1 = \text{unknowns} \tag{3.2.2.7}$$
$$3(n+1) = \text{equations} \tag{3.2.2.8}$$

where n is the number of flexible joints. By inspection, the minimum number of flexible segments needed are 2 (3 including the base) in order to rely only on the free body diagram equations. For any added segment i the corresponding equilibrium equations are:

$$\sum F^x_i = F^x_{i-1,i} - F^x_{i,i+1} = 0$$
$$\sum F^y_i = F^y_{i-1,i} - F^y_{i,i+1} = 0$$
$$\sum M_i = -\kappa_i\theta_i + \kappa_{i+1}\theta_{i+1} + y_{i-1,i}F^x_{i,i+1} - x_{i-1,i}F^y_{i,i+1}$$

Thus, the over constrained system of equations for an n-segment antenna can be constructed as:

$$\underbrace{\left[\begin{array}{cccccccccccc}
1 & 0 & -1 & 0 & & & \dots & & & & & 0 \\
0 & 1 & 0 & -1 & 0 & & \dots & & & & & 0 \\
\vdots & & & \ddots & & & & & & & & \\
 & & & & & & \ddots & & & & & \vdots \\
\vdots & & & & & & & & & & & \\
0 & & & & & & \dots & 1 & 0 & -1 & 0 & \\
\hdashline
0 & 0 & y_{G,0} & -x_{G,0} & 0 & & & & \dots & 0 & 1 & \\
 & & 0 & 0 & y_{0,1} & -x_{0,1} & 0 & & \dots & & 0 & \\
\vdots & & & & & & \ddots & & & & \vdots & \\
0 & \dots & & & & & & 0 & y_{n-1,n} & -x_{n-1,n} & 0 &
\end{array}\right]}_{3(n+1)\times 2(n+2)+1}
\left[\begin{array}{c} F^x_{G,0} \\ F^y_{G,0} \\ F^x_{0,1} \\ F^y_{0,1} \\ \vdots \\ \\ \\ F^x_{n,E} \\ F^y_{n,E} \\ \tau_{\text{servo}} \end{array}\right]
=
\left[\begin{array}{c} 0 \\ \\ \vdots \\ \\ 0 \\ -\kappa_1\theta_1 \\ -\kappa_2\theta_2 + \kappa_1\theta_1 \\ \vdots \\ -\kappa_n\theta_n + \kappa_{n-1}\theta_{n-1} \\ M_{n,E} + \kappa_n\theta_n \end{array}\right]$$

(3.2.2.9)

The system of equations given in 3.2.2.9 is quite powerful because it provides all internal and ground (environment) reaction forces along with the base torque τ_{servo} for an n-segmented antenna in static equilibrium. Now consider the antenna as an n-link manipulator arm where all joint torques τ are externally controlled. From the principle of virtual work, the relationship between the end effector force applied to the environment $F_{n,E}$ and the joint torques τ is:

$$\tau = \begin{pmatrix} \tau_1 \\ \vdots \\ \tau_n \end{pmatrix} = J_{Gn}^{\top} \begin{pmatrix} F_{n,E} \\ \tau_{n,E} \end{pmatrix} \tag{3.2.2.10}$$

where J_{Gn} is the hybrid Jacobian matrix (see section 2.2.2.1 from the ground frame $\mathcal{C}_G$ to $\mathcal{C}_n$. Solving 3.2.2.10 directly for the end effector force $F_{n,E}$ yields:

$$\underbrace{\left(J_{Gn}J_{Gn}^{\top}\right)^{-1}J_{Gn}}_{J_{Gn}^{\top}{}^{\dagger}}\tau = \begin{pmatrix} F_{n,E} \\ \tau_{n,E} \end{pmatrix} \tag{3.2.2.11}$$

where $J_{Gn}^{\top}{}^{\dagger}$ is the generalized left pseudo-inverse of $J_{Gn}^{\top}$.

In this case of redundant manipulator systems, the joint forces that can be used to produce a given operational force vector are not unique [50]. However, the geometry of the antenna is directly proportional to the joint torques due to Hooke's Law. Thus, the angular displacements can be fed into both equations 3.2.2.11 and 3.2.2.9 to get the forces applied to the environment. Furthermore, since the configuration of the antenna is also directly related to the potential energy of the antenna, I take advantage of Castigliano's theorems to prove this proportionality between the joint displacements and torque.

Castigliano's second theorem states: *The first partial derivative of the total internal energy in a structure with respect to the force (torque) applied at any point is equal to the deflection at the point of application of that force in the direction of its line of action.*

$$\frac{\partial U_T}{\partial \tau_i} = \delta\theta_i \tag{3.2.2.12}$$

Substituting *Hooke's Law* into the total energy gives yields the energy expression purely dependent on joint torques and stiffnesses:

$$\begin{aligned} U_T &= \frac{1}{2}\sum_{i=1}^{n} \mathcal{K}_i \left(\frac{\tau_i}{\mathcal{K}_i}\right)^2 \\ &= \frac{1}{2}\sum_{i=1}^{n} \frac{\tau_i^2}{\mathcal{K}_i} \end{aligned} \tag{3.2.2.13}$$

Taking the first partial derivative of equation 3.2.2.13 for all joints per Castigliano's second theorem (equation 3.2.2.12) yields the gradient of the total energy:

$$\begin{aligned} \nabla U_T = \begin{pmatrix} \frac{\partial U_T}{\partial \tau_1} \\ \vdots \\ \frac{\partial U_T}{\partial \tau_n} \end{pmatrix} = \begin{pmatrix} \delta\theta_1 \\ \vdots \\ \delta\theta_n \end{pmatrix} &= \begin{pmatrix} \frac{\tau_1}{\mathcal{K}_1} \\ \vdots \\ \frac{\tau_n}{\mathcal{K}_n} \end{pmatrix} \\ &= \begin{pmatrix} \frac{1}{\mathcal{K}_1} & & \\ & \ddots & \\ & & \frac{1}{\mathcal{K}_n} \end{pmatrix} \begin{pmatrix} \tau_1 \\ \vdots \\ \tau_n \end{pmatrix} \end{aligned} \tag{3.2.2.14}$$

Equation 3.2.2.14 relates the joint torques to joint displacements $\delta\theta_i$. Thus, assuming the antenna is an equilibrium state, i.e. $\dot{\theta}_i = 0$ for all $i = \{1, \cdots, n\}$, then any

added joint torques change the antenna configuration according to this relationship (Equation 3.2.2.14). Lets assume the antenna is fixed at the ground coordinate frame $\mathcal{C}_G$ and there is an external generalized force $\begin{pmatrix} F_{ext} & \tau_{ext} \end{pmatrix}^\top$ applied at the tip of the antenna (origin of frame $\mathcal{C}_n$). Then substituting 3.2.2.10 into 3.2.2.14 will relate the tip force F_n to joint displacements $\delta\theta$:

$$\begin{pmatrix} \delta\theta_1 \\ \vdots \\ \delta\theta_n \end{pmatrix} = \begin{pmatrix} \frac{1}{\mathcal{K}_1} & & \\ & \ddots & \\ & & \frac{1}{\mathcal{K}_n} \end{pmatrix} J_{Gn}^\top \begin{pmatrix} F_{ext} \\ \tau_{ext} \end{pmatrix} \tag{3.2.2.15}$$

Equations 3.2.2.11 and 3.2.2.9 provide identical results when the antenna is truly in the equilibrium state, that is when its at a local minimum in terms of potential energy. However, the pseudo-inverse method does not produce the correct output when the joint limits are involved, which happens during my physical experiments. The free body diagram method, however, can be altered slightly to incorporate the joint limits since there are more equations than unknowns for number of joints more than 3. Thus, I added unknown torques τ^γ into equation 3.2.2.9 in my simulation, which provided the correct joint torques when substituted back into $\tau = J_{Gn}^\top F_{n,E}$.

In the next section, I corroborate our biological findings with the numerical model and robotic antenna.

3.3 The Physical Antenna

Using my tunable physical model of an arthropod antenna inspired by the American cockroach [51], I further explored biomechanical factors that influence antenna reconfiguration. The physical model enabled me to manipulate mechanical parameters that would otherwise be difficult or impossible to test in animals. In my experimental trials, I considered different initial conditions for wall roughness, hair geometry, hair orientation, antenna stiffness, base angle, base velocity, and wall distance. I showed that the robotic antenna's flipping statistics were categorically affected by the existence of appropriately oriented hairs for a given wall roughness.

3.3.1 Sufficiency of Distally Pointing Hairs

In this section, I show that passive mechanical hair sensillae on the antenna are *sufficient* for mediating a change in the postural state of the antenna. Instead of removing hairs from the biological antenna, I added artificial sensillae to my tunable physical model inspired by arthropod antennae. Through these independent robotic experiments, I showed that large mechanosensory hairs play a crucial mechanical role in mediating sensor reconfiguration. Combining my results with those from the laser ablation experiments, we propose a novel function for these structures, previously described as having an exclusively sensory function.

3.3.1.1 Methods

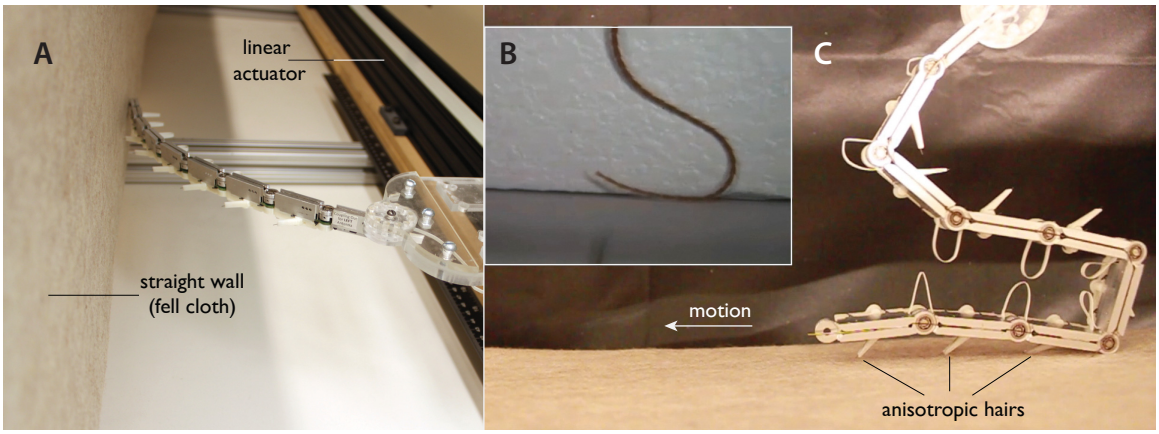

Figure 3.14: Flipping experiment with the robotic antenna to independently test the hypothesis that hairs enable the passive reconfiguration of an antenna. **A**: The eight-segment robotic antenna with anisotropic hairs is tangent to a felt-cloth-covered wall in the forward-projecting posture. **B**: Biological antenna during the transition phase from forward- to backward-projecting posture. **C**: Robotic antenna stiffness profile tuned such that the transition phase mechanics are similar to those of the biological antenna.

To test the sufficiency of passive hairs in changing the antenna state, I added artificial hairs to my highly tunable and modular physical model inspired by arthropod antennae [51]. I approximated the stiffness distribution of insect antennae [11] on an eight-segment model (Fig. 3.14B,C) and ran the robotic antenna at a constant base velocity, $\dot{p}_G = 15^{mm}/_s$, along a wall (Fig. 3.14A). In the middle of each segment, I placed a $18mm$ long anisotropic "hair" protruding $45deg$ towards the distal end of the antenna. Here, anisotropy refers to the direction in which a hair can collapse. The hairs were inspired by the known biomechanical feature of the thick-wall chemosensory/mechanosensory sensilla (chaetica B) of the cockroach *P. americana* [38].

I performed a total of seven experiments each with ten trials. The base angle, θ_0, was kept constant at $30deg$, and the distance from the wall to the antenna base, d, was kept at $135mm$. As an initial condition, the robotic antenna posture was always projecting in the direction of motion (forward). The forward velocity of the base was chosen such that the antenna was at a quasi-static state to minimize inertial effects. The linear actuator was a belt-driven Velmex BiSlide (Velmex Inc., Bloomfield, NY, USA) with a resolution of $25\mu m$ and a travel distance of $1m$. Antenna segment data were sampled via a common I2C bus facilitated by a $600MHz$ Gumstix Verdex Pro base computer (Gumstix Inc., Portola Valley, CA, USA). Both the linear actuator and base computer were controlled asynchronously by custom-designed client software (see appendix 6.5). I recorded each segment joint angle with a resolution of $0.35deg$ at $120Hz$. (Fig. 3.15A) shows computer-aided design (CAD) renderings of the antenna segment with possible hair orientations. Two hairs —one at each side— can be placed per segment on one of the two available cylindrical extrusions, about which the hair is free to rotate (Fig.3.15B). I designed two different hair types: distally and proximally projecting. They mirror each other about the segment's sagittal plane. A hair could abduct to at most $45deg$ from the segment after which a mechanical hard stop was encountered (Fig.3.15C). Each hair was spring-loaded to swing open to $45deg$ by a $0.1mm$ diameter nitinol wire, which simultaneously acted as the hair tip that "anchored" the segment to the wall surface (Fig. 3.14C). In the event of a collapse, the hair triggered the contact sensor at its base. During a trial, when a distally

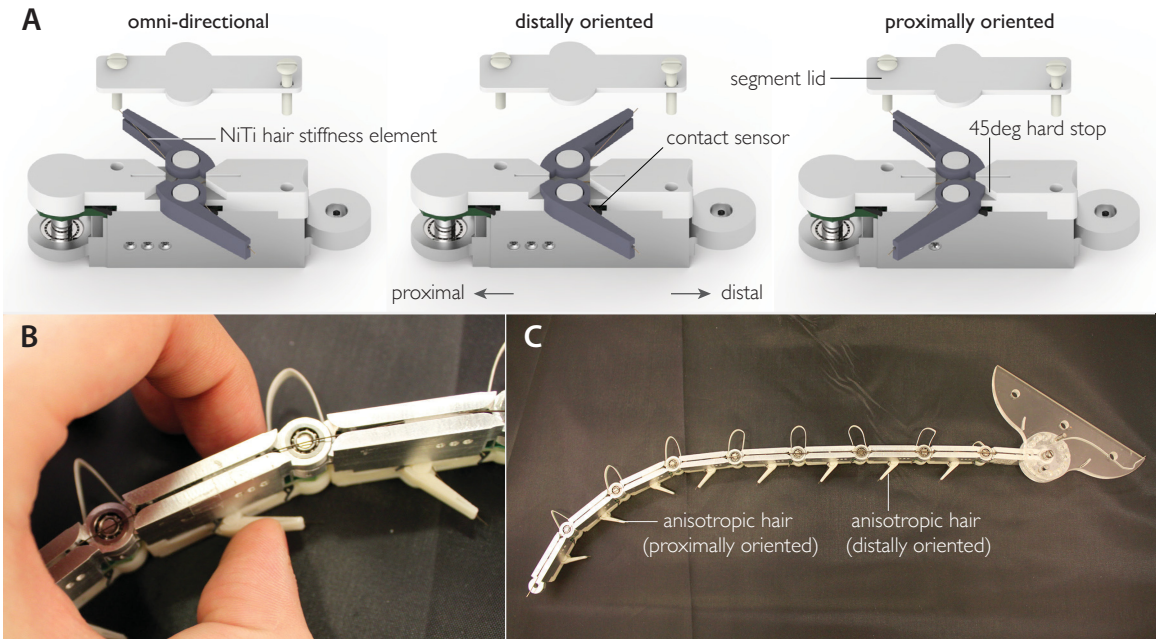

Figure 3.15: **A**: Robotic antenna segment renders with different anisotropic hair orientations. **B**: Every hair was spring-loaded via a nitinol wire that enabled them to swing open when there was no contact with a surface. **C**: The entire 8-segment experiment antenna with the most distal segments having proximally oriented hairs.

oriented hair anchored to asperities in the wall (Fig. 3.16A), the entire antenna went into a transition phase which could result in a flip (the antenna switches to a backwards-projecting configuration). I define a flip as a transition in which the most distal segment angle exceeds $90deg$ with respect to the wall (Fig. 3.16B).

A base angle of $30deg$ was chosen to be consistent with prior studies of rapid wall-following in *P. americana* [12] [52]. Additional control trials were conducted at 10, 20, 60 and $70deg$ to test the sensitivity of flipping to the base angle. For each angle, I maximized the distance to the wall while ensuring that the final antennal segment contacted the wall. During each trial, I recorded whether or not the hairs disengaged

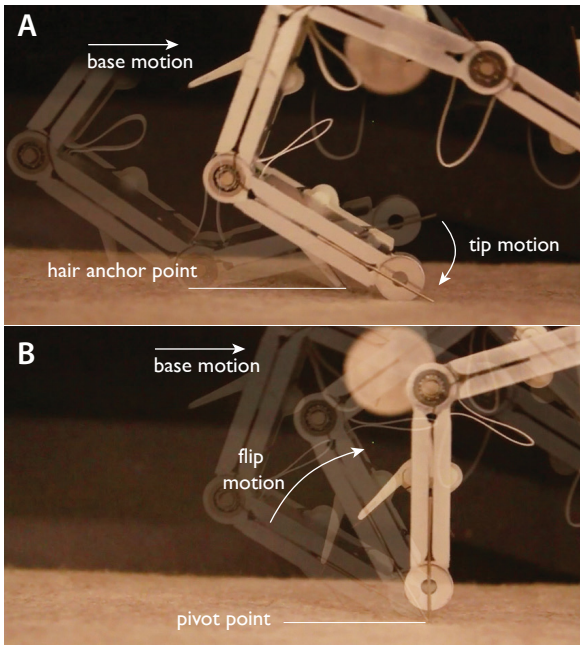

Figure 3.16: **A**: The distally oriented hair anchored to the wall forced the tip toward the wall, which initiated flipping. **B**: A successful flip was achieved when the most distal segment angle exceeded $90deg$ with respect to the wall.

from the wall before the antenna flip occurred.

3.3.1.2 Results

Across the six experiments, I varied the wall surface and the hair orientation using the following combinations:

1. Rough (felt-cloth) wall, distally pointing hairs.

2. Rough wall, three distal segments with no hairs.

3. Rough wall, proximally pointing hairs.

4. Smooth (glossy paper) wall, distally pointing hairs.

5. Smooth wall, three distal segments with no hairs.

6. Smooth wall, proximally pointing hairs.

In experiment 1, I observed that the hair tips of the distal segments anchored to the asperities of the rough (felt) material almost immediately. Figure 3.17A illustrates data from one trial of experiment 1 where the antenna initiated a flip immediately after the smooth zone (glossy paper) of the wall. A similar response was observed for the remaining nine trials. For experiment 2, I removed the three distal hairs, analogous to the laser ablation experiments for the biological cockroach flagellum. I did not observe a flip in any of the ten trials. In four out of the ten trials, I observed "anchoring" (Fig. 3.16B) at the most distal segment, but these hair-substrate interactions were insufficient to flip the antenna (Fig. 3.17B). For experiment 3, I reversed the orientation of the hairs to evaluate the effects of the hair orientation. This control would have been infeasible to test on a cockroach flagellum. In all ten trials, the antenna did not flip. For all the other experiments $(4-6)$ with the smooth wall, the antenna slid over the corresponding surface without initiating a flip. In some cases, the biological antenna changed state via torsion around the flagellum (Fig. 3.4A), but it was insufficient to flip the robotic antenna (Fig. 3.17B,C). This degree of freedom was not available by design.

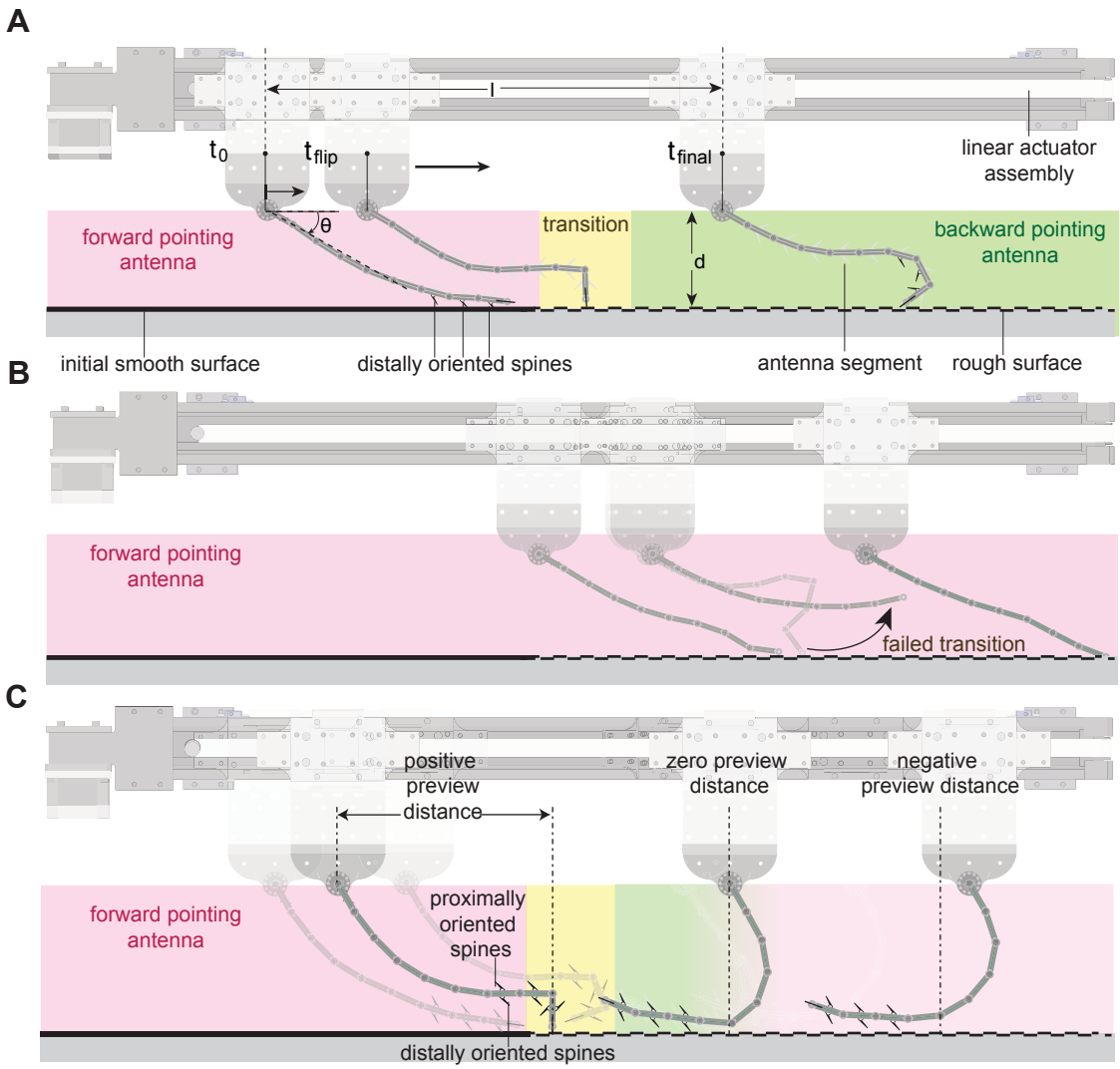

Figure 3.17: **A,B**: Data from individual joint angle sensors from the robotic antenna during an experimental trial from the initial time, t_0, until t_{final}, where d was the distance between the base of the antenna and the wall. A flip was registered when the anchored segment (most distal) was perpendicular to the wall. **A**: At t_{flip} the distally oriented hairs engaged with the wall, which resulted in the antenna transitioning (yellow) from a forward-pointing (pink) to a backward-pointing (green) position. During this trial, the wall was covered with rough felt cloth and the hairs were oriented distally. **B**: The wall was covered with felt cloth and the three distal-most hairs of the robotic antenna were removed. This panel shows a failed transition from experimental data as the antenna remained forward-projecting (pink) during the entire trial (arrow). **C**: Data from one trial in which robotic antennal hairs ipsilateral to the wall pointed distally while those on the other side were pointed proximally (omni-directional). After the antenna flipped, the proximally pointing hairs engaged, causing the contact point to move behind the base and thus significantly diminishing the preview distance. Image credit [46]

To complement experiment 1 (rough wall, distally pointing hairs), I conducted a control to determine whether flipping was sensitive to the base angle by repeating the experiment with base angles of 10, 20, 60 and 70 *deg*. In all trials, the antenna flipped from forward to backward. Specifically, the hairs never disengaged from the wall before flipping occurred. This suggested that antennal reconfiguration is insensitive to base angle, validating the biological antenna experiments.

When a flip was completed with distally pointing hairs, the hairs pointed proximally and thus could not interlock with the asperities during forward motion. I observed that the wall contact point initially moved with the same velocity as the base, remaining well ahead and thus providing an effective preview distance. From this observation, I hypothesized that distally pointing hairs were crucial to maintain a wall contact point well ahead of the animal or robot on rough surfaces. For smooth surfaces, I expected the coefficient of friction to become more important. To test the hypothesis that distally pointing hairs were crucial to maintain an effective preview distance, I performed an additional experiment in which the side of the antenna ipsilateral to the wall had distally pointing hairs while the other side had proximally pointing hairs. When the antenna flipped, the proximally pointing hairs came into contact with the wall, pointing toward the direction of movement. In all trials ($^{10}/_{10}$), the preview distance relative to the base became negative after the flip (Fig. 3.17C). These results demonstrated the importance of distally pointing hairs in maintaining an adequate preview distance following a flip on rough surfaces. Similarly, I

expected unidirectional friction to be an important property affecting preview distance on smooth surfaces. From an engineering point of view, I have shown that distally oriented hairs facilitated a change of mechanical state of a physical model of an antenna when coupled with forward motion. Distally projecting hairs tended to anchor themselves immediately, and the shear forces at the surface easily overcame the inter-segmental joint stiffness along the antenna. As the base moved at constant velocity, the joint angles changed continually either until the distal segments became perpendicular to the wall (flip) or until the shear forces between the distal segments and the wall overcame the hair-asperity contact strength (no flip). These results from the physical model confirmed that distally pointing hairs increase the probability of engaging wall asperities, the main physical interaction in mediating the flip on rough surfaces.

3.3.2 Tip forces vs Stiffness Profile

In this section, I investigate the tip forces that occur during the postural transition of the antenna. Since the tip is the most distal point on the antenna, the flagellum pivots about it to realize the transition from forward looking to backward looking posture. It's during that transition phase where the antenna will most likely to lose contact with the wall and therefore hinder robust wall-following. Thus it's crucial to passively tune the forces during this phase so that sensory acuity can be maintained

continuously. I claim that the stiffness profile is the key mechanical property that governs robust wall-following and to test that assertion, I ran several different decreasing and constant stiffness profiles in my experimental testbed designed to cause the antenna to flip at a certain place where a load-cell measured the forces. I tracked the antenna optically and compared the experimental results with my simulation.

3.3.2.1 Methods

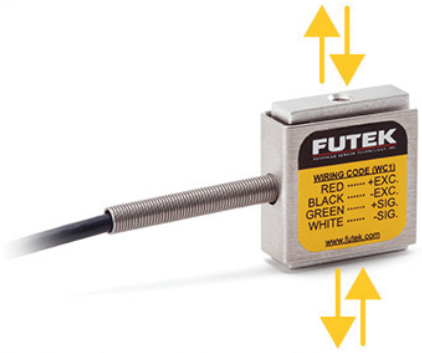

Figure 3.18: FUTEK LSB200 is an in-line load cell using the threaded hole on top and bottom. Off center load, side load and moments should be avoided. [53]

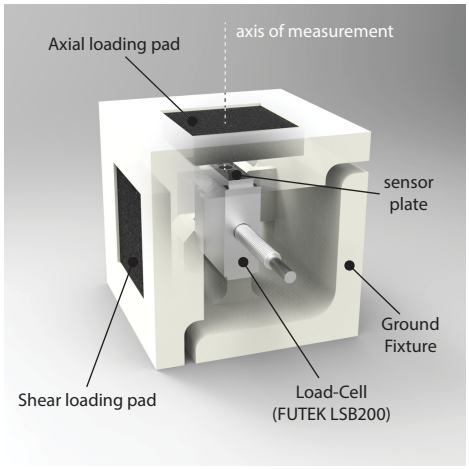

Figure 3.19: Custom load-cell fixture I manufactured using FDM rapid prototyper.

The force sensor was a *miniature S-beam load cell* designed to handle axial tension and compression (Fig. 3.18). I incorporated this sensor in a custom fixture (Fig. 3.19) so that normal or shear loads were measured with the same sensor. Since this required the loading plate have an offset from the measuring axis, I ensured that the axes of measurements did not have a significant coupling. This offset created moments, and

I determined their effect on measurement accuracy (Appendix 6.4) and found that forces on both axes were accurately measured just by reorienting the force sensor. Specifically, I made a custom symmetric force sensing fixture to collect normal and shear force data in two separate trials (Fig. 3.20).

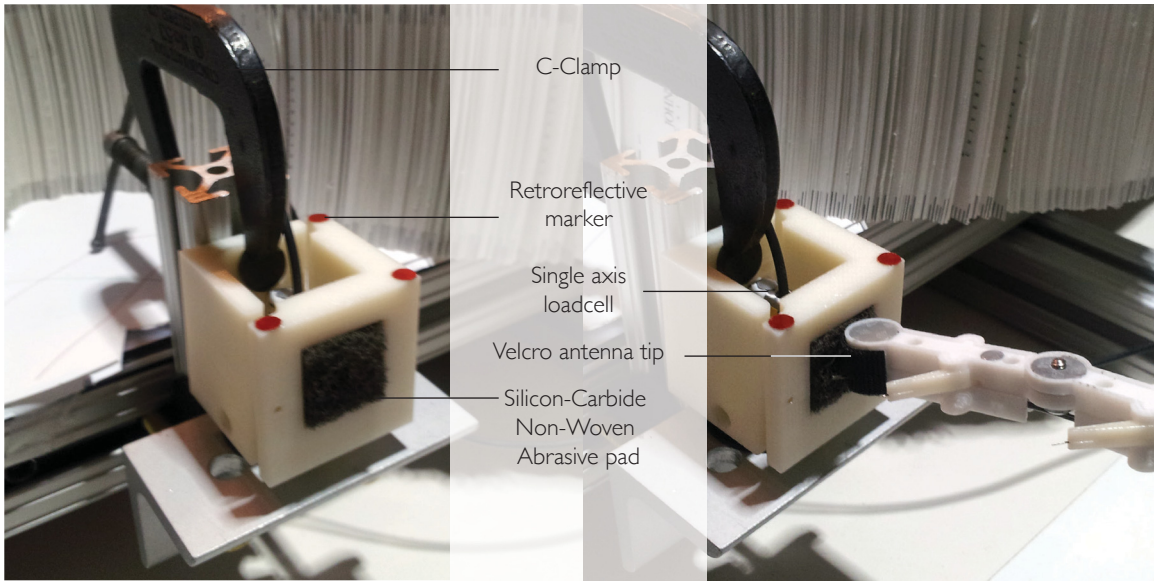

Figure 3.20: A single axis FUTEK LSB200 was mounted on symmetrical force pad I designed to measure normal and shear forces. The tip of the model antenna and the abrasive plate had significant coefficient of friction to prevent the antenna from slipping during force measurements.

In the first set of experiments, I used a nine segment physical antenna with distally pointing anisotropic spines. The antenna was run at a 30° angle across the force sensing platform for 15 centimeters at a quasi-static velocity of $15^{mm}/_{s}$. The orthogonal distance between the antenna's tip and the wall was 16.2 centimeters so that the final segment made contact with the smooth surface of the wall the beginning of each trial. The otherwise smooth wall ends with a flush strip of silicon-carbide fibrous abrasive material designed to entangle with the most distally pointing hair of

the antenna. This anchoring of the anisotropic hair forced the antenna to flip with the tip pivoting about the force sensing pad (Fig. 3.21). I recorded the normal and shear forces at 5000 Hz using my data collection software described in Appendix 6.5. As the antenna base continued to move at constant velocity, the tip was released from the force sensing pad and swung forward again.

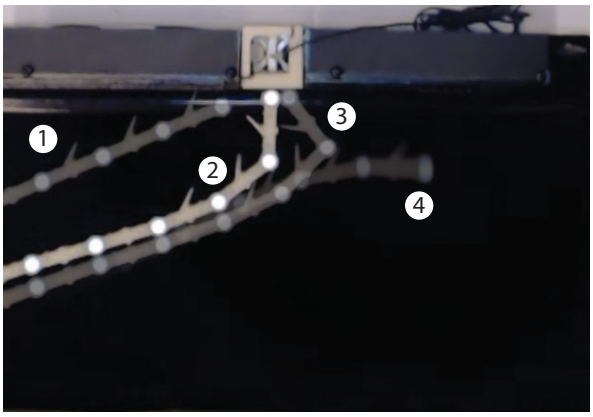

Figure 3.21: Four overlaid images from a single experiment trial. **1** The antenna started in the forward-looking extended posture; **2** The antenna tip was caught by the rough surface and flipped on the force sensing loading pad; **3** The antenna posture switched to "backward looking"; **4** The antenna swung back to "forward looking" posture as the wall roughness switches from rough to smooth.

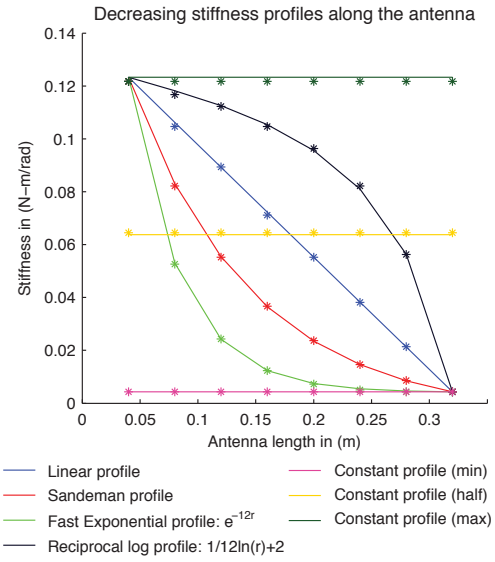

Figure 3.22: Normalized decreasing and constant stiffness profiles employed in my tip forces experiments. The lines correspond to the desired profile, whereas the stars (∗) correspond to the nearest available stiffness element.

I employed a total of seven stiffness profiles, four categorically different decreasing profiles and three constant profiles with different magnitudes (Figs. 3.22, 3.23). For every stiffness profile experiment, I performed five trials for the normal force mea-

surements and five trials for the shear force measurements.

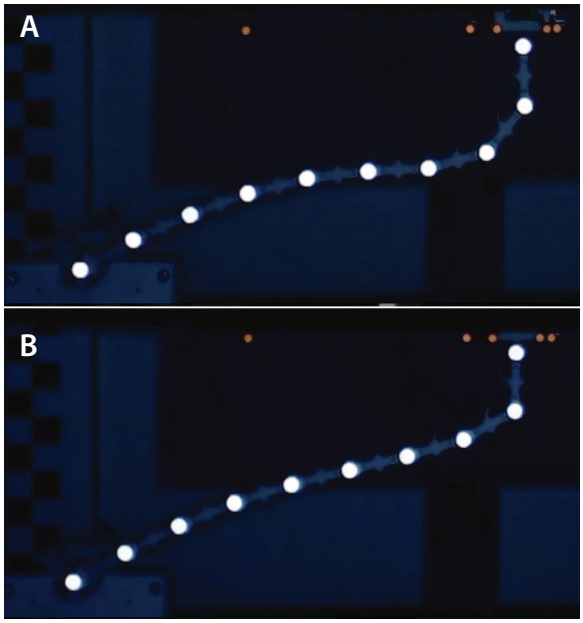

Figure 3.23: **A** Exponentially (Sandeman) decreasing and **B** linearly decreasing stiffness profile antenna at their postural transition phases.

The 30° base angle experiments described earlier failed to produce sufficient friction force on the sensing pad for fast exponential profile experiments. Thus, another set of experiments were designed with 60° base angle. In this second experiment, the tip of a nine segment antenna was directly placed on the force sensor at a forward looking configuration where the appropriate orthogonal distance between the tip and base of the antenna turned out to be 27.0 centimeters. Again, the antenna base was moved for a total of 15 centimeters at a quasi-static velocity of $2^{mm}/_{s}$. I recorded both normal and shear forces at 5000 Hz and tracked the joint marker positions from video collected at 30 frames per second with 1280 × 720 pixel resolution (Fig. 3.24). I compared the flipping instances between the reciprocally logarithmic decreasing

stiffness profile and constant stiffness profile (Fig. 3.25).

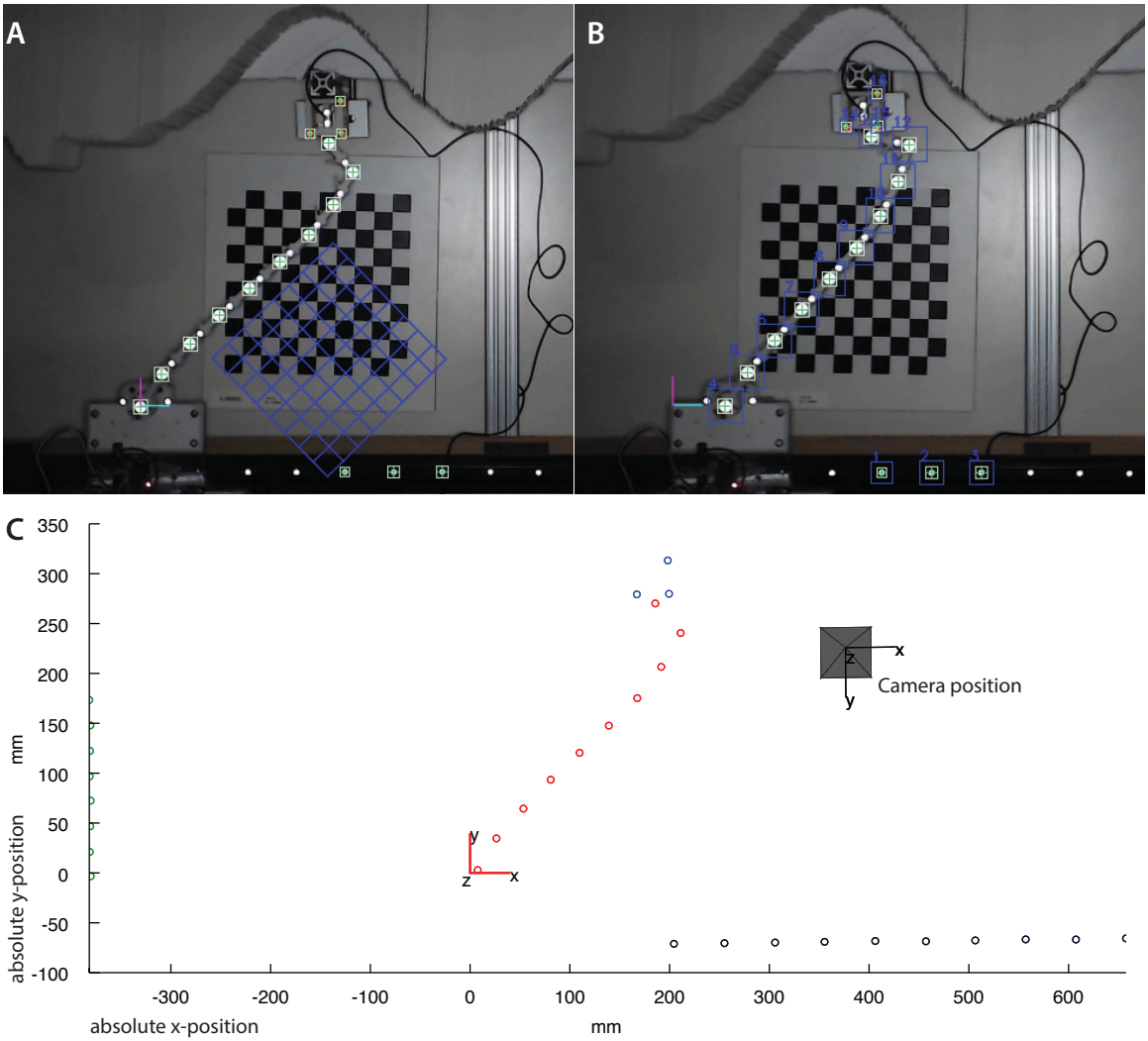

Figure 3.24: I used my optical tracking software to determine the ground truth position of the antenna model.**A**: Tracking software screenshot showing the antenna at its initial equilibrium configuration. The blue grid represented the plane where all the markers belong. **B**: Tracking software screenshot showing the tracked markers after the base moved towards the right. **C**: Positions of the markers back-projected from pixel space to 3D space.

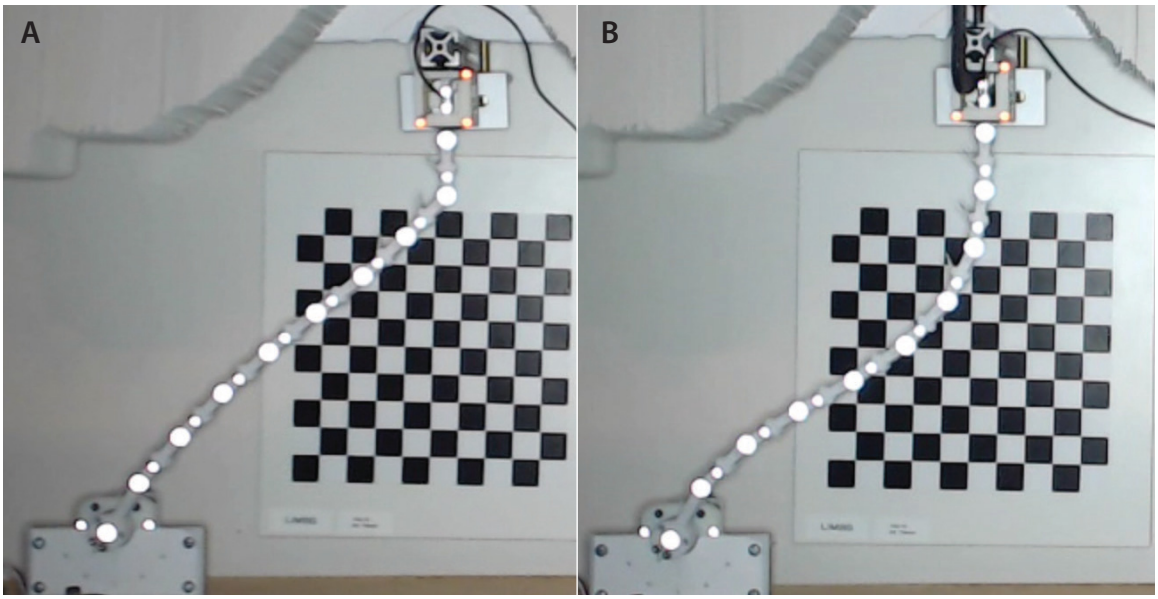

Figure 3.25: Reciprocal logarithmic decreasing stiffness profile vs constant stiffness profile antenna at transition phase.

3.3.2.2 Results

Here I present the simulation results of to the tip force experiments I described in physical antenna section.

3.3.2.3 Discussion

The introduction of anisotropic distally pointing collapsible hairs to the antenna broke the symmetry of the postural transition mechanics from forward to backward looking configuration in terms of friction forces. When the antenna had forward looking posture, the effective coefficient of friction between the antenna and the wall was high. In contrast when the antenna had a backward-looking posture, the coefficient

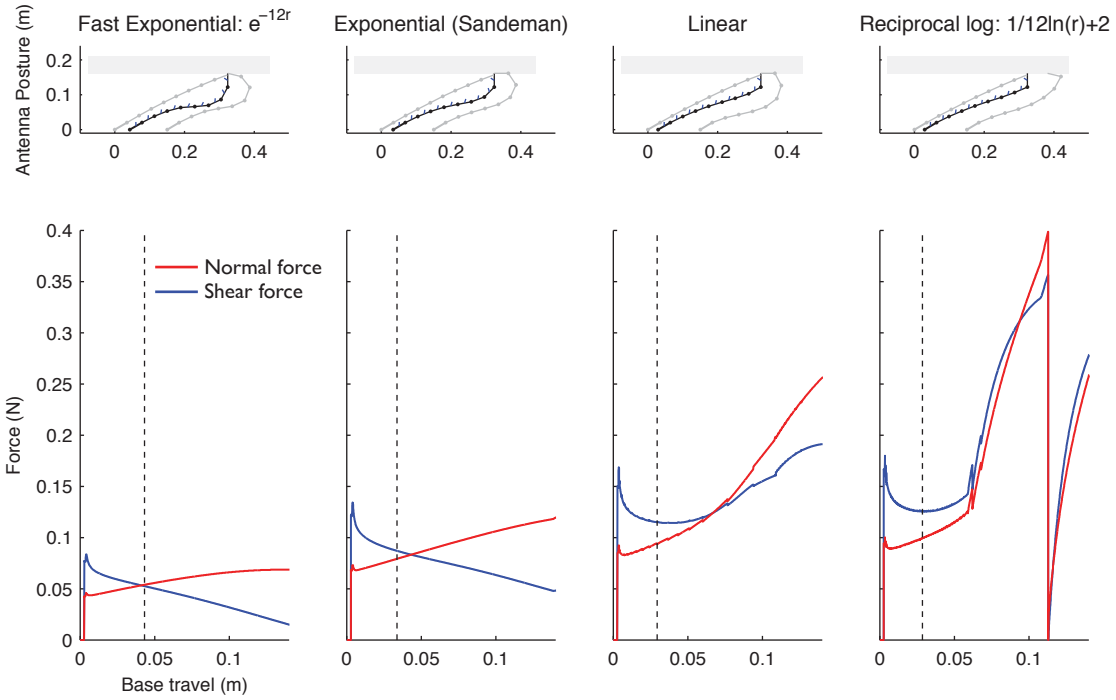

Figure 3.26: Postural transition forces of the antennae with different decreasing stiffness profiles. Maintaining wall contact during transition required low shear forces and high normal forces, which was best manifested in the fast exponential profile antenna. On the reciprocal log profile, high shear forces caused the tip to disengage from the wall before anchoring.

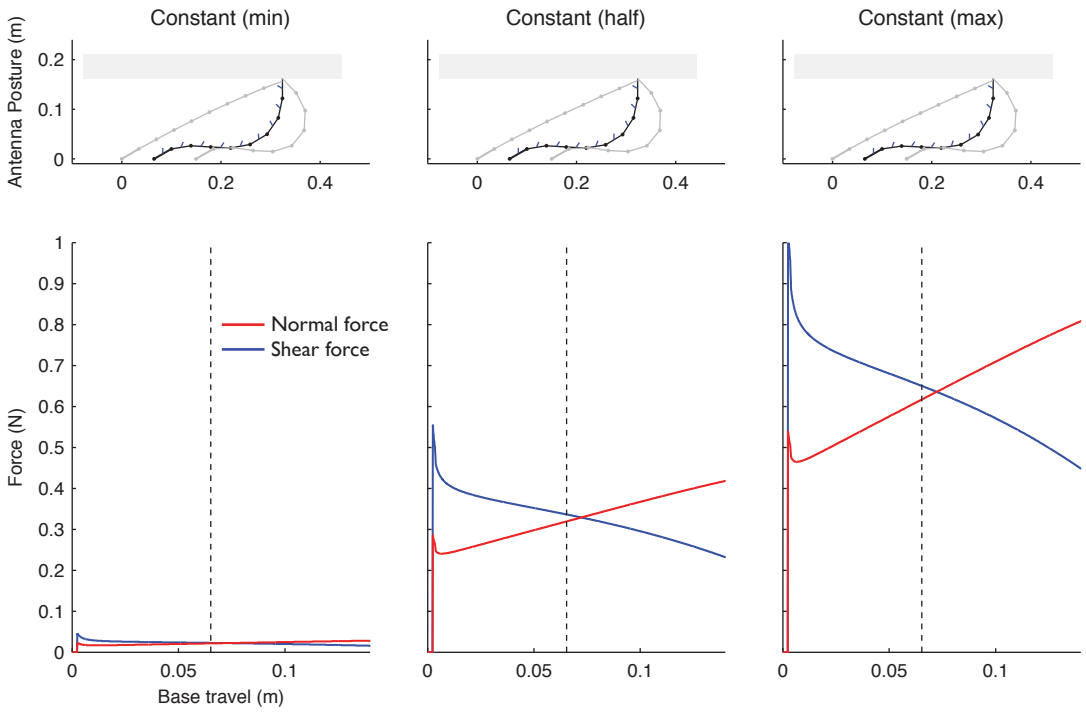

Figure 3.27: Postural transition forces on the constant profile antennae. I used the mimimum, average and maximum attainable intersegmental bending stiffnesses I could employ on the physical model. Surprisingly, the force profiles were similar to thos of the exponentially decreasing antennae.

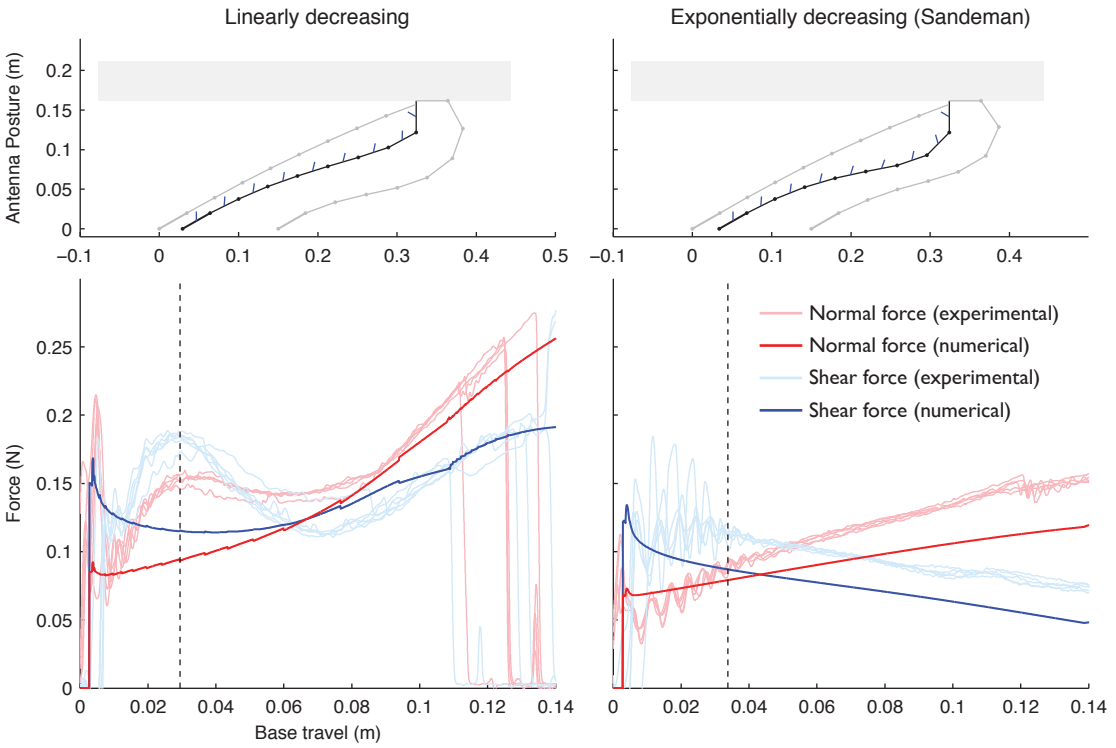

Figure 3.28: Postural transition for linearly versus exponentially decreasing stiffness profile antennae. The upper panels show simulated antenna configurations at the beginning of the trial, during flipping, and at the end. The dashed line marks the instance at which the tip segment was perpendicular to the motion.

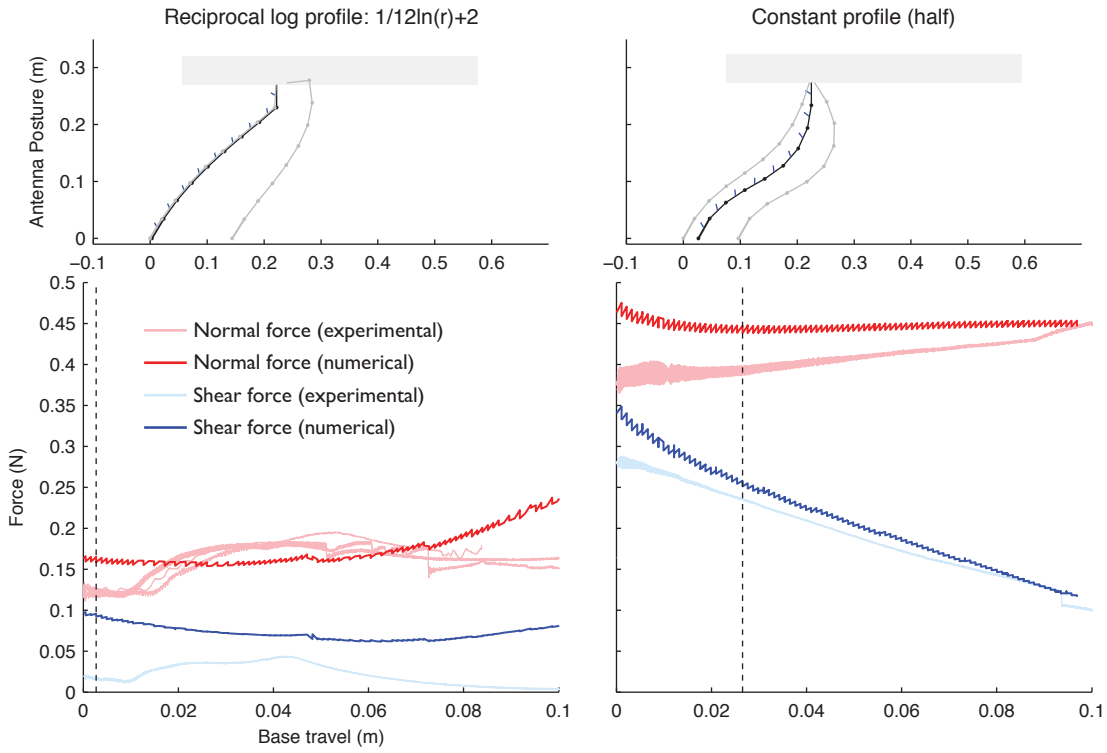

Figure 3.29: Reciprocal logarithmic decreasing stiffness profile vs constant stiffness profile antenna at tip forces comparison

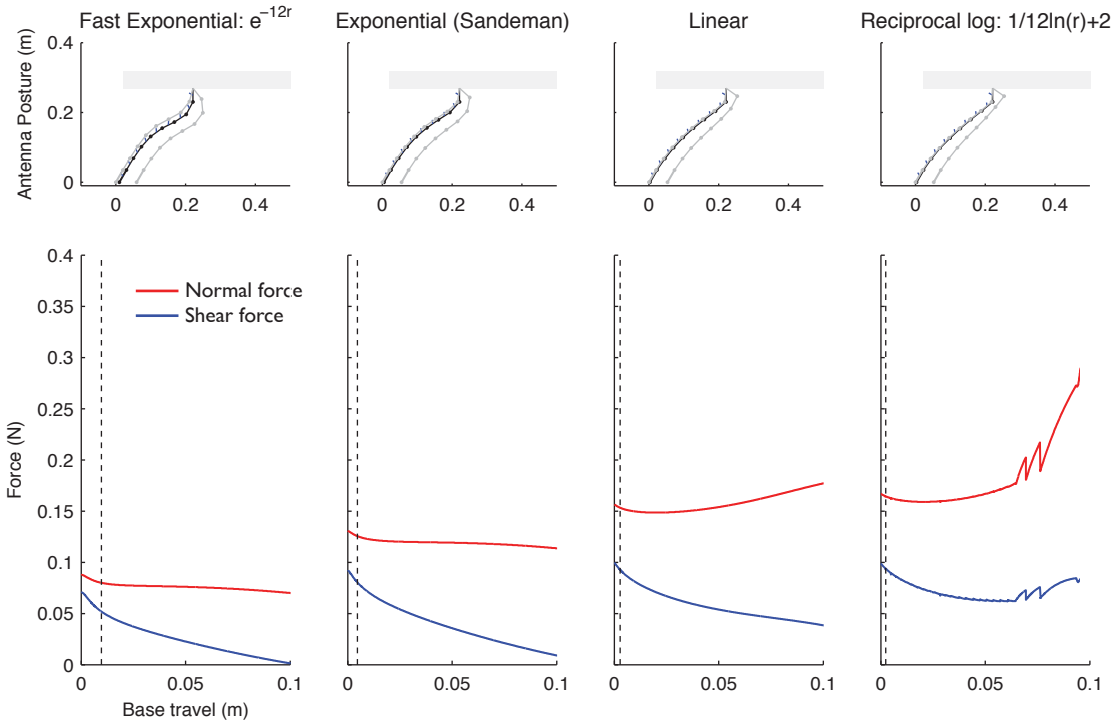

Figure 3.30: Postural transition forces of the antennae with different decreasing stiffness profiles with a 60° base angle.

of friction was low. These passive mechanics helped the the antenna stay in the backward looking configuration as long as the base had a net forward motion.

Earlier, I showed that distally pointing hairs were sufficient to facilitate the flipping of the antenna given a high enough wall roughness. In this section, I presented numerical simulations and physical experiments that quantified the friction forces necessary to hold the antenna tip in place and facilitate a postural transition. Since this friction force is dependent on the coefficient of static friction and the normal force, the only way to tune the friction force is either to change the roughness of contacting surfaces or the normal force. I found a clear dependence of the tip forces on the stiffness profile and base angle (Figs. 3.26, 3.30). The base angle is the easiest parameter to change during a wall-following task to achieve the desired tip forces but decreases the preview distance, as I show in the next chapter. Therefore, it's desirable to choose a stiffness profile that gives rise to generally high normal forces until the flipping is completed. As the final segment of the antenna pivots about the tip, the distally pointing hairs cease resisting the motion of the antenna, which in turn decreases the coefficient of friction. It is therefore imperative that the shear forces do not exceed the static friction force during flipping. Otherwise, the antenna tip slips and the whole antenna swings forward until it catches the wall surface again. Such losses of tip contact during failed transitions are an important source of instability during high-speed wall following, so higher normal forces *and* lower shear forces are necessary to facilitate robust postural transitions.

Linearly and reciprocally logarithmic decreasing stiffness profiles led to higher normal and shear forces and are therefore unsuitable for wall following (Fig. 3.26). Since the reciprocally logarithmic profile is representative of a family of profiles whose stiffness rates changes more aggressively near the tip compared to near the base, I conjecture that all profiles completely above the linear profile (Fig. 3.22) are not appropriate for wall following. On the contrary, profiles between the fast exponential and *Sandeman* [10] profile, as well as constant stiffness profiles, exhibited the desired trends for both the normal and shear forces. Furthermore, the fast exponential profile was the most appropriate for the 30° base angle, since the shear force was almost identical to the normal force at the instance of flipping.

As I mentioned earlier, the base angle also has a profound effect on the tip forces. In fact, the biologically relevant 30° base angle always led to higher shear forces than normal forces at the beginning of the transition process, which is prone to slippage (Fig. 3.26). In contrast, a 60° base angle always led to higher normal forces at the cost of lower preview distances (Fig. 3.30). To get the best of two worlds, I suggest a maneuver or basal actuation to increase the base angle until the postural transition is performed. Once the transition is complete, the base angle can be reduced to maximize the preview distance.

Chapter 4

High Speed Wall-following

In this section, I describe the effects of antenna stiffness profile on the perception of environment the associated wall following performance. Significant portions of section 4.1 of this chapter is published in [46] and [41] and reproduced verbatim. Similarly, section 4.2 of this chapter is published in [41] and [51].

When animals perform extremely rapid control tasks such as predatory escape, where the neuromechanical system is pushed near its operating limit due to neural conduction delays [54], sensorimotor control bandwidth constraints impose fundamental limits on the gains that can be achieved for stable closed-loop control [52] [55]. In such cases, animals require a well-tuned control system to compensate for the delays and locomotor dynamics. Thus, they rely on shared processing between the neu-

ral and mechanical systems [52] [56]. In some cases, biomechanical sensory structures themselves simplify downstream neural computations by performing mechanical computations on the incoming stimulus before sensory transduction. [49]. For example, during echolocation in bats, the mechanics of the pinnae and tragi act as a filter, enabling to bat to determine the elevation of prey [57]. In flies, the geometry and wiring of photoreceptors in the eye simplify optical flow computations [58], and in barn owls, asymmetries in the arrangement of the facial ruff play a crucial role in sound localization [59].

4.1 The Biological Antenna

In this section, I examine whether cockroaches benefit from their locomotion energy to control the state of their sensor when the neuromechanical system is pushed near its limit during escape. In particular, my collaborator and I investigated if the passive mechanical sensory hairs are adapted to their natural environment to simplify control by reconfiguring the sensor's state parameters according to the sensing strategy [60] (Fig. 4.1A).

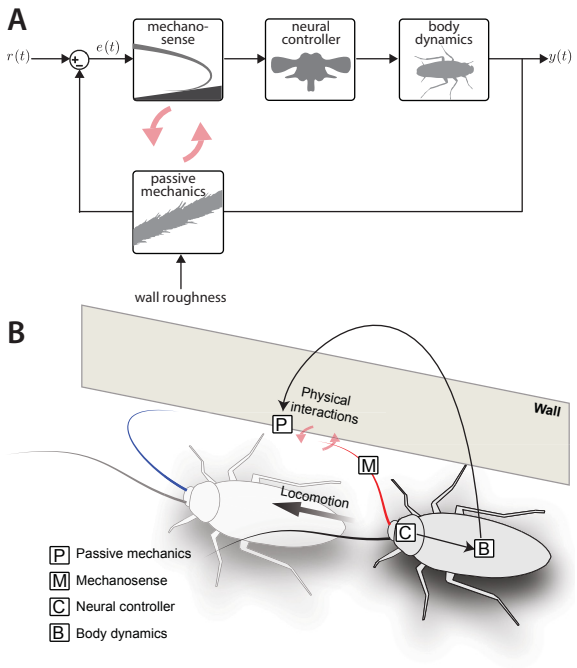

Figure 4.1: **A**: Wall-following task from a control-theoretic perspective. We modeled the behavior as a feedback system to drive the error between the animal's desired position and the actual position with respect to the wall to zero. The mechanosensing itself is affected by the physical interactions with the environment through passive mechanics and locomotion. **B**: We illustrate that the physical interactions between a locomoting organism and its environment lead to a reconfiguration of the mechanosensing antenna (from forward- to backward-projecting) via passive mechanics.

4.1.1 Background

During high-speed wall following, cockroaches use their antennae to sense obstacles such as walls and control their body by executing rapid turns [12]. While the natural habitat of *P. americana* is uncertain, these artificial walls represent extended obstacles that may be relevant to the natural ecological context of the genus *Periplaneta* in the form of caves and/or large rocks [61]. Its hypothesized cave-like native environment is likely one reason this species predominantly adopts present-day, human-made structures such as dwellings [42]. It has been hypothesized that to avoid collisions with extended obstacles such as walls, these animals control or track their relative distance to the wall, even at very high speeds [52]. For task-level control of this behavior, cockroaches predominantly use information from the flagellum, the long (up to 1.3 times body length), unactuated part of the antenna. Cockroaches can initiate a turn in response to a wall projection in less than 30 ms, leaving little time for processing by the nervous system [12]. This minute sensorimotor delay is within the range of rapid turns in other insects such as 90 deg turns in fruit flies (50 ms) [62] and dragonflies' turns in prey pursuit ($33 - 50$ ms) [63]. Moreover, it appears that cockroaches hold the angle of their antennae relative to their body midline relatively constant during high-speed wall following [12] [52], and thus whole-body motions dominate sensory movements. This contrasts low-speed exploration tasks in which local joint activity dominates sensory motion [39]. Distributed along cockroach flagella is a vast

array of mechanosensors that includes hair sensillae and campaniform sensillae. As I mentioned earlier, the antennal nerve relays information from over 270000 sensillae, forming a vast network of exteroceptive and interoceptive sensors [38] [64]. It has been shown that a proportional-derivative (PD) controller operating on a whole-body or template model is sufficient to reliably predict wall-following behavior [52]. Furthermore, this controller is sufficient for task-level control when integrated into a dynamically representative model of running [24].

4.1.2 Postural state vs Wall-following distance

Here, I show that the change in postural state affects control and performance. Specifically, the mechanical state of the antenna affected the body-to-wall distance, the proposed state variable for control.

4.1.2.1 Methods

We built a rectangular arena [52] (Fig. 4.2A). Within the rectangular arena ($85 \times 45 \times 15$ *cm* length×width×height), we placed acrylic (smooth) and wood (rough) blocks cut at angles of 30, 45 and 60 *deg* to induce turning in wall-following cockroaches. To capture the high-speed escape behavior, two high-speed video cameras (Kodak Ekta Pro 1000, Eastman Kodak Company, Rochester, NY, USA) were positioned

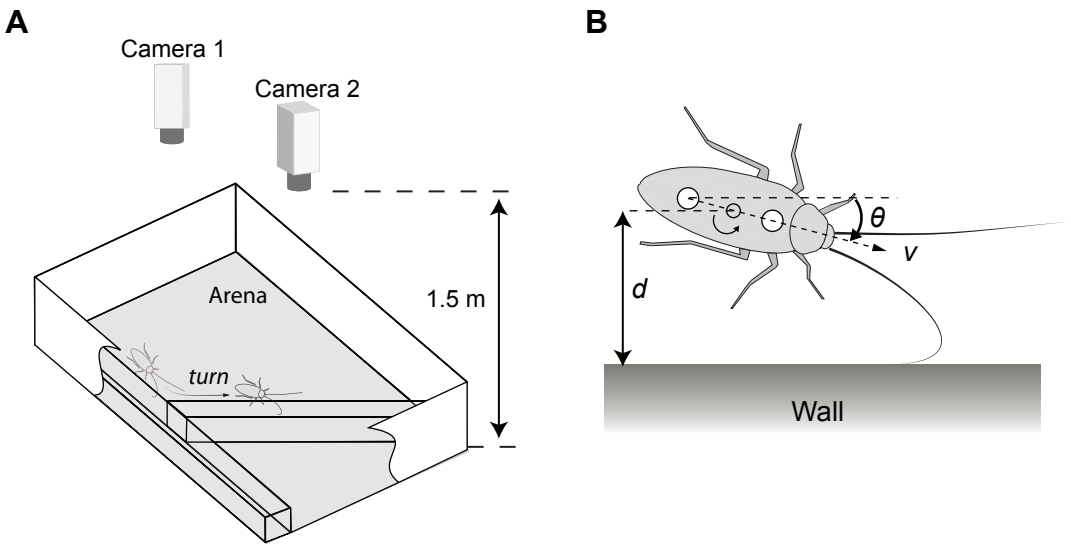

Figure 4.2: Experimental setup to study high-speed wall following. **A**: Arena with a turn perturbation for eliciting high-speed escape and wall following in *P. americana*. We recorded the time prior to and after a turn using two synchronized high-speed video cameras. (Image adapted from Cowan et al. [52]). **B**: Kinematic parameters evaluated for wall following. We digitized the two markers on the cockroach body (large white circles) to extract the point of rotation (POR; small circle with arrow) and body angle θ relative to the wall. v was the forward velocity of the animal; d was the distance between the body and the wall.

$1.5m$ above the area. Adjacent camera views overlapped to enable calibration and provide continuity of data for each trial sequence. Video sequences were synchronously captured at $500fps$ with an average resolution of 0.8 mm per pixel. To enhance contrast and tracking of cockroach body and legs, the running substrate was made from retroreflective sheets (3M, St Pauls, MN, USA), and we placed retroreflective markers on the cockroach body.

We used the camera calibration procedure described previously [52] for digitization. For each frame, we digitized the two markers on the cockroach body to extract the point of rotation (POR) and body angle (Fig. 4.2B). The procedure for determining the POR involves performing a least-square fit using the velocity and angular velocity for two consecutive frames assuming cockroaches run like an ideal no-slip planar unicycle [52]. Here, the POR metric estimates the body-to-wall distances of the cockroach. We filtered the position data using a zero-phase low-pass Butterworth filter with a cut-off frequency of $62.5Hz$, which was nearly three times the fastest turning rates described in cockroach wall-following [12]. We accepted all trials when the animals rapidly followed the wall and executed a turning response when contacting the angled wall, but excluded trials when animals tried to climb the wall or stopped. Trials were rejected when the distance of the POR to the wall exceeded 2.5 cm.

To determine the effect of the antenna state on body-to-wall distance, we ran a separate set of animals ($N = 12$ animals; body length 3.290.18 cm; ipsilateral antenna

length $3.96 \pm 0.37\ cm$) using the same track. We selected trials with clearly identifiable antenna positions (either projecting forward or backward) before the turn perturbation and computed the shortest distance between the POR and a vector from points on the wall using custom-written scripts (Matlab, The MathWorks Inc., Natick, MA, USA). We categorized the effect of body-to-wall distance on wall-following performance by manually tracking the videos of running cockroaches on a stride-to-stride basis. We determined the initiation of a stride by manually determining the onset of stance initiation of the hindleg contralateral to the wall perturbation. We rejected strides when (1) the antenna position could not be clearly determined to be either projecting forward or projecting backward for the entire stride (8% of all strides), (2) the antenna was not in contact with the wall for at least 80% of the stride (29% of all strides), or (3) the antenna flipped (either forward or backward; 17% of all strides). For each stride, we manually recorded leg contact by the tibia and femur joints (excluding contact of the tarsal segment) and body (head, thorax and/or abdomen) contact with the wall.

4.1.2.2 Results

Animals ran with a mean speed of $46.2 {}^{cm}/_{s}$ (37.7 to $53.1 {}^{cm}/_{s}$). We analyzed 80 trials after a turn perturbation and divided the data into two groups based on the position or state of the antenna, and we measured the body-to-wall distance, the putative

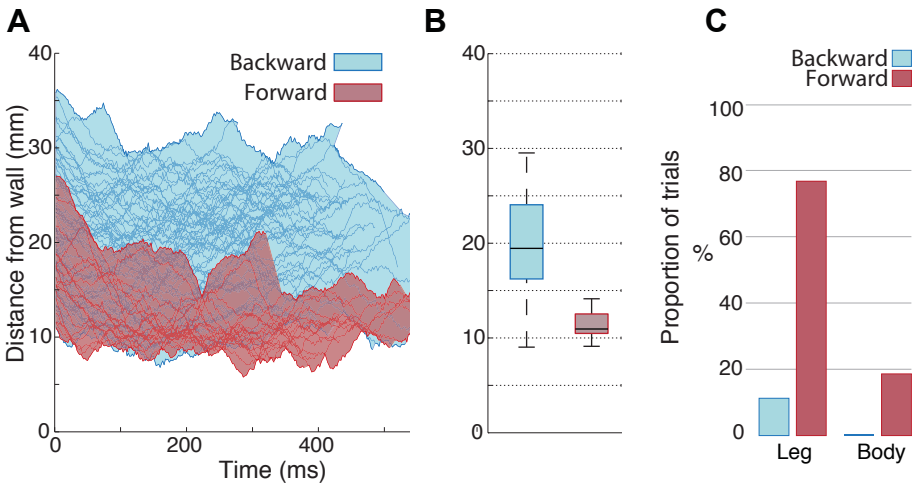

Figure 4.3: Locomotor performance as a function of antenna mechanical state. **A**: Body-to-wall distance of cockroaches wall following for antennae projecting backward or forward as a function of time following a turn perturbation. The shaded blue and red regions show the full range of body-to-wall distances while individual lines represent single trials. Animals running with an antenna projecting forward following a turn ran significantly closer to the wall than those running with an antenna projecting backward. **B**: The box plot summarizes body-to-wall distances shown in A for backward and forward groups ($*P < 0.001$). **C**: Proportion of trials where the leg and/or body contacted the wall for strides with forward- and backward-projecting antennae. Overall, the antenna state had a statistically significant association with the frequency of leg and body contacts ($P < 0.001$).

control variable for wall following [52], for both groups. Animals with an antenna projecting forward following a turn perturbation ran significantly closer to the wall (12.0 ± 1.72 mm, $N = 18$ trials; t-test $P < 0.001$) than those running with an antenna projecting backward ($19.9 \pm 4.86mm$, $N = 62$ trials) after including the effect of individuals (random factor) and running speed (covariate) using a mixed-effect model (F-test, $P < 0.001$; Fig. 4.3A,B). This change in body-to-wall distance corresponded to approximately the body width of *P. americana*. We found that the variance between the two groups was significantly different (F-test for equivariance, $P = 0.002$). As running speed has been shown to be correlated with body-to-wall distance [12], we tested for the effect of speed. We found no significant difference in running speed (backward $44.8 \pm 8.22^{cm}/_{s}$, forward $41.0 \pm 7.35^{cm}/_{s}$) between the two groups (t-test, $P = 0.728$), even after correcting for the possible effect of individuals (F-test, $P = 0.792$).

4.1.2.3 Discussion

Our previous control model of antenna-mediated wall following predicted that control is more challenging as the velocity increases and simpler with a greater preview distance (i.e. a longer antenna) [52]. We hypothesized that a forward state would give the cockroach a greater preview distance by geometry alone, i.e. that wall following control would be easier according to the model developed by Cowan and colleagues [52].

By comparing body-to-wall distance, a putative state variable for control of wall following hypothesized by Cowan and colleagues [52], we showed that animals running at similar speeds with an antenna projecting forward ran closer to the wall on average compared to those running with an antenna projecting backward (Fig. 4.3A,B). This change in body-to-wall distance corresponds to approximately a whole body width of *P. americana*. Interestingly, the body-to-wall distance for cockroaches running in the bent-forward antenna state was similar to that measured for cockroaches running with an ablated antennae ipsilateral to the wall [12], which suggests that the mechanical state potentially affects the encoding of information and the strategy that the animals are employing.

4.1.3 Postural Transitions vs Wall-following

The cockroach's distance to the wall during wall-following postural has implications for performance and control strategy. Since we have established that postural transitions affected the wall distance, we hypothesized that a dynamic change in the state of the sensor would result in changes in wall-following control, which is also evidenced by a change in body angle. We investigated how the postural transitions (a flip when the antenna moved from a backward to a forward position) affected the general success of wall-following. We used the number of wall collisions and the wall-following velocity as performance metrics.

4.1.3.1 Methods

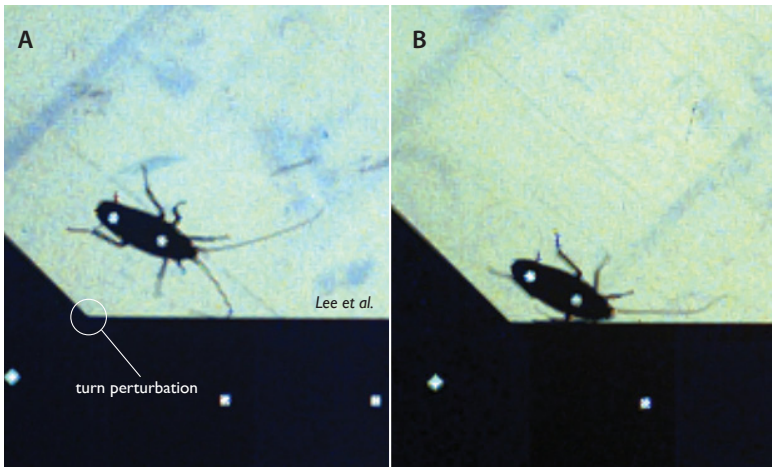

Figure 4.4: The postural state of the antenna affects wall-following performance. **A**: A successful evasion maneuver of the cockroach with the backward projecting antenna. **B**: A body/leg collision with the wall is more likely to happen with a forward-projecting antenna.

To test the effect of antenna flips on wall-following control, we ran male cockroaches on rough (wood) surfaces ($N = 11$ cockroaches, body length 3.70 ± 0.17 cm, mass $0.77 \pm 0.11g$, ipsilateral antenna length $4.36 \pm 0.41cm$). We quantified the effects of backward-to-forward antenna flips on wall-following control by manually identifying flips within our dataset after cockroaches encountered the turn perturbation. We recorded the frame at the onset of the flip for each instance. We rejected all events when the antenna flip was initiated by the cockroach turning; that is, when the body angle was greater than or equal to ± 15 deg from the wall within the stride when the flip occurred. ($5\%, {}^{1}/_{19}$ of flips). We estimated the stride time (≈ 80 ms) by taking the reciprocal of the median stride frequency ($11.9^{\text{strides}}/_{s}$). For each flip, we normalized the body angle of the animals by their respective averages ≈ 1 stride prior

to the flip (80 ms). Body angles were computed by taking the arctangent between the vector formed by the two dots on the animal's body and the reference wall vector (Fig. 4.2B). We analyzed the normalized body angles ≈ 3 strides (240 ms, one stride ≈ 80 ms) after the onset of the flip. To determine any significant effect of these flip events on wall-following control, we compared the kinematic variables with control sequences with no antenna flips by randomly selecting trials 240 ms after turning (average timing of flip occurrences after turn) within a 100 ms window downstream of the turn. The same body angle normalization procedure was applied to the control dataset. To determine statistical significance between the two groups, we applied a statistical mixed-effect model of the form $|\text{angle}| = time + animal + group + (animal \times time) + (group \times time)$ where angle was the angle measurement at each time point (2 ms interval), animal was a random factor and group was a fixed effect (flip versus control). To determine whether the statistical result was sensitive to the possible effect of a small sample size and a non-normal distribution, we calculated 95% confidence intervals on bootstrapped means for both groups using 1000 replications. We compared bootstrapped means from an original sample of 18 flip events and 30 control events.

4.1.3.2 Results

To determine possible effects of body-to-wall distance on running performance, we tracked individual strides of wall-following cockroaches running alongside rough and smooth walls using the same dataset to measure body-to-wall distances presented earlier. We accepted a total of 129 strides with the ipsilateral antenna projecting forward and 231 strides with the antenna projecting backward. When comparing wall-following performance for cockroaches before and after a turn perturbation, we found that animals running with an antenna projecting forward had a significant increase in frequency of leg (tibia and/or femur) and body contact with the adjacent wall (Fig. 4.3C and Fig. 4.4). The state of the antenna had a statistically significant association with leg contacts and body contacts (Pearson χ^2-test, $P < 0.001$ for both leg and body contacts). This association remained significant even after correcting for the possible effect of individuals (Cochran-Mantel-Haenszel test, $P < 0.001$ for both leg and body contacts). For strides where the body contacted the wall (35 strides total), these collisions often led to a decrease in speed, likely due to the impact. We found the median change in velocity to be $?7.48 \pm 6.84 {}^{cm}/_{s}$ when comparing approximately two strides before and after contact. We estimated the stride time (70.0 ms) by taking the reciprocal of the median stride frequency for all trials ($14.3 {}^{\text{strides}}/_{s}$). Thus, animals slowed down after body contact on average. This change in speed following body contact is consistent with previous observations [65].

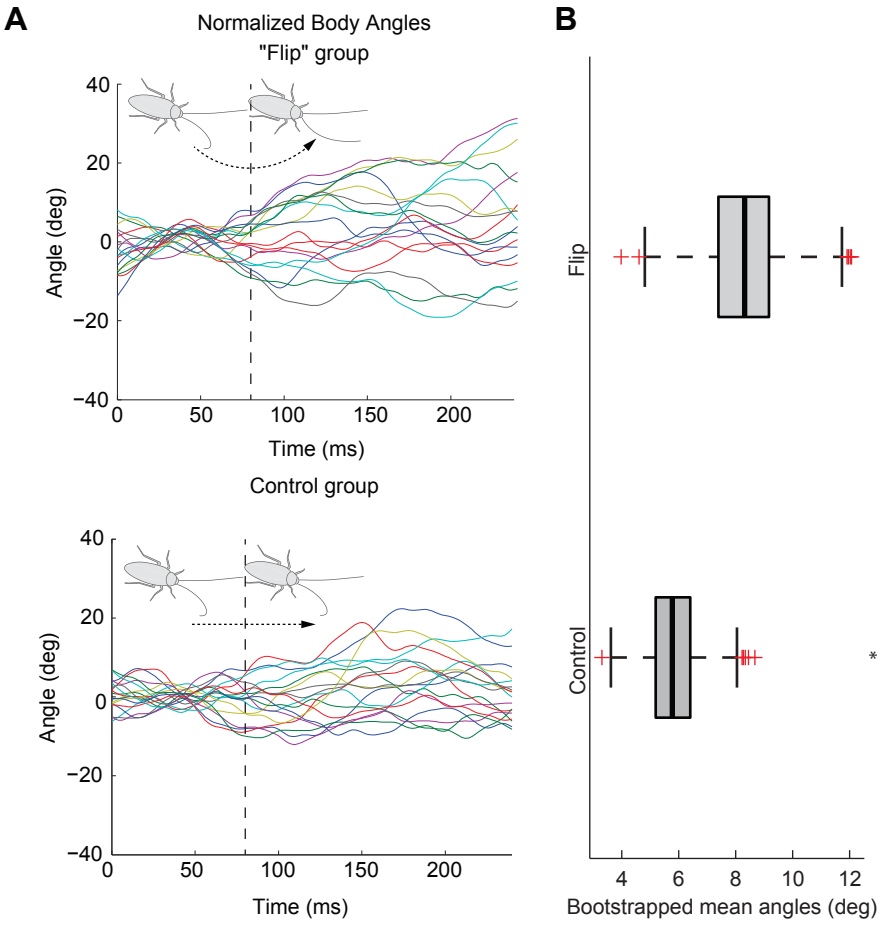

Figure 4.5: **A**: (top) Body angles for animals running while the antenna flipped from forward to backward projecting. Individual lines represent single trials. The vertical dashed line represents the onset of the antenna flip. (Bottom) Body angles for the non-flip control group. Individual lines were randomly selected trials where the antenna remained backward. The vertical dashed line represents randomly selected time events. Positive angles indicate the cockroach was turning away from the wall and negative angles indicate the cockroach was turning toward the wall. **B**: The box plot summarizes the bootstrapped body angles (absolute value) following a flip and for non-flip controls. Angles were statistically significant when comparing 95% confidence intervals ($*P < 0.05$). For the box plot, the central line is the median, the bottom and top edges of the box are the 25^{th} and 75^{th} percentiles and the whiskers extend to ± 2.7 s.d. Red crosses represent outliers lying outside whiskers.

Animals ran at a mean speed of $46.2 \pm 8.4^{cm}/_{s}$, ranging from 34.8 to $62.5^{cm}/_{s}$. We averaged body angles for approximately three strides following a flip or no-flip control (Fig. 4.5A). We estimated the stride time (80.0 ms) by taking the reciprocal of the median stride frequency ($11.9^{\text{strides}}/_{s}$). Here, our control was defined as any randomly chosen time point in our wall-following dataset after a turn perturbation that was not flagged as a flip. Body angles greater than or equal to 15 deg suggest that a cockroach initiated a body turn [12]. We found that flips occurred infrequently (18 strides with flips out of 676 strides). Using the mixed-effect model described in methods, we found that flips had a significant effect on body angle. Specifically, we found that the term group (intercept) and group×time (slope) were both statistically significant in our model (F-test, $P < 0.001$). This result remained significant after testing for a possible non-normal distribution of angles using a logarithmic transformation (F-test, $P < 0.001$). When comparing bootstrapped 95% confidence intervals of the normalized mean angles (absolute value) for both groups, we found no overlap [flip= $(6.91 - 9.69\ deg)$; control=$(4.91 - 6.67\ deg)$; Fig. 4.5B]. Applying the same test on angles without taking the absolute value did not change the statistical outcome.

4.1.3.3 Discussion

We determined that dynamic changes in the state of the antenna were correlated with changes in wall-following tracking behavior, specifically the initiation of body turns.

Changes in mean body angle following a flip were statistically significant between the flip and control data (Fig. 4.5A,B). To determine whether this change in tracking strategy had important consequences for wall-following performance, we tracked the frequency of leg and body contact for both cases. Our results showed a significant difference in the proportion of leg and body contact associated with the antenna state (Fig. 4.3). We observed that both leg and body contact, but especially body contact, were linked with body-to-wall collisions, often leading to a decrease in speed due to body redirection. We found the median change in velocity to be ?7.48$^{cm}/_{s}$ when comparing approximately two strides before and after contact. Our observations and measurement on wall collisions were in agreement with published observations [65]. Baba and colleagues noted that cockroaches that ran sufficiently close to the wall "touched it with their body and this sometimes cause[d] them to fall" [65].

In summary, for animals running with their antenna projecting forward, we observed marked changes in behavioral strategy including increased leg and body contact and wall collision leading to significant decreases in speed. Our results raise the possibility that increased leg contact could allow a cockroach to sense the wall with its legs, thus relying on different sensory modalities (e.g. tarsus or leg hair contact) for thigmotaxis, as suggested previously [12]. Relying on leg and body contact for sensing comes with a cost: the increased probability of body decelerations from collisions presents clear consequences in the context of high-speed predator evasion.

4.1.4 Decreasing Stiffness Profile on Wall-following

Next, I evaluate lumped mechanical properties of the cockroach antenna and provide evidence that the cockroach's particular flagellar stiffness profile may simplify control during high-speed tactile navigation tasks by increasing preview distance and providing a one-dimensional map between antenna bending and body-to-wall distance.

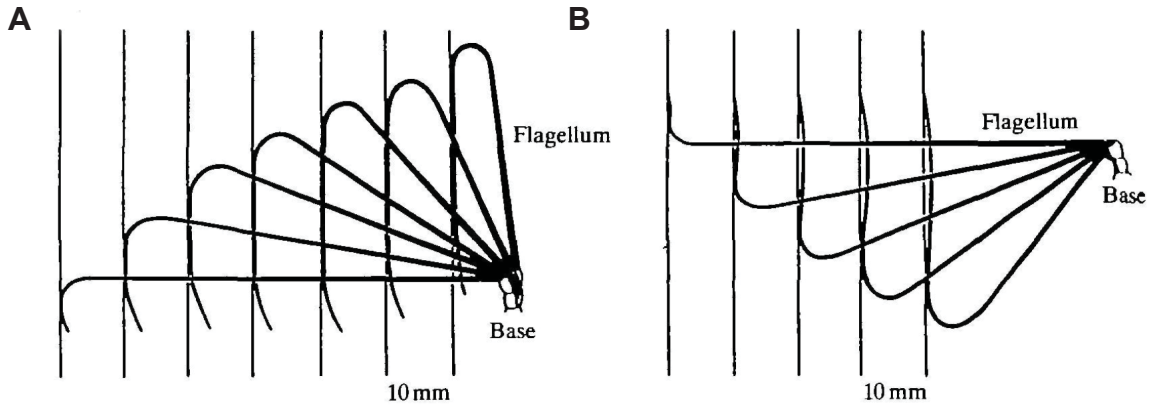

Figure 4.6: Lateral (**A**) and medial (**B**) bending of the antenna due to a contact with a flat wall (Image credit: [10]).

4.1.4.1 Background

Antennal bending properties include how the point of bend (relative to the base of the antenna) and/or the contact point shift as the antenna bends and have been previously linked directly to body-to-wall distance discrimination during high-speed wall following [12]. As cockroaches [12] and crayfish [66] [10] move closer to an object, the straight portion of their antenna (from base of antenna to bend) shortens as the

bend "moves" towards the base (Fig. 4.6). Camhi and Johnson [12] proposed that the point of bend or the contact point could constitute a one-dimensional map along the length of the antenna to provide a cue to induce a change in body angle, a form of mechanical processing. We hypothesized that the flexural stiffness (EI) of the antennal flagellum enables effective morphological processing.

4.1.4.2 Methods

The animal is sedated with CO2 for $\approx 5min$ after which we cut the antenna at the head-scape joint and weighed the flagellum to the nearest $0.1mg$. The first few segments of the flagellum were glued to a microscope glass slide using epoxy to mount it as flat as possible and minimize hemolymph loss. The slide was rigidly mounted on a single axis micro-positioning stage and placed under a microscope with back-lighting to maximize contrast of the flagellum against the background. The flagellum was then photographed in overlapping segments of approximately 15 annuli with a high-definition camera (Canon Vixia HF S20, Tokyo, Japan; 3264×2456 pixels) mounted on an optical microscope. Starting at the first flagellum segment, images were taken along the length of the antenna with care taken to ensure overlapping features across images. Frames were calibrated with an objective micrometer with a resolution of 0.010 mm. Single images ranged from 428 to $460^{\text{pixels}}/_{mm}$ in spatial resolution and were used to manually reconstruct an entire high-resolution image of

the flagellum (Adobe Photoshop CS3, Adobe Systems Inc., San Jose, CA, USA). We measured geometrical properties of the flagellum based on a 2D reconstruction using custom-written scripts in MATLAB (The MathWorks Inc., Natick, MA, USA). We first subtracted the background from the composite image and converted it to binary. Detecting the contour and finding the median point along its length gave us the approximate central axis of the flagellum irrespective of its inherent curvature. We applied a spatial moving average filter spanning 400 pixels ($\approx 2mm$) to reduce noise associated with annuli intersections.

We estimated the second moment of area I of the flagellum by assuming a circular cross section, thus:

$$I = \frac{\pi r^4}{4} \tag{4.1.4.1}$$

where r was the radius along the length of the flagellum directly measured from high-resolution images. The assumption of a circular cross-section is strongly supported by the morphological studies of Kapitskii [67]. While the flagellum is a hollow structure with an inner radius (epithelium) and outer radius (cuticle), this relationship gave us an upper bound on I. Because both the thickness of the epithelium and cuticle co-vary with the radius of the antenna, our estimates are a good approximation of the upper bound [67].

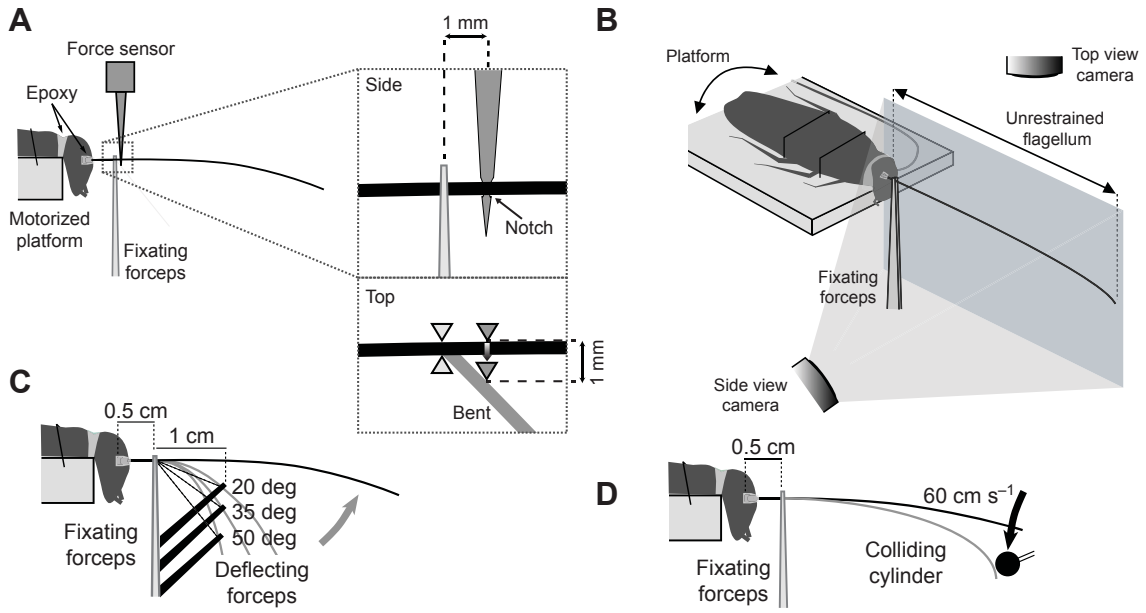

Figure 4.7: Setup for static bending and dynamic response measurements of the flagellum. **A** Apparatus for determining the variation in flexural stiffness of the antenna. The flagellum was held near the base with a pair of fine forceps. A force sensor 1 *mm* away from the fixation site mounted on a motorized stage deflected the flagellum laterally (away from the midline) by 1 *mm* while measuring the resistance-to-bending force. A small notch at the base of the arm of the force sensor prevented out-of-plane motion. This procedure was repeated for different points along the flagellum by moving the platform in steps of 2 *mm* towards the tip. We immobilized the head, scape, and pedicel with epoxy and imposed lateral and medial deflections. **B** Apparatus for determining the dynamic response of the flagellum. The flagellum was fixated 0.5 *cm* away from the base with a pair of fine forceps. The head and basal segments were immobilized with silicone (green). Two high-speed cameras recorded horizontal and vertical motions during recovery from either **C** a step deflection or **D** an impulse-like collision. For the step deflection, a second pair of forceps was used to deflect the flagellum to different initial angles (20, 30 and 50 *deg*). Animals were mounted on a rotatable platform to measure the tip response in the lateral, medial, dorsal and ventral planes. In the case of the collision response, a small cylinder hit the flagellum dorsally at $\approx 60^{cm}/_{s}$ near the tip to simulate obstacle contact during high-speed running. Antenna not drawn to scale.

We built an apparatus to characterize flexural stiffness along the length of the flagellum (Fig. 4.7A). Cockroaches were cold-anesthetized for $30min$ and weighed. We then fixed neck-lesioned cockroaches onto the edge of a platform using epoxy glue so that the flagellum projected outside the platform surface, unobstructed. This procedure left the antenna auxiliary hearts intact. We fixed the head, scape, and pedicel joints with epoxy to prevent movement of the antenna during an experiment. The platform was mounted rigidly to a linear micro-translation stage operating in closed loop with a minimum step size of 50 nm (M112.1DG, Physik Instrumente, Palmbach, Germany).

We measured the resistance-to-bending forces generated by the antenna flagellum at different positions along its length, similar to the method employed by Sandeman [10] to characterize the mechanical properties of crayfish antennae (Fig. 4.7A). First, we clamped the antenna using fine forceps while a digital microscope camera (Dino-Lite Premier AD4113TL, AnMo Electronics Corporation, Taipei, Taiwan) while we visually confirmed that the flagellum was held rigidly. We carefully brought a rigid arm attached to a force sensor (Series 300, Aurora Scientific Inc., Ontario, Canada) in contact with the antenna using the micron-resolution stage. The arm was brought in contact whith the antenna while the measured force remained at baseline. For all experiments, the arm was carefully positioned 1 mm distally from the fixation point of the antenna (Fig. 4.7A). The first, proximal fixation point was taken five segments distal from the pedicelflagellum joint. The force lever was driven perpendicularly

into the antenna with a fixed displacement of 1 mm and speed of $2^{mm}/_{s}$ using a linear translation stage with submicron resolution, while forces were sampled at $1000Hz$. To minimize out-of-plane motion, the antenna was positioned within a small groove etched at the base of the arm (Fig. 4.7A). The 1 mm displacement imposed large angle (45 deg) deflections of the antenna, similar to what an antenna may experience when contacting an object when running. This position was held for $15s$ before the lever was returned to its original position. We measured the resistance-to-bending force in steps of 2 mm, which required releasing the antenna and clamping at a new position $2mm$ distally from the previous measurement point. We repeated this procedure until measured forces were lower than the 0.3 mN resolution of the force lever, which covered over one-third of the length of the flagellum from the base. We recorded forces for both the lateral and medial planes, with three trials for each position. Only antennae with more than five measurements along the length were included in the final analysis. Raw forces obtained from the static bending experiment were smoothed by convolving a moving average window of 200 ms with the response. For analysis, we recorded the peak force prior to relaxation of the viscoelastic-like response; this corresponds to the time when the force lever reaches its final displacement of 1 mm (Fig. 4.8A).

To estimate the order of magnitude and variation of E along the antenna, we modeled our static bending experimental conditions using cantilever beam theory. Since we imposed deflections of ≈ 45 deg in our experiment, we used a 2D Euler-Bernoulli beam

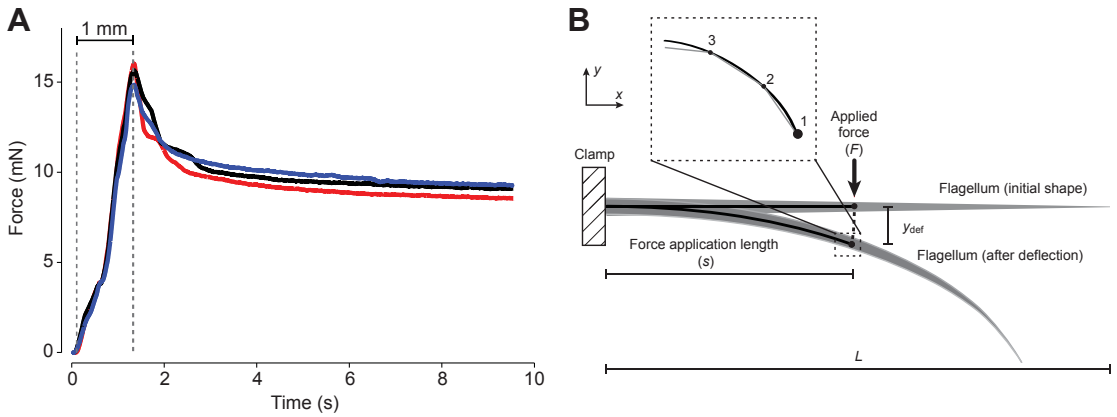

Figure 4.8: Example of force time course for static bending experiment. Responses exhibit a viscoelastic-like response. Different colored lines represent three different trials at a position of 8 mm away from the base for a fixed lateral displacement of 1 mm applied medially. Gray vertical dashed lines represent the onset and final position of the force lever, thus peak forces represented the time at which the stage reaches 1 mm. **B**: Responses were filtered with a moving average filter with a window width of 200 ms. Diagram of 2D Euler-Bernoulli beam model. The flagellum of length L was modeled as a conical cantilever beam under the action of a point force F at distance s from the clamp, with the prescribed deflection y_{def}. The flagellum was discretized into a series of rigid links with nodes labeled in the inset. The nodes were evenly spaced along the antenna model with a total of 1001 points. Antenna not drawn to scale.

$$\kappa(x) = \frac{\left|\frac{\mathrm{d}^2 y}{\mathrm{d}x^2}\right|}{\left[1 + \left(\frac{\mathrm{d}y}{\mathrm{d}x}\right)^2\right]^{3/2}} = \frac{M(x)}{E(x)I(x)} \tag{4.1.4.2}$$

Figure 4.9: Cantilever beam model equation, where $\kappa(x)$ is the curvature, y and x were the 2D position of the antenna, $M(x)$ was the moment along the antenna, $E(x)$ was the elastic modulus and $I(x)$ was the second moment of area [68]

model to test our hypothesis that E did not significantly vary along the antenna. We made estimates of E by numerical integration, which required approximating: We adapted the numerical simulation method of Quist and Hartmann [69] to relate the flagellum deflection to the measured force. The model is quasi-static and assumes that the material of the flagellum remains within the elastic limit and that the antenna is inextensible such that the arc length after deflection is equal to the initial length of the flagellum. For the purpose of this simulation, the cockroach flagellum is modeled as a 2D continuously tapering cantilever beam with a circular cross-section [67] under the action of a point force acting perpendicular to the contact at a distance s measured along the length L of the flagellum from the clamp position. The simulation computes local curvature of the flagellum at the location of the applied force and then successively calculates changes in the local curvature back to the base of the cantilever (or the clamp position). As a first step, the flagellum was discretized into a series of rigid links connected by elastic torsional springs (Fig. 4.8B). At a given node i, the curvature, κ_i, is related to the applied moment M_i, by the equation:

$$\kappa_i = \frac{M_i}{E_i I_i} \tag{4.1.4.3}$$

where E_i is the elastic modulus and I_i is the second moment of area of node i using the experimentally determined relationship between radius and flagellum length. Using the computed curvature information at each node, the algorithm iterates until the final flagellar shape can be computed passing through the experimentally defined deflection ($y_{def} = 1\ mm$) at the point of force application ($s = 1\ mm$). We assume that the elastic modulus within each experimental condition $[F_i(s), y_{def}(s)]$ does not change along the length such that $E_i = E(s)$ is constant for each simulated condition and $E(s)$ is left as a free parameter to be optimized for obtaining the unique flagellar shape with the least deviation from the desired point $[y_{def}(s)]$. The effect of the continuously changing clamp positions in the experiments is replicated in simulation by using an equivalent flagellum truncated at the clamp position.

4.1.4.3 Results

We measured the radius of the antenna and approximated the second moment of area, a determinant of flexural stiffness that predicted the resistance to bending of the antenna along its length. From $N = 10$ animals (body mass$= 0.81 \pm 0.12g$; mean $\pm$ s.d. unless otherwise specified; six right antennae, four left antennae), we computed

a mean flagellum length of $47.16 \pm 3.97\ mm$ and a mass of $0.0023 \pm 0.0001 g$. The length of segments remained constant until approximately the 30^{th} annulus from the base ($\approx 20\%$ flagellum length), after which there was a marked increase in annulus length up to the 80^{th} annulus ($\approx 60\%$ flagellum length) followed by a plateau (Fig. 4.10A). This sigmoidal increase in annulus length was consistent with a previous study by Kapitskii [67]. The number of segments ranged between 134 and 152 with a median of 146. When averaged across individual animals, the flagella had a base radius of $0.22 \pm 0.01\ mm$, whereas the tip was over four times finer with a radius of 0.05 ± 0.01 mm. In contrast to a perfect cone, the radius decreased exponentially towards the tip (Fig. 4.10B). An exponential model ($\alpha e^{\beta x}$; $\alpha = 0.95$, $\beta = -0.012$, where α and β are free parameters) captured 94.7% of the variance in normalized radii across individuals [range $95 - 97\%$ per individual; root mean square error (RMSE)$= 0.044$; $N = 10$]. In contrast, a linear model captured less of the variance (91.9%; range $92 - 96\%$ per individual; RMSE$= 0.054$; $N = 10$), with larger residuals particularly near the base and tip of the antenna. We thus approximated the radius of the antenna along its length with an exponential model rather than a linear model. The observed non-linear change in radius is consistent with previous morphometric measurements of the antenna of *P. americana* by Kapitskii [67]. From our measurements of the radii, we estimated an upper bound of the second moment of area using Eqn 4.1.4.3. Since the second moment of area at the tip ($9.48 \times 10^{-18} m^4$) was three orders of magnitude lower than at the base ($2.06 \times 10^{-15} m^4$), we surmise that the flexural stiffness EI

is determined primarily by geometry. The decreasing flexural stiffness profile of the antenna was consistent with other measurements in tapered arthropod antennae, including the crayfish Cherax destructor [10] and Procambarus spiculifer [70].

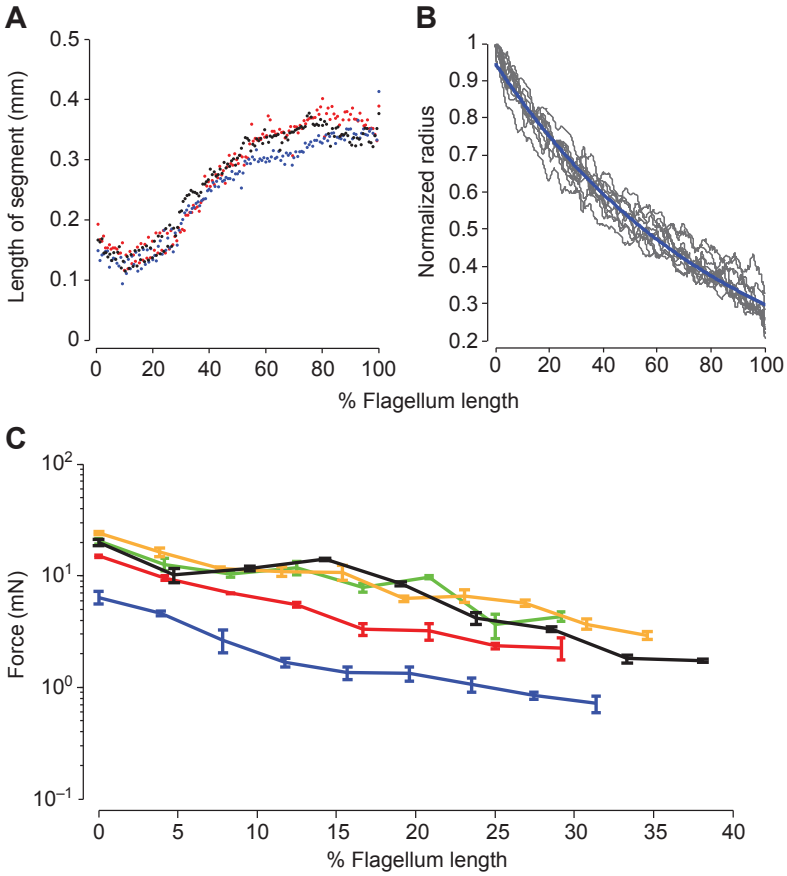

Figure 4.10: **A**: Length of segments (annuli) measured. The length of segments increased from base to tip, with a transition near 20% of the flagellum length. For clarity, three flagella out of ten are shown using different colors. **B**: Variation in normalized radius along the length for 10 animals. The radius decreased exponentially from base to tip. Using a logarithmic model (blue line), all slopes are significantly different from 0 with $\alpha = 0.01$.**C**: Log of resistance-to-bending force versus distance from base for five flagella bent 1 mm laterally. The force exponentially decreased from base to tip. Using a logarithmic model, all slopes were significantly different from 0 with $\alpha = 0.01$.

As predicted from our approximation of the second moment of area estimated from our measurements of the radius of the flagellum, the bending resistance of the antenna was greater at the base than at more distal positions (Fig. 4.10C). We found an exponential decrease in resistance-to-bending force as a function of distance from the base. We found that all slopes were significantly different from 0 (t-test, $P < 0.01$ for all animals) after applying a logarithmic transformation. We found no statistically significant effect of plane (lateral versus medial) on the resistance-to-bending forces after including the continuous covariate distance and random factor animal using a logarithmic transformation of force (mixed effect model: $F = 0.04$, $d.f. = 1$, $P = 0.847$). Solving for EI using a 2D Euler-Bernoulli model given in equation (eq:timoshenko) yielded a mean of $5.78 \times 10^{?9} \pm 4.73 \times 10^{-9} Nm^2$ (median= 4.31×10^{-9}; 25% quartile= 2.00×10^{-9}; 75% quartile= 8.34×10^{-9}) over the measured length. This estimate is the same order of magnitude as the flexural stiffness reported for the house cricket *Acheta domesticus* — an insect with a flagellar morphology similar to *P. americana* (mean EI of $10 \times 10^{-9} Nm^2$ for dorsal and ventral directions at 5 mm from the base) [71]—. To determine whether the resistance-to- bending measurements could be explained by geometry alone, i.e. second moment of area, we used our cantilever beam model to estimate how the elastic modulus E varied along the measured region of the antennae, applying an upper bound estimate of I from geometrical measurements. We found that E was not statistically different for distances along the length even when considering the possible effect of individuals

and plane (mixed effect model: $F = 1.14$, $d.f. = 1$, $P = 0.288$). When pooling E across different measurement distances along the antenna, we estimated a mean elastic modulus of $6.91 \times 10^6 \pm 4.47 \times 10^6 Pa$ (median= 5.89×10^6; 25% quartile= 2.87×10^6; 75% quartile= 1.01×10^7).

4.1.4.4 Discussion

During contact, antennal bending is determined by its flexural stiffness and the applied load. From estimates of the second moment of area and measurements of the resistance-to-bending forces along the flagellum (Fig. 4.10A,B), we determined that the flexural stiffness of the cockroach antennal flagellum decreases rapidly from base to tip (Fig. 4.10C). We found that the forces decreased exponentially, whereas the elastic modulus did not change significantly within the measured length, suggesting that geometrical properties, i.e. tapering, are the main determinant of flexural stiffness (Fig. 4.10C)

These results are consistent with simple mechanical considerations. The curvature, κ, will be the greatest at the point of bend. For a discretized beam with a force near the tip and with constant stiffness, κ will vary according to equation 4.9 such that κ will be greatest where I is smallest, assuming first-mode bending. Thus, more bending should be expected at the tip than at the base. The fact that the point of bend

(or point of greatest curvature) is always closest to the wall and appears to "move" considerably as the animal changes its distance to the wall can be attributed to a decreasing second moment of area (assuming E is constant). In contrast, we would expect the point of bend for a beam or antenna with a constant I to remain constant. In addition, tapering may mechanically simplify the discrimination of large deflections due to flow or end loads for underwater robots [26]. Under these two conditions, a tapering antenna will produce very different curvature profiles along its length, thus mechanically simplifying discrimination of stimuli. Interestingly, tapering in rat whiskers can improve the reliability of information during slower feature extraction tasks [72] [73] [31] [74], and we suspect that similar principles apply to exploratory object localization with antennae.

4.2 The Robotic Antenna

For roboticists seeking to design tactile probes to add new capabilities to mobile robots, choosing mechanical design parameters that integrate with the body remains a challenge. The next generation of agile and multifunctional robots will undoubtedly benefit from building sensors with the body in mind. Our physical model enabled us to test biological hypotheses that would otherwise be extremely difficult to test in live, behaving animals.

4.2.1 Stiffness Profile vs Wall-following

In this section, I test how the stiffness profile could simplify control by regulating preview distance —the distance that the antenna can sense ahead of the body. Our previous control theoretic model predicts that control is simplified by a greater preview distance [52].

4.2.1.1 Methods

I ran a nine-segment ($9 \times 40\ mm$) robotic antenna along a smooth, angled ($8\ deg$) wall with a constant base velocity of $16.7^{mm}/_{s}$ for $50s$ per trial. The velocity was sufficiently low for the antenna to stay in a quasi-static state to minimize inertial effects. I set the antenna angle of attack to a biologically relevant value of 30 deg [12] and adjusted the initial wall distance so that the final segment (ninth) was bent backwards and in contact with the wall. The antenna traveled a total of 80 cm while the wall distance decreased from 20 to 9 cm. I tested seven different stiffness profiles on the robotic antenna and repeated each trial five times (Fig. 4.12). I randomized the order of experiments according to the stiffness profile, but each replicate for a given profile was done consecutively. I normalized the stiffness distributions for the total length of my antenna ($0.36m$) and the available range ($0.004 - 0.082^{Nm}/_{rad}$). For the constant stiffness profile, all joints had the minimum rotational stiffness of

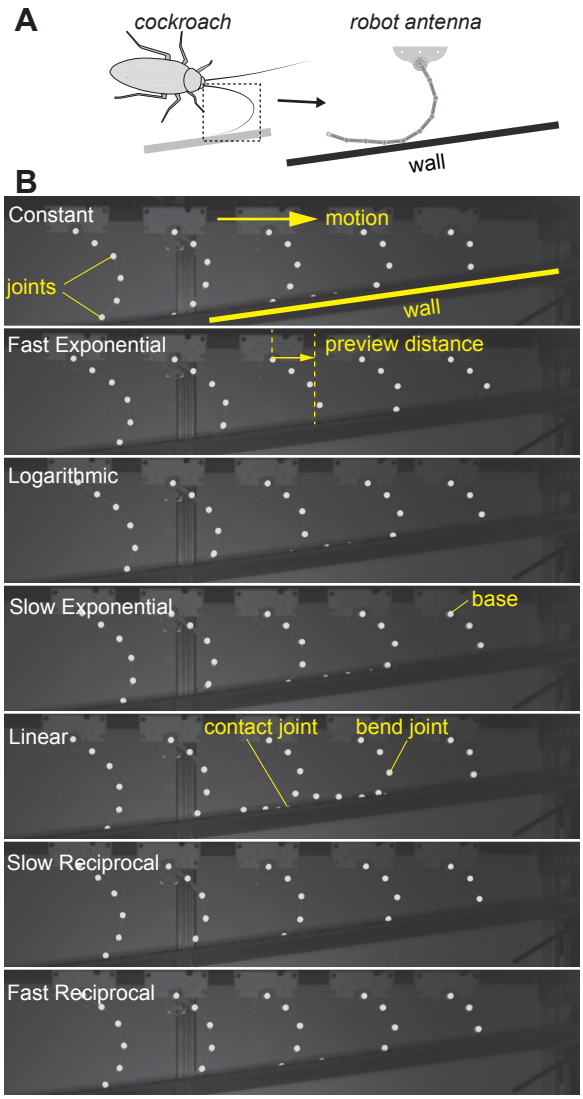

Figure 4.11: Robotic antenna as a physical model to simulate antenna- mediated wall-following. **A**: Diagram depicting a cockroach wall-following along an angled wall (left), with the ipsilateral antenna in a bent-backward configuration, and the corresponding multi-segmented physical model of the antenna (right). **B**: Nine-segment physical model of antenna sliding at constant velocity along a smooth, angled wall. I tested seven different stiffness profiles (named in white text on left) and measured how the profiles affected bending properties by tracking the angle of individual joints. The point of bend is the point of greatest curvature computed from individual joint angles. The point of contact is the joint of most proximal contact with the wall. The base is the proximal-most segment from the motorized platform. The preview distance is the distance between the point of wall contact and base.

$0.004^{Nm}/_{rad}$. All other profiles were decreasing. To sample a spectrum of decreasing mechanical stiffness profiles, I employed the following profiles: linear, exponential ($\propto e^{-2x}$ and $\propto e^{-12x}$), reciprocal ($\propto {}^{-1}/_{x}$ and $\propto {}^{-1}/_{12logx}$) and logarithmic ($\propto logx$), where x is the position along the length of the antenna (Fig. 4.12H). During each trial, I recorded the joint angles at $100Hz$ and the position of the antenna base at $30Hz$. For each trial I also captured an overhead video at 30 frames per second for cross-validation, where each joint was marked with retro-reflective markers.

First, I tested how stiffness profile affects the discrimination of the point of bend or contact point by computing the correlation coefficient between the points of greatest curvature and contact point with the base-to-wall distance. Second, I tested how the stiffness profile affects the preview distance of the antenna, the distance between the distal-most point in contact with the wall and the base of the antenna fixed to the linear platform (Fig. 4.11B). For analysis, I averaged trials for each condition and averaged the joint angle distributions for every 10 ms interval. For every frame, I determined the point of maximum bending and point of contact.

4.2.1.2 Results

Compared to an antenna with a constant stiffness, I found that a decreasing stiffness profile better linearly maps base-to-wall distance and the point of maximum bend,

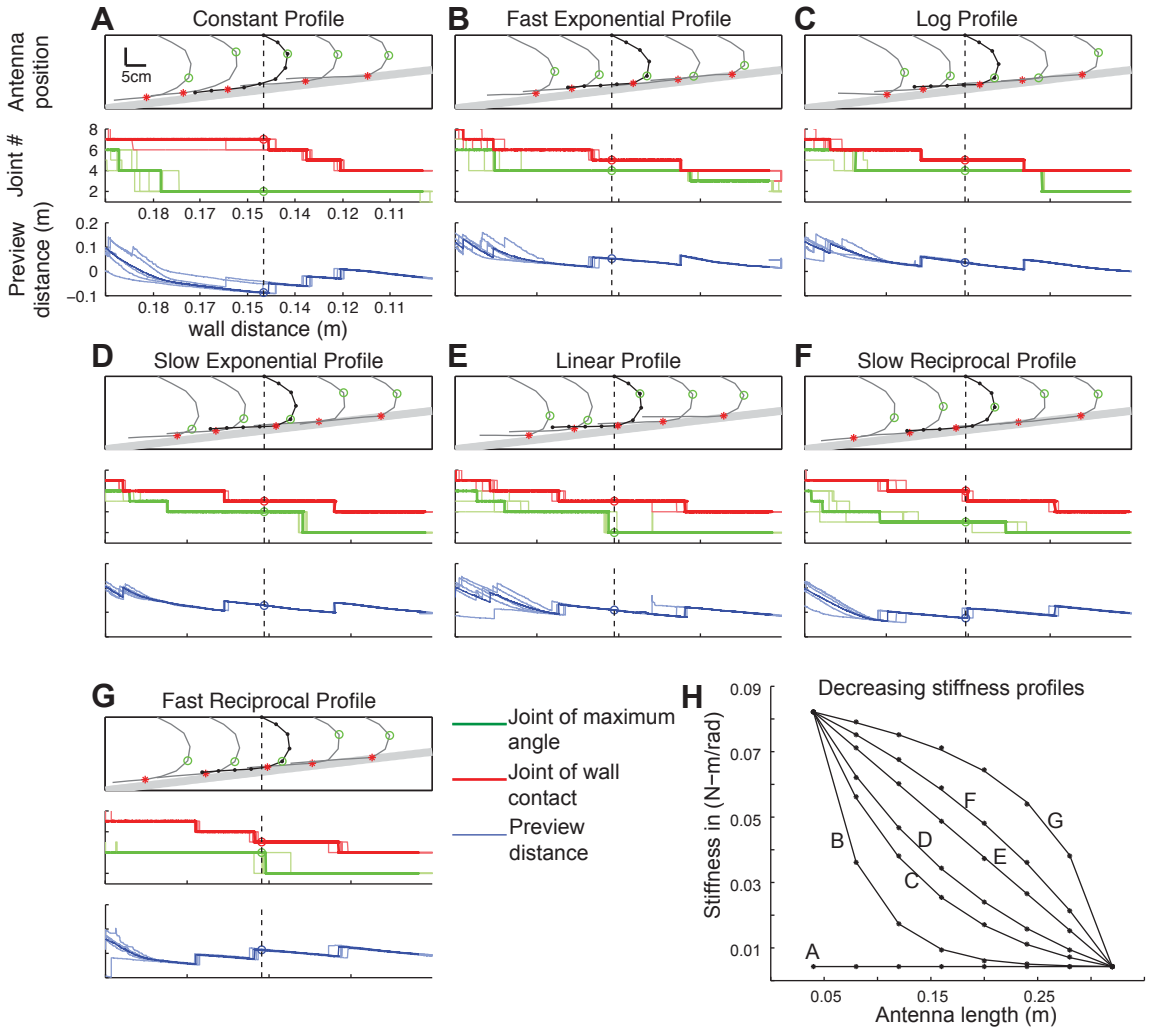

Figure 4.12: A decreasing flexural stiffness profile increases preview distance and better maps body-to-wall distance compared with a constant stiffness profile. **A-G**: Plots of antenna position, joint of maximum angle and wall contact and preview distance for seven different stiffness profiles. For the antenna position plots (top), the gray thick line represents the angled wall. The joints of bend and contact are shown by green, open circles and red asterisks, respectively. The vertical, dashed line represents one frame (dark antenna, top) from a 50s trial. For the joint no. plot, the red and green lines show the joint of maximum bend and the joint of wall contact, respectively. Thick lines represent one trial matching the trial shown in the top graph. Thin lines represent individual trials. For visual clarity, axes label and scaling are shown for "A" only but are identical for "B-G". These data are summarized in Table 4.1. **H**: Stiffness profiles as a function of antenna length for "A-G".

as evidenced by the higher correlation coefficients (Fig. 4.12, Table 4.1). For exponentially decreasing stiffness profiles, I observed that the point of bend or greatest curvature is often located close to the wall, a finding consistent with previous studies of the cockroach [12] [52] and crayfish [10]. In the Discussion, I describe how this observation is predicted from mechanics. I found a marginal increase in correlation coefficient between the base-to-wall distance and the point of contact when comparing a constant with a decreasing flexural stiffness. Secondly, I found that a decreasing stiffness profile increased the preview distance. Overall, there was a significant association between the stiffness profile and preview distance (ANOVA, $F = 76.70$, $d.f. = 6$, $P < 0.001$; Fig. 4.1). Post hoc analysis revealed that the preview distance was significantly longer for an antenna with a decreasing stiffness profile compared with one with a constant flexural stiffness (Tukey's test, $P < 0.001$ for all comparisons). For decreasing stiffness profiles, the preview distance generally decreased as the antenna base-to-wall distance decreased, consistent with previous observations that cockroaches ran closer to the wall as their speeds increase [12] [52].

4.2.1.3 Discussion

We tested the hypotheses that a decreasing flexural stiffness profile enables effective mapping of the point of bend and/or point of contact to body-to-wall distance and increases the preview distance. By testing different stiffness profiles, we found that

	Correlation with body-to-wall distance		Preview distance	
Stiffness profile	Point of bend	Point of contact	Mean ± s.d.	Median
Constant	0.56 (0.60)	0.91 (0.91)	-2.9 ± 1.2	-3.0
Fast exponential	0.83 (0.88)	0.94 (0.95)	4.4 ± 0.5	4.0
Logarithmic	0.87 (0.88)	0.94 (0.94)	3.5 ± 0.3	3.2
Slow exponential	0.91 (0.92)	0.94 (0.94)	2.5 ± 0.1	2.2
Linear	0.86 (0.87)	0.93 (0.94)	1.3 ± 1.0	0.6
Slow reciprocal	0.84 (0.89)	0.96 (0.96)	0.1 ± 0.5	0.0
Fast reciprocal	0.86 (0.86)	0.96 (0.96)	-0.6 ± 0.3	-0.6

Table 4.1: Performance metrics of robotic antenna with different stiffness profiles.Pearsons and Spearmans rank (in parentheses) correlation coefficients are shown. Preview distance is measured from point of attachment of antenna.

the point of bend maps better to the body-to-wall distance for a decreasing stiffness compared with a constant stiffness profile (Fig. 4.12, Table 4.1). The implications for sensing are that antenna mechanics could condition sensing during high-speed tactile navigation with the position of the point of bend acting as a one-dimensional sensory map, as originally proposed in *P. americana* [12] and in the crayfish *Cherax destructor* [66] [10]. Especially during rapid running where neural delays can impose severe constraints on control [52], sensory mapping conditioned by mechanics could simplify sensing and control. Having a highly flexible tip could also improve the reliability of tactile flow computation during high-speed running tasks, since the antenna better conforms to the shape of obstacles, allowing more physical contacts.

We found that the preview distance was longer for a decreasing stiffness compared with a constant stiffness profile (Fig. 4.12, Table 4.1). To our knowledge, the flexural stiffness of a tactile sensor has never been linked to an animal's or robot's preview distance. The practical implication of this result is that a rapidly moving animal

or mobile robot equipped with an antenna with decreasing stiffness will detect an obstacle earlier, and thus have more time for an appropriate motor response. For biological systems, particularly when constrained by neural conduction delays which have been estimated to be 2030 ms from mechanoreception to muscle activation [12] [24], preview distance is critical to stabilize closed-loop tactile navigation. Its utility has been demonstrated in control theoretic studies of wall following using simple [52] and dynamically representative [24] models of running *P. americana*. These studies determined that the difficulty of closed-loop stabilization is captured by a non-dimensional constant, τ, inversely proportional to the preview distance, l. Thus, as preview distance increases while other parameters such as speed remain constant, τ decreases, making the system easier to stabilize with feedback.

If we assume geometric similarity between my robotic antenna (antenna length= 36 cm) and *P. americana* (antenna length= 1.3× body length), we would expect the length of the robot body to be $\approx$ 28 cm, the approximate scale of small hexapedal robots [75]. Under simplifying assumptions [52], preview distance can be measured from the center of mass (COM) of the robot or animal (i.e. about 14 cm would be added to the preview distances listed in Table 4.1) for a 28 cm robot with COM in the geometric center). Therefore, for the "constant" stiffness profile the preview distance would be $\approx$ 11 cm, while for the "fast exponential" stiffness profile the preview distance would be $\approx$ 18 cm or $\approx$ 0.6× body length. This corresponds to a 64% increase in preview distance from the COM, which decreases τ by about a factor of 2,

thereby making the system significantly easier to control, again assuming geometric similarity and all other parameters equal. In contrast to my physical model, wall-following *P. americana* maintain antennal contact distances (measured from COM to point of contact) ranging from ≈ 4 to 5 cm, which is $\approx 1.1 - 1.3\times$ body length [52]. These overall differences in preview distance between model and organism are likely due to differences in friction between the antenna and environment and necessary simplifications in the mechanical design of the physical model to test our hypotheses.

In summary, we show that biomechanical tuning of the antenna facilitates rapid course control, which can in turn inform the design of wall-following robots moving at multiple body lengths per second.

4.2.2 Wall Shape vs. Wall-Following

In this section I present the dependence of sensory accuracy on the stiffness profile. In particular, we show that a decreasing stiffness profile enabled perception of finer spatial frequency components of a wall.

4.2.2.1 Results

From the mapping results, the change in antenna posture was apparent between the*decreasing stiffness* and the *constant stiffness* profiles (Fig. 4.13), where the relatively higher stiffness at the distal segments clearly prevented the inclined surfaces to be picked up by the hairs. Conversely, the relatively lower stiffness at the proximal segments caused the antenna to mostly drag behind the linear actuator car, which led to some loss of accuracy towards the corners. I computed the mean spatial error of the detected contact points with the ground truth of wall as 5.0 mm for the decreasing stiffness and 9.4 mm for the constant stiffness profile.

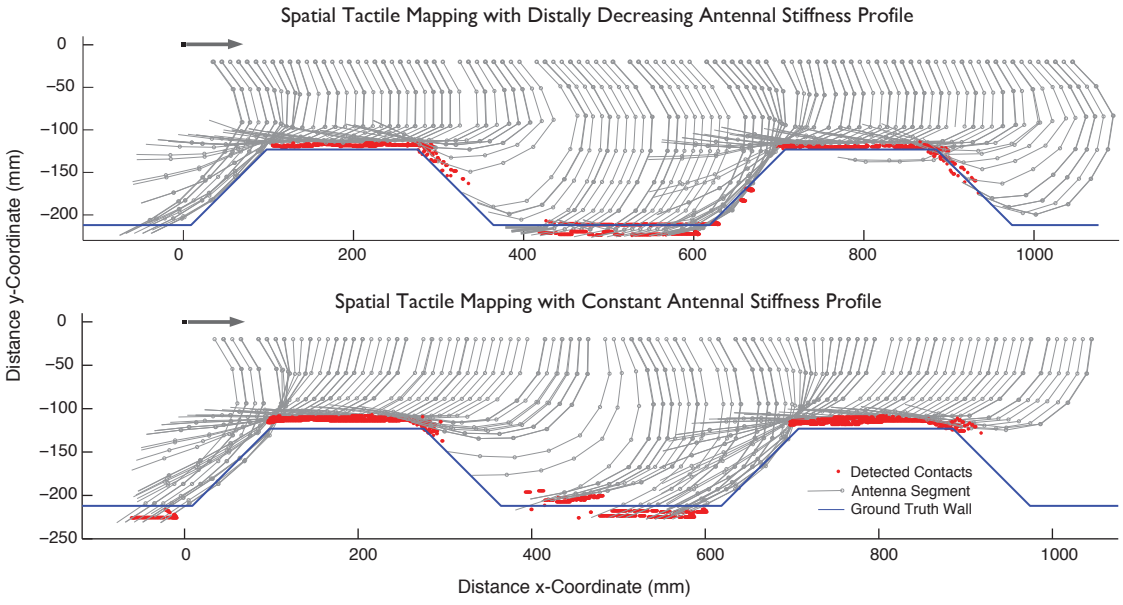

Figure 4.13: Trapezoidal wall mapping experiment with 2 different stiffness profiles (one decreasing, one constant). The antenna sweeps the wall at $24^{mm}/_{s}$. The average mapping error is computed as 10.7 mm from the ground truth.

I performed the spatial mapping experiments on a sinusoidal wall shape with spatial frequencies of $2.8^1/_m$, $4.2^1/_m$, $6.3^1/_m$, $9.5^1/_m$ and $14.2^1/_m$. The aim of this experiment was to reveal the effects of different stiffness profiles on the tactile spatial resolution. Hence, I imposed the previously employed stiffness profiles—distally decreasing and constant—to the antenna. Comparing the spatial mapping results, the performance difference between profiles is clear (Fig. 4.15). Specifically, at the highest ($14.2^1/_m$) wall frequency the average distance discrepancy from the ground truth for the distally decreasing stiffness is almost the same as the distance discrepancy for the constant stiffness configuration at the frequency of $6.3^1/_m$.

Figure 4.16 describes the same data from the perspective of the environment instead of the robot. The gray shaded areas indicate the amount of time spend mapping a particular section of the wall. The darker the shade, the slower the antenna mapped the environment at that location. The velocity of the antenna during mapping had profound implications on the quality of the data since the number of data points per wall length was inversely proportional to the velocity. I found that decreasing stiffness profile also provided a more uniform distribution of mapping velocity compared to the constant stiffness profile. The green to blue shades following the antenna curvature indicate the contact location of the antenna, which mapped that particular region of the wall. Greener shades are correlated with larger preview distances and can be used for doing obstacle avoidance maneuvers whereas bluer regions are mapped after the robot passed by that region and thus are not usable for navigation. Clearly, the

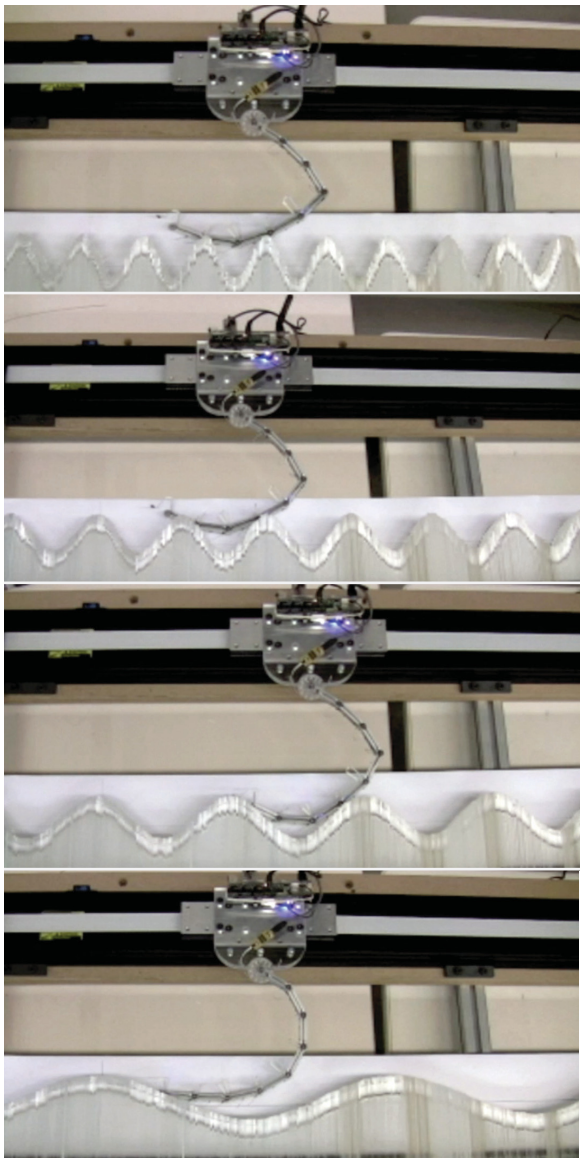

Figure 4.14: Spatial mapping experiments on configurable walls with changing spatial frequency.

decreasing stiffness profile facilitated larger preview distances on average, so more of the wall was perceived to execute obstacle avoidance.

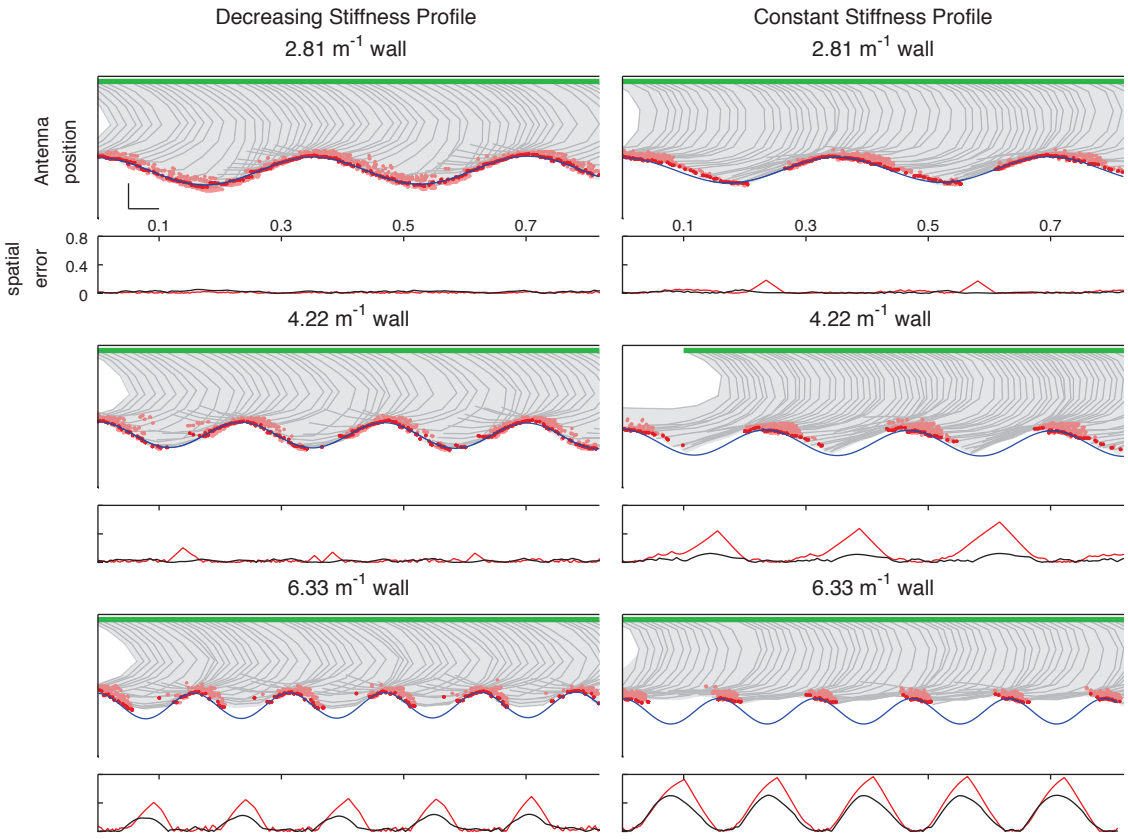

Figure 4.15: Comparison of two spatial frequency experiments: antenna with a distally decreasing stiffness profile and antenna with constant stiffness profile. The frequency of the wall shape increased linearly in logarithmic scale. As the frequency increases, the wall shape was not captured accurately. For the antenna with decreasing stiffness, the mean spatial errors from bottom to top were: 2.7 mm, 5.1 mm, 12.1 mm and 25.0 mm. For the constant stiffness antenna the mean spatial errors were (bottom to top): 5.0 mm, 14.7 mm and 25.9 mm. The wall shape frequencies for adjacent plots were identical.

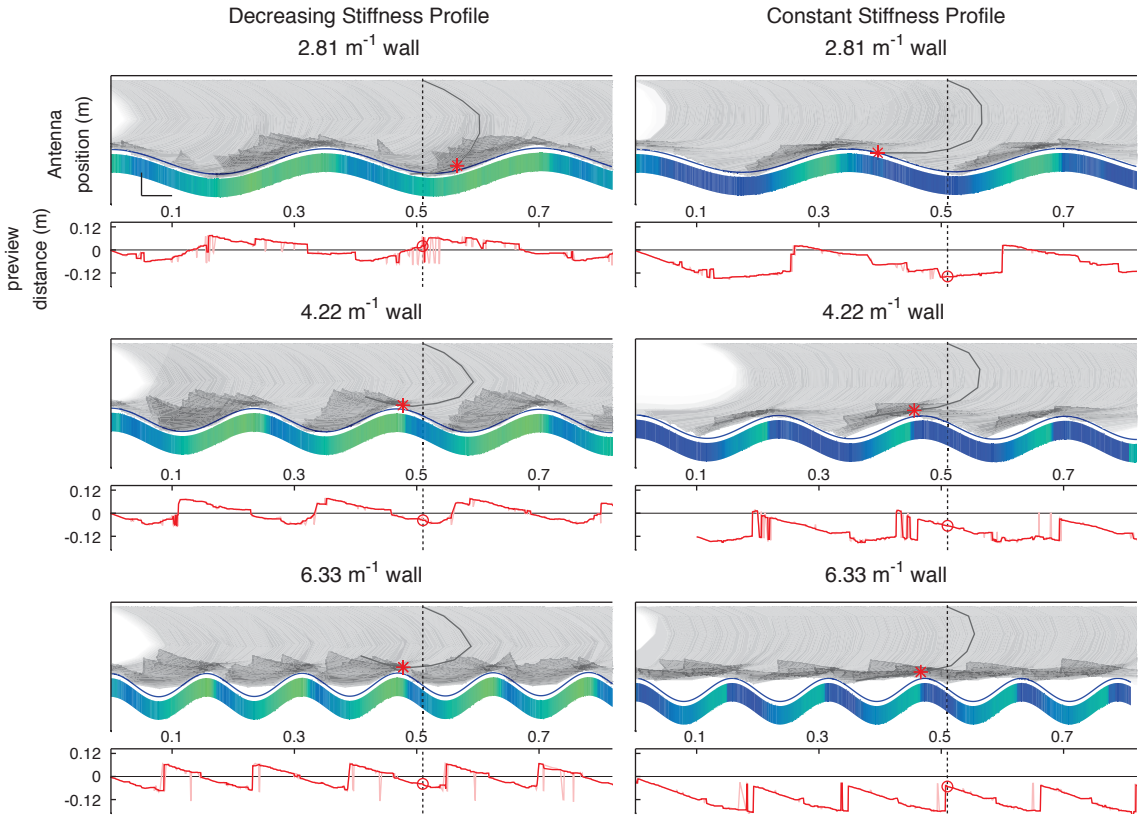

Figure 4.16: Gray shades indicate the velocity of the antenna at that region. Darker shades correspond to slower speeds and thus more data points. Green to blue shades indicate the availability of the data for navigation purposes and are directly correlated to the preview distance (red line)

Chapter 5

Conclusion

In this dissertation, I treated the cockroach, "legendary" [12] for its antenna-enabled rapid escape maneuvers, as a model system for developing antenna-inspired flexible distributed tactile sensors for future agile robotic platforms. My collaborators and I used prior knowledge [11, 12, 23, 45] of this model system to develop hypotheses to facilitate the robust, stable, high-bandwidth antennal sensing performance. Based on quasi-static analysis, I identified and isolated the stiffness profile along the antenna as the fundamental parameter that affects performance metrics such as contact maintenance, preview distance, spatial acuity, and sensory encoding for wall-following.

I investigated ways to simplify wall-following control and found that stiffness profiles which decreased faster than linearly decreasing profiles resulted in longer preview

distances and higher spatial accuracy compared to those with uniform stiffness. Furthermore, I showed that the fast exponentially decreasing stiffness profile caused a linear one-dimensional mapping between the antenna bending and body-to-wall distance, which would enable efficient sensory encoding of the wall distance.

Regarding contact maintenance and wall-following robustness, we showed evidence that the change in mechanical state of the antenna—which we characterized as projecting "forward" or "backward"—was mediated passively via interactions between the antenna and the environment. We compared the frequency of states smooth and rough surfaces. We found that surfaces with low friction caused frequent state changes and loss of contact. Furthermore, we showed backward-projecting antennae decreased the body-to-wall distance—the proposed state variable for wall-following control— which increased the probability of collisions. Contrary to the hypothesis that an increased preview distance afforded by a forward-projecting antenna leads to improved wall following, we determined tracking performance and task-level control were superior with a backward-projecting antenna. To address the negative effect of low surface friction and the consequential backward-to-forward state change, I investigated the effect of antenna stiffness profile on the normal and shear forces during state changes. I showed that constant and faster than linearly decreasing stiffness profiles mitigated the low coefficient of friction by increasing the relative normal forces at the contact point. After demonstrating that the antenna state was crucial for task-level control, we hypothesized that the mechanical tuning of the antenna—in particular,

the mechanical role played by sensory hairs—may enable passive switching to the desired backward-projecting state. We found that passive mechanical hair sensillae on the antenna were sufficient for mediating the desired change in the overall mechanical state of the antenna from its resting position to projecting backward. This conclusion was reached through a set of experiments in which the hairs were ablated with a high-precision laser system and was corroborated independently by experiments with my tunable physical model inspired by arthropod antennae. This led to the discovery that distally pointing anisotropic rigid mechanosensory micro structures, which were thought to be just contact sensors along the flagellum, actually self-reconfigure the antenna during wall-following.

It is my sincere belief that synergistic sensory integration of computer vision and passive tactile sensing is the keystone of robust autonomous navigation on otherwise inaccessible terrestrial environments. Still, for engineers seeking to design tactile probes to add new capabilities to mobile robots, choosing mechanical design parameters that integrate with the robot locomotion remains a challenge. This dissertation describes our collaborative work transferring biological features of an excellent navigator to engineering. We provided the mechanical recipe for designing and building the next generation of flexible distributed near-field tactile sensors for agile and multifunctional robots.

Chapter 6

Appendix

6.1 Antenna Kinematics

6.1.1 Positions, Orientations & Coordinate Frames

Our goal is simply to find a function that generates the position of any point p^a and its body frame orientation θ^a_{sb} on a desired segment body "b" with respect to any desired coordinate frame, "s" given the joint coordinates θ. In short, we want to find $\{p^a_{sb}, \theta^a_{sb}\} = f(\theta, \Pi)$ with given parameters $\Pi = \{l, s, b, p^a_b\}$.

- Let $\mathcal{C}_s \in \{\mathcal{C}_{-1}, \mathcal{C}_0, \mathcal{C}_1, \ldots, \mathcal{C}_n\}$ be the desired spatial frame to which all other frames $\mathcal{C}_i \;\; i \in \{0, \ldots, n\}$ will be relative to.

- Let $\mathcal{C}_b \in \{\mathcal{C}_{-1}, \mathcal{C}_0, \mathcal{C}_1, \ldots, \mathcal{C}_n\}$ be the desired body frame.

- Let $\mathcal{C}_{sG} = \mathcal{C}^{-1}_{Gs} \in SE(2)$ be the homogeneous representation of the rigid body transformation from the ground frame to the desired spatial frame $\mathcal{C}_s$.

- Let $\theta_i \in \mathbb{S}^1 \; i \in \{0, \ldots, n\}$ be the i^{th} relative joint angle in radians.

- Let $\theta \in \underbrace{\mathbb{S}^1 \times \ldots \times \mathbb{S}^1}_{n+1} = \mathbb{T}^{n+1}$ be the vector of joint angles and base angle in radians s.t.
  $\theta = \begin{pmatrix} \theta_0 & \theta_1 & \ldots & \theta_n \end{pmatrix}^\top$

- Let θ_{sb} be the orientation of the rigid body coordinate frame $\mathcal{C}_b$ with respect to

the spatial coordinate frame $\mathcal{C}_s$.

- Let $\theta^a_{sb} = \theta_{sb}$ be the orientation of any point p^a on rigid body $\mathcal{C}_b$.

- Let the notation $p_{sb} \in \mathbb{R}^2$ be the origin of a rigid body "b" with respect to a spatial coordinate frame $\mathcal{C}_s$.

- Let $p_{G0} = \begin{pmatrix} x_0 & y_0 \end{pmatrix}^\top \in \mathbb{R}^2$ be the base frame position in meters with respect to the ground frame. Note that p_{G0} also coincides with the first joint location.

- Let $p_{Gj} = \begin{pmatrix} x_j & y_j \end{pmatrix}^\top \in \mathbb{R}^2$ $j \in \{1, 2, \ldots, n\}$ be the flagellum frame positions in meters, where each p_{Gj} coincides with the $(j+1)^{th}$ joint. Also note that $p_{Gn} = \begin{pmatrix} x_n & y_n \end{pmatrix}^\top$ coincides with the tip position.

- Let the notation $p^a_b \in \mathbb{R}^2$ be the coordinates of point "a" on the rigid body "b" written in body coordinate frame $\mathcal{C}_b$.

- Let the notation $p^a_{sb} \in \mathbb{R}^2$ be the coordinates of point "a" on the rigid body "b" written in spatial coordinate frame $\mathcal{C}_s$.

- Let $l \in \mathbb{R}$ be the uniform length in meters for all links including the base.

Then the forward kinematics for the tip p_{Gn} is a mapping from the $n+1$ dimensional torus to the Euclidean plane $f_n : \mathbb{T}^{n+1} \mapsto \mathbb{R}^2$.
Specifically:

$$p_{GG} = \begin{bmatrix} 0 \\ 0 \end{bmatrix}$$

$$
\begin{aligned}
p_{G0} &= \begin{bmatrix} \cos\theta_0 \\ \sin\theta_0 \end{bmatrix} l \\
p_{G1} &= \begin{bmatrix} \cos\theta_0 + \cos(\theta_0+\theta_1) \\ \sin\theta_0 + \sin(\theta_0+\theta_1) \end{bmatrix} l \\
&\vdots \\
p_{G,n-1} &= \begin{bmatrix} \cos\theta_0 + \cos(\theta_0+\theta_1) + ... + \cos(\theta_0+\theta_1+...+\theta_{n-1}) \\ \sin\theta_0 + \sin(\theta_0+\theta_1) + ... + \sin(\theta_0+\theta_1+...+\theta_{n-1}) \end{bmatrix} l \\
p_{Gn} &= \begin{bmatrix} \cos\theta_0 + \cos(\theta_0+\theta_1) + ... + \cos(\theta_0+\theta_1+...+\theta_{n-1}) + \cos(\theta_0+\theta_1+...+\theta_{n-1}+\theta_n) \\ \sin\theta_0 + \sin(\theta_0+\theta_1) + ... + \sin(\theta_0+\theta_1+...+\theta_{n-1}) + \sin(\theta_0+\theta_1+...+\theta_{n-1}+\theta_n) \end{bmatrix} l \\
&= \begin{bmatrix} \cos\theta_0 \\ \sin\theta_0 \end{bmatrix} l + \sum_{j=1}^{n} \begin{bmatrix} \cos\sum_{k=0}^{j}\theta_k \\ \sin\sum_{k=0}^{j}\theta_k \end{bmatrix} l
\end{aligned}
$$

A compact form of the general mapping f_i where $i \in \{-1, 0, 1, 2, \ldots, n\}$ are the positions of the base, joints and the tip is given by:

$$
p_{Gi} = \sum_{i^*=0}^{i} \begin{pmatrix} \cos\sum_{k=0}^{i^*}\theta_k \\ \sin\sum_{k=0}^{i^*}\theta_k \end{pmatrix} l
$$

Note that $i = -1$ represents the ground frame (an identity matrix) and included for completeness (i.e. $\mathcal{C}_G = \mathcal{C}_{-1}$).

As shown in Figure 2.6, we have Cartesian coordinate frames $\mathcal{C}_i = (p_{Gi}, R_{Gi}) \in SE(2)$ where $i \in \{-1, 0, 1, 2, \ldots, n\}$ at the ground, every joint and the tip point p_{Gi} oriented with θ_{Gi} degrees $R_{Gi} \in SO(2)$ with respect to the ground frame, which is the default spatial frame $\mathcal{C}_G \equiv \mathcal{C}_s$. Note we would also normally write $\mathcal{C}_i$ as $\mathcal{C}_{Gi}$ to indicate that the coordinate frame is with respect to the ground, but the $_G$ is dropped in this default case. The homogeneous representation of each frame with respect the ground

frame is:

$$\mathcal{C}_{Gi} = \mathcal{C}_i = \left[\begin{array}{c:c} R_{Gi} & p_{Gi} \\ \hdashline 0 & 1 \end{array}\right] \quad , \quad R_{Gi} = \begin{pmatrix} \cos\theta_{Gi} & -\sin\theta_{Gi} \\ \sin\theta_{Gi} & \cos\theta_{Gi} \end{pmatrix}$$

- Let the default spatial frame s be the ground frame G at the world origin with its x-axis aligned with the base motion direction (i.e. $p_{GG} = 0$, $R_{GG}(0) = I$). Then we have $s \equiv G$ such that $\mathcal{C}_s = (p_{Gs}, R_{Gs}) \equiv (p_{GG}, R_{GG}) \in SE(2)$ s.t:

$$\mathcal{C}_G \equiv \mathcal{C}_s = \left[\begin{array}{cc:c} 1 & & \\ & 1 & 0 \\ \hdashline & 0 & 1 \end{array}\right]$$

- Let $R_{Gi} \in SO(2)$ be the rotation associated with the i'th frame with respect to the ground frame $\mathcal{C}_G$. If θ is known, we have:

$$\begin{aligned} R_{G0} =& R_{GG}R(\theta_0) = \begin{pmatrix} \cos\theta_0 & -\sin\theta_0 \\ \sin\theta_0 & \cos\theta_0 \end{pmatrix} \\ R_{G1} =& R_{G0}R(\theta_1) = \begin{pmatrix} \cos(\theta_0+\theta_1) & -\sin(\theta_0+\theta_1) \\ \sin(\theta_0+\theta_1) & \cos(\theta_0+\theta_1) \end{pmatrix} \\ & \vdots \\ R_{Gn} =& R_{G,n-1}R(\theta_n) = \begin{pmatrix} \cos(\theta_0+\theta_1+\ldots+\theta_n) & -\sin(\theta_0+\theta_1+\ldots+\theta_n) \\ \sin(\theta_0+\theta_1+\ldots+\theta_n) & \cos(\theta_0+\theta_1+\ldots+\theta_n) \end{pmatrix} \end{aligned}$$

Then the rotation of the any frame with respect to the ground frame is simply:

$$R_{Gi} = \begin{pmatrix} \cos \sum_{k=0}^{i} \theta_k & -\sin \sum_{k=0}^{i} \theta_k \\ \sin \sum_{k=0}^{i} \theta_k & \cos \sum_{k=0}^{i} \theta_k \end{pmatrix} \tag{1.2}$$

Combining (1.1) and (1.2) yields a more complete forward mapping $f_G : \mathbb{T}^{n+1} \mapsto SE(2)$ of any frame $\mathcal{C}_i$ with respect to the ground frame. We use the homogeneous representation of the mapping s.t:

$$\mathcal{C}_i = \left[\begin{array}{cc:c} \cos \sum_{k=0}^{i} \theta_k & -\sin \sum_{k=0}^{i} \theta_k & \sum_{i^*=0}^{i} \begin{pmatrix} \cos \sum_{k=0}^{i^*} \theta_k \\ \sin \sum_{k=0}^{i^*} \theta_k \end{pmatrix} l \\ \sin \sum_{k=0}^{i} \theta_k & \cos \sum_{k=0}^{i} \theta_k & \\ \hdashline \multicolumn{2}{c:}{0} & 1 \end{array}\right] \tag{1.3}$$

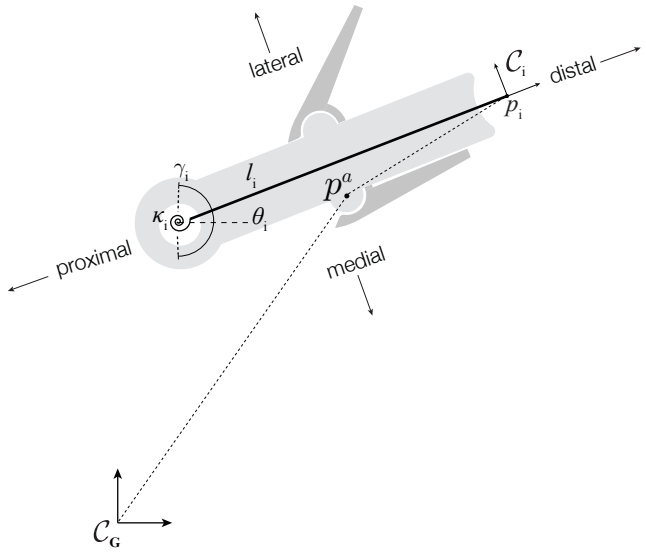

Figure 6.1: Anntena segment as a rigid body.

The homogeneous representation not only describes the configuration of each link, but also allows computation of any point p^a on a given link body with respect to the ground frame:

- Let a coordinate frame $\mathcal{C}_i$ also be the rigid body transformation from the ground frame to the i^{th} frame (i.e. $\mathcal{C}_i = \mathcal{C}_{Gi}$).
- Let $p_i^a = \begin{pmatrix} x^a & y^a \end{pmatrix}^\top \in \mathbb{R}^2$ be an arbitrary point on the i^{th} link given in the i^{th} coordinate frame $\mathcal{C}_i$ (i.e. body frame). Note that the vector to this point from the coordinate frame origin p_i is constant regardless of the antenna configuration.
- Let $p_G^a \equiv p_i^a = \begin{pmatrix} x_i^a & y_i^a \end{pmatrix}^\top \in \mathbb{R}^2$ be the same point (p_i^a) on the i^{th} link given in the ground frame $\mathcal{C}_G$ (See Figure 6.1).

Then, given p_i^a, the coordinates with respect to the ground frame is:

$$\begin{pmatrix} p_G^a \\ 1 \end{pmatrix} = \mathcal{C}_{Gi} \cdot \begin{pmatrix} p_i^a \\ 1 \end{pmatrix}$$

Conversely, given p_G^a, the coordinates with respect to the i^{th} frame is:

$$\begin{pmatrix} p_i^a \\ 1 \end{pmatrix} = \mathcal{C}_{Gi}^{-1} \cdot \begin{pmatrix} p_G^a \\ 1 \end{pmatrix}$$

where $\mathcal{C}_{Gi}^{-1} = \mathcal{C}_{iG}$ is the rigid body transformation from the i^{th} frame to the ground frame. It can also be computed from p_{Gi} (1.2) and R_{Gi} (1.2) as:

$$\mathcal{C}_{Gi}^{-1} = \mathcal{C}_{iG} = \left[\begin{array}{c|c} {R_{Gi}}^{\top} & -{R_{Gi}}^{\top} p_{Gi} \\ \hline 0 & 1 \end{array}\right] \tag{6.1.1.1}$$

or just from R_{Gi}:

$$\mathcal{C}_{Gi}^{-1} = \mathcal{C}_{iG} = \left[\begin{array}{c|c} R_{Gi}^{\top} & \displaystyle\sum_{i^*=0}^{i} \begin{pmatrix} -\cos \displaystyle\sum_{k=i^*+1}^{i} \theta_k \\ \sin \displaystyle\sum_{k=i^*+1}^{i} \theta_k \end{pmatrix} l \\ \hline 0 & 1 \end{array}\right]$$

or directly from θ_i:

$$\mathcal{C}_{Gi}^{-1} = \mathcal{C}_{iG} = \left[\begin{array}{c|c} \underbrace{\begin{matrix} \cos \displaystyle\sum_{k=0}^{i} \theta_k & \sin \displaystyle\sum_{k=0}^{i} \theta_k \\ -\sin \displaystyle\sum_{k=0}^{i} \theta_k & \cos \displaystyle\sum_{k=0}^{i} \theta_k \end{matrix}}_{R_{Gi}^{\top}} & \displaystyle\sum_{i^*=0}^{i} \begin{pmatrix} -\cos\left(\displaystyle\sum_{k=0}^{i} \theta_k - \sum_{k=0}^{i^*} \theta_k\right) \\ \sin\left(\displaystyle\sum_{k=0}^{i} \theta_k - \sum_{k=0}^{i^*} \theta_k\right) \end{pmatrix} l \\ \hline 0 & 1 \end{array}\right]$$

Note that equation 6.1.1.1 represents the position and orientation of the ground frame $\mathcal{C}_G$ with respect to the—now spatial— i^{th} frame. To illustrate the pattern of the forward kinematics in this "reverse" fashion let the spatial frame s be the tip frame $s = i = n$. Then after some trigonometric manipulation we can expand the position of the frames like 1.2, which show the form of the forward kinematics when the desired body frame is more proximal to the base than the spatial frame.

$$p_{nG} = \begin{bmatrix} -\cos(\theta_1 + ... + \theta_{n-1} + \theta_n) - \cos(\theta_2 + ... + \theta_{n-1} + \theta_n) + ... - \cos(\theta_{n-1} + \theta_n) - \cos(\theta_n) - 1 \\ \sin(\theta_1 + ... + \theta_{n-1} + \theta_n) + \sin(\theta_2 + ... + \theta_{n-1} + \theta_n) + ... \sin(\theta_{n-1} + \theta_n) + \sin(\theta_n) \end{bmatrix} l$$

$$p_{n0} = \begin{bmatrix} -\cos(\theta_2 + ... + \theta_{n-1} + \theta_n) + ... - \cos(\theta_{n-1} + \theta_n) - \cos(\theta_n) - 1 \\ \sin(\theta_2 + ... + \theta_{n-1} + \theta_n) + ... \sin(\theta_{n-1} + \theta_n) + \sin(\theta_n) \end{bmatrix} l$$

$$\vdots$$

$$p_{n,n-3} = \begin{bmatrix} -\cos(\theta_{n-1}+\theta_n) - \cos(\theta_n) - 1 \\ \sin(\theta_{n-1}+\theta_n) + \sin(\theta_n) \end{bmatrix} l$$

$$p_{n,n-2} = \begin{bmatrix} -\cos(\theta_n) - 1 \\ \sin(\theta_n) \end{bmatrix} l$$

$$p_{n,n-1} = \begin{bmatrix} -1 \\ 0 \end{bmatrix} l$$

$$p_{nn} = \begin{bmatrix} 0 \\ 0 \end{bmatrix}$$

Combining (1.2), (1.2), (1.3) and (6.1.1.1) yields the forward mapping $f_s : \mathbb{T}^{n+1} \mapsto SE(2)$ with respect to any desired antenna coordinate frame $\mathcal{C}_s \in \{\mathcal{C}_{-1}, \mathcal{C}_0, \mathcal{C}_1, \ldots, \mathcal{C}_n\}$. That is the spatial frame s can be changed from the ground frame $\mathcal{C}_G = \mathcal{C}_{-1}$ to any other frame $\mathcal{C}_i$.

Then we call $\mathcal{C}_{sb}$ the homogeneous representation of desired body frame $\mathcal{C}_b$ with respect to the desired spatial frame $\mathcal{C}_s$. It's computed as:

$$\begin{aligned} \mathcal{C}_{sb} &= \mathcal{C}_{Gs}^{-1} \cdot \mathcal{C}_b \\ &= \left[\begin{array}{c:c} {R_s}^\top & -{R_s}^\top p_s \\ \hdashline 0 & 1 \end{array}\right] \left[\begin{array}{c:c} R_i & p_i \\ \hdashline 0 & 1 \end{array}\right] v \end{aligned} \tag{6.1.1.2}$$

Note that as expected, the spatial frame $\mathcal{C}_s$ with respect to itself becomes identity:

$$\begin{aligned} \mathcal{C}_{ss} &= \mathcal{C}_{Gs}^{-1} \cdot \mathcal{C}_s \\ &= \left[\begin{array}{c:c} {R_s}^\top & -{R_s}^\top p_s \\ \hdashline 0 & 1 \end{array}\right] \left[\begin{array}{c:c} R_s & p_s \\ \hdashline 0 & 1 \end{array}\right] \end{aligned}$$

$$= \left[\begin{array}{cc:c} 1 & & \\ & 1 & 0 \\ \hdashline & 0 & 1 \end{array}\right]$$

Manipulating (6.1.1.2) for all possible body frames b leads to the piecewise forward mapping function parametrized by s and b that we use in our simulation to compute any desired frame $\mathcal{C}_b$ with respect to any desired frame $\mathcal{C}_s$:

$$\mathcal{C}_{sb} = f(\theta, l, s, b)$$

$$\mathcal{C}_{sb} = \begin{cases} \left[\begin{array}{cc:c} \cos\sum_{k=b+1}^{s} -\theta_k & -\sin\sum_{k=b+1}^{s} -\theta_k & \sum_{k^*=b+1}^{s}\left(-\cos\sum_{k=k^*+1}^{s}\theta_k\right) l \\ \sin\sum_{k=b+1}^{s} -\theta_k & \cos\sum_{k=b+1}^{s} -\theta_k & \left(\sin\sum_{k=k^*+1}^{s}\theta_k\right) \\ \hdashline 0 & & 1 \end{array}\right] & \text{if } -1 \le b < s \le n \\ \left[\begin{array}{cc:c} 1 & & \\ & 1 & 0 \\ \hdashline & 0 & 1 \end{array}\right] & \text{if } b = s \\ \left[\begin{array}{cc:c} \cos\sum_{k=s+1}^{b}\theta_k & -\sin\sum_{k=s+1}^{b}\theta_k & \sum_{k^*=s+1}^{b}\left(\cos\sum_{k=s+1}^{k^*}\theta_k\right) l \\ \sin\sum_{k=s+1}^{b}\theta_k & \cos\sum_{k=s+1}^{b}\theta_k & \left(\sin\sum_{k=s+1}^{k^*}\theta_k\right) \\ \hdashline 0 & & 1 \end{array}\right] & \text{if } n \ge b > s \ge -1 \end{cases} \tag{6.1.1.3}$$

Again, $s = -1$ corresponds to the default case $\mathcal{C}_s \equiv \mathcal{C}_G$, where the spatial frame is the ground frame. Similarly $b = -1$ implies that the desired body frame is the ground frame $\mathcal{C}_b \equiv \mathcal{C}_G$.

$$\begin{aligned}\begin{pmatrix} p_{sb}^a \\ 1 \end{pmatrix} &= \mathcal{C}_{sb} \cdot \begin{pmatrix} p_b^a \\ 1 \end{pmatrix} \\ &= \left[\begin{array}{c:c} R_{sb} & p_{sb} \\ \hdashline 0 & 1 \end{array}\right] \begin{pmatrix} p_b^a \\ 1 \end{pmatrix} \\ p_{sb}^a &= R_{sib} p_b^a + p_{sb}\end{aligned} \tag{6.1.1.4}$$

Equation 6.1.1.4 with the explicit expression for $\mathcal{C}_{sb}$ in 6.1.1.3 provides the desired position p_{sb}^a that we are interested in.

Next we need an expression for the angular orientation of the body coordinate frame $\mathcal{C}_b$ with respect to the spatial frame $\mathcal{C}_s$ in terms of the joint angles vector θ, which is simply given as:

$$\theta_{sb} = \sum_{k=s+1}^{b} \theta_k - \sum_{k=b+1}^{s} \theta_k \quad \text{where } s, b \in \{-1, 0, ..., n\}$$

$$\theta_{sb}^a = \theta_{sb} = \begin{cases} -\sum\limits_{k=b+1}^{s} \dot{\theta}_k & \text{if } -1 \leq b < s \leq n \\ 0 & \text{if } b = s \\ \sum\limits_{k=s+1}^{b} \dot{\theta}_k & \text{if } n \geq b > s \geq -1 \end{cases} \tag{6.1.1.5}$$

Taking advantage of the planar nature of the problem, we can slightly manipulate $\mathcal{C}_{sb}$ to get the hybrid transformation H_{sb} which also provides the desired frame orientation θ_{sb}. We define H_{sb} as:

$$\begin{aligned}\begin{pmatrix} p^a_{sb} \\ \theta^a_{sb} \end{pmatrix} &= H_{sb} \cdot \begin{pmatrix} p^a_b \\ 1 \end{pmatrix} \\ &= \left[\begin{array}{c:c} R_{sb} & p_{sb} \\ \hdashline 0 & \theta_{sb} \end{array}\right] \begin{pmatrix} p^a_b \\ 1 \end{pmatrix} \end{aligned} \tag{6.1.1.6}$$

Equation 6.1.1.6 is the function $\{p^a_{sb}, \theta^a_{sb}\} = f(\theta, \Pi) : \mathbb{T}^{n+1} \mapsto SE(2)$ with given parameters $\Pi = \{l, s, b, p^a_b\}$ we were seeking to find in the beginning of this section.

6.1.2 Velocities

Our goal is to find a function that generates the instantaneous translational velocity $\dot{p}^a_{sb}$ and rotational velocity ω^a_{sb} of any point p^a_b on a desired segment body b with respect to any desired coordinate frame s given the relative joint angle positions θ and joint velocities $\dot{\theta}$. In short we want to find $\{\dot{p}^a_{sb}, \omega^a_{sb}\} = df(\theta, \dot{\theta}, \Pi)$ with given parameters $\Pi = \{l, s, b, p^a_b\}$. This is referred as the *hybrid velocity* of a rigid body in [43].

- Let $\dot{\theta} \in \mathbb{R}^{n+1}$ be the vector of joint velocities and base angle velocity around their respective joint axes $\hat{\phi}_{si}$ in radians per second (rad/s) s.t: $\dot{\theta} = \left(\dot{\theta}_0, \dot{\theta}_1, \ldots, \dot{\theta}_n\right)^\top$

- Let the notation $\dot{p}_{sb} \in \mathbb{R}^2$ be the total translational velocity of a rigid body frame $\mathcal{C}_b$ measured with respect to a spatial coordinate frame $\mathcal{C}_s$ and written in spatial coordinate frame $\mathcal{C}_s$ in meters per second (m/s).

- Let $\hat{\phi}_{sb} \in \mathbb{R} = 1$ be the instantaneous "axis" of rotation of the body "b" relative to the spatial frame $\mathcal{C}_s$. Note that the notion of "rotation axis" –which is a unit vector– is a constant scalar vector 1 in $2D$. The rationale is that, the axis $\hat{\phi}$ is orthogonal to the Euclidean vector space in $\mathbb{R}^2$ (if it were not, rigid body rotations in 2D would not have preserved distance) and thus the projection of the rotation axis is always a point invariant of the frame of reference $\mathcal{C}_s$.

$$\hat{\phi}_{sb} \equiv \hat{\phi} = \frac{\phi}{||\phi||} = 1 \implies \widehat{1} = \widehat{\hat{\phi}} = \begin{pmatrix} 0 & -1 \\ 1 & 0 \end{pmatrix} \quad \forall s, b$$

- Let p^{ϕ} be the instantaneous *point* (or center) of rotation (not to be confused with the axis of rotation $\hat{\phi}$). This is the Cartesian coordinates of a point whose translational velocity is zero with respect to all points on the body, i.e ($\dot{p}_b^a \perp (p_b^a - p_b^{\phi})$). Note that the word *instantaneous* refers to the fact that $p_{b\phi}$ is not rigidly attached to the body and $\dot{p}_{b\phi} = 0$ holds only for an infinitesimal time interval δt before the coordinates of $p_{b\phi}$ changes.

- Let $p_{sb}^{\phi} = p_{s\phi}$ be the instantaneous center of rotation relative to the spatial frame $\mathcal{C}_s$.

- Let $p_b^{\phi} = p_{b\phi}$ be the instantaneous center of rotation relative to the body frame $\mathcal{C}_b$

- Let $\mathcal{C}_{\phi}$ be the coordinate frame whose origin is the instantaneous center of

rotation. All points of the body "b" undergoes pure rotation with respect to $\mathcal{C}_\phi$ with the angular velocity $\omega_{\phi b}$.

- Let the notation $\omega_{\phi b} = \omega_{sb} \in \mathbb{R}$ be the angular velocity of a rigid body "b" around it's instantaneous point of rotation $p_{s\phi} = p^{\phi}_{sb}$. Note that the orientation of $\mathcal{C}_\phi$ does not matter in regarding the angular velocity.

- Let $v_{G0} = \begin{pmatrix} \dot{p}_{G0} & \omega_{G0} \end{pmatrix}^\top \in \mathbb{R}^3$ describe the base frame translational velocity with respect to the ground frame in meters per second and the angular velocity around the ground frame origin $\hat{\phi}_{G0}$ in radians per second, respectively.

- Let $v_{Gj} = \begin{pmatrix} \dot{p}_{Gj} & \omega_{Gj} \end{pmatrix}^\top \in \mathbb{R}^3$ be the flagellum frame translational velocities with respect to the ground frame in meters per second and the angular velocities around their joint axes $\hat{\phi}_{Gj}$ in radians per second, respectively.

- Let $v_{Gn} = \begin{pmatrix} \dot{p}_{Gn} & \omega_{Gn} \end{pmatrix}^\top \in \mathbb{R}^3$ be the tip frame translational velocity with respect to the ground frame in meters per second and the angular velocity around the final joint axis $\hat{\phi}_{Gn}$ in radians per second, respectively.

- Let $\omega^a_{j-1,j} = \dot{\theta}_j \in \mathbb{R}$ be the relative angular velocity of any point p^a_j on the j^{th} segment around the j^{th} joint axis $\hat{\phi}_{j-1,j}$, which is given with respect to the previous frame $\mathcal{C}_{j-1}$ in radians per second. As illustrated in figure 6.2 the coordinate frame $\mathcal{C}_{j-1}$ corresponds to the axis of rotation for the j^{th} segment.

- Let the notation $\dot{p}^a_{sb}$ be the translational velocity of the point "a" measured with respect to the spatial frame $\mathcal{C}_s$ in m/s and written in the spatial frame $\mathcal{C}_s$.

- Let the notation ω^a_{sb} be the angular velocity of the point "a" about it's instantaneous center of rotation $p_{s\phi}$, which is given with respect to the spatial coordinate frame $\mathcal{C}_s$.

- Let the notation $v^a_{sb} = \begin{pmatrix} \dot{p}^a_{sb} & \omega^a_{sb} \end{pmatrix}^\top$ be the generalized velocity vector (or twist in [43]) describing the translational and angular velocity of the point p^a_{sb}. Note that the velocity of any point on the rigid body is zero ($v^a_{sb} = 0$) if the spatial frame and the body frame are identical i.e $s = b$.

- Let the notation $\dot{p}_b$ be the translational velocity of the body frame $\mathcal{C}_b$ origin measured with respect to the spatial frame $\mathcal{C}_s$ in m/s and written in the body frame $\mathcal{C}_b$.

Notice that the forward kinematics we presented in the previous section $f : \mathbb{T}^{n+1} \mapsto SE(2)$ is a matrix-valued function and thus taking it's first derivative to find the velocities is not straightforward.

Since we are interested in the velocity of any point p^a_b, we start from equation 6.1.1.4. The desired translation velocity $\dot{p}^a_{sb}$ can be derived as:

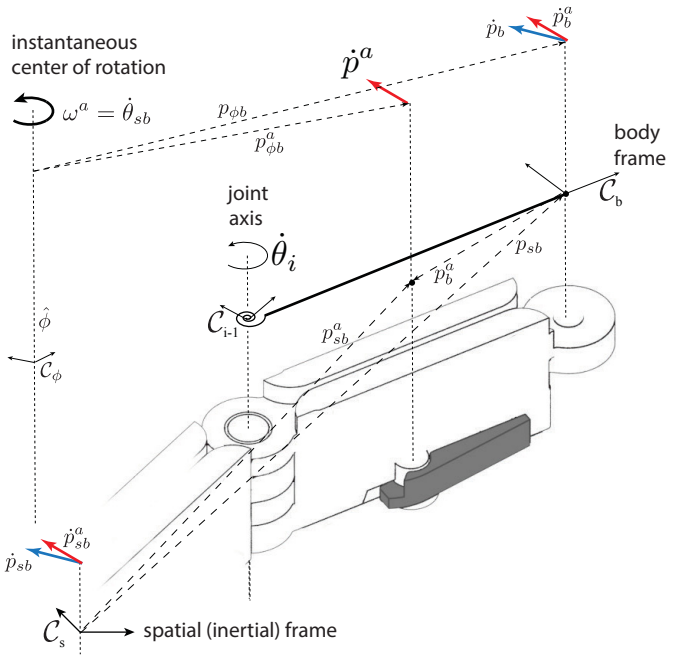

Figure 6.2: Anntena segment velocities. Notice that the colored velocity vectors are *free vectors*.

$$\begin{aligned}\frac{\mathrm{d}}{\mathrm{d}t}p^a_{sb} =& \frac{\mathrm{d}}{\mathrm{d}t}(R_{sb}p^a_b + p_{sb}) \\ &= \dot{R}_{sb}p^a_b + R_{sb}\cancelto{0}{\dot{p}^a_b} + \dot{p}_{sb} \\ \begin{pmatrix}\dot{p}^a_{sb}\\ 0\end{pmatrix} &= \underbrace{\left[\begin{array}{c:c}\dot{R}_{sb} & \dot{p}_{sb}\\ \hdashline 0 & 0\end{array}\right]}_{\dot{c}_{sb}}\begin{pmatrix}p^a_b\\ 1\end{pmatrix}\end{aligned} \tag{6.1.2.1}$$

Equation 6.1.2.1 is not a function of $\dot{\theta}$, and we do not yet have an expression for the angular velocity ω^a_{sb}. Rotation matrices can be written in terms of a rotation axis unit vector $\hat{\phi} = \frac{\phi}{||\phi||}$ and a rotation angle $\theta = ||\phi||$ such that: $R \equiv e^{\widehat{\phi}} = e^{\widehat{1}\theta}$. Note the distinction between the *unit vector* notation $\hat{\cdot}$ and the *hat operator* $\widehat{\cdot}$ that maps

vector $a \in \mathbb{R}^3$ to skew-symmetric matrix $A = -A^\top$. Continuing from equation 2.2 by substituting $\dot{R}_{sb}$ with its exponential parametrization yields:

$$
\begin{aligned}
\dot{R}_{sb} &= \frac{\mathrm{d}}{\mathrm{d}t} e^{\widehat{\phi}_{sb}} \\
&= \frac{\mathrm{d}}{\mathrm{d}t}\left(e^{\widehat{1}\theta_{sb}}\right) \quad \text{where } \theta_{sb} \text{ is the angle from spatial to body frame.} \\
&= \frac{\partial}{\partial \theta_{sb}}\left(e^{\widehat{1}\theta_{sb}}\right) \underbrace{\frac{\partial \theta_{sb}}{\partial t}}_{\dot{\theta}_{sb}} \\
&= \widehat{1} e^{\widehat{\phi\theta}_{sb}} \dot{\theta}_{sb} \\
&= \widehat{\phi}\dot{\theta}_{sb} R_{sb} \\
\dot{R}_{sb} &= \underbrace{\begin{pmatrix} 0 & -\dot{\theta}_{sb} \\ \dot{\theta}_{sb} & 0 \end{pmatrix}}_{\widehat{\omega}^a_{sb} = \widehat{\omega}_{sb}} R_{sb} \qquad (6.1.2.2) \\
\widehat{\omega}_{sb} &= \widehat{\omega}^a_{sb} = \dot{R}_{sb} R^\top_{sb} \\
\omega_{sb} &= \omega^a_{sb} = \dot{\theta}_{sb}
\end{aligned}
$$

Equation 6.1.2.2 expresses $\dot{R}_{sb}$ in terms of the angular velocity $\dot{\theta}_{sb}$ (*spatial* angular velocity) of the desired body b around the instantaneous rotation axis ϕ_{sb}, which is given in the spatial frame. Again, in our planar case, all axes of rotations are equivalent $\phi_{sb} \equiv \phi$.

This angular velocity $\dot{\theta}_{sb}$ about the instantaneous center of rotation can also be measured from the body frame b, which is precisely what a gyro sensor measures. This particular angular velocity is called *instantaneous body angular velocity* denoted as

ω_b, and it can be computed from $\widehat{\omega}_b = R_{sb}^\top \dot{R}_{sb}$. Using equation 6.1.2.2, we can show that $\omega_b = \omega_{sb}$:

$$\begin{aligned}
\underbrace{R_{sb}^\top \dot{R}_{sb}}_{\widehat{\omega}_b} &= R_{sb}^\top \begin{pmatrix} 0 & -\dot{\theta}_{sb} \\ \dot{\theta}_{sb} & 0 \end{pmatrix} R_{sb} \\
\widehat{\omega}_b &= \overbrace{R_{sb}^\top \underbrace{\begin{pmatrix} 0 & -1 \\ 1 & 0 \end{pmatrix}}_{\in SO(2)} R_{sb}}^{\text{SO2 can commute}} \dot{\theta}_{sb} \\
&= \underbrace{\begin{pmatrix} 0 & -\dot{\theta}_{sb} \\ \dot{\theta}_{sb} & 0 \end{pmatrix}}_{\widehat{\omega}_{sb}} \\
&= \dot{R}_{sb} R_{sb}^\top \\
\omega_b &= \omega_{sb}
\end{aligned} \tag{6.1.2.3}$$

In equation 6.1.2.2, $\dot{\theta}_{sb}$ can be written with respect to joint angular velocity vector $\dot{\theta}$ whose components $\dot{\theta}_j$ are with respect to the j^{th} joint axis, similarly to way angular orientation is presented in equation 6.1.1.5.

$$\dot{\theta}_{sb} = \sum_{k=s+1}^{b} \dot{\theta}_k - \sum_{k=b+1}^{s} \dot{\theta}_k \quad \text{where } s, b \in \{-1, 0, ..., n\}$$

$\omega_{\phi b}^a = \omega_{\phi b} = \omega_{sb}^a$ is the angular velocity of the point p_b^a, with respect to the spatial frame about the *instantaneous center of rotation* p^ϕ. Since p^ϕ is the same for all points of a rigid body b, any point p_b^a will have the same angular velocity. Therefore, the desired quantity ω_{sb}^a is equal to the body frame angular velocity ω_{sb}.

Proof. By the definition of angular velocity pertaining pure rotation, the velocity of the body origin can be written as:

$$\begin{aligned} \widehat{\omega}_{\phi b} p_{\phi b} &= \dot{p}_{\phi b} \\ R_{s\phi} \widehat{\omega}_{\phi b} p_{\phi b} &= R_{s\phi} \dot{p}_{\phi b} \\ &= \dot{p}_{sb} \end{aligned}$$

Similarly, for the velocity of the point "a" on the body we have:

$$\begin{aligned} \widehat{\omega}^a_{\phi b} p^a_\phi = \widehat{\omega}_{\phi b} p^a_\phi &= \dot{p}^a_{\phi b} \\ R_{s\phi} \widehat{\omega}_{\phi b} p^a_\phi &= R_{s\phi} \dot{p}^a_{\phi b} \\ &= \dot{p}^a_{sb} \\ &= \dot{R}_{sb} p^a_b + \dot{p}_{sb} \end{aligned}$$

Subtracting both equations we get:

$$\begin{aligned} R_{s\phi} \widehat{\omega}_{\phi b} p^a_\phi - R_{s\phi} \widehat{\omega}_{\phi b} p_{\phi b} &= \dot{R}_{sb} p^a_b \\ R_{s\phi} \widehat{\omega}_{\phi b} (p^a_\phi - p_{\phi b}) &= \dot{R}_{sb} p^a_b \\ R_{s\phi} \widehat{\omega}_{\phi b} R^\top_{s\phi} R_{sb} p^a_b &= \dot{R}_{sb} p^a_b \\ \widehat{\omega}_{\phi b} R_{sb} p^a_b &= \dot{R}_{sb} p^a_b \\ \widehat{\omega}_{\phi b} &= \dot{R}_{sb} R^\top_{sb} = \widehat{\omega}_{sb} \\ \widehat{\omega}^a_{\phi b} = \widehat{\omega}_{\phi b} &= \widehat{\omega}_{sb} = \widehat{\omega}_b \end{aligned} \tag{6.1.2.4}$$

Now, we can write the angular velocity $\widehat{\omega}^a_b$ with respect to any other body frame b'

such that $b' \neq b$ while keeping the spatial frame $\mathcal{C}_s$ the same. Unsurprisingly, the angular velocity remains the same in the planar case.

$$\begin{aligned} \widehat{\omega}_{\phi b} p_{\phi b} &= \dot{p}_{\phi b} \\ \widehat{\omega}_{\phi b} p_b &= \dot{p}_b \\ R_{bb'}^\top \widehat{\omega}_{\phi b} R_{bb'} R_{bb'}^\top p_b &= R_{bb'}^\top \dot{p}_b \\ \omega_{\phi b} R_{bb'}^\top \widehat{1} R_{bb'} p_{b'} &= \dot{p}_{b'} \\ \widehat{\omega}_{\phi b} p_{b'} &= \widehat{\omega}_{b'} p_{b'} \end{aligned} \tag{6.1.2.5}$$

□

$$\omega_{sb}^a = \omega_{sb} = \dot{\theta}_{sb} = \begin{cases} -\sum_{k=b+1}^{s} \dot{\theta}_k & \text{if } -1 \leq b < s \leq n \\ 0 & \text{if } b = s \\ \sum_{k=s+1}^{b} \dot{\theta}_k & \text{if } n \geq b > s \geq -1 \end{cases} \tag{6.1.2.6}$$

Substituting into 6.1.2.2 yields the desired parametric $\dot{R}_{sb}$:

$$\dot{R}_{sb} = \begin{cases} \underbrace{-\sum_{k=b+1}^{s} \dot{\theta}_k \begin{pmatrix} 0 & -1 \\ 1 & 0 \end{pmatrix}}_{\widehat{\omega}_{sb}} R_{sb} & \text{if } -1 \leq b < s \leq n \\ 0 & \text{if } b = s \\ \underbrace{\sum_{k=s+1}^{b} \dot{\theta}_k \begin{pmatrix} 0 & -1 \\ 1 & 0 \end{pmatrix}}_{\widehat{\omega}_{sb}} R_{sb} & \text{if } n \geq b > s \geq -1 \end{cases} \tag{6.1.2.7}$$

$$= \begin{cases} \left(\sum_{k=b+1}^{s} -\dot{\theta}_k \right) \begin{pmatrix} \sin \sum_{k=b+1}^{s} \theta_k & -\cos \sum_{k=b+1}^{s} \theta_k \\ \cos \sum_{k=b+1}^{s} \theta_k & \sin \sum_{k=b+1}^{s} \theta_k \end{pmatrix} & \text{if } -1 \leq b < s \leq n \\ 0 & \text{if } b = s \\ \left(\sum_{k=s+1}^{b} \dot{\theta}_k \right) \begin{pmatrix} \sin \sum_{k=s+1}^{s} -\theta_k & -\cos \sum_{k=s+1}^{s} -\theta_k \\ \cos \sum_{k=s+1}^{s} -\theta_k & \sin \sum_{k=s+1}^{s} -\theta_k \end{pmatrix} & \text{if } n \geq b > s \geq -1 \end{cases} \tag{6.1.2.8}$$

Equation 6.1.2.8 is the explicit form of $\dot{R}_{sb}$ parametrized by body and spatial frame indices, joint angles and joint velocities.

In equation 6.1.2.1, the translational velocity of the desired frame origin $\dot{p}_{sb}$ can be computed by taking the time derivative of p_{sb}, the last column of C_{sb} in equation 6.1.1.3:

$$\begin{aligned} \dot{p}_{sb} &= \frac{d}{dt} p_{sb} \\ &= \frac{\partial p_{sb}}{\partial \theta} \dot{\theta} \\ &= \left[\begin{array}{c:c:c:c} \frac{\partial p_{sb}}{\partial \theta_0} & \frac{\partial p_{sb}}{\partial \theta_1} & \cdots & \frac{\partial p_{sb}}{\partial \theta_n} \end{array} \right] \begin{pmatrix} \dot{\theta}_0 \\ \vdots \\ \dot{\theta}_n \end{pmatrix} \end{aligned} \tag{6.1.2.9}$$

$$\text{where} \quad \frac{\partial p_{sb}}{\partial \theta_i} = \begin{cases} \sum_{k^*=b+1}^{i-1} \begin{pmatrix} -\sin \sum_{k=k^*+1}^{s} -\theta_k \\ \cos \sum_{k=k^*+1}^{s} -\theta_k \end{pmatrix} l & \text{if } -1 \leq b < i \leq s \leq n \\ \begin{pmatrix} 0 \\ 0 \end{pmatrix} & \text{else} \\ \sum_{k^*=i}^{b} \begin{pmatrix} -\sin \sum_{k=s+1}^{k^*} \theta_k \\ \cos \sum_{k=s+1}^{k^*} \theta_k \end{pmatrix} l & \text{if } n \geq b \geq i > s \geq -1 \end{cases}$$

Substituting the explicit expressions $\dot{R}_{sb}$ and $\dot{p}_{sb}$, respectively, into equation 6.1.2.1 yields the explicit expression for $\dot{p}^a_{sb}$.

$$\begin{pmatrix} \dot{p}^a_{sb} \\ 0 \end{pmatrix} = \underbrace{\begin{bmatrix} \dot{R}_{sb} & \dot{p}_{sb} \\ 0 & 0 \end{bmatrix}}_{\dot{\mathcal{C}}_{sb}} \begin{pmatrix} p^a_b \\ 1 \end{pmatrix} \tag{6.1.2.10}$$

Like with the hybrid transformation H_{sb}, we can slightly alter equation 6.1.2.10 and combine it with the expression 6.1.2.6 to get the complete velocity vector $\begin{pmatrix} \dot{p}^a_{sb} & \omega^a_{sb} \end{pmatrix}^\top = df(\theta, \dot{\theta}, \Pi)$ with given parameters $\Pi = \{l, s, b, p^a_b\}$ we were seeking to find in the beginning of this section:

$$\begin{pmatrix} \dot{p}^a_{sb} \\ \omega^a_{sb} \end{pmatrix} = \underbrace{\begin{bmatrix} \dot{R}_{sb} & \dot{p}_{sb} \\ 0 & \dot{\theta}_{sb} \end{bmatrix}}_{\dot{H}_{sb}} \begin{pmatrix} p^a_b \\ 1 \end{pmatrix} \tag{6.1.2.11}$$

We call $\dot{H}_{sb}$ the hybrid transformation that takes any planar body point coordinate p_b^a and provides the translational and angular velocity of that point with respect to the spatial frame $\mathcal{C}_s$ and written in the spatial frame $\mathcal{C}_s$.

6.1.3 Hybrid Velocity vs Body Velocity

We define the body velocity vector $V_b = (v_b, \omega_b)$ as the translational and angular velocities v_b, ω_b of the body origin p_b with respect to the spatial frame $\mathcal{C}_s$ in the body frame coordinates $\mathcal{C}_b$. In the 2D case, this vector is expressed in a matrix form in the book, *A Mathematical Introduction to Robotic Manipulation* by *Murray, Li, Sastry* [43], as $V_b^\wedge$ ($\wedge$ is the *wedge* operator) in the following form:

$$
\begin{aligned}
V_b &= \begin{pmatrix} v_b \\ \omega_b \end{pmatrix} = \begin{pmatrix} \dot{p}_b \\ \omega_b \end{pmatrix} \\
V_b^\wedge &= \mathcal{C}_{sb}^{-1}\dot{\mathcal{C}}_{sb} \\
&= \left[\begin{array}{c:c} R_{sb}^\top \dot{R}_{sb} & R_{sb}^\top \dot{p}_{sb} \\ \hdashline 0 & 0 \end{array}\right] \\
&= \left[\begin{array}{c:c} \widehat{\omega}_b & \dot{p}_b \\ \hdashline 0 & 0 \end{array}\right] \\
&= \left[\begin{array}{cc:c} 0 & -\omega_b & \dot{p}_b \\ \omega_b & 0 & \\ \hdashline 0 & 0 & 0 \end{array}\right]
\end{aligned}
\tag{6.1.3.1}
$$

The matrix 6.1.3.1 takes the coordinates of a point p_b^a given in $\mathcal{C}_b$, and returns the

velocity $\dot{p}_b^a$ of that point with respect to the spatial frame written in body frame. In the planar case, the angular velocity of p_b^a is the same as the body frame angular velocity ω_b as we showed in 6.1.2.3 and 6.1.2.6. So with a slight modification of $V_b^\wedge$, we get the transformation from the homogeneous coordinates p_b^a to $(\dot{p}_b^a, \omega_b^a)$; namely:

$$\begin{aligned} \omega_{sb}^a = \omega_b^a = \omega_{sb} = \omega_b = \dot{\theta}_{sb} \\ \begin{pmatrix} \dot{p}_b^a \\ \omega_b^a \end{pmatrix} &= \underbrace{\left[\begin{array}{c:c} \widehat{\omega}_b & \dot{p}_b \\ \hdashline 0 & \omega_b \end{array}\right]}_{V_b^\wedge} \begin{pmatrix} p_b^a \\ 1 \end{pmatrix} \\ &= \underbrace{\left[\begin{array}{c:c} \widehat{\omega}_b & V_b \\ \hdashline 0 & \end{array}\right]}_{V_b^\wedge} \begin{pmatrix} p_b^a \\ 1 \end{pmatrix} \end{aligned} \tag{6.1.3.2}$$

These body coordinate quantities are useful since they usually correspond to the outputs of a robot's onboard sensors. Also, this modified body velocity matrix for the planar case has V_b as its last column. Like in the above equation 6.1.3.2, earlier in equation 6.1.2.11, we computed $(\dot{p}_{sb}^a, \omega_{sb}^a)$, which is simply $(\dot{p}_{sb}^a, \omega_{sb}^a)$ given in the spatial frame coordinates $\mathcal{C}_s$. Therefore, the last column of that transformation $\dot{H}_{sb}$ is the translational and angular velocities of the body origin p_b with respect to the spatial frame $\mathcal{C}_s$ in the *spatial* frame coordinates $\mathcal{C}_s$. This column is referred as the *Hybrid velocity* vector V_h in [43]. Here we show that transformation between $V_b^\wedge$ and $\dot{H}_{sb}$ is $\in SE(2)$.

$$
\begin{aligned}
\text{Recall:} \quad \begin{pmatrix} \dot{p}^a_{sb} \\ \omega^a_{sb} \end{pmatrix} &= \underbrace{\left[\begin{array}{c:c} \dot{R}_{sb} & \dot{p}_{sb} \\ \hdashline 0 & \omega_{sb} \end{array}\right]}_{\dot{H}_{sb}} \begin{pmatrix} p^a_b \\ 1 \end{pmatrix} \\
&= \underbrace{\left[\begin{array}{c:c} \dot{R}_{sb} & V_h \\ \hdashline 0 & \end{array}\right]}_{\dot{H}_{sb}} \begin{pmatrix} p^a_b \\ 1 \end{pmatrix} \\
&= \left[\begin{array}{c:c} \widehat{\omega}_{sb} R_{sb} & R_{sb} \underbrace{\dot{p}_b}_{v_b} \\ \hdashline 0 & \omega_{sb} \end{array}\right] \begin{pmatrix} p^a_b \\ 1 \end{pmatrix} \\
&= \left[\begin{array}{c:c} R_{sb} & 0 \\ \hdashline 0 & 1 \end{array}\right] \underbrace{\left[\begin{array}{c:c} \widehat{\omega}_{sb} & \dot{p}_b \\ \hdashline 0 & \omega_{sb} \end{array}\right]}_{\equiv V_b^\wedge} \begin{pmatrix} p^a_b \\ 1 \end{pmatrix}
\end{aligned}
$$

$$
\begin{pmatrix} \dot{p}^a_{sb} \\ \omega^a_{sb} \end{pmatrix} = \left[\begin{array}{c:c} R_{sb} & 0 \\ \hdashline 0 & 1 \end{array}\right] \begin{pmatrix} \dot{p}^a_b \\ \omega^a_b \end{pmatrix}
$$

$$
\dot{H}_{sb} = \left[\begin{array}{c:c} R_{sb} & 0 \\ \hdashline 0 & 1 \end{array}\right] V_b^\wedge \tag{6.1.3.3}
$$

It's also obvious that the *hybrid velocity* of the body frame with respect to the spatial frame $V_h = \begin{pmatrix} \dot{p}_{sb} & \omega_{sb} \end{pmatrix}^\top$ has the same relation with the body velocity V_b:

$$
V_h = \left[\begin{array}{c:c} R_{sb} & 0 \\ \hdashline 0 & 1 \end{array}\right] V_b \tag{6.1.3.4}
$$

6.1.4 Hybrid Velocity vs Spatial Velocity

As we showed earlier in equation 6.1.2.11, $\dot{H}_{sb}$ relates relative coordinates of a point "a" p_b^a to spatial translational and angular velocity coordinates $\begin{pmatrix} \dot{p}_{sb}^a & \omega_{sb}^a \end{pmatrix}^\top$. In contrast, $V_b^\wedge$ in equation 6.1.3.2 relates the same relative coordinates to the body velocity coordinates $\begin{pmatrix} \dot{p}_b^a & \omega_b^a \end{pmatrix}^\top$. Note that both $\begin{pmatrix} \dot{p}_{sb}^a & \omega_{sb}^a \end{pmatrix}^\top$ and $\begin{pmatrix} \dot{p}_b^a & \omega_b^a \end{pmatrix}^\top$ are measured with respect to the same spatial frame s but written in different reference frames s and b respectively.

When position coordinates p^a are not given in body frame coordinates but instead given in spatial frame coordinates, i.e. p_{sb}^a is available instead of p_b^a, then we can similarly define a relationship between p_{sb}^a and the spatial velocities $\begin{pmatrix} \dot{p}_{sb}^a & \omega_{sb}^a \end{pmatrix}^\top$. In [43], this transformation is referred as the *spatial velocity* matrix $V_s^\wedge$ such that:

$$\begin{aligned} V_s^\wedge &= \dot{\mathcal{C}}_{sb}\mathcal{C}_{sb}^{-1} \\ &= \left[\begin{array}{c:c} \dot{R}_{sb}R_{sb}^\top & -\dot{R}_{sb}R_{sb}^\top p_{sb} + \dot{p}_{sb} \\ \hdashline 0 & 0 \end{array}\right] \end{aligned} \tag{6.1.4.1}$$

For the planar case, we use equations 6.1.2.6 and 6.1.2.11 to derive a slightly modified the expression for $V_s^\wedge$ which also incorporates angular velocity:

Recall: $\omega_b = \omega_{sb}$

$$
\begin{aligned}
\text{Recall:} \quad \begin{pmatrix} \dot{p}^a_{sb} \\ \omega^a_{sb} \end{pmatrix} &= \underbrace{\left[\begin{array}{c:c} \dot{R}_{sb} & \dot{p}_{sb} \\ \hdashline 0 & \omega_{sb} \end{array}\right]}_{\dot{H}_{sb}} \begin{pmatrix} p^a_b \\ 1 \end{pmatrix} \\
\text{Recall:} \quad \begin{pmatrix} p^a_b \\ 1 \end{pmatrix} &= \mathcal{C}^{-1}_{sb} \begin{pmatrix} p^a_{sb} \\ 1 \end{pmatrix} \\
\begin{pmatrix} \dot{p}^a_{sb} \\ \omega^a_{sb} \end{pmatrix} &= \underbrace{\left[\begin{array}{c:c} \dot{R}_{sb} & \dot{p}_{sb} \\ \hdashline 0 & \omega_{sb} \end{array}\right] \mathcal{C}^{-1}_{sb}}_{V_s^\wedge} \begin{pmatrix} p^a_{sb} \\ 1 \end{pmatrix} \\
&= \underbrace{\left[\begin{array}{c:c} \dot{R}_{sb} & \dot{p}_{sb} \\ \hdashline 0 & \omega_{sb} \end{array}\right] \left[\begin{array}{c:c} {R_{sb}}^\top & -{R_{sb}}^\top p_{sb} \\ \hdashline 0 & 1 \end{array}\right]}_{V_s^\wedge} \begin{pmatrix} p^a_{sb} \\ 1 \end{pmatrix} \\
&= \left[\begin{array}{c:c} \dot{R}_{sb} R^\top_{sb} & -\dot{R}_{sb} R^\top_{sb} p_{sb} + \dot{p}_{sb} \\ \hdashline 0 & \omega_{sb} \end{array}\right] \begin{pmatrix} p^a_{sb} \\ 1 \end{pmatrix} \\
\begin{pmatrix} \dot{p}^a_{sb} \\ \omega^a_{sb} \end{pmatrix} &= \left[\begin{array}{c:c} \widehat{\omega}_{sb} & -\widehat{\omega}_{sb} p_{sb} + \dot{p}_{sb} \\ \hdashline 0 & \omega_{sb} \end{array}\right] \begin{pmatrix} p^a_{sb} \\ 1 \end{pmatrix}
\end{aligned} \tag{6.1.4.2}
$$

So, similar to the body velocity V_b the *spatial velocity* vector V_s is defined as:

$$
V_s = \begin{pmatrix} -\widehat{\omega}_{sb} p_{sb} + \dot{p}_{sb} \\ \omega_{sb} \end{pmatrix} \tag{6.1.4.3}
$$

Also it's evident that the relationship between $\dot{H}_{sb}$ and $V_s^\wedge$ holds in the planar case as given in [43]:

$$
\dot{H}_{sb} = V_s^\wedge \mathcal{C}_{sb} \tag{6.1.4.4}
$$

Finally we can construct the relation between the *hybrid velocity* and *spatial velocity* and show that its also $\in SE(2)$:

$$\underbrace{\begin{pmatrix}\dot{p}_{sb}\\ \omega_{sb}\end{pmatrix}}_{V_h} = \left[\begin{array}{c:c} I & \begin{pmatrix}0 & -1\\ 1 & 0\end{pmatrix} p_{sb} \\ \hdashline 0 & 1 \end{array}\right] \underbrace{\begin{pmatrix}-\widehat{\omega}_{sb}p_{sb} + \dot{p}_{sb}\\ \omega_{sb}\end{pmatrix}}_{V_s} \tag{6.1.4.5}$$

where I is the identity matrix and $\begin{pmatrix}0 & -1\\ 1 & 0\end{pmatrix} = \widehat{\phi}$ corresponds to the axis of rotation $\hat{\phi} = 1$ for the planar case.

For completeness, we will use the relations V_h vs V_b and V_h vs V_s given in equations 6.1.3.4 and 6.1.4.5 respectively to derive the relationship between V_s and V_b. Equating the two relationships yield:

$$\begin{aligned}
\left[\begin{array}{c:c} I & \begin{pmatrix}0 & -1\\ 1 & 0\end{pmatrix} p_{sb} \\ \hdashline 0 & 1 \end{array}\right] V_s &= \left[\begin{array}{c:c} R_{sb} & 0 \\ \hdashline 0 & 1 \end{array}\right] V_b \\
V_s &= \left[\begin{array}{c:c} I & -\begin{pmatrix}0 & -1\\ 1 & 0\end{pmatrix} p_{sb} \\ \hdashline 0 & 1 \end{array}\right] \left[\begin{array}{c:c} R_{sb} & 0 \\ \hdashline 0 & 1 \end{array}\right] V_b \\
&= \underbrace{\left[\begin{array}{c:c} R_{sb} & \begin{pmatrix}0 & 1\\ -1 & 0\end{pmatrix} p_{sb} \\ \hdashline 0 & 1 \end{array}\right]}_{Ad_H} V_b
\end{aligned} \tag{6.1.4.6}$$

This particular matrix $Ad_H \in SE(2)$ which relates body velocities to spatial velocities in the planar case is called the *Adjoint Matrix* in [43].

6.2 Stiffness of Nitinol

Purpose

This report presents the NiTi-wire-inherited inter-segmental stiffness characteristics of our gen-3.5 antenna with varying NiTi diameters ranging from 0.01 to 0.030 inches. Our goal is to come up with a reliable empirical functional relationship between the NiTi wire diameter and the resulting inter-segmental rotational stiffness value.

Experiment

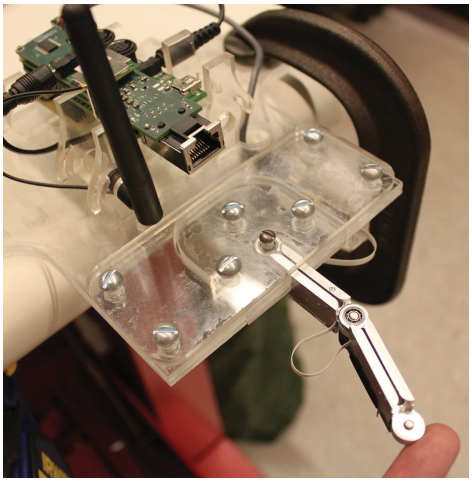

Figure 6.3: Experimental setup

Procedure

- A single antenna segment was attached to another immobilized segment mounted on a test platform. The second segment hinges freely with respect to the first segment which is connected via I^2C to a base *Gumstix* computer. Note that this is the intended default antenna configuration and thus the results of this experiment will be valid for the normal operation of the antenna on mobile platforms (such as RDK). (Figure 6.3)

- An approximately 2 inch long cylindrical Nitinol wire with chosen diameter was placed on the inter-segmental joint with both ends sitting inside the 0.033 inch wide aluminum channels.

- The wire is fixed at one of the channels (in this case the immobilized channel) via an integrated set screw. The other end of the wire is allowed to slide free inside the channel. (Figure 6.4)

- The hinged segment is brought to an arbitrary angle while the base computer is ready to sample the angle data from the segment.

- The hinged segment is let to oscillate while the base computer samples at approximately 1000Hz.

- The experiment for a given wire diameter is repeated 5 times.

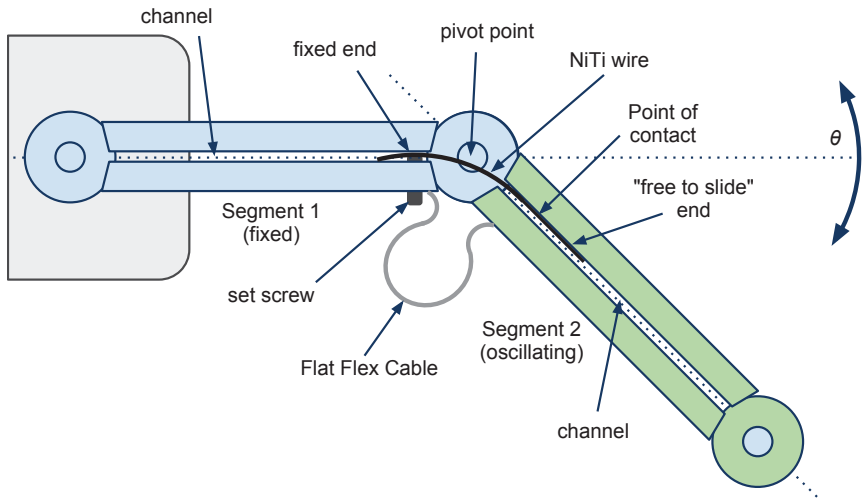

Figure 6.4: Top view drawing of the experiment

- The experiment is repeated for a total of 20 different diameters.

- To address the effects of the FFC coupling, the NiTi wire element is then taken out and the apparatus is rotated such that the segment oscillation becomes parallel to the direction of gravity. See Figure 6.5 for the changed configuration.

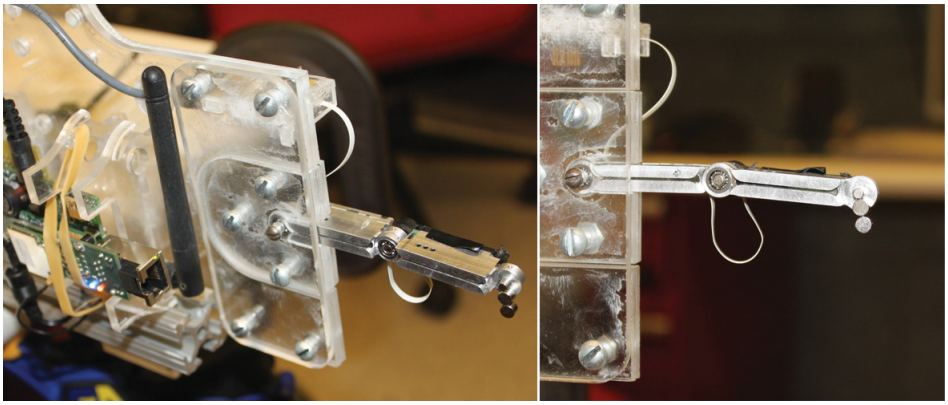

Figure 6.5: Experimental setup for addressing FFC stiffness

- In order to bring the relative angle between the two segments to 180 degrees (by compressing the FFC), additional mass consisting of two disk magnets ($m = 0.94g$) was attached to the end of the hinged segment.

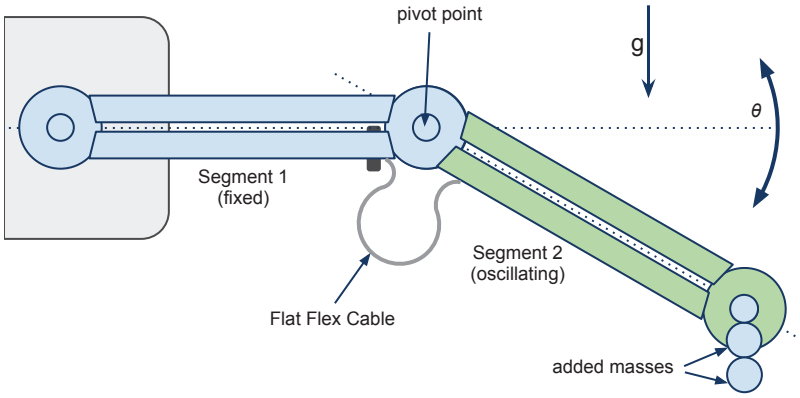

Figure 6.6: Top view drawing of the FFC experiment

- 10 trials are performed in which the data is collected by letting the free segment to oscillate against the gravity See Figure 6.6 .

- The masses of the segment and NiTi specimens were measured using precision equipment (Figure 6.7) with an error margin of $0.1mg$

- The length of each used NiTi wire is measured with a caliper of $0.01mm$ accuracy.

Figure 6.7: All mass measurements have an accuracy of $0.1mg$

Theory

We can solve this problem by approaching from two coupled perspectives:

1. A cantilevered beam deflection problem.

2. A 1-DOF underdamped simple harmonic oscillator problem.

The first perspective to the experiment as a beam deflection problem allows the computation of the NiTi stiffness directly via material and geometrical properties. Assuming the NiTi wire is a cylindrical rod fixed at one end and loaded at a single point at length L, then the stiffness κ of an equivalent rotational spring or k of an equivalent linear spring would be:

$$\kappa, k = \frac{3EI}{L^3} \tag{6.2.0.7}$$

where E is the Young's Modulus of the particular NiTi alloy; I is the area moment of inertia of the cross-section and L is the length of the cantilever beam. Their multiplication EI is also called the *bending stiffness*. Although a very straight forward computation, the Young's Modulus value of NiTi alloy is tricky to figure out. *SAES Memry*[1], a US based shape memory alloy manufacturer, has the following remark about the elastic modulus of Nitinol:

> The question about the Young's Modulus of Nitinol is very difficult to answer. In fact there are a multitude of moduli that could be derived from a stress-strain diagram. And even worse: none of them make sense for conventional calculations based on a linear elasticity theory. The reason is the stress-strain plateau that we find in the stress range of interest between 1 and approximately 8%. Here the Young's Modulus is very close to zero and even worse, there is one value for loading and one for unloading. The only approach which makes sense is based on a numerical approach using a non-linear and hysteresis-afflicted material model.

Thus, this approach's problem is the lack of accurate and robust information of either the bending stiffness EI or E of NiTi. L can be measured directly and the area moment inertia I for circular cross-sections can be computed from the radius data. See Table 6.2 for the relevant information.

[1] http:/www.memry.com

$$I = \frac{\pi r^4}{4} \tag{6.2.0.8}$$

The second perspective is more promising. We know that there is a simple relationship between the undamped natural angular frequency ω_n of a simple harmonic oscillator with its corresponding linear stiffness k.

$$\omega_n = \sqrt{\frac{k}{m}} \tag{6.2.0.9}$$

where m corresponds to the mass of the equivalent mass-spring system. For rotational systems (our case) this relationship can be expressed as:

$$\omega_n = \sqrt{\frac{\kappa}{J}} \tag{6.2.0.10}$$

where J corresponds to the mass moment of inertia of the oscillating body with respect to its center of rotation and κ is the associated rotational stiffness. Note that the units for linear stiffness k and rotational stiffness κ are different; which are N/m and Nm/rad respectively. Figure 6.8 shows the distinction between the rotational and linear models which have the same fundamental frequencies.

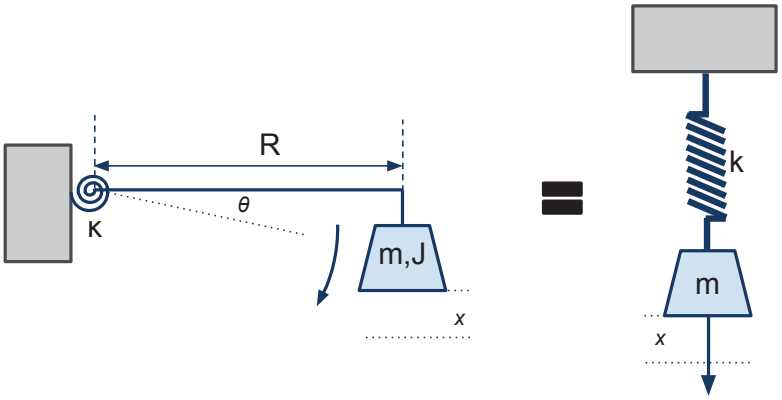

Figure 6.8: A rotational and linear harmonic oscillators with identical natural frequencies

We also know from our data, categorically, that the damped natural response of the oscillator remain underdamped. See Nitinol Raw Data for the complete set of plots for all the trials. It is possible to extract this damped natural frequency ω_d by noting the largest frequency response from the *Fast Fourier Transform* (FFT) of the sampled time-domain signal. The relationship between the observed damped natural angular frequency ω_d and ω_n is defined as:

$$\omega_d = \omega_n \sqrt{1 - \zeta^2} \tag{6.2.0.11}$$

where ζ is defined as the *damping ratio*, which characterizes the exponential decay envelope of the transient response as:

$$y(t) = y(0)e^{-\zeta\omega_n t} \tag{6.2.0.12}$$

ζ can be extracted from the observed data if the response is oscillatory, meaning underdamped. Given the amplitudes of the local maxima, one can compute the difference of their natural logarithms (*logarithmic decrement,* Δ) which is proportional to the damping ratio ζ.

$$\Delta = \frac{1}{j-i} \ln \left(\frac{peak_i}{peak_j} \right), peak_i > peak_j, j > i \in \mathbb{Z} \tag{6.2.0.13}$$

$$\zeta = \frac{\Delta/2\pi}{\sqrt{1 + (\Delta/2\pi)^2}} \tag{6.2.0.14}$$

where $peak_i, j$ are the local maxima of the decaying signal. $peak_i$ is an earlier local maximum (and thus has a larger value) than $peak_j$. In this experiment we calculated every possible Δ for each trial of a given NiTi diameter and then took the average to compute ζ.

$$\bar{\Delta} = \frac{\sum_{i=1}^{n-1} \sum_{j=i+1}^{n} \frac{1}{j-i} \ln \left(\frac{peak_i}{peak_j} \right)}{\sum_{i=1}^{n-1} i} \tag{6.2.0.15}$$

where n is the number of detected local maxima. Figure 6.9 shows an example data (NiTi diameter $0.016in$, trial #1) with the detected local maxima (red circles) and

the decay envelope based on ζ and ω_n.

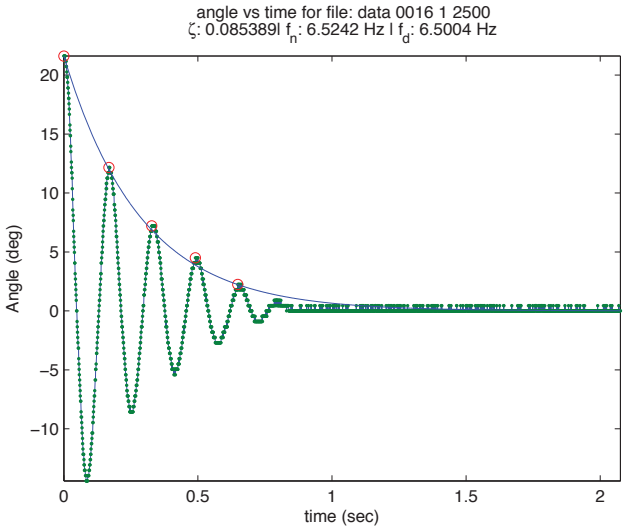

Figure 6.9: Damping ratio is found using logarithmic decrements between the local maxima

The theory and methods described above allow the computation of the equivalent linear stiffness k_{eq} or the equivalent rotational stiffness κ_{eq} of our mechanical oscillator, which is affected by two stiffness components. Even though the dominant stiffness is inherited from the NiTi wire, κ_{eq} (and k_{eq}) is still contaminated by the spring-like *Flat Flex Cable* component spanning between the two segments. Thus it would be more accurate to model our system as a mass suspended by two parallel springs. Figure 6.10 shows these equivalent models.

We know that the equivalent stiffness κ_{eq} of two torsional springs in parallel is the sum of the individual stiffnesses (same as the linear case):

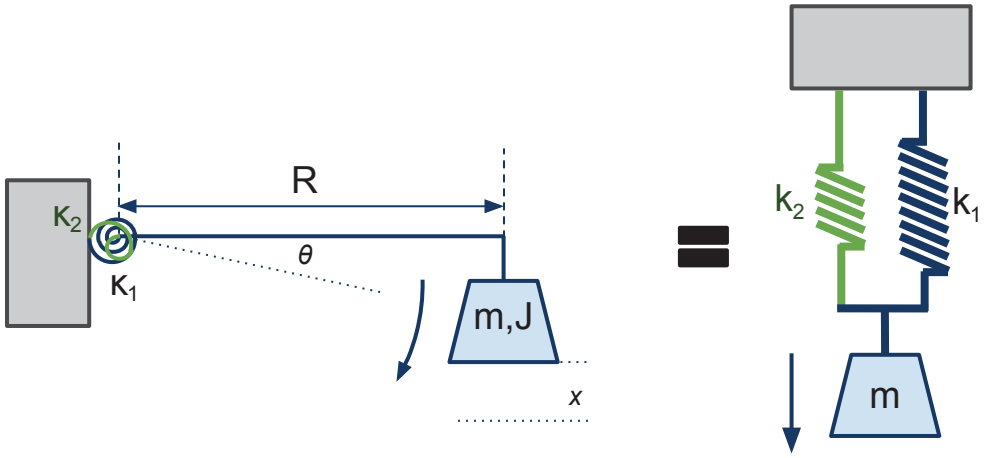

Figure 6.10: Two systems with equivalent fundamental frequencies

$$\kappa_{eq} = \kappa_1 + \kappa_2 \tag{6.2.0.16}$$

From our data, we know that the system remains underdamped even when no NiTi wire is present. See Flat Flex Cable (FFC) Data for the plot showing the systems response on all 10 trials. Therefore it is possible to employ the same methods to compute the rotational stiffness of the joint that only has the FFC coupling (κ_2) from the data. Subtracting this base stiffness from the intersegmental-joint stiffness κ_{eq} (with the NiTi wire) would then provide the rotational stiffness of the joint with only the tunable NiTi wire κ_1. Here we assume that the effect of the FFC coupling cable in terms of mass and inertia is negligible to the overall system as the mass ratio between the whole segment and FFC is about 2 orders of magnitude.

It should be noted here that we treat Coulomb friction at the joint (ball bearing) as the primary source of damping. This is as opposed to the viscous damping in which damping is proportional to velocity. If damping was dominated by viscous forces, we would expect the damping ratio to increase as the angular velocity increased. Yet, as we can see from Figure 6.13, the damping decreases as radius (also angular frequency) increases. In fact the correlation coefficient between angular frequency and damping comes out to be -0.9168, which suggests a strong dependency. In the case of very small diameter NiTi wires (See Nitinol Raw Data), it can be seen that the high damping ratios cause the total number of oscillations under 3, which makes the *logarithmic decrement* method inapplicable. However, we know that the Coulomb friction introduced to the oscillator stays constant except in the case of large diameter wires, where additional friction is introduced at the sliding end of the segment (See Figure 6.11). So the ζ of the very small diameter NiTi wires can be estimated by extrapolating from the rest of the data. In order to figure out what kind of curve fitting should be used for the extrapolation, we need to relate NiTi diameter to ζ. For a damped rotational harmonic oscillator we have:

$$\zeta = \frac{c}{2\sqrt{\kappa J}} \tag{6.2.0.17}$$

where c is the damping coefficient. Substituting equations 6.2.0.7 and 6.2.0.8 into 6.2.0.17 yields:

$$\zeta^2 = \frac{c^2 L^3}{3EJ\pi r^4} \tag{6.2.0.18}$$

$$\zeta = \sqrt{\frac{c^2 L^3}{3EJ\pi}} \frac{1}{r^2} \tag{6.2.0.19}$$

$$\zeta \propto \frac{1}{d^2} \tag{6.2.0.20}$$

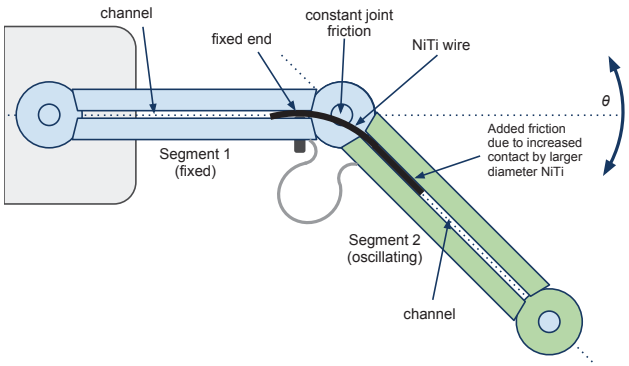

Figure 6.11: Damping sources: Friction at the joint stays constant for all diameters. For small diameter wires, *sliding-end* friction is negligible. For large diameter wires, there is an overall increase of friction in the system

It shows that there is an *inverse-squre* relationship between the damping ratio ζ and radius. Again, it is important to note that the mass moment of inertia J of the system is assumed to be constant regardless of which diameter NiTi wire is used. One should always be careful if this assumption could still be made for larger diameters. As a side note, if the NiTi wire is to oscillate as a free cantilever thin rod without any additional mass, the damping-radius relationship would be *inverse-cubic*. Figure 6.13 shows the result of the inverse-square extrapolation. We feel confident that the accuracy loss

due to this estimation is minimal as we know the effects of damping to the natural frequency (and thus to the stiffness) in general is already quite small ($< 1\%$).

Finally, knowing f_n for a given NiTi wire diameter provides the desired inter-segmental joint rotational stiffness value κ. At this point, the only step left to find is the empirical constant between NiTi diameter and that joint stiffness by fitting a curve to their theoretical relationship. Our equivalent model of a torsional spring can be translated into a bending rod model by substituting equation 6.2.0.8 directly into 6.2.0.7, which yields the order of the power law:

$$\kappa = \frac{3E\pi r^4}{4L^3} \tag{6.2.0.21}$$

$$\kappa \propto r^4 \tag{6.2.0.22}$$

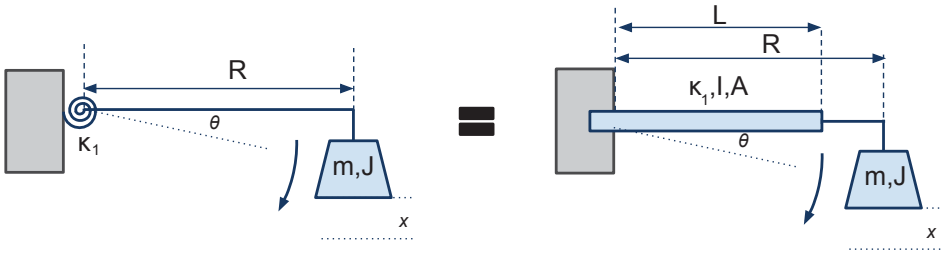

Figure 6.12: The equivalent "mass-torsional spring" model can be translated to a "mass-elastic rod" model.

Fortunately, we can solve for the constant $\frac{E}{L^3}$ directly using the experimentally determined stiffness values κ and then substitute it back into the relationship in order to finish the formula.

Data

Table 1 lists the constant values regarding the segment and the NiTi wire. The inertia values for the segment with respect to the joint is computed using a CAD model. The inertia of the added disk magnets are computed using the formula $J_{add} = \frac{1}{12}m_{add}(3r_{add}^2 + h_{add}) + m_{add}L_s^2$. The effective NiTi arc-length L is measured from the point where the Nitinol is fixed on the proximal segment to the point of contact on the distal segment.

Parameter	*Denotation*	*Unit*	*Value*
NiTi diameter range	d_{niti}	mm	0.254–0.762
Nickel Young's Modulus	E_{ni}	GPa	200
Titanium Young's Modulus	E_{ti}	GPa	116
Nickel density	ρ_{ni}	g/cm^3	8.908
Titanium density	ρ_{ti}	g/cm^3	4.507
Manufacturer's NiTi composition	$Ni_{vs}Ti$	%	$56vs44$
Segment mass	m_s	g	6.7175
Segment length	L_s	mm	40
Added masses (disk magnet x2)	m_{add}	g	0.94
Added mass radius	r_{add}	mm	2.39
Added mass height	h_{add}	mm	3.14
Joint to Segment COM distance	R	mm	17.6
Segment inertia	J_s	kgm^2/rad	$3.25 \cdot 10^{-6}$
Added mass inertia	J_{add}	kgm^2/rad	$1.506 \cdot 10^{-6}$
Effective NiTi length	L	mm	18

Table 6.1: Parameters which have a potential to affect the antenna performance

For individual component mass values of the segment, please refer to Mass Data.

From the manufacturer's composition values and the individual elements' densities we can compute the alloy density:

$$\rho_{niti} = 0.442\rho_{ti} + 0.558\rho_{ni} = 6.963 g/cm^3 \tag{6.2.0.23}$$

Table 6.2 shows the geometric and mass properties of each NiTi specimen with a different diameter used in this experiment.

d (in)	*A* (mm^2)	L_{niti} *(mm)*	*I* (mm^4)	*Measured* m_{niti} *(g)*	*Predicted* m_{niti} *(g)*	*mass % error*
0.010	0.0507	48.47	0.000204	0.0159	0.0171	7.551
0.011	0.0613	53.21	0.000299	0.0208	0.0227	9.208
0.012	0.0730	51.56	0.000424	0.0241	0.0262	8.692
0.013	0.0856	50.06	0.000584	0.0282	0.0298	5.844
0.014	0.0993	52.77	0.000785	0.0343	0.0365	6.387
0.015	0.1140	50.83	0.001034	0.0370	0.0403	9.053
0.016	0.1297	44.26	0.001339	0.0377	0.0400	6.035
0.017	0.1464	49.00	0.001706	0.0468	0.0500	6.755
0.018	0.1642	50.35	0.002145	0.0537	0.0576	7.179
0.019	0.1829	46.85	0.002663	0.0557	0.0597	7.127
0.020	0.2027	54.46	0.003269	0.0723	0.0769	6.301
0.021	0.2235	52.63	0.003974	0.0760	0.0819	7.745
0.022	0.2452	51.78	0.004786	0.0837	0.0884	5.638
0.024	0.2919	59.25	0.006779	0.1120	0.1204	7.506
0.025	0.3167	46.92	0.007981	0.0980	0.1035	5.572
0.026	0.3425	53.90	0.009337	0.1194	0.1286	7.664
0.027	0.3694	50.32	0.010858	0.1207	0.1294	7.226
0.028	0.3973	51.34	0.012558	0.1349	0.1420	5.269
0.029	0.4261	54.08	0.014451	0.1526	0.1605	5.152
0.030	0.4560	51.92	0.016550	0.1554	0.1649	6.088

Table 6.2: Measured vs Predicted mass values for the used NiTi specimen

The predicted mass is computed by the computed density of NiTi and the measured geometric dimensions. Based on the values above, the mean percent error or bias of

the measurements (or given constants) is 6.9% with a standard error of just 1.2%. This suggests of a systematic error of about 5% somewhere in our measurements or given composition values. In the stiffness computation, we will use our the direct mass measurements as the true mass values.

Results

The stiffness of the inter-segmental joint due to the FFC coupling κ_2 is computed by:

$$\kappa_2 = \frac{1}{10}\sum_{i=1}^{10}(J_s + J_{add})\omega_{n(i)}^2 \tag{6.2.0.24}$$

where 10 is the number of trials for this experiment.

$f_d \pm \sigma_{f_d}\ (Hz)$	$\zeta \pm \sigma_\zeta$	$f_n \pm \sigma_{f_n}\ (Hz)$	$\kappa_2 \pm \sigma_{\kappa_2}(\frac{Nm}{rad})$
2.900 ± 0.140	0.140 ± 0.0041	2.930 ± 0.0658	0.0016 ± 0.0005

Table 6.3: Stiffness and frequency values without the NiTi wires. σ_{f_d} shows the standard deviation of the damped natural frequency for the set of 10 trials. σ_ζ shows the standard error associated with the damping ratio.

The rotational stiffness of the inter-segmental joint $\kappa_{eq(i)}$ due to each individual NiTi wire with the FFC coupling is computed by:

$$\kappa_{eq(i)} = \frac{1}{5}\sum_{j=1}^{5} J_s \omega_{n(i,j)}^2 \tag{6.2.0.25}$$

where $i \in \mathbb{Z} \leq 20$ is the diameter index and $j \in \mathbb{Z} \leq 5$ denotes the index of the trials per diameter (5 trials each). Please note again that for the $0.010, 0.011, 0.012$ inch diameter wires, the undamped angular natural frequency ω_n could not be computed through logarithmic decrement method since the response did not have at least three distinguishable peaks (even though the response was indeed underdamped). In these cases the undamped angular natural frequencies are predicted by extrapolating through a inverse square power law fit (Figure 6.13). The fitted curve (*ezyfit toolbox for Matlab*) for empirically predicting ζ shown in the figure is:

$$\zeta = 2.2125 \cdot 10^{-}5 \cdot d^2 \tag{6.2.0.26}$$

Finally the rotational stiffness of the joint due to the NiTi wire $\kappa_{1(i)}$ per diameter is computed by:

$$\kappa_{1(i)} = \kappa_{eq(i)} - \kappa_2 \tag{6.2.0.27}$$

The frequencies (f_n, f_d), damping ratios (ζ) and stiffness values (κ_{eq}, κ_1) for a given NiTi diameter is presented in Table 6.4.

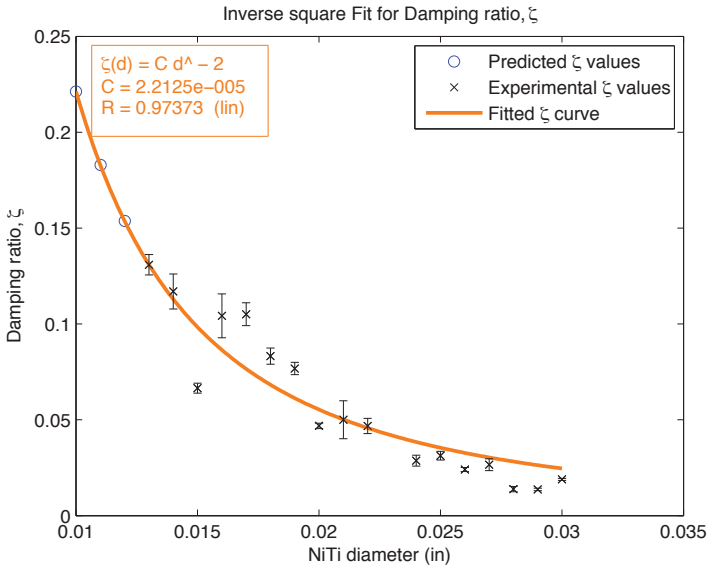

Figure 6.13: Damping ratio ζ decreases as radius (and frequency) increases. ζ values for the first three diameters have been extrapolated from the remaining data.

d (in)	$f_d \pm \sigma_{f_d}$ (Hz)	$\zeta \pm \sigma_\zeta$	$f_n \pm \sigma_{f_n}$ (Hz)	$\kappa_{eq} \pm \sigma_{\kappa_{eq}} (\frac{Nm}{rad})$	$\kappa_1 (\frac{Nm}{rad})$
0.010	2.867 ± 1.543	$0.161^* \pm 0.004$	$2.905^* \pm 0.260$	$0.0011^* \pm 0.0012$	< 0.0006
0.011	4.068 ± 0.303	$0.149^* \pm 0.004$	$4.113^* \pm 0.066$	$0.0022^* \pm 0.0004$	0.0006 ± 0.0002
0.012	4.268 ± 0.384	$0.137^* \pm 0.004$	$4.308^* \pm 0.081$	$0.0024^* \pm 0.0005$	0.0008 ± 0.0003
0.013	5.134 ± 0.075	0.131 ± 0.005	5.179 ± 0.0448	0.0035 ± 0.0004	0.0019 ± 0.0003
0.014	5.434 ± 0.091	0.117 ± 0.009	5.472 ± 0.0815	0.0039 ± 0.0007	0.0023 ± 0.0006
0.015	5.868 ± 0.218	0.066 ± 0.003	5.881 ± 0.0696	0.0045 ± 0.0007	0.0029 ± 0.0005
0.016	6.468 ± 0.074	0.104 ± 0.011	6.503 ± 0.1244	0.0054 ± 0.0013	0.0038 ± 0.0012
0.017	6.834 ± 0.204	0.105 ± 0.006	6.873 ± 0.0929	0.0061 ± 0.0010	0.0045 ± 0.0009
0.018	7.468 ± 0.183	0.083 ± 0.004	7.494 ± 0.0880	0.0072 ± 0.0011	0.0056 ± 0.0010
0.019	8.068 ± 0.150	0.077 ± 0.003	8.092 ± 0.0762	0.0084 ± 0.0010	0.0068 ± 0.0009
0.020	9.034 ± 0.075	0.047 ± 0.001	9.044 ± 0.0546	0.0105 ± 0.0008	0.0089 ± 0.0006
0.021	9.601 ± 0.253	0.050 ± 0.010	9.614 ± 0.3391	0.0119 ± 0.0052	0.0103 ± 0.0052
0.022	10.435 ± 0.149	0.047 ± 0.004	10.447 ± 0.1627	0.0140 ± 0.0027	0.0124 ± 0.0027
0.024	12.335 ± 0.118	0.029 ± 0.003	12.340 ± 0.2114	0.0196 ± 0.0042	0.0180 ± 0.0042
0.025	12.968 ± 0.182	0.031 ± 0.002	12.975 ± 0.1764	0.0217 ± 0.0037	0.0201 ± 0.0037
0.026	13.736 ± 0.091	0.024 ± 0.001	13.740 ± 0.1085	0.0243 ± 0.0024	0.0227 ± 0.0024
0.027	15.469 ± 0.074	0.027 ± 0.003	15.475 ± 0.2984	0.0308 ± 0.0075	0.0292 ± 0.0074
0.028	17.102 ± 0.091	0.014 ± 0.001	17.104 ± 0.2852	0.0377 ± 0.0079	0.0361 ± 0.0079
0.029	18.101 ± 0.091	0.014 ± 0.001	18.103 ± 0.1537	0.0422 ± 0.0045	0.0406 ± 0.0045
0.030	17.903 ± 0.278	0.019 ± 0.001	17.907 ± 0.1258	0.0413 ± 0.0036	0.0397 ± 0.0036

Table 6.4: Stiffness and frequency values for the given diameter NiTi wires. σ_{f_d} shows the standard deviation of the damped natural frequency for a given set of 5 trials per diameter. σ_ζ shows the standard error associated with the damping ratios. *: Extrapolated values.

In doing the error analysis for this experiment, we treated the mass values as accurate and took the standard deviations of the damped natural frequencies (σ_{f_d}) and the damping ratios (σ_ζ) as the only random error sources. Note that we assigned the mean standard error for the ζ values (0.0041) as the standard error of the predicted ζ values. Hence the standard error propagation of the results are computed in the following fashion:

$$\sigma_{\omega_d} = \sqrt{4\pi^2\sigma_{f_d}^2} \tag{6.2.0.28}$$

$$\sigma_{\omega_n} = \omega_n\sqrt{\left(\frac{\sigma_{\omega_d}}{\omega_d}\right)^2 + \left(\frac{\sigma_\zeta}{\zeta}\right)^2 + 2\left(\frac{\sigma_{\omega_d}\sigma_\zeta}{\omega_d\zeta}\right)0.9168} \tag{6.2.0.29}$$

$$\sigma_{f_n} = \sqrt{\left(\frac{1}{2\pi}\right)^2\sigma_{\omega_n}^2} \tag{6.2.0.30}$$

$$\sigma_{\kappa_{eq}} = 2\kappa_{eq}\left(\frac{\sigma_{\omega_n}}{\omega_n}\right) \tag{6.2.0.31}$$

$$\sigma_{\kappa_1} = \sqrt{\sigma_{\kappa_{eq}}^2 + \sigma_{\kappa_0}^2} \tag{6.2.0.32}$$

where -0.9168 is the correlation coefficient $\rho_{\omega_d,\zeta}$ computed via *Matlab's corrcoef* method.

The final task of figuring out the functional relationship between the NiTi radius and stiffness requires the computation of the constant $\frac{3E\pi}{4L^3}$.

$$\frac{3E\pi}{4L^3} = \frac{1}{20}\sum_{i=1}^{20}\frac{\kappa_{1_i}}{r_i^4} = 2.0614 \cdot 10^{12} \tag{6.2.0.33}$$

Figure 6.14 shows the relationship between NiTi radius and stiffness. The red curve is the theoretical prediction function from equation 6.2.0.33. So, the empirical relationship between the radius of a NiTi wire and the joint stiffness can be expressed as:

$$\boxed{\kappa_1 = 2.0614 \cdot 10^{12} r^4} \tag{6.2.0.34}$$

where r is the radius of the wire in meters and κ_1 in Nm/rad.

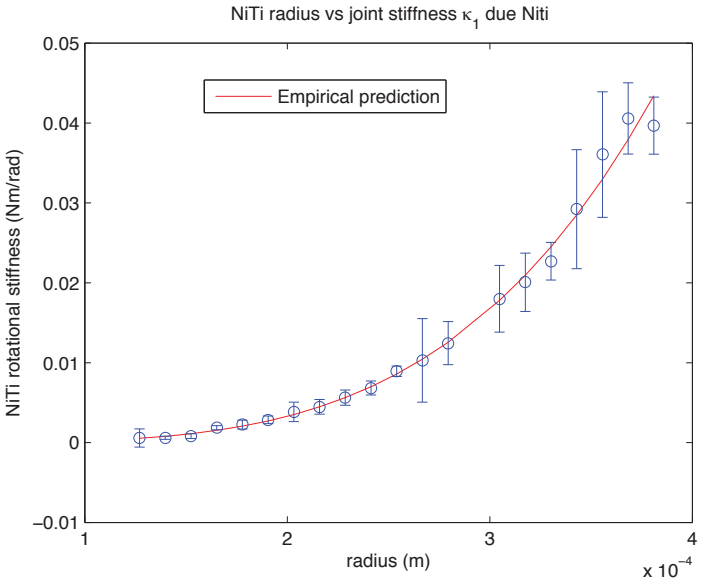

Figure 6.14: The relationship between NiTi radius and joint stiffness.

Nitinol Raw Data

The following 20 plots show the angle (in degrees) vs time (in seconds) data of the experiment. Each plot contains the five trials associated with a given NiTi diameter. Each data has been trimmed such they start from their global extremum and then centered on the x-axis based on their respective steady-state response. The set of trials are then cross-correlated via matlab's *xcorr* method.

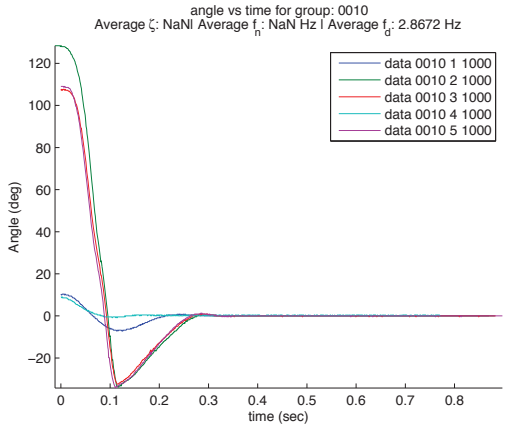

Figure 6.15: Trials for NiTi $d = 0.010$in

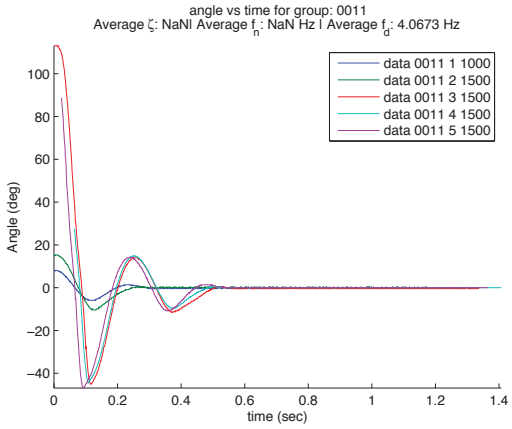

Figure 6.16: Trials for NiTi $d = 0.011$in

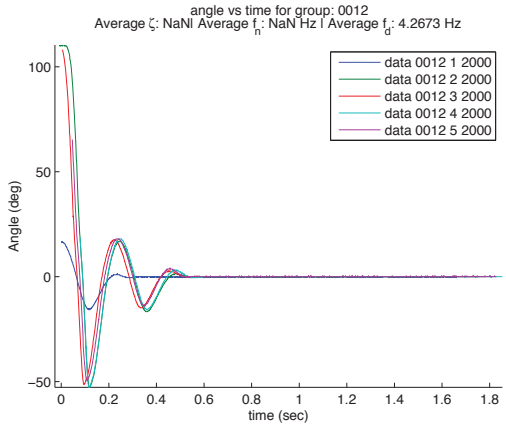

Figure 6.17: Trials for NiTi $d = 0.012$in

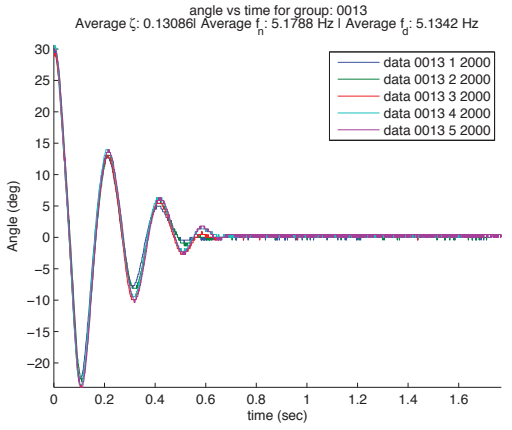

Figure 6.18: Trials for NiTi $d = 0.013$in

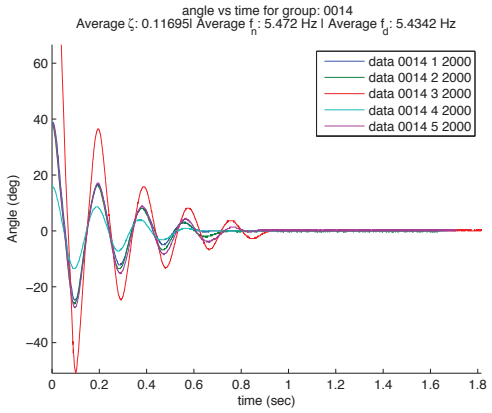

Figure 6.19: Trials for NiTi $d = 0.014$in

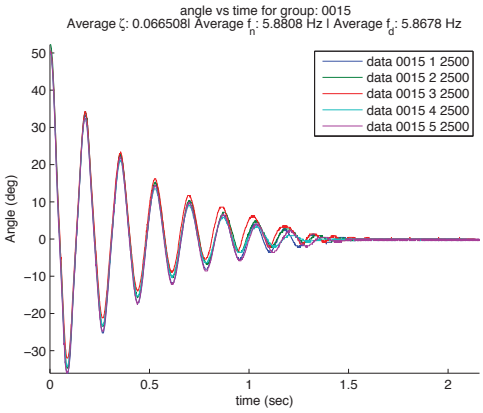

Figure 6.20: Trials for NiTi $d = 0.015$in

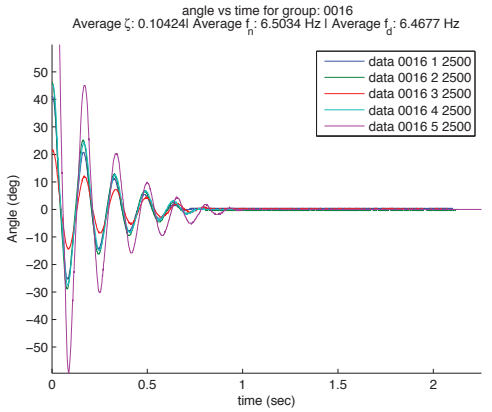

Figure 6.21: Trials for NiTi $d = 0.016$in

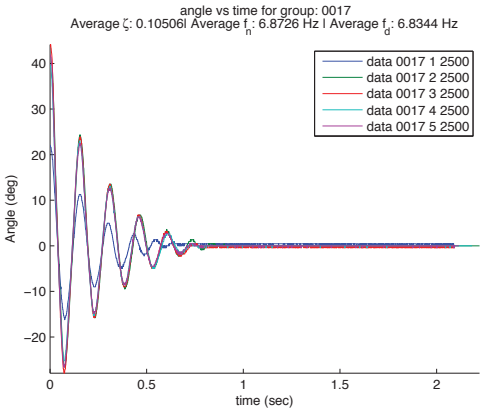

Figure 6.22: Trials for NiTi $d = 0.017$in

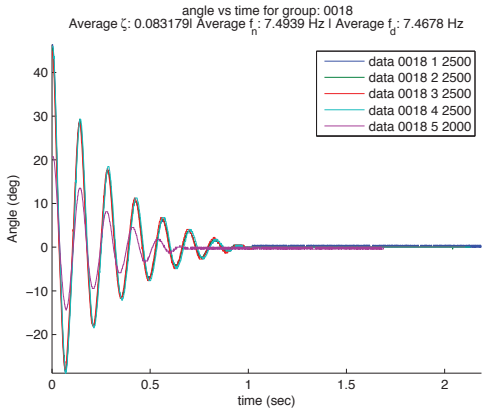

Figure 6.23: Trials for NiTi $d = 0.018$in

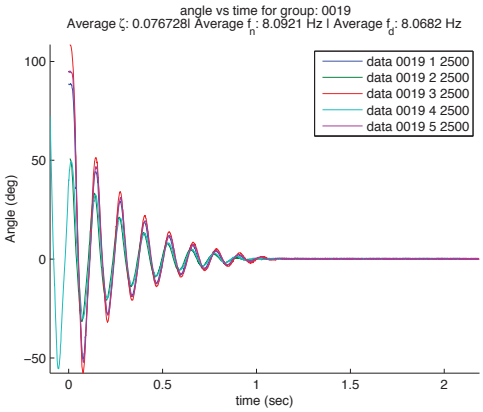

Figure 6.24: Trials for NiTi $d = 0.019$in

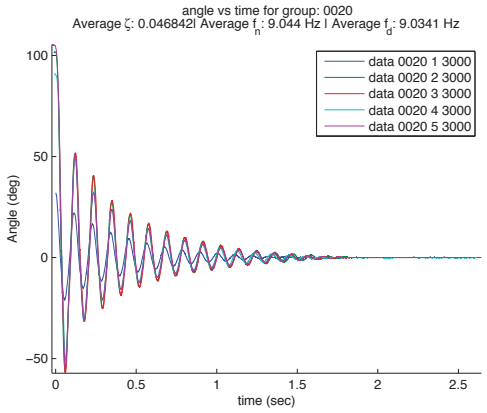

Figure 6.25: Trials for NiTi $d = 0.020$in

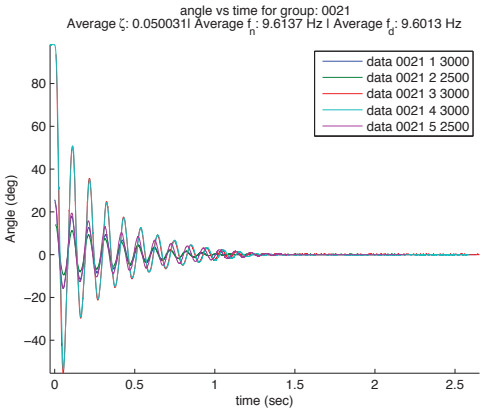

Figure 6.26: Trials for NiTi $d = 0.021$in

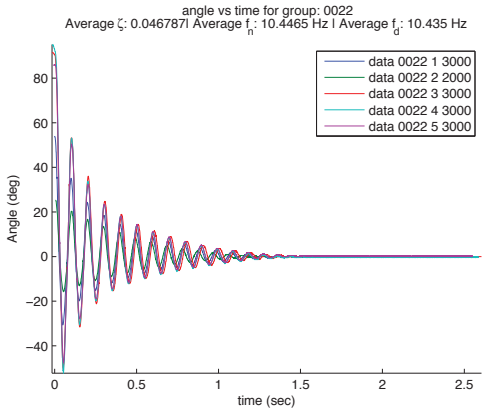

Figure 6.27: Trials for NiTi $d = 0.022$in

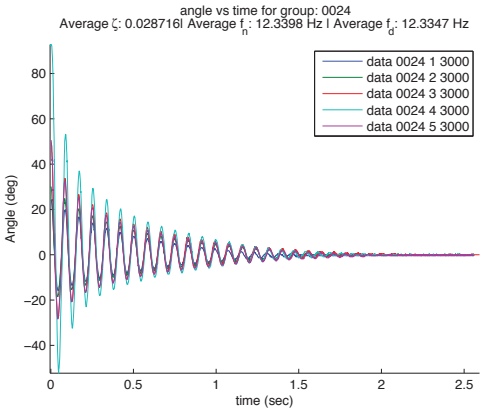

Figure 6.28: Trials for NiTi $d = 0.024$in

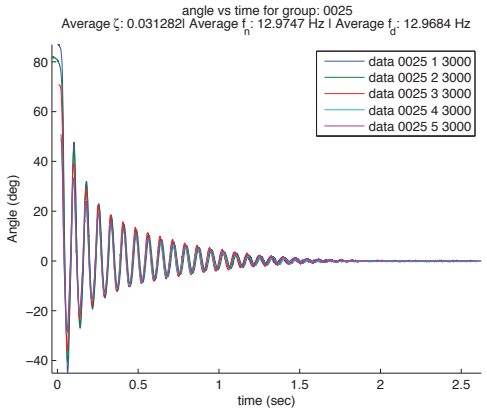

Figure 6.29: Trials for NiTi $d = 0.025$in

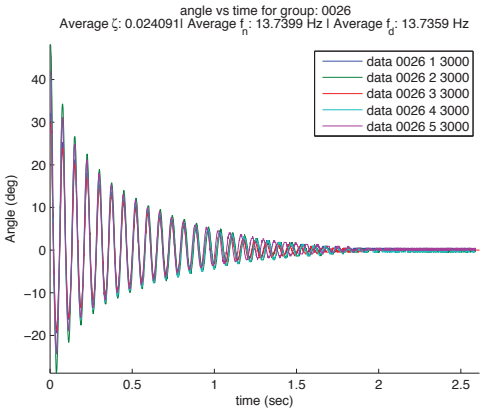

Figure 6.30: Trials for NiTi $d = 0.026$in

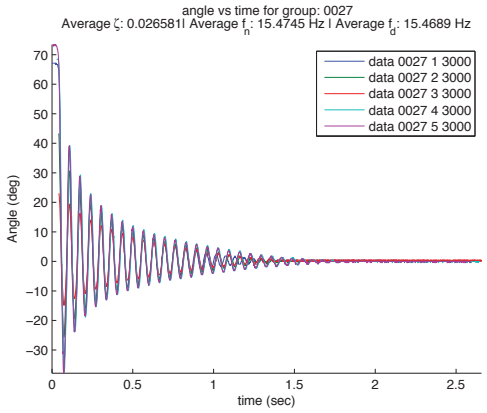

Figure 6.31: Trials for NiTi $d = 0.027$in

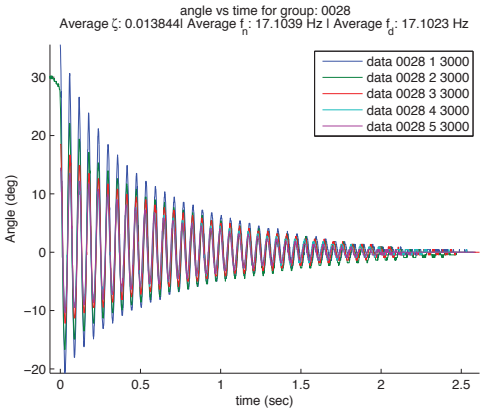

Figure 6.32: Trials for NiTi $d = 0.028$in

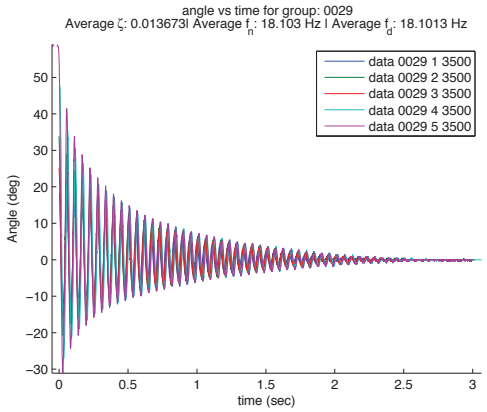

Figure 6.33: Trials for NiTi $d = 0.029$in

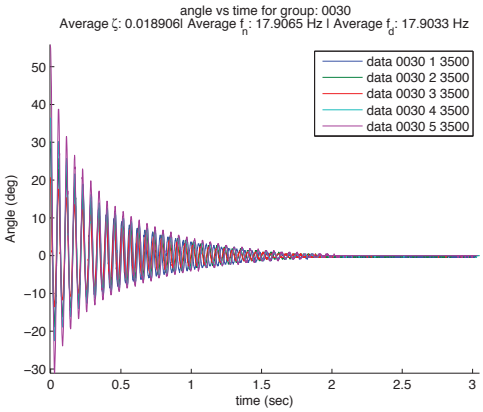

Figure 6.34: Trials for NiTi $d = 0.030$in

Flat Flex Cable (FFC) Data

The following plot shows the angle (in degrees) vs time (in seconds) data for all 10 trials in the absence of a NiTi wire. The oscillatory response is due to the flat flex cable spanning between the segments. This cable carries the essential signal and power flow between the segments. Again, each data has been trimmed such they start from their global extremum and then centered on the x-axis based on their respective steady-state response. The set of trials are then cross-correlated via matlab's *xcorr* method.

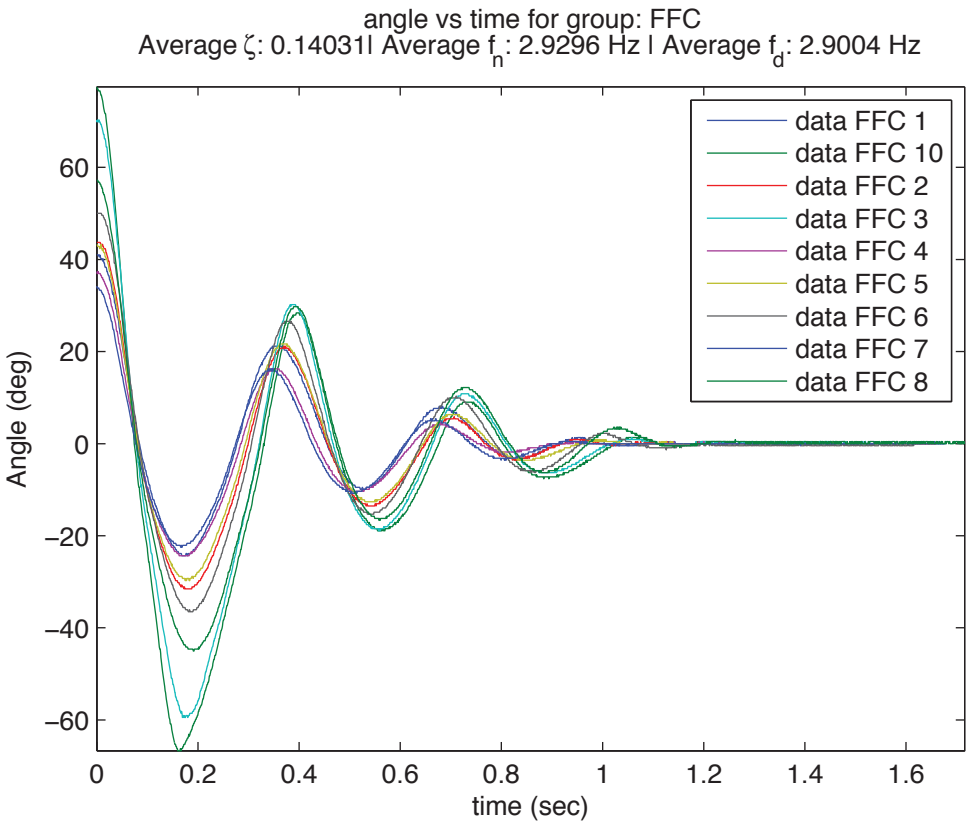

Figure 6.35: Trials without the NiTi element

Mass Data

The following table presents the mass and volume values of a version 3.5 antenna segment components. Each relevant piece has been modeled in CAD (Pro/E) for their volume information. The solder weight is computed by subtracting the sum of individual components from the fully assembled PCB weight. This information can be used to compute density distribution of a segment, which is used in finding the coordinates of the center of mass.

Component	*Mass (g)*	*CAD Volume (mm^3)*
Shell (top)	3.3775	1408.590
Shell (bottom) (aluminum)	1.4207	527.100
Shell (bottom) (plastic)	0.5743	527.100
Assembled PCB (all)	2.0203	882.071
Assembled PCB (vertical)	1.0863	444.732
Assembled PCB (horizontal)	0.9378	437.339
PCB (vertical)	0.6820	339.781
PCB (horizontal)	0.7272	365.012
MCU	0.0968	29.4847
Magnet	0.3366	50.2368
Segment Connector	0.0215	8.43598
Programming Connector	0.1059	27.0934
Ball Bearing	0.2930	46.7869
Contact Sensor (left)	0.0217	9.66091
Contact Sensor (right)	0.0213	9.66075
Resistor	0.0051	1.4548
Capacitor	0.0168	4.78516
Angle Sensor	0.0784	27.8653
LED	0.0180	0.273584
FFC Coupling	0.0786	N/A
Set Screw	0.0186	N/A
Shell Screw	0.1152	N/A
Solder	0.0692	N/A

Table 6.5: Mass and volume values of individual segment components.

Below are the renders of the component cad models used to approximate volume

information.

Figure 6.36: Shell (top)

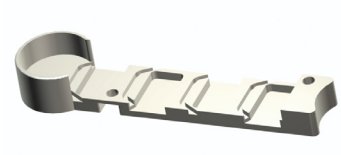

Figure 6.37: Shell (bottom)

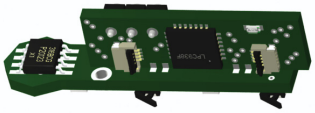

Figure 6.38: Assembled PCB (all)

Figure 6.39: Assembled PCB (vertical)

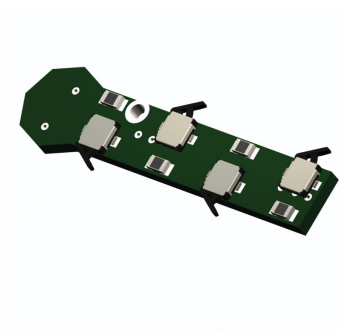

Figure 6.40: Assembled PCB (horizontal)

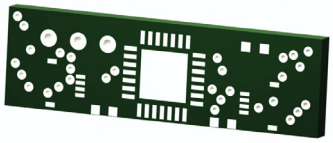

Figure 6.41: PCB (vertical)

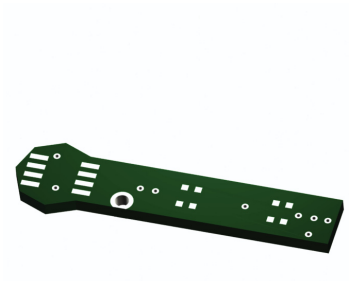

Figure 6.42: PCB (horizontal)

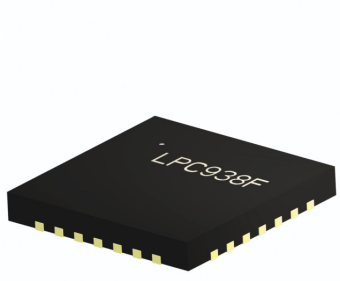

Figure 6.43: MCU

Figure 6.44: Magnet

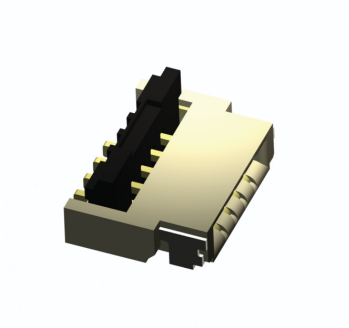

Figure 6.45: Segment Connector

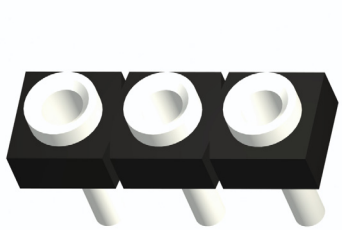

Figure 6.46: Programming Connector

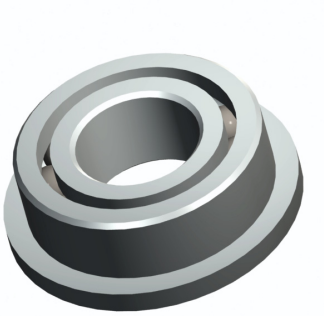

Figure 6.47: Ball Bearing

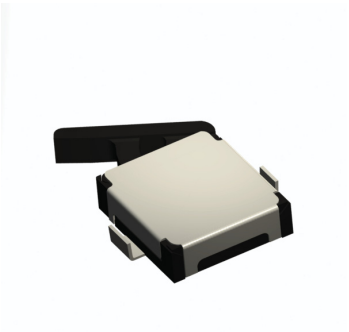

Figure 6.48: Contact Sensor (left)

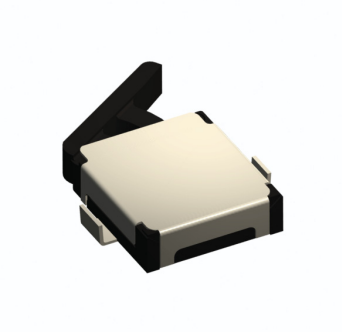

Figure 6.49: Contact Sensor (right)

Figure 6.50: Resistor

Figure 6.51: Capacitor

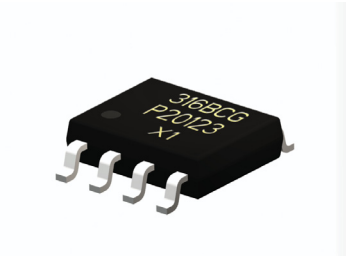

Figure 6.52: Angle Sensor

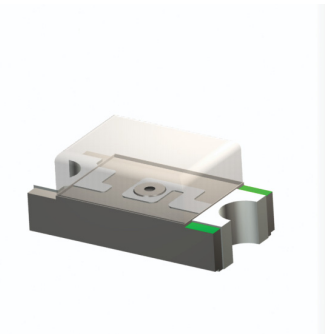

Figure 6.53: LED

Figure 6.54: Set Screw

Figure 6.55: Shell Screw

Below is the complete render of the segment assembly. The total mass is 6.7175 grams.

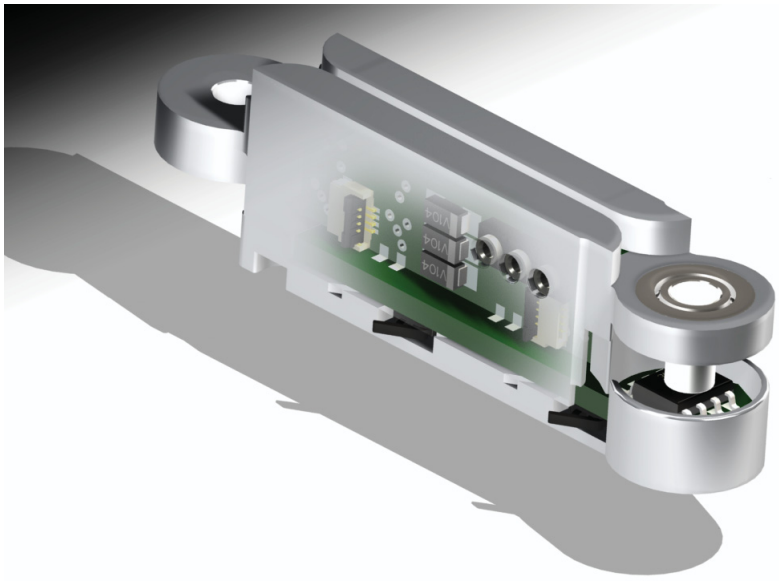

Figure 6.56: Limbs Lab Antenna Segment v3.5

6.3 Animal Handling

Animal handling and related experiments were done by Jusuk Lee and Jean-Michel Mongeau at the *Poly-Petal Lab* in the University of California, Berkeley.

Adult male American cockroaches, *Periplaneta americana* (Linnaeus 1758), were acquired from a commercial vendor (Carolina Biological Supply Company, Burlington, NC, USA) and housed in plastic cages maintained at a temperature of $27°C$. Cockroaches were exposed to a $12h : 12h$ light:dark cycle and given fruits, dog chow and water ad libitum.

Prior to each experiment, we prepared each cockroach using a previously described protocol [52]. While the cockroaches were anesthetized, we taped two small round retroreflective dots dorsally aligned with the body anterior-posterior axis. The dots were placed directly over the wings but did not restrict their motion. These two dots allowed us to estimate the cockroach position and heading vector from the high-speed videos. To prevent visual cues from influencing wall-following behavior, we covered the compound eyes and ocelli with white nail polish while carefully avoiding the headscape joint. Following the preparation we allowed cockroaches at least $24h$ for recovery at room temperature prior to conducting experiments.

6.4 Optical Tracking

Apparatus

To verify the orientation and translation accuracy of our three dimensional reconstruction we built a simple experimental platform (6.57). It consists of a 1920×1280 digital camera (*Logitech C920*) and a macro lens with $10\times$ magnification mounted on a fixed frame concentrically. We attached a 15×15 checkerboard pattern with 4mm squares to a manual ball-socket tilt stage which is free to move on a graph paper divided into 0.25 inch squares. The focal distance of the lens is adjusted manually to keep the checkerboard pattern in focus when it's parallel to the camera CCD.

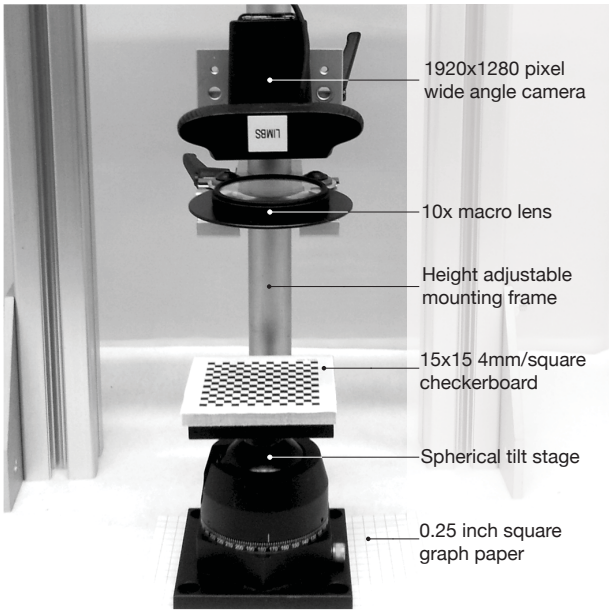

Figure 6.57: Camera calibration verification apparatus

Software

We interact with our camera via our in-house developed cross-platform software [2] written in C++ . It's built on the *Boost* libraries for handling user interface, image capturing and processing threads; maintaining asynchronous communication between the circular buffers without redundant data cloning; parsing command-line options and configurations; serving date-time information as well as clocks for periodic operations; and handling OS-independent directory operations. The software is solely dependent on *OpenCV* for frame grabbing and image processing and on *matio+HDF5* libraries for interfacing with *Mathworks Matlab* type data.We handle the OS-specific library options and linking via *Cmake*.

The *camera calibration* feature of our software is based on *OpenCV*'s conventional camera calibration routines and takes checkerboard pattern definition, number of desired calibration images, and the output directory path as inputs (see figure 6.58).

During the calibration process, the user holds the checkerboard pattern in arbitrary orientations while all pattern corners remain visible. When the program is launched, a startup screen displays the instructions to the user with an illustration of the target checkerboard pattern (see figure 6.59 top). When the program recognizes the pattern, the primary screen displays the processed camera frames in which the checkerboard inner corners are drawn. A smaller picture-in-picture display shows the real-time

[2] https://svn.lcsr.jhu.edu/limbs-antenna/codes/garciaCameraTrack/

```
-- CAM server R1
-- LIMBS Lab, 2013
-- Alican Demir

Options::

Program modes:
  -c [ --calibrate ]    starts calibration procedure

Calibration options:
  -w [ --cols ] arg (=5)          number of checkerboard columns
  -h [ --rows ] arg (=5)          number of checkerboard rows
  -l [ --length ] arg (=10)       length of a single checkerboard square in mm
  -s [ --shots ] arg (=10)        number of images to acquire
  -i [ --interval ] arg (=0)      interval between shots in seconds (0 is
                                  manual)
  -d [ --dir ] arg (=calibration) output directory path
```

Figure 6.58: "-calibrate" mode of our software is used for computing camera intrinsic and extrinsic parameters from given checkerboard pattern definition.

camera preview. The user can decide to start the calibration process at any time, after which the program will either start a pre-defined count-down to take n consecutive calibration shots automatically or will wait for the user to capture the images manually. Upon the count-down expiration (or user command), the software takes the first available frame, where all corners are successfully detected. This step (figure 6.59 bottom) is repeated until n calibration images are taken. Then, the camera parameters are computed and saved. Finally, the primary screen displays the undistorted camera preview using the computed calibration parameters until the user quits the program.

The program outputs the camera distortion coefficients and intrinsic and extrinsic parameters as both *.xml* and *.mat* (*Matlab*) files as well as the raw calibration images and the corresponding undistorted versions (see figure 6.60) for user convenience. The details of the *Matlab* output structure from the calibration process is presented

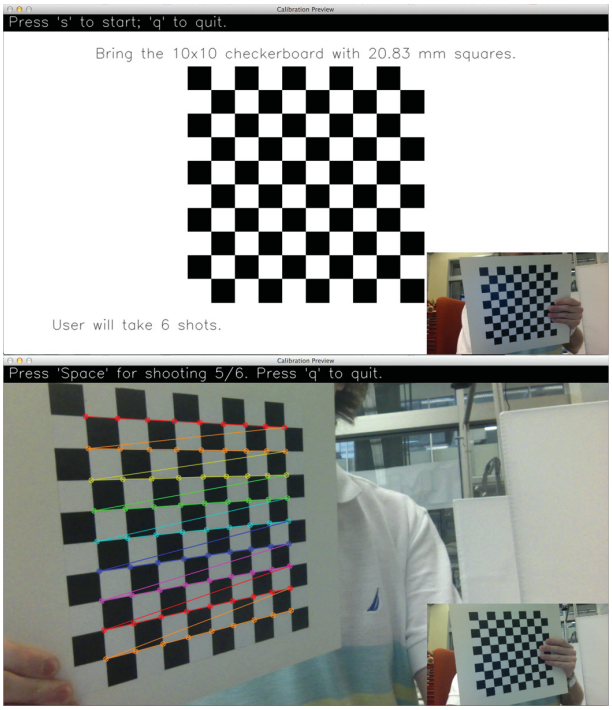

Figure 6.59: Two screenshots from the calibration mode of our software. The upper screenshot is taken during the startup and the lower screenshot is taken from during the calibration shots.

in table 6.6.

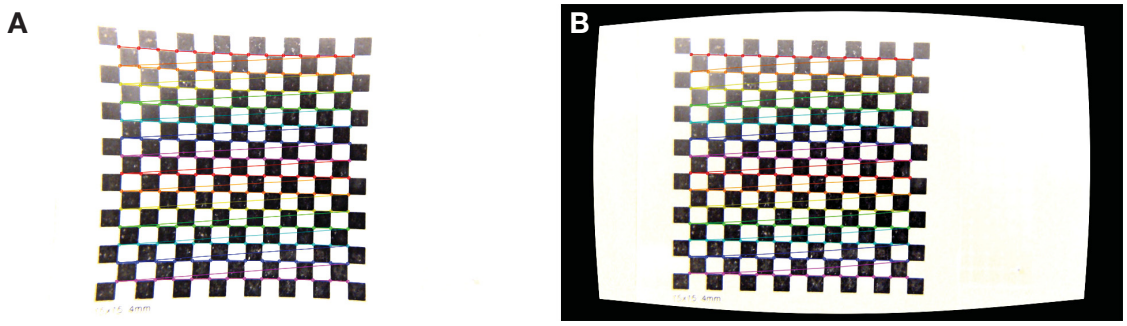

Figure 6.60: Panels **A** and **B** show a sample raw calibration image and its undistorted version respectively. Both versions are saved after calibration.

Experimental Validation

The aim of this experiment is to test the accuracy of optical tracking with the given intrinsic parameters and distortion coefficients. To that end, we took 3 images of the calibration pattern at three different orientations (φ_i, γ_i) $i \in \{1, 2, 3\}$ of the tilt stage. Then we translated the entire stage a known amount from p^A to p^B ($d = 1$ inch) on the grid paper and took another set of three images (φ_i, γ_i) $i \in \{4, 5, 6\}$ with different orientations. The goal is to recover the known translation distance d solely from the images, the camera matrix, and the distortion coefficients. Figure 6.61 illustrates the experiment.

variable	type	description
`num_of_frames`	*integer*	Number of images (n)
`image_width`	*integer*	Image width in pixels
`image_height`	*integer*	Image height in pixels
`pattern_rows`	*integer*	Checkerboard pattern rows (r)
`pattern_cols`	*integer*	Checkerboard pattern columns (c)
`pattern_square_mm`	*float*	Length of checkerboard square in mm
`pattern_coords`	$3 \times (r-1)(c-1)$ *float array*	Checkerboard inner corner homogeneous coordinates in mm.
`calibration_time`	*character array*	Calibration date
`shots_distorted`	$n \times 1$ *frame struct*	Raw calibration images
`shots_undistorted`	$n \times 1$ *frame struct*	Undistorted images
`shots_pattern_coords`	$1 \times n$ *cell*	Observed checkerboard inner corner pixel coordinates for all images.
`camera_matrix`	3×3 *matrix*	Intrinsic parameters: $\begin{pmatrix} f_x & 0 & c_x \\ 0 & f_y & c_y \\ 0 & 0 & 1 \end{pmatrix}$ where f_x and f_y are focal lengths in pixels. c_x and c_y are the the principal point coordinates in pixels measured from the top left corner $(1,1)$ of the image.
`distortion_coefficients`	5×1 *vector*	Distortion coefficients: $(k_1 \quad k_2 \quad p_1 \quad p_2 \quad k_3)^\top$ where k_1, k_2, k_3 are radial coefficients; p_1 and p_2 are tangential coefficients.
`extrinsic_r_axis`	$1 \times n$ *cell*	All extrinsic rotation axis vectors of R
`extrinsic_matrix`	$1 \times n$ *cell*	All extrinsic matrices $[R\|t]_{3\times4}$
`avg_reprojection_error`	*float*	Average reprojection error for all images in pixels.
`per_view_reprojection_errors`	$n \times 1$ *vector*	Reprojection errors for individual images in pixels.

Table 6.6: Summary table for *.mat* (*Matlab*'s) file output for the "calibrate" mode of the software. The XML output has similar information except the images, pattern pixel coordinates and extrinsic parameters.

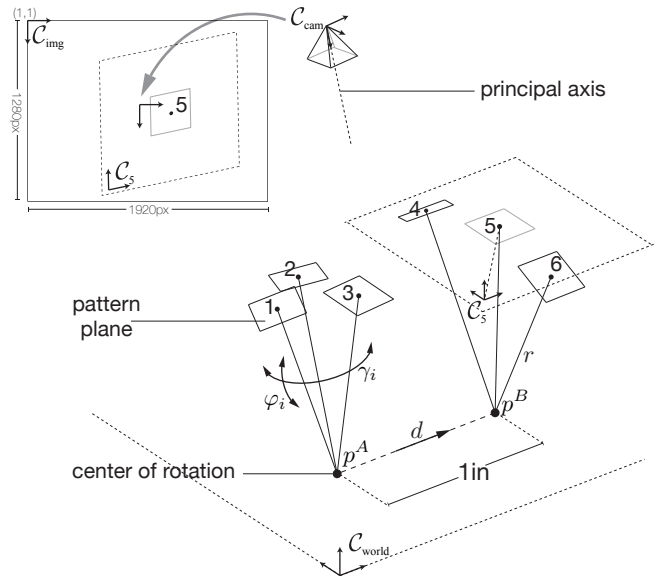

Figure 6.61: Optical tracking verification experiment. An object (rotary tilt stage) is translated by a known distance d and we aim to recover this distance from the images taken before and after the translation.

Correcting radial distortion

The camera we used for the optical tracking has a built-in wide angle lens without noticeable radial distortion to the naked eye for the scenes we are interested in. To dramatize the effect of the radial distortion we placed a separate macro lens in front of the camera, so that distortion removal can be appropriately tested. After the camera and the lens is aligned, we computed the intrinsic and extrinsic parameters along with the distortion coefficients of our camera using our software. These parameters are retrieved from 15 calibration images at different angles, with each image providing 196 control points.

- Let $p_d = \begin{pmatrix} u & v \end{pmatrix}^\top$ be a 2×196 array of *distorted* control points coordinates in

pixels with respect to the image origin $\mathcal{C}_{img}$. Note that the origin is at $(1, 1)$ and its located at the top left of the image (see figure 6.61).

- Let (f_x, f_y) and (c_x, c_y) be the focal lengths and principal axis coordinates in pixels with respect to the image origin $\mathcal{C}_{img}$, respectively.

- Let $\begin{pmatrix} x_d & y_d \end{pmatrix}^\top$ be the 2×196 array of normalized *distorted* control point coordinates with respect to the principal axis on the image plane. Note that $\begin{pmatrix} x_d & y_d \end{pmatrix}^\top$ is related to the $p_d = \begin{pmatrix} u & v \end{pmatrix}^\top$ with the intrinsic camera matrix A.

- Let $\{k_1, k_2, k_3\}$ and $\{p_1, p_2\}$ be the radial and tangential distortion coefficients respectively.

- Let $\begin{pmatrix} x_u & y_u \end{pmatrix}^\top$ be the 2×196 array of normalized *undistorted* control point coordinates with respect to the principal axis on the image plane.

- Let $p_u = \begin{pmatrix} u' & v' \end{pmatrix}^\top$ be the 2×196 array of *undistorted* control point coordinates in pixels with respect to the image origin $\mathcal{C}_{img}$.

The distortion model for the coefficients we get from *OpenCV* is:

$$p_u = \begin{pmatrix} u' \\ v' \end{pmatrix} = \begin{pmatrix} f_x \cdot x_u + c_x \\ f_y \cdot y_u + c_y \end{pmatrix}$$

$$\begin{pmatrix} x_d \\ y_d \end{pmatrix} = \underbrace{1 + k_1 r^2 + k_2 r^4 + k_3 r^6 \begin{pmatrix} x_u \\ y_u \end{pmatrix}}_{\text{radial}} + \underbrace{\begin{pmatrix} 2p_1 x_u y_u + p_2(r^2 + 2x_u^2) \\ 2p_2 x_u y_u + p_1(r^2 + 2y_u^2) \end{pmatrix}}_{\text{tangential}}$$

$$\text{where} \quad r^2 = x_u^2 + y_u^2$$

$$p_d = \begin{pmatrix} u \\ v \end{pmatrix} = \begin{pmatrix} f_x \cdot x_d + c_x \\ f_y \cdot y_d + c_y \end{pmatrix}$$

The undistortion task is to perform the inverse of this model and compute p_u from the observed distorted points p_d. In our case tangential distortion coefficients (p_1, p_2) are zero, which makes the problem easier. We solve the inverse problem via the following steps:

$$\begin{pmatrix} x_d \\ y_d \end{pmatrix} = \begin{pmatrix} \frac{u-c_x}{f_x} & \frac{v-c_y}{f_y} \end{pmatrix}^\top$$

$$\begin{pmatrix} x_d \\ y_d \end{pmatrix} = 1 + k_1 r^2 + k_2 r^4 + k_3 r^6 \begin{pmatrix} x_u \\ y_u \end{pmatrix} \tag{2}$$

$$\text{where} \quad r^2 = x_u^2 + y_u^2$$

$$x_d^2 + y_d^2 = \left(1 + k_1 r^2 + k_2 r^4 + k_3 r^6\right)^2 \cdot \underbrace{(x_u^2 + y_u^2)}_{r^2}$$

$$\sqrt{x_d^2 + y_d^2} = (1 + k_1 r^2 + k_2 r^4 + k_3 r^6) \cdot r$$

$$0 = k_3 r^7 + k_2 r^5 + k_1 r^3 + r - \sqrt{x_d^2 + y_d^2} \tag{3}$$

Equation 3 is a 7^{th} order polynomial whose seven roots are candidate values for r. We numerically solve for these roots and choose the one that has a positive real part and zero imaginary part and is also simultaneously less than $\sqrt{x_d^2 + y_d^2}$. There are always two pairs of complex conjugates and it appears that out of the remaining three roots

there is only one solution that satisfies all these conditions. After r is computed the computation of p_u is straightforward from equation 2.

$$\begin{pmatrix} x_u \\ y_u \end{pmatrix} = \frac{1}{1 + k_1 r^2 + k_2 r^4 + k_3 r^6} \begin{pmatrix} x_d \\ y_d \end{pmatrix}$$

$$p_u = \begin{pmatrix} f_x \cdot x_u + c_x \\ f_y \cdot y_u + c_y \end{pmatrix}$$

One should note that the undistortion procedure of the image is not computed this way. For undistorting the image one performs the forward distortion to a canvas with the same size as the distorted image. The mapping between the canvas pixel coordinates before and after the distortion is then used to interpolate the distorted image to recover the undistorted version. In figure 6.62, the undistorted point coordinates are computed via the inverse distortion, whereas the images themselves are undistorted using the forward distortion coupled with interpolation.

Computing homography

Once the observed point pixel coordinates p_d are distortion free, a perspective transformation (or homography) H can be computed between these coordinates p_u and their corresponding 3D coordinates $\begin{pmatrix} x & y \end{pmatrix}^\top$ on the actual checkerboard with respect to the checkerboard origin $\mathcal{C}_i$.

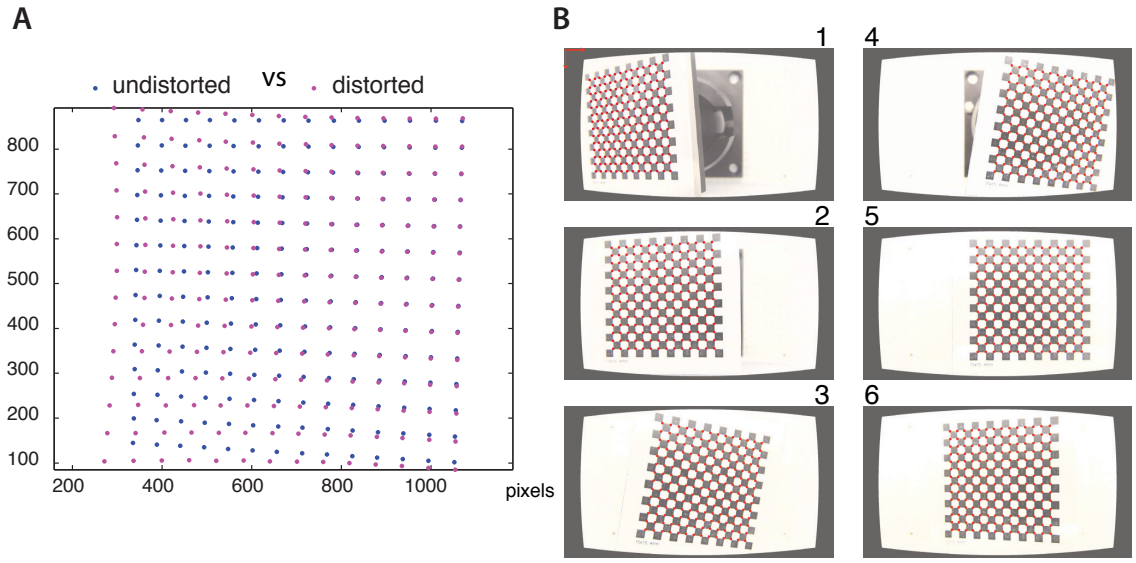

Figure 6.62: (**A**: A sample ($i = 2$) undistortion of sparse points on an image. **B**: Undistorted control points p_u for all six experiment images.

- Again, let $p_u = \begin{pmatrix} u' & v' & 1 \end{pmatrix}^\top$ be the 3×196 array of homogeneous *undistorted* control point coordinates in pixels with respect to the image origin $\mathcal{C}_{img}$.

- Let $\mathcal{C}_{world}$ be the right handed spatial 3D coordinate frame at a fixed origin.

- Let $\mathcal{C}_i$ be the right handed 3D coordinate frame, whose x and y axes are aligned with the pattern's orthogonal edges spanning the checkerboard plane. For a square symmetric $\mathcal{C}_i$ the origin of the checkerboard is at one of the four inner corners as depicted in figure 6.63.

- Let $p = \begin{pmatrix} x & y & 1 \end{pmatrix}^\top$ be a 3×196 array of checkerboard inner corner coordinates in meters with respect to $\mathcal{C}_i$.

- Let H be the 3×3 perspective transformation such that $p_u \propto Hp$.

$$\underbrace{\begin{bmatrix} u' \\ v' \\ \cdots\cdots \\ 1 \end{bmatrix}}_{p_u} \begin{pmatrix} \lambda_1 & & & \\ & \lambda_2 & & \\ & & \ddots & \\ & & & \lambda_{196} \end{pmatrix} = \underbrace{\begin{pmatrix} h_{11} & h_{12} & h_{13} \\ h_{21} & h_{22} & h_{23} \\ h_{31} & h_{32} & h_{33} \end{pmatrix}}_{H} \cdot \underbrace{\begin{bmatrix} x \\ y \\ \cdots\cdots \\ 1 \end{bmatrix}}_{p} \tag{4}$$

where the $\{\lambda_1, ..., \lambda_{196}\}$ are the homogeneous scaling factors for every point-to-point correspondence.

The linear method *normalized Direct Linear Transformation* (nDLT) or non-linear iterative methods such as *RANdom SAmple Consensus* (RANSAC) can be used for computing the homography. The important underlying assumption in any case is that all light rays coming from checkerboard intersect at one point before hitting the image plane (a.k.a the pinhole camera model).

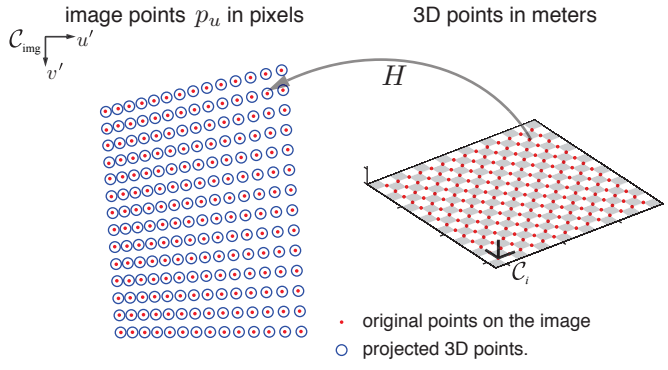

Figure 6.63: We compute the perspective transformation (homography) between the points $(x, y)^\top$ on the checkerboard plane and their undistorted projections p_u on the image plane. Red dots on the left are captured directly from images, whereas the blue circles are projected from the red dots on the right.

It's insightful to show the derivation of the *DLT* method. Given p_u and their corresponding 3D coordinates p (the 3^{rd} dimension is ignored), we start from equation 4 and only consider a single arbitrary i^{th} point-to-point correspondence:

$$\lambda_i p_{ui} = H \cdot p_i$$

The scaling factor λ_i can be eliminated if we take the cross product of both sides with p_{ui}:

$$\begin{aligned}
\lambda_i \cancelto{0}{(p_{ui} \times p_{ui})} &= p_{ui} \times (H \cdot p_i) \\
0 &= \begin{bmatrix} u_i' \\ v_i' \\ \cdots\cdots \\ 1 \end{bmatrix} \times \underbrace{\begin{pmatrix} | & | & | \\ h_1 & h_2 & h_3 \\ | & | & | \end{pmatrix}^\top}_{H^\top} \cdot p_i \\
&= \begin{bmatrix} u_i' \\ v_i' \\ \cdots\cdots \\ 1 \end{bmatrix} \times \begin{pmatrix} h_1^\top p_i \\ h_2^\top p_i \\ h_3^\top p_i \end{pmatrix} \\
&= \begin{pmatrix} 0 & -1 & v_i' \\ 1 & 0 & -u_i' \\ -v_i' & u_i' & 0 \end{pmatrix} \cdot \begin{pmatrix} h_1^\top p_i \\ h_2^\top p_i \\ h_3^\top p_i \end{pmatrix} \\
&= \begin{pmatrix} v_i' h_3^\top p_i - h_2^\top p_i \\ h_1^\top p_i - u_i' h_3^\top p_i \\ u_i' h_2^\top p_i - v_i' h_1^\top p_i \end{pmatrix} \qquad (5)
\end{aligned}$$

The unknown column vectors of $H^\top$ (h_1, h_2 and h_3) can be factored out from equation 5 to achieve the form $Cx = 0$:

$$\underbrace{\left[\begin{array}{ccc:ccc:ccc} 0 & 0 & 0 & -p_i^\top & & v_i' p_i^\top \\ \hdashline p_i^\top & & & 0 & 0 & 0 & -u_i' p_i^\top \\ \hdashline -v_i' p_i^\top & & & u_i' p_i^\top & & & 0 & 0 & 0 \end{array}\right]_{3\times 9}}_{C} \cdot \underbrace{\left[\begin{array}{c} h_1 \\ \hdashline h_2 \\ \hdashline h_3 \end{array}\right]}_{x} = 0$$

Upon inspection we see that the block matrix C has only two linearly independent rows. This means a single point-to-point correspondence provides 2 equations toward solving the 9 unknowns of x. Since one of the unknowns is a free homogeneous scaling factor, four correspondences are sufficient to compute the homography matrix H. In other words, h_33 can be set to 1 without changing the perspective geometry. More points will result in an overdetermined system which can be solved in the least squares fashion (pseudo-inverse). Once the stacked $x = \begin{pmatrix} h_1 & h_2 & h_3 \end{pmatrix}^\top$ vector is solved, it can be reshaped into the homography H matrix:

$$H^\top = \begin{pmatrix} | & | & | \\ h_1 & h_2 & h_3 \\ | & | & | \end{pmatrix}$$

Extracting camera position & orientation

The position and orientation of the camera $\mathcal{C}_{cam}$ with respect to the given checkerboard frame $\mathcal{C}_i$ can be computed if the *intrinsic camera matrix* A and the perspec-

tive transformation H is known. Recall that A relates planar point coordinates $p_{cam} = \begin{pmatrix} x & y \end{pmatrix}^\top$ given with respect to camera frame $\mathcal{C}_{cam}$ to the coordinates $\begin{pmatrix} u & v \end{pmatrix}^\top$ with respect to image frame $\mathcal{C}_{img}$. Similarly, H relates coordinates $p_i = \begin{pmatrix} x & y \end{pmatrix}^\top$ given with respect to the checkerboard frame $\mathcal{C}_i$ to the coordinates $\begin{pmatrix} u & v \end{pmatrix}^\top$ with respect to image frame $\mathcal{C}_{img}$. These relationships are illustrated in figure 6.64.

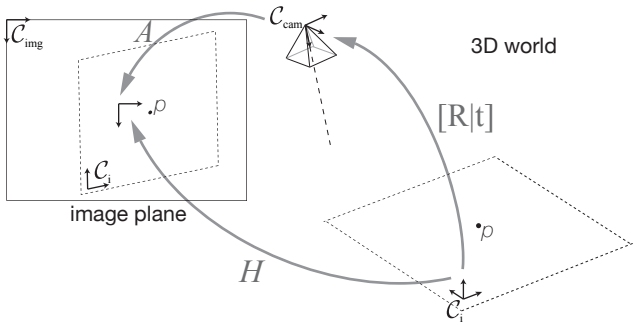

Figure 6.64: The extrinsic camera matrix $[R|t]$ changes the point coordinates given in camera frame $\mathcal{C}_{cam}$ to coordinates in the checkerboard frame $\mathcal{C}_i$

The transformation that converts coordinates given in the camera frame $\mathcal{C}_{cam}$ into coordinates with respect to the checkerboard frame $\mathcal{C}_i$ is called the *extrinsic camera matrix*, $[R|t]$. Assume that normalized undistorted checkerboard point coordinates $\begin{pmatrix} x_u & y_u \end{pmatrix}^\top$ with respect to $\mathcal{C}_{cam}$ as well as the intrinsic camera matrix A and the homography H are known. Since checkerboard 3D point coordinates $\begin{pmatrix} x & y & z \end{pmatrix}^\top$ with respect to its own frame $\mathcal{C}_i$ are also known a priori, $[R|t]$ can be extracted.

- Let $[R|t] \in SE(3)$ be the 3×4 extrinsic camera matrix such that:

$$\begin{pmatrix} x_u \\ y_u \\ 1 \end{pmatrix} = \underbrace{\begin{pmatrix} | & | & | & | \\ r_1 & r_2 & r_3 & t \\ | & | & | & | \end{pmatrix}}_{[R|t]} \begin{pmatrix} x \\ y \\ z \\ 1 \end{pmatrix}$$

  where x_u, y_u are coordinates given in camera frame $\mathcal{C}_{cam}$ and x, y, z are given in checkerboard frame $\mathcal{C}_i$.

- Let $R \in SO(3)$ be the rotation matrix such that $R = \begin{pmatrix} | & | & | \\ r_1 & r_2 & r_3 \\ | & | & | \end{pmatrix}$ describing the orientation from $\mathcal{C}_i$ to $\mathcal{C}_{cam}$.

- Let $t \in \mathbb{R}^3$ describing the translation from $\mathcal{C}_i$ to $\mathcal{C}_{cam}$.

From previous definitions we have:

$$\lambda \begin{bmatrix} p_u \\ \cdots \\ 1 \end{bmatrix} = \underbrace{\begin{pmatrix} f_x & 0 & c_x \\ 0 & f_y & c_y \\ 0 & 0 & 1 \end{pmatrix}}_{A} \begin{pmatrix} x_u \\ y_u \\ 1 \end{pmatrix}$$

$$\lambda \begin{bmatrix} p_u \\ \cdots \\ 1 \end{bmatrix} = H \begin{pmatrix} x \\ y \\ 1 \end{pmatrix}$$

Substitution yields:

$$A \begin{pmatrix} x_u \\ y_u \\ 1 \end{pmatrix} = H \begin{pmatrix} x \\ y \\ 1 \end{pmatrix}$$

$$A \underbrace{\begin{pmatrix} | & | & | & | \\ r_1 & r_2 & r_3 & t \\ | & | & | & | \end{pmatrix}}_{[R|t]} \begin{pmatrix} x \\ y \\ z \\ 1 \end{pmatrix} = H \begin{pmatrix} x \\ y \\ 1 \end{pmatrix}$$

Recall that $z = 0$ for all checkerboard points since they are all in a plane. Then we get:

$$\lambda \begin{bmatrix} p_u \\ \cdots \\ 1 \end{bmatrix} = \underbrace{A \begin{pmatrix} | & | & | \\ r_1 & r_2 & t \\ | & | & | \end{pmatrix}}_{H} \begin{pmatrix} x \\ y \\ 1 \end{pmatrix} = H \begin{pmatrix} x \\ y \\ 1 \end{pmatrix}$$

Since A is invertible, we can solve for the columns r_1, r_2 and t towards the extrinsic matrix $[R|t]$.

$$\begin{pmatrix} | & | & | \\ r_1 & r_2 & t \\ | & | & | \end{pmatrix} = A^{-1}H$$

The third column, r_3, can be computed by taking advantage of the properties of R, a rotation matrix. Specifically, all three columns must be unit vectors and orthogonal

to each other. Then:

$$\hat{r}_1 = \frac{r_1}{||r_1||} \quad \hat{r}_2 = \frac{r_2}{||r_2||}$$

$$\hat{r}_3 = \hat{r}_1 \times \hat{r}_2$$

$$R = \begin{pmatrix} | & | & | \\ \hat{r}_1 & \hat{r}_2 & \hat{r}_3 \\ | & | & | \end{pmatrix}$$

Since the columns are normalized by $||r_1||$ and $||r_2||$, which are theoretically equal, the translation vector t should also be scaled. The mean of $||r_1||$ and $||r_2||$ can be used as the scaling factor.

$$\hat{t} = \frac{t}{\frac{||r_1||+||r_2||}{2}}$$

Finally the extrinsic camera matrix $[R|t]$ is:

$$[R|t] = \begin{pmatrix} | & | & | & | \\ \hat{r}_1 & \hat{r}_2 & \hat{r}_3 & \hat{t} \\ | & | & | & | \end{pmatrix}$$

We had six undistorted images in our experiment. After computing the perspective transformations $\{H_1, ..., H_6\}$ and using the camera matrix A that we determined earlier from the 15 calibration images, we extracted the extrinsic camera matrices $\{[R|t]_1, ..., [R|t]_6\}$. The extrinsic transformations are also the coordinate frames of the checkerboards with respect to the camera frame. Figure 6.65 shows the position and the orientation of the checkerboard at six different instances with respect to the

camera .

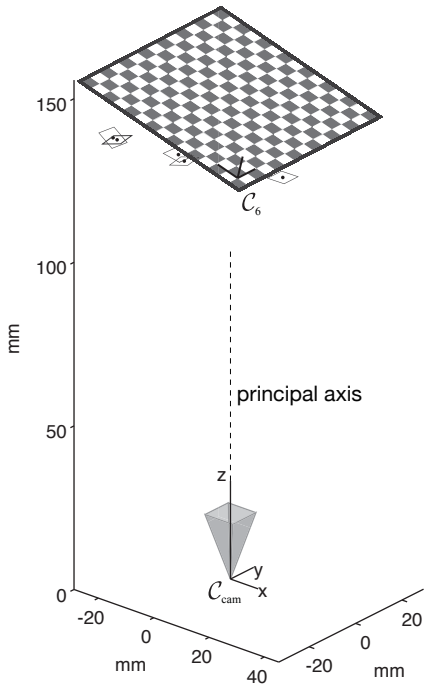

Figure 6.65: Extrinsic matrices are used to place all 6 checkerboard instance frames $\mathcal{C}_i$ from our experiment with respect to the camera frame $\mathcal{C}_{cam}$. Only the 6^{th} checkerboard is drawn completely to avoid clutter.

6.5 Force Sensor Calibration

Calibration Experiments

We used 100 and 200 grams reference weights to calibrate the sensor. These weights are applied both parallel and perpendicular to the sensor's measuring axis. For each case, the center of pressure was either aligned (axially or traversally) or had a constant offset with respect to the measuring axis. We conducted six experiments, each consisting of five trials with 10 second duration. During every trial we recorded a few seconds of no-load value and then applied the reference weight until the end of the trial. The experiment descriptions are given below (Figure: 6.66).

1. 100 gram weight; Axial loading with no offset.

2. 200 gram weight; Axial loading with no offset.

3. 100 gram weight; Axial loading with offset.

4. 200 gram weight; Axial loading with offset.

5. 200 gram weight; Traversal loading with no offset.

6. 200 gram weight; Traversal loading with offset.

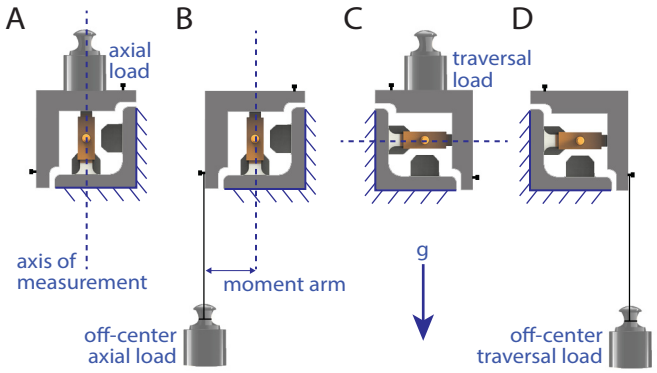

Figure 6.66: **A**: Experiments 1 and 2. **B**: Experiments 3 and 4. **C**: Experiment 5. **D**: Experiment 6.

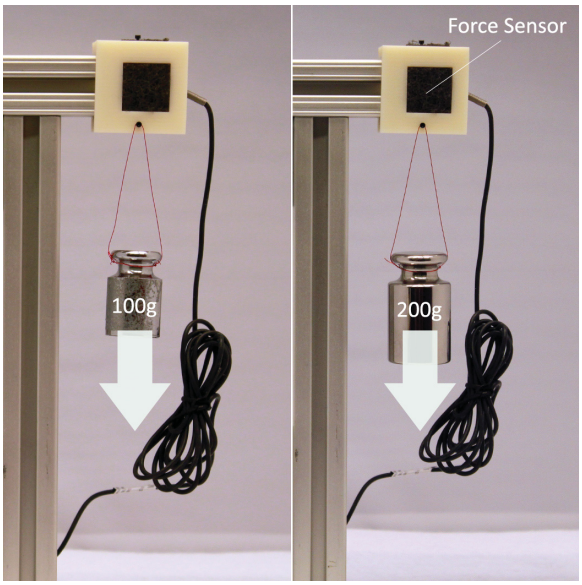

Figure 6.67: off-axis axial loading

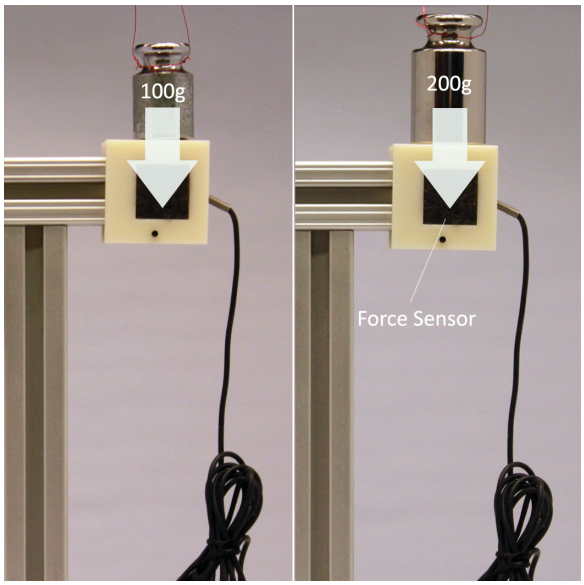

Figure 6.68: direct axial and traversal loading

Results

We present the data from each of the six experiments. For presentation purposes we subtracted the average no-load value for each dataset so that the reference values cor-

experiments	**means**	**std**
Direct axial loading (100g)	-0.1979	-0.1979
Off-axis loading (100g)	-0.1948	-0.1948
Direct axial loading (200g)	-0.3952	-0.3952
Off-axis loading (200g)	-0.3894	-0.3894
Traverse loading with moment (200g)	-0.0138	-0.0138
Direct traverse loading (200g)	-0.0089	-0.0089

Table 6.7: table

responded to zero. Every color represents an individual trial for the given experiments where lighter and darker colors correspond to raw and filtered data respectively. A zero-phase first-order butterworth filter used to clean the raw data. The mean voltage values for the loads are found by averaging the last four seconds of each trial.

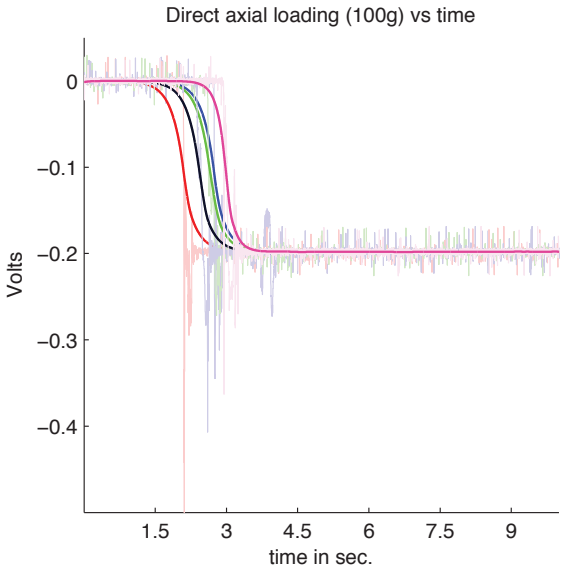

Figure 6.69: 5 Trials; $-0.1979 \pm 0.0022V$

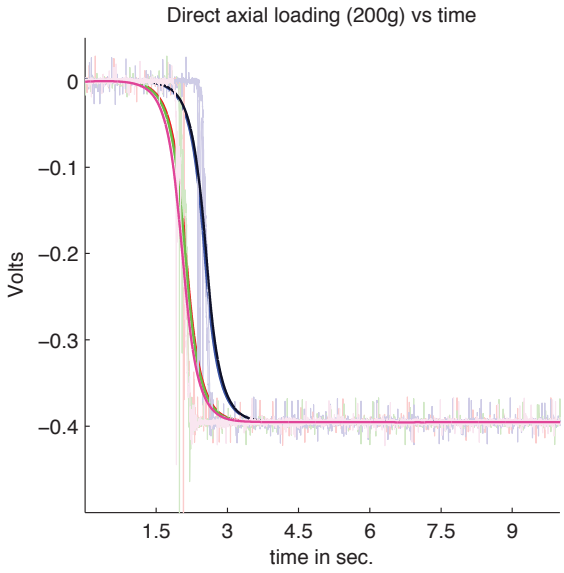

Figure 6.70: 5 Trials; $-0.3952 \pm 0.0022V$

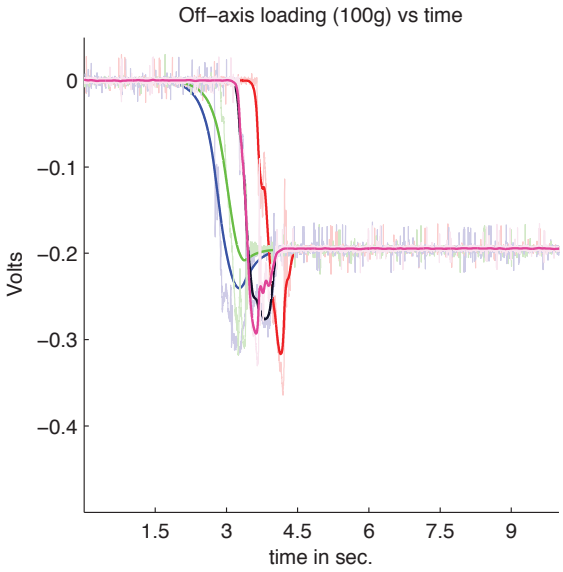

Figure 6.71: 5 Trials; $-0.1948 \pm 0.0023V$

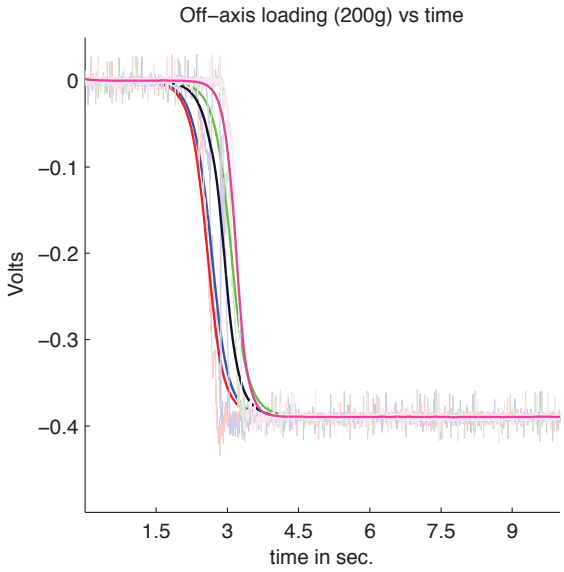

Figure 6.72: 5 Trials; $-0.3894 \pm 0.0025V$

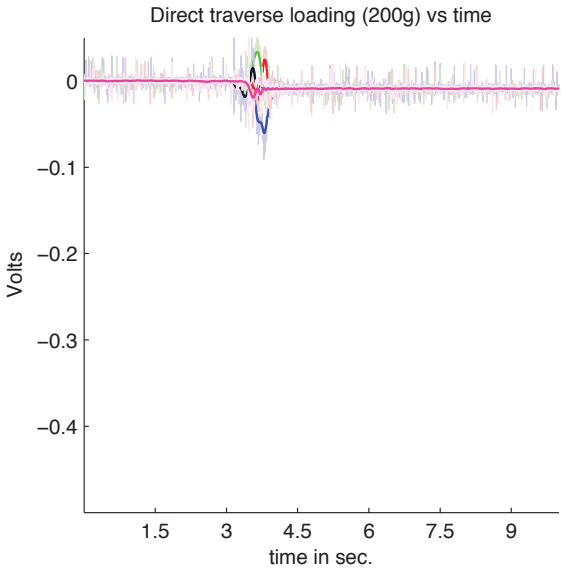

Figure 6.73: 5 Trials; $-0.0089 \pm 0.0023V$

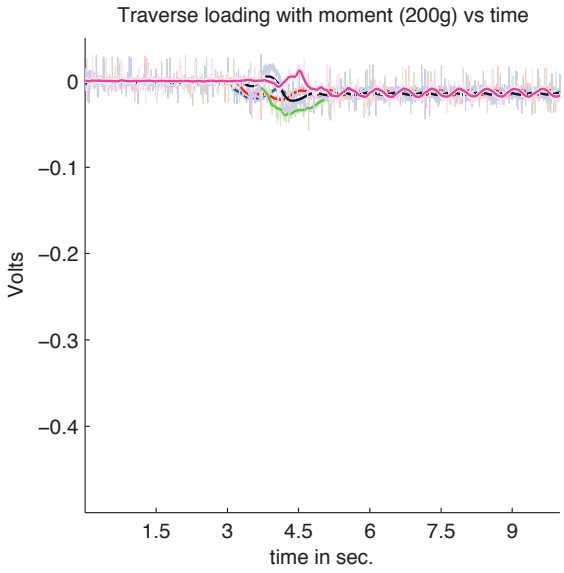

Figure 6.74: 5 Trials; $-0.0138 \pm 0.0036V$

The effect of moments to the measurement accuracy is negligible. The sinusoidal data for the off-axis traversal loading (experiment 6) is attributed to the swinging of the $200g$ reference weight.

6.6 Data Collection Software

We streamlined our data collection procedures through our in-house developed cross-platform software [3] written in Python. Currently in its fourth iteration, the user interface enables data acquisition from multiple hardware and software sources over various communication protocols including TCP, Serial, SSH and ROS. The program allows the user to create and save independent experiments involving separate hardware, settings and trials. Irrespective of the nature of the experiment, relevant data is saved in MATLAB *.mat* and *.xml* formats after each session with a uniform structure.

The original software was developed to incorporate multiple hardware to the experimental apparatus. A basic robotic antenna experiment involves communicating with the antenna base computer —A 600Mhz ARM processor *Gumstix Verdex Pro* with Linux— over SSH, running the antenna host program [4] on the Gumstix with the relevant program arguments (such as the number of segments, the base angle etc.), opening a TCP socket and connecting to the host program from the workstation, and acquiring the data. In addition, if the experimenter requires the linear motion of the antenna for a trial, then a serial communication port needs to be opened simultaneously, and the position commands need to be sent in a timely manner to achieve the desired motion of the antenna. Furthermore, if a specific base angle needs to be

[3] https://svn.lcsr.jhu.edu/limbs-antenna/codes/limbsClientR4/
[4] https://svn.lcsr.jhu.edu/limbs-antenna/codes/antennaHostGumstix/

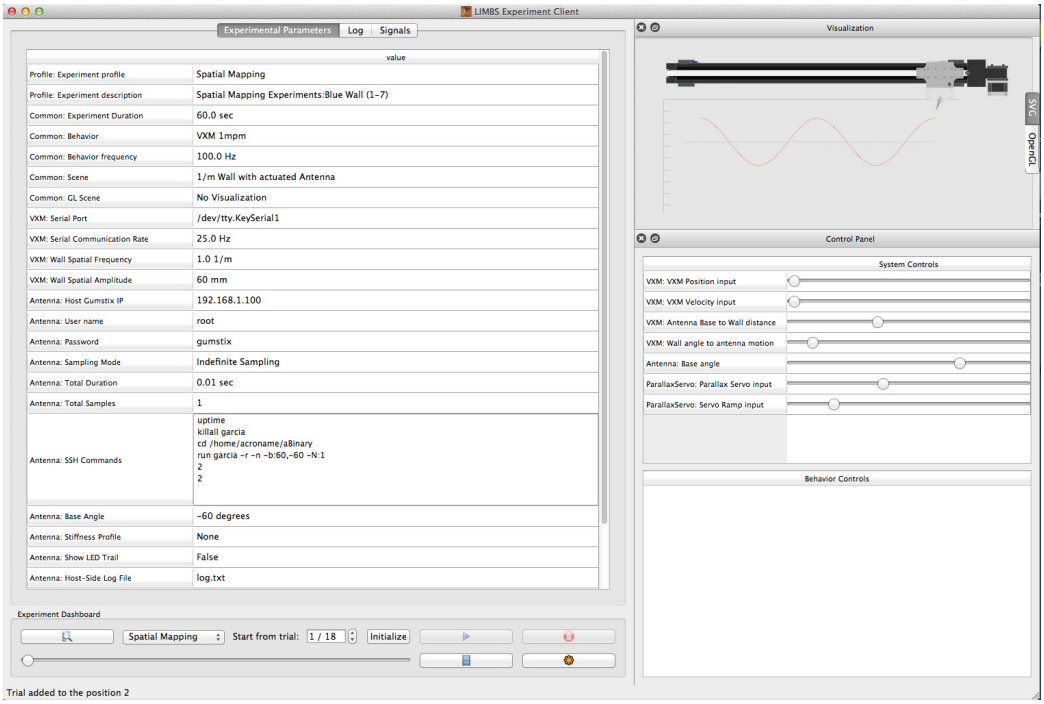

Figure 6.75: Main window of the data collection software. The left side lists the experimental parameters for the currently selected experiment and trial. The bottom left side is the dashboard in which users start and stop an experiment and switch to between experiments or trials. The top right shows the experiment visualization (also set individually for every experiment). The bottom right side contains the controls for the user to set initial conditions of the relevant apparatus before the experiment.

maintained during a trial, then a secondary serial port needs to be opened to communicate with the PWM controller, which then adjusts the servo motor to change the base angle. Every experiment and trial have different requirements, and thus, different settings. Since the parameter space for antennal sensing was large, we felt it was necessary to automate the data collection routines.

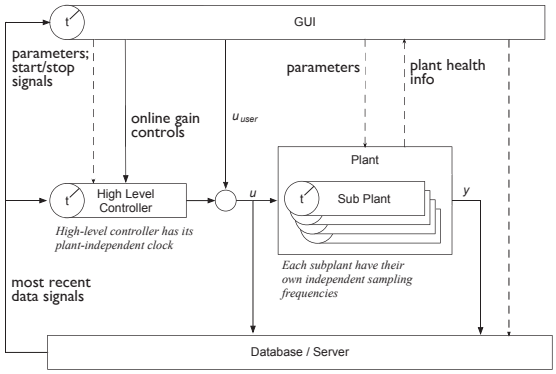

Figure 6.76: Basic block diagram of the data collection software. There are two main threads: *GUI* and *Server*. The Server handles the main closed-loop unified clock and copies the most recent data from the auxiliary *plant* threads, which are responsible for getting the data from their associated hardware and timestamping it. The GUI thread runs at a separate clock for users to monitor the trial run.

The basic principle of our software is illustrated in figure 6.76. The two main threads, *GUI* and *Server*, are always running, regardless of the nature of experiment. The Server handles the main closed-loop unified clock and copies the most recent data from the auxiliary *module* or (plant) threads, which are responsible for getting the data from their associated hardware and timestamping it. These auxiliary threads run when the selected experiment is *initialized* at different speeds based on the experiment settings. For example, a camera data sampling module may run at $30Hz$ while the

robotic antenna sampling module is running at $100Hz$. Thus there exist a separate thread for every module involved in the particular experiment. These modules are single Python files with a unifying template and contain data-stream *decoding* and *encoding* procedures as well as parameter widgets specific to the hardware in question. The GUI main thread runs at a separate clock for users to monitor the trial.

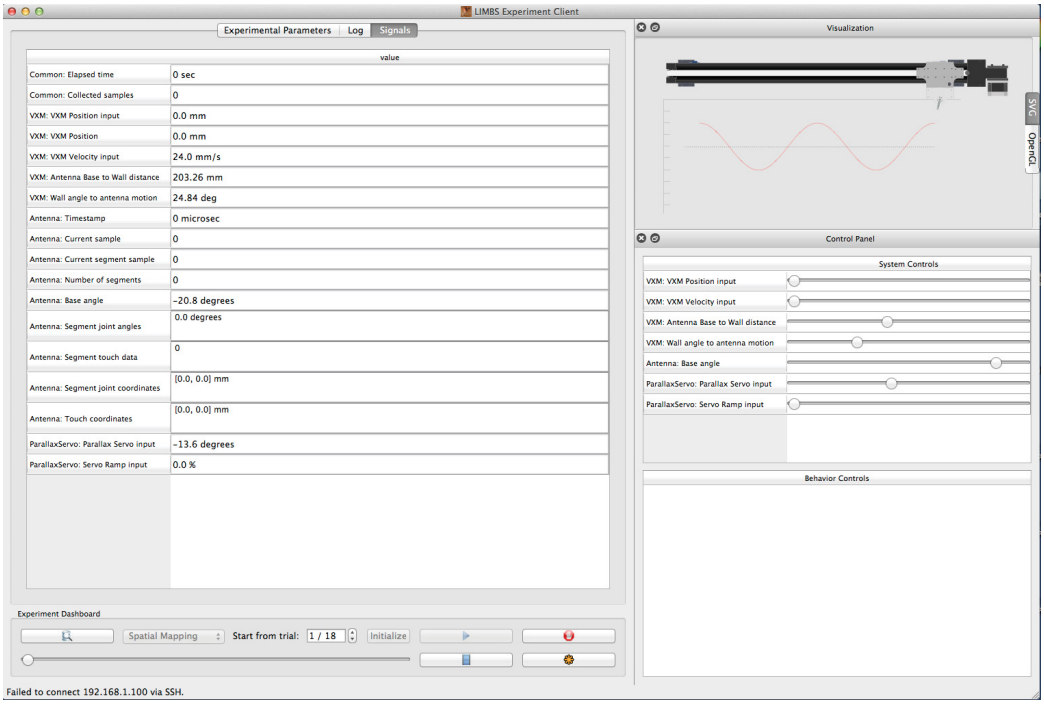

Figure 6.77: The signals tab shows data being received from the experimental apparatus after an experiment is initialized.

Once an experiment is initialized, flows from every module involved through their respective communication channels. Users can monitor the incoming data from the *signals* tab in the left side (see figure 6.77). The user starts the experiment from the dashboard, and any preprogrammed behaviors, such as moving the linear actuator to a desired position with a given velocity, are immediately executed. When the set

time for the particular trial is reached, the data is saved as a MATLAB file and the modules disconnect.

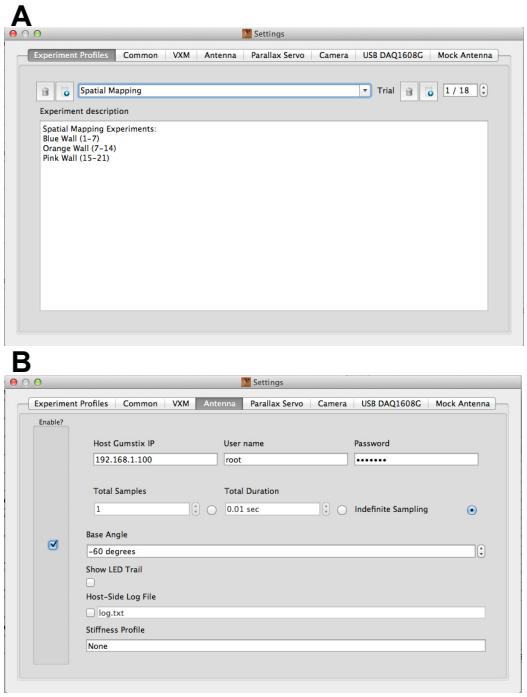

Figure 6.78: The settings window where the experimental parameters are set for the individual modules.

Bibliography

[1] A. Demir, "A modular, tunable tactile antenna for exploring the mechanics of sensing," Master's thesis, Johns Hopkins University, 2009. [Online]. Available: https://catalyst.library.jhu.edu/catalog/bib_3985789

[2] M. H. Lee and H. R. Nicholls, "Review article tactile sensing for mechatronicsa state of the art survey," *Mechatronics*, vol. 9, no. 1, pp. 1–31, 1999.

[3] J. Dargahi and S. Najarian, "Human tactile perception as a standard for artificial tactile sensinga review," *The International Journal of Medical Robotics and Computer Assisted Surgery*, vol. 1, no. 1, pp. 23–35, 2004.

[4] H. R. Nicholls and M. H. Lee, "A survey of robot tactile sensing technology," *The International Journal of Robotics Research*, vol. 8, no. 3, pp. 3–30, 1989.

[5] J. M. Loomis and S. J. Lederman, "Tactual perception," *Handbook of perception and human performances*, vol. 2, p. 2, 1986.

[6] S. J. Lederman and R. L. Klatzky, "Haptic perception: A tutorial," *Attention, Perception, & Psychophysics*, vol. 71, no. 7, pp. 1439–1459, 2009.

[7] K. Ilango, "Morphological characteristics of the antennal flagellum and its sensilla chaetica with character displacement in the sandfly Phlebotomus argentipes Annandale and Brunetti sensu lato (Diptera: psychodidae)." *Journal of biosciences*, vol. 25, no. 2, pp. 163–172, 2000.

[8] S. Ye, V. Leung, A. Khan, Y. Baba, and C. Comer, "The antennal system and cockroach evasive behavior. i. roles for visual and mechanosensory cues in the response," *Journal of Comparative Physiology A*, vol. 189, no. 2, pp. 89–96, 2003.

[9] H. Nishino, M. Nishikawa, F. Yokohari, and M. Mizunami, "Dual, multilayered somatosensory maps formed by antennal tactile and contact chemosensory afferents in an insect brain," *The Journal of Comparative Neurology*, vol. 493, no. 2, 2005.

[10] D. C. Sandeman, "Physical properties, sensory receptors and tactile reflexes of the antenna of the Australian freshwater crayfish cherax destructor," *Journal of Experimental Biology*, vol. 141, no. 1, pp. 197–217, 1989.

[11] E. Staudacher, M. Gebhardt, and V. Dürr, "Antennal movements and mechanoreception: neurobiology of active tactile sensors," in *Advances in Insect Physiology*, 2005, vol. 32, pp. 49–205.

[12] J. Camhi and E. Johnson, "High-frequency steering maneuvers mediated by tactile cues: antennal wall-following in the cockroach," *Journal of Experimental Biology*, vol. 202, no. 5, pp. 631–643, 1999.

[13] M. A. Neimark, M. L. Andermann, J. J. Hopfield, and C. I. Moore, "Vibrissa resonance as a transduction mechanism for tactile encoding," *The Journal of neuroscience*, vol. 23, no. 16, pp. 6499–6509, 2003.

[14] M. H. Lee, "Tactile sensing: new directions, new challenges," *The International Journal of Robotics Research*, vol. 19, no. 7, pp. 636–643, 2000.

[15] C. Zimmer, "A pair of wings took evolving insects on a nonstop flight to domination," *The New York Times*, November 2005. [Online]. Available: http://www.nytimes.com/2005/11/29/science/29inse.html

[16] R. M. May, "How many species are there on earth?" *Science*, vol. 241, no. 4872, pp. 1441–1449, 1988.

[17] K. J. Gaston, "The magnitude of global insect species richness," *Conservation Biology*, vol. 5, no. 3, pp. 283–296, 1991.

[18] T. L. Erwin, "How many species are there?: Revisited," *Conservation Biology*, vol. 5, no. 3, pp. 330–333, 1991.

[19] J. Adis, "Thirty million arthropod species–too many or too few?" *Journal of*

tropical ecology, vol. 6, no. 01, pp. 115–118, 1990.

[20] D. Grimaldi and M. S. Engel, *Evolution of the Insects*. Cambridge University Press, 2005.

[21] R. F. Chapman, *The insects: structure and function*. Cambridge university press, 1998.

[22] D. Schneider, "Insect antennae," *Annual review of entomology*, vol. 9, no. 1, pp. 103–122, 1964.

[23] J. Okada and Y. Toh, "Antennal system in cockroaches: a biological model of active tactile sensing," in *International Congress Series*, vol. 1269. Elsevier, 2004, pp. 57–60.

[24] J. Lee, S. N. Sponberg, O. Y. Loh, A. G. Lamperski, R. J. Full, and N. J. Cowan, "Templates and anchors for antenna-based wall following in cockroaches and robots," *IEEE Trans Robot*, vol. 24, no. 1, pp. 130–143, Feb. 2008.

[25] J. Lee, "Identifying feedback control strategies of running cockroaches and humans," Ph.D. dissertation, Johns Hopkins University, Jan. 2009.

[26] T. Barnes, T. Truong, G. Adams, and N. McGruer, "Large deflection analysis of a biomimetic lobster robot antenna due to contact and flow," *Journal of applied mechanics*, vol. 68, no. 6, pp. 948–951, 2001.

[27] N. J. Cowan, E. J. Ma, M. Cutkosky, and R. J. Full, "A biologically inspired passive antenna for steering control of a running robot," in *Robotics Research*, ser. Springer Tracts in Advanced Robotics. Siena, Italy: Springer, 2003, pp. 540–550.

[28] B. L. Kutcher, "Mapping and following walls using a mobile robot equipped with an antenna-like tactile sensor," Master's thesis, Johns Hopkins University, 2004.

[29] A. Lamperski, O. Loh, B. Kutscher, and N. J. Cowan, "Dynamical wall-following for a wheeled robot using a passive tactile sensor," in *Proc IEEE Int Conf Robot Autom*, 2005, pp. 3838–3843.

[30] J. Lee, O. Y. Loh, and N. J. Cowan, "A hierarchy of neuromechanical and robotic models of antenna-based wall following in cockroaches," in *Intelligent Robots and Systems, 2007. IROS 2007. IEEE/RSJ International Conference on.* IEEE, 2007, pp. 3547–3553.

[31] J. H. Solomon and M. J. Hartmann, "Radial distance determination in the rat vibrissal system and the effects of weber's law," *Philosophical Transactions of the Royal Society B: Biological Sciences*, vol. 366, no. 1581, pp. 3049–3057, 2011.

[32] ——, "Extracting object contours with the sweep of a robotic whisker using torque information," *The International Journal of Robotics Research*, vol. 29, no. 9, pp. 1233–1245, 2010.

[33] M. J. Pearson, A. G. Pipe, C. Melhuish, B. Mitchinson, and T. J. Prescott, "Whiskerbot: a robotic active touch system modeled on the rat whisker sensory system," *Adaptive Behavior*, vol. 15, no. 3, pp. 223–240, 2007.

[34] J. H. Solomon and M. J. Hartmann, "Biomechanics: robotic whiskers used to sense features," *Nature*, vol. 443, no. 7111, pp. 525–525, 2006.

[35] A. E. Schultz, J. H. Solomon, M. A. Peshkin, and M. J. Hartmann, "Multifunctional whisker arrays for distance detection, terrain mapping, and object feature extraction," in *Robotics and Automation, 2005. ICRA 2005. Proceedings of the 2005 IEEE International Conference on*. IEEE, 2005, pp. 2588–2593.

[36] M. Lungarella, V. V. Hafner, R. Pfeifer, and H. Yokoi, "An artificial whisker sensor for robotics," in *Intelligent Robots and Systems, 2002. IEEE/RSJ International Conference on*, vol. 3. IEEE, 2002, pp. 2931–2936.

[37] R. A. Russell, "Using tactile whiskers to measure surface contours," in *Robotics and Automation, 1992. Proceedings., 1992 IEEE International Conference on*. IEEE, 1992, pp. 1295–1299.

[38] R. Schafer and T. V. Sanchez, "Antennal sensory system of the cockroach, Periplaneta americana: postembryonic development and morphology of the sense organs," *Journal of Comparative Neurology*, vol. 149, no. 3, pp. 335–353, 1973.

[39] J. Okada and Y. Toh, "The role of antennal hair plates in object-guided tactile orientation of the cockroach (Periplaneta americana)," *Journal of Comparative Physiology A*, vol. 186, no. 9, pp. 849–857, 2000.

[40] H. Nishino, M. Nishikawa, F. Yokohari, and M. Mizunami, "Dual, multilayered somatosensory maps formed by antennal tactile and contact chemosensory afferents in an insect brain," *Journal of Comparative Neurology*, vol. 493, no. 2, pp. 291–308, 2005.

[41] J.-M. Mongeau, A. Demir, C. J. Dallmann, K. Jayaram, N. J. Cowan, and R. J. Full, "Mechanical processing via passive dynamic properties of the cockroach antenna can facilitate control during rapid running," *J Exp Biol*, vol. 217, no. 18, pp. 3333–3345, 2014. [Online]. Available: http://jeb.biologists.org/content/early/2014/07/02/jeb.101501.abstract

[42] G. Seelinger, "Sex-specific activity patterns in Periplaneta americana and their relation to mate-finding," *Zeitschrift für Tierpsychologie*, vol. 65, no. 4, pp. 309–326, 1984.

[43] R. M. Murray, Z. Li, and S. S. Sastry, *A mathematical introduction to robotic manipulation*, 1994.

[44] S. Wright and J. Nocedal, *Numerical optimization*. Springer New York, 1999, vol. 2.

[45] R. J. Full and D. E. Koditschek, "Templates and anchors: neuromechanical hypotheses of legged locomotion on land," *Journal of Experimental Biology*, vol. 202, no. 23, pp. 3325–3332, 1999.

[46] J.-M. Mongeau, A. Demir, J. Lee, N. J. Cowan, and R. J. Full, "Locomotion- and mechanics-mediated tactile sensing: antenna reconfiguration simplifies control during high-speed navigation in cockroaches," *J Exp Biol*, vol. 216, no. 24, pp. 4530–4541, 2013. [Online]. Available: http://jeb.biologists.org/content/216/24/4530.abstract

[47] M. Polak and A. Rashed, "Microscale laser surgery reveals adaptive function of male intromittent genitalia," *Proceedings of the Royal Society B: Biological Sciences*, p. rspb20091720, 2010.

[48] J. C. Spagna, D. I. Goldman, P.-C. Lin, D. E. Koditschek, and R. J. Full, "Distributed mechanical feedback in arthropods and robots simplifies control of rapid running on challenging terrain," *Bioinspiration & biomimetics*, vol. 2, no. 1, p. 9, 2007.

[49] S. P. Sane and M. J. McHenry, "The biomechanics of sensory organs," *Integrative and Comparative Biology*, p. icp112, 2009.

[50] O. Khatib, "A unified approach for motion and force control of robot manip-

ulators: The operational space formulation," *Robotics and Automation, IEEE Journal of*, vol. 3, no. 1, pp. 43–53, 1987.

[51] A. Demir, E. W. Samson, and N. J. Cowan, "A tunable physical model of arthropod antennae," in *Proc IEEE Int Conf Robot Autom*, Anchorage, AK, USA, May 2010, pp. 3793–3798. [Online]. Available: http://ieeexplore.ieee.org/xpls/abs_all.jsp?arnumber=5509323&tag=1

[52] N. J. Cowan, J. Lee, and R. J. Full, "Task-level control of rapid wall following in the American cockroach," *J Exp Biol*, vol. 209, no. 9, pp. 1617–1629, 2006. [Online]. Available: http://dx.doi.org/10.1242/jeb.02166

[53] F. Inc. (2013) Product view: LSB200, FSH00103. [Online]. Available: http://www.futek.com/prod_views.aspx?stock=FSH00103&m=lsb200&img=lsb200BL.jpg&view=C

[54] H. L. More, J. R. Hutchinson, D. F. Collins, D. J. Weber, S. K. Aung, and J. M. Donelan, "Scaling of sensorimotor control in terrestrial mammals," *Proceedings of the Royal Society B: Biological Sciences*, vol. 277, pp. 3563–3568, 2010.

[55] M. J. Elzinga, W. B. Dickson, and M. H. Dickinson, "The influence of sensory delay on the yaw dynamics of a flapping insect," *Journal of The Royal Society Interface*, vol. 9, no. 72, pp. 1685–1696, 2012.

[56] P. Holmes, R. J. Full, D. Koditschek, and J. Guckenheimer, "The dynamics of legged locomotion: Models, analyses, and challenges," *Siam Review*, vol. 48, no. 2, pp. 207–304, 2006.

[57] J. M. Wotton, T. Haresign, and J. A. Simmons, "Spatially dependent acoustic cues generated by the external ear of the big brown bat, Eptesicus fuscus," *The Journal of the Acoustical Society of America*, vol. 98, no. 3, pp. 1423–1445, 1995.

[58] M. Egelhaaf, R. Kern, H. G. Krapp, J. Kretzberg, R. Kurtz, and A.-K. Warzecha, "Neural encoding of behaviourally relevant visual-motion information in the fly," *Trends in neurosciences*, vol. 25, no. 2, pp. 96–102, 2002.

[59] R. B. Coles and A. Guppy, "Directional hearing in the barn owl (Tyto alba)," *Journal of Comparative Physiology A*, vol. 163, no. 1, pp. 117–133, 1988.

[60] R. Bajcsy, "Active perception," *Proceedings of the IEEE*, vol. 76, no. 8, pp. 966–1005, 1988.

[61] W. J. Bell, L. M. Roth, and C. A. Nalepa, *Cockroaches: ecology, behavior, and natural history*. JHU Press, 2007.

[62] M. H. Dickinson, "The initiation and control of rapid flight maneuvers in fruit flies," *Integrative and comparative biology*, vol. 45, no. 2, pp. 274–281, 2005.

[63] R. Olberg, A. Worthington, and K. Venator, "Prey pursuit and interception in

dragonflies," *Journal of Comparative Physiology A*, vol. 186, no. 2, pp. 155–162, 2000.

[64] D. Schaller, "Antennal sensory system of Periplaneta americana l." *Cell and tissue research*, vol. 191, no. 1, pp. 121–139, 1978.

[65] Y. Baba, A. Tsukada, and C. M. Comer, "Collision avoidance by running insects: antennal guidance in cockroaches," *The Journal of experimental biology*, vol. 213, no. 13, pp. 2294–2302, 2010.

[66] J. Zeil, R. Sandeman, and D. Sandeman, "Tactile localisation: the function of active antennal movements in the crayfish Cherax destructor," *Journal of Comparative Physiology A*, vol. 157, no. 5, pp. 607–617, 1985.

[67] S. Kapitskii, "Morphology of the antennae in the male of the americana cockroach Periplaneta americana," *Journal of Evolutionary Biochemistry and Physiology*, vol. 20, pp. 59–66, 1984.

[68] S. Timoshenko, *Theory of Elasticity*. McGraw-Hill, 1934.

[69] B. W. Quist and M. J. Hartmann, "Mechanical signals at the base of a rat vibrissa: the effect of intrinsic vibrissa curvature and implications for tactile exploration," *Journal of neurophysiology*, vol. 107, no. 9, pp. 2298–2312, 2012.

[70] R. C. Taylor, "Physical and physiological properties of the crayfish antennal

flagellum," *Journal of neurobiology*, vol. 6, no. 5, pp. 501–519, 1975.

[71] D. W. Kellogg, "Antennal biomechanics of house crickets (Acheta domesticus l.)," Master's thesis, University of Kansas, 2007.

[72] S. A. Hires, L. Pammer, K. Svoboda, and D. Golomb, "Tapered whiskers are required for active tactile sensation," *Elife*, vol. 2, 2013.

[73] L. Pammer, D. H. O'Connor, S. A. Hires, N. G. Clack, D. Huber, E. W. Myers, and K. Svoboda, "The mechanical variables underlying object localization along the axis of the whisker," *The Journal of Neuroscience*, vol. 33, no. 16, pp. 6726–6741, 2013.

[74] C. M. Williams and E. M. Kramer, "The advantages of a tapered whisker," *PLoS One*, vol. 5, no. 1, p. e8806, 2010.

[75] U. Saranli, M. Buehler, and D. E. Koditschek, "Rhex: A simple and highly mobile hexapod robot," *The International Journal of Robotics Research*, vol. 20, no. 7, pp. 616–631, 2001.

Vita

Alican Demir received his BS and MSE degrees in Mechanical Engineering from Johns Hopkins University, Whiting School of Engineering, MD, in 2007 and 2009 respectively. He worked and studied under the supervision of Prof. Noah J. Cowan in the LIMBS (Locomotion in Mechanical and Biological Systems) lab. During his MSE studies, he designed and developed a multi-segmented, modular sensory antenna with embedded computing as a research platform for robotic tactile sensing. Between 2009 and 2011, he worked as a full-time research specialist in the Laboratory for Computational Sensing and Robotics, where he developed various experimental setups for multi-sensory fusion in electric fish. For his PhD starting2011, he studied the mechanics and interplay between locomotion and environment through cockroach inspired tactile sensing. In 2012, he investigated flight stability of moths based on abdominal movements and successfully implemented the concept of inertial redirection of thrust to stabilize a

commercial quad-rotor. Throughout his graduate studies, Alican Demir was a teaching assistant for several courses including, Design and Analysis of Dynamical Systems, Freshman ME Labs and Manufacturing Engineering. He received the Creel Family Teaching Assistant Award in 2007 and 2008. Upon graduation, Alican will work in Clear Guide Medical as a senior mechanical Engineer.